STABILITY, TRANSFORMATION AND DETECTION OF TOPOLOGICAL MAGNETIC SPIN TEXTURES IN NANOSTRUCTURES

By

Nitish Mathur

A dissertation submitted in partial fulfillment of
the requirements for the degree of

DOCTOR OF PHILOSOPHY
(MATERIALS SCIENCE AND ENGINEERING)

at the
UNIVERSITY OF WISCONSIN–MADISON
2021

Date of final oral examination: May 6th, 2021

The dissertation is approved by the following members of the Final Oral Committee:
Song Jin, Professor – Chemistry
Chang-Beom Eom, Professor – Materials Science and Engineering
Jason Kawasaki, Assistant Professor – Materials Science and Engineering
Victor Brar, Assistant Professor – Physics
Daniel Rhodes, Assistant Professor – Materials Science and Engineering

PREFACE

STABILITY, TRANSFORMATION AND DETECTION OF TOPOLOGICAL MAGNETIC SPIN TEXTURES IN NANOSTRUCTURES

NITISH MATHUR, PHD

UNIVERSITY OF WISCONSIN-MADISON

2021

Topology, a branch of mathematics that successfully describes several fundamental physical phenomena in the field of condensed matter physics. Understanding the role of topology plays in materials science has led to the development of several material platforms which come under the category of topological materials. The properties associated with the topological states in materials are robust against the continuous transformation and small perturbations that do not change topology. Hence, the research behind the exploration and utilization of topological materials in a goal specific application is currently advancing with a frantic pace.

In magnetic materials, the marriage of topology and magnetism exists as a new form of magnetic ordering with whirlpool-like spin arrangements known as magnetic skyrmions. These topologically protected particle-like spin textures were first discovered a decade ago in non-centrosymmetric magnetic materials. Confining magnetic skyrmions in nanostructures leads to interesting fundamental insights on skyrmion stability and could provide convenient platforms for potential practical applications of skyrmions in information storage technology. In Chapter 1, I have introduced and summarized the recent advances on studying magnetic skyrmions in nanostructures of skyrmion hosting non-centrosymmetric materials (especially the cubic B20 materials) made *via* bottom-up synthesis or top-down fabrication methods. I further discussed

various real space imaging (such as Lorentz transmission electron microscopy or electron holography) or physical property measurement (such as magneto-transport) techniques that have been used to observe and detect these exotic magnetic domains in both nanostructure and bulk samples, which have proven critical to fully understanding them. The morphology and dimensionality of skyrmion hosting materials in stabilizing isolated magnetic skyrmions in confined geometry and their benefits are critical for the implementation in magnetic memory applications. In Chapters 3 and 4, I have presented a comprehensive study of purely electrical detection methods corroborated with real space observation of magnetic skyrmions. This allows us to develop a complete toolkit to investigate stability, magnetic phase transformation and detection of magnetic skyrmion in confined geometries of nanostructures. With these investigations, we extend our understanding of the three-dimensional spin structure (known as skyrmion strings) in confined geometries of nanostructures.

Magnetism mediated by symmetry breaking is ubiquitous in condensed matter systems as also depicted in case of non-centrosymmetric skyrmion hosts. Intrinsic crystal defects are often unavoidable during the growth processes of materials which break the local symmetry of the crystal in the vicinity of the defect site and could potentially influence the magnetic spin ordering. In Chapter 2, I have discussed the role of defects in controlling and manipulating the key fundamental properties in widely explored two-dimensional (2D) van der Waals (vdW) materials. Defect-tunable magnetism has not been studied in broad class of 2D magnetic van der Waals (vdW) materials. Furthermore, it might lead to an inaccurate interpretation of intrinsic magnetic ordering in 2D vdW magnets if the presence of crystal defects is not acknowledged with detailed structural characterization. In Chapter 5, I presented a study of defect-mediated ferromagnetism influenced by the presence of sulfur vacancy defects in strongly correlated 2D vdW

antiferromagnet of $NiPS_3$. These findings demonstrate the concept of tuning defect-mediated magnetic interactions to manipulate spin ordering in magnetic vdW materials. Interestingly, defects like dislocation in materials are distinguishable from other lattice imperfections as these are characterized by topological invariant known as Burgers vector and they fall under the category of topological defects. In Chapter 6, we have designed a first ever controlled vapor deposition method for the screw dislocation driven growth of layered vdW antiferromagnets, namely NiI_2 and $NiBr_2$. The presence of screw dislocation in magnetic vdW materials could allow the exploration of dislocation-spin interactions and magnetic spin structures that are governed by the principles of topology.

ACKNOWLEDGEMENTS

I can say with full confidence that this journey of graduate school at UW Madison could be not possible without the strong support of my family, friends, and mentors. I feel like a very lucky person to know these wonderful people and I express my deepest gratitude.

First and foremost, I like to thank my extremely supportive and loving parents, my father, Trilok Mathur and my mother, Bindu Mathur. Without their support and sacrifices, I will not be able to pursue and achieve any of my goals. My elder brother, Nitin Mathur, someone who I always admired throughout my life. He has perfectly played so my role in my life, such as a helpful brother, local guardian, guy with whom I discuss sports, movie recommender, someone who listens to my boring science monologues etc. etc. My sister-in-law, Anusha Mathur, is equally affectionate and caring like my brother and she is no less than a mother figure to me. Back at home in India, my brother, Abhishek Mathur, who is partner through my academic life – primary school to undergraduate college, always keeps me sane with his long and heated discussion regarding movies and cricket, even he is far away with a 12 hours' time difference. I like to thank my extended family as well for their encouragement and constant support during my time in graduate school.

I am extremely fortunate to have great mentors, who have impacted my growth and development as a curious scientist and a research professional. I would like to thank my advisor Prof. Song Jin for his unwavering support during my PhD research. I believe as a graduate student the synergy between curiosity and knowledge is a key ingredient for the scientific research. I am immensely impressed by Song's curiosity to explore new research avenues with the expertise and knowledge gained from the years of research work. Throughout my PhD journey, Song has never

discouraged me to explore variety of research topics and helped me to think, articulate and present big research questions that I was trying to solve. Song is a big proponent of “learning comes by doing and while doing things you will make mistakes” and he often shares his experiences during his academic career and pass that knowledge for the betterment of graduate students. His constant support is instrumental in smooth and safe transitioning from home-stay to the lab work during the pandemic. Apart from my advisor, I fortunate enough to have a caring, friendly, patient and very knowledgeable graduate mentor, Dr. Matthew J. Stolt. Besides the scientific knowledge I gained under his guidance, I was extremely impressed by his exceptional commitment to building community in our research group, the department, and beyond, which I feel is important for the overall development of a graduate student. Even after his graduation, he is always available and ready to help me whenever needed. I also like to thank all the past and current Jin group members who have created a fun and cooperative lab environment. I will really be going to miss attending and organizing the Jin group camping, summer/winter parties and group lunches.

I had a great opportunity to work with highly knowledgeable and hard-working collaborators during my PhD program, notably, Prof Yoshinori Tokura, Dr. Xiuzhen Yu, Dr. Kodai Niitsu and Dr. Fehmi S. Yasin and Dr. Fengmei Wang. Special mention to Neil Campbell for his constant support and expertise which enabled smooth operation of PMMS system in our lab - the instrument I have used extensively throughout my PhD research. I also like to thank my committee members for their valuable guidance throughout my academic journey at UW Madison, namely, Prof Chang-beom Eom, Prof Jason Kawasaki, Prof. Victor Brar, Prof. Mark Erickson, Prof Xudong Wang, and Prof. Daniel Rhodes. I like to thank the former and current support staff both at Chemistry and Materials Science Department, especially Diana Rhodes, Cynthia Rothwell, Char

Horsfall, Janna Pollock, Mike Bradley, Jeff Nielsen, Sue Martin-Zernicke, Arrietta Clauss and Jeanne S. Hamers.

Finally, I need to thank my group of amazing friends who made my journey of graduate school enjoyable and exciting. I am lucky enough to have a close and crazy group of friends in the Department of Chemistry itself, especially Matthew Hautzinger, Rebeca Fernandez, Lauren Whitmire, Zack Jones, Melissa Cendejas, Andjela Radmilovic, Jaya Borgatta and Aris Vasilopoulos. I can say with full confidence that food/ drinks taste much better, and places are so fun when they are around. I am thankful to be a part of two amazing teams of chemistry graduate students for the ultimate frisbee (team name: dank strats) and softball (team name: tadpoles) leagues. They are the best group of people to play these sports and share pitchers of beers. I am grateful for the close-knit group of friends and a support group I built during my PhD, especially with my roommates Aashrith Saraswathibhatla, Kshiteej Mahajan, Dr. Vivek Saraswat (who are also amazing cooks and taught me life-long cooking hacks) and my dear friends, Dr. Raunak Bardia, Dr. Arpit Agarwal, Dr. Yash Govind, Neha Godwal, Nidhi Tyagi, Kaivalya Molugu, Soumil Gurjar, Kunal Bhagat, Dr. Mrugank Bhatt, Debaditya Chatterjee, Dr. Swapnil Haria, Sukriti Singh and Kausik Chandrasekhar.

Of all the things which wisdom provides to make us entirely happy, much the greatest is the possession of friendship

- *Epicurus*

Table of Contents

Chapter 1 : Magnetic Skyrmions in Nanostructures of Non-centrosymmetric Materials..... 1

1.1 Introduction 1

1.2 Spin Textures and Crystal Symmetry..... 8

1.3 Evolution of Detection Techniques of Magnetic Skyrmions in B20 Materials 11

1.3.1 Reciprocal Space Detection of Magnetic Skyrmions in Bulk Crystals 11

1.3.2 Magnetic Susceptibility and Spectroscopy Detection of Skyrmions..... 13

1.3.3 Real Space Observation of Magnetic Skyrmions 15

1.4 Skyrmions in Nanostructured Geometry..... 19

1.4.1 Detection of Skyrmion Stability in NW Morphology using Cantilever Magnetometry..... 20

1.4.2 Magnetic Skyrmions in Various Nanostructure Morphologies 21

1.5 Electrical Detection of Skyrmions and Skyrmion Dynamics in Nanowires 24

1.5.1 Magnetoresistance Measurement for Determination of Skyrmion Stability Regime 25

1.5.2 Quantized Magnetoresistance Transitions of Isolated Skyrmion in Nanowires..... 27

1.5.3 Topological Hall Effect Detection and Skyrmions Dynamics in B20 Nanostructures 29

1.6 Summary and Outlook 33

1.7 Contribution to the research field from this work..... 35

Chapter 2 : Defects in Two-Dimensional Magnetic Van Der Waals Materials 44

2.1 Introduction..... 44

2.2 Vacancy Defects in Correlated Magnetic Van Der Waals Materials..... 45

2.3 Topological Defects in 2D Van Der Waals Materials..... 46

2.3.1 Screw Dislocation Driven Growth of Spiral 2D Van Der Waals Nanoplates 47

2.4 Contribution to the research field from this work..... 50

Chapter 3 : Electron Holography and Magnetotransport Measurements Reveal Stabilized Magnetic Skyrmions in $Fe_{1-x}Co_xSi$ Nanowires 53

3.1 Abstract 53

3.2 Introduction 53

3.3 Results and Discussion 56

3.3.1 Synthesis and Characterization of $Fe_{1-x}Co_xSi$ NWs 56

3.3.2 Real Space Observation of Magnetic Structures in $Fe_{0.75}Co_{0.25}Si$ NW 59

3.3.3 Temperature Dependent Magnetotransport Behavior of $Fe_{1-x}Co_xSi$ NW of Different Compositions 64

3.3.4 Assessment of the Critical Field for Magnetic Phase Transition from Magnetotransport Measurements 65

3.3.5 Representative Magnetic Phase Diagram 70

3.4 Conclusion 71

3.5 Experimental Section 71

3.5.1 Chemical Vapor Deposition Synthesis of $Fe_{1-x}Co_xSi$ Nanowires 71

3.5.2 Structural Characterization and Elemental Compositional Analysis 72

3.5.3 Electron holography of $Fe_{1-x}Co_xSi$ Nanowires 73

3.5.4 Magnetotransport measurements of $Fe_{1-x}Co_xSi$ Nanowires 74

Chapter 4 : In-Plane Magnetic Field-Driven Creation and Annihilation of Magnetic Skyrmion Strings in Nanostructures 79

4.1 Abstract 79

4.2 Introduction 79

4.3 Results and Discussion 82

4.3.1 Anisotropic and Sensitive In-Plane Magnetotransport Response in FeGe NWs during Magnetic Phase Transitions 82

4.3.2 Analysis of SkS Stability and Magnetotransport Features under In-Plane Magnetic Field in FeGe Nanostructures 84

4.3.3 Real Space Observation of SkS and its Magnetic Phase Transformations under Purely In-Plane Magnetic Field 88

4.3.4 Representative Magnetic Phase Diagram of FeGe Nanostructures under In-Plane Magnetic Field 92

4.4 Conclusion 93

4.5 Experimental Section 94

4.5.1 Synthesis and Structural Characterization of FeGe Nanostructures 94
4.5.2 Device fabrication for electrical measurements 95
4.5.3 Magnetotransport measurements 96
4.5.4 LTEM measurements 97
4.5.5 Micromagnetic Simulations 97

Chapter 5 : Defect-Mediated Ferromagnetism in Correlated Two-Dimensional Transition Metal Phosphorus Trisulfides 101

5.1 Abstract 101

5.2 Introduction 101

5.3 Results and Discussion 104

5.3.1 Synthesis and Structural Characterization of $Ni_{1-x}Co_xPS_3$ Nanosheets and Single Crystals 104
5.3.2 Determination of Sulfur Vacancy Defects in $Ni_{1-x}Co_xPS_3$ Samples 106
5.3.3 Defect-Mediated Ferromagnetic State in $Ni_{1-x}Co_xPS_3$ Nanosheets. 108
5.3.4 Governing Mechanism for the Defect-Mediated Magnetism in $Ni_{1-x}Co_xPS_3$ Nanosheets 111

5.4 Conclusion 114

5.5 Experimental Methods 115

5.5.1 Synthesis of $Ni_{1-x}Co_xPS_3$ ($0 \leq x < 0.5$) Nanosheets 115
5.5.2 Growth of $Ni_{1-x}Co_xPS_3$ ($0 < x < 0.5$) Single Crystals 115
5.5.3 Structural characterization 116
5.5.4 X-ray absorption spectroscopy 117
5.5.5 Magnetic measurements 117
5.5.6 Theoretical calculations 118

Chapter 6 : Growth and Characterization of Two-Dimensional Van Der Waals Magnets with Topological Defects 124

6.1 Abstract 124

6.2 Introduction 124

6.3 Results and Discussion 126

6.3.1 NiX_2: a layered antiferromagnet 126

6.3.2 Screw dislocation driven growth of NiX_2 127
6.3.3 Topography and complex stacking of spiral NiX_2 nanoplates..... 128
6.4 Conclusion..... 130

Appendix 1 : Supporting Information for Chapter 3* 133

Appendix 2: Supporting Information for Chapter 4* 142

Appendix 3: Supporting Information for Chapter 5* 154

List of Figures

Figure 1.1 : An introduction to magnetic skyrmions in the cubic B20 phase. (a) Magnetic moment vector map of a Bloch-type magnetic skyrmion. (b) Other spin structures present in cubic B20 structures such as the ground state helimagnetic phase and field polarized conical phase. (c) The cubic B20 crystal structure with single unit cell outlined as a box. (d) SANS diffraction pattern of a MnSi single crystal revealing magnetic skyrmion lattice phase (e) Magnetic phase diagram of MnSi mapped out using SANS. (f) LTEM image of skyrmion lattice structure under a weak magnetic field (50 mT) applied perpendicular to the $Fe_{0.5}Co_{0.5}Si$ thin film. [Panel b is reproduced with permission from Nano Lett. 10, 1605 (2010), Copyright 2010 ACS. Panel c is reproduced with permission from Phys. Rev. Lett. 120, 217201 (2018), Copyright 2018 American Physical Society. Panel d,e are reproduced with permission from Science 323, 915 (2009), Copyright 2009 AAAS. Panel f is reproduced with permission from Nature 465, 901 (2010), Copyright 2010 Springer Nature Limited]. 2

Figure 1.2 : Schematic of a magnetic racetrack memory device design. (a) Example of a magnetic racetrack memory device with ferromagnetic domains as the information bits. (b) Cartoon representation of electron flow in the presence of emergent magnetic field of magnetic skyrmions which results in THE and skyrmion motion under spin transfer torque. (c) An envisioned design of magnetic racetrack memory device where skyrmion are binary information bits and spin current moves the domains along the racetrack. The inset shows the array of racetracks arranged in three dimensions for high density memory storage application. [Panel a is reproduced with permission Nat. Mater. 11, 372 (2012), Copyright 2012 Springer Nature Limited. Panel b is reproduced with permission from Nat. Nanotechnol. 8, 899 (2013), Copyright 2013 Springer Nature Limited. Panel c is reproduced with permission from Sci. Rep. 5, 15773 (2015). Copyright 2015 Springer Nature Limited] 5

Figure 1.3 : Magnetic skyrmion stability in B20 nanostructures and the crystal morphology of B20 NWs and various bottom-up synthesized nanostructures grown via CVD growth. (a) Magnetic phase diagrams showing skyrmion phase stability (a) bulk crystals (b) thin plate, and (c) nanowire samples of MnSi, respectively. (d) SEM image of a MnSi NW with a smooth (111) surface and <110> growth direction. (e) A cross-sectional TEM image of the MnSi NW with a merohedral twin boundary, where the (001) twin plane is parallel to the <110> growth direction. (f) High-resolution TEM image of the cross-section at the twin boundary. CVD grown (g) well faceted $Fe_{1-x}Co_xSi$ microwire along the <110> growth direction and (h) FeGe NW along the <111> growth direction. Non-conventional morphology such as (i) nanoplates, (j) nano-octahedra, (k) nanorod of FeGe B20 nanostructures grown using CVD process. [Panel a-c are reproduced with permission from Nano Lett. **13**, 3755 (2013), Copyright 2013 ACS. Panel d-f are reproduced with permission from Nat. Commun. **6**, 7637 (2015), Copyright 2015 Springer Nature Limited, Panel g is reproduced with permission from ACS Nano **13**, 7833 (2019), Copyright 2019 ACS. Panel h, j, k are reproduced with permission from Nano Lett. **17**, 508 (2017), Copyright 2017 ACS. Panel i is reproduced with permission from Adv. Funct. Mater. **29**, 1805418 (2019), Copyright 2019 Wiley-VCH]. 7

Figure 1.4. Magnetic phase determination using magnetic susceptibility and spectroscopy measurements. (a) Magnetic susceptibility measurements of bulk $Fe_{0.95}Co_{0.05}Ge$ powder using ACMS shows transitions in the AC field sweeps that are characteristic of a skyrmion phase, and the relevant magnetic phase transitions have been highlighted with dashed lines used to plot (b) the magnetic phase diagrams for $Fe_{0.95}Co_{0.05}Ge$ illustrating the stability for the skyrmion phase as well as the existence of other relevant magnetic phases such as helimagnetic, conical, field polarized, and paramagnetic states. (c-f) All-electrical broadband spectroscopy spectra $\Delta|S_{21}|$ for MnSi at various magnetic fields at T = 27.5 K. (g) The corresponding resonance frequencies (marked by arrows) as a function of applied magnetic field calculated for different temperature (below T_c). (h) Illustration of the anticlockwise and clockwise gyration modes as well as the breathing mode of the skyrmion lattice phase at different times t during a period τ. [Panel a, b are reproduced with permission from Chem. Mater. **30**, 1146 (2018), Copyright 2018 ACS. Panel c-h are reproduced with permission from Nat. Mater. **14**, 478 (2015), Copyright 2015 Springer Nature Limited]..... 14

Figure 1.5 : Real space observation of magnetic skyrmion in B20 nanostructures using LTEM and EH. LTEM observation of B20 FeGe NW show no magnetic contrast in zero magnetic field for (a) In-focus, (b) over-focused, and (c) under-focused LTEM images of the NW with zero magnetic field, showing the striped magnetic contrast corresponding to the helical phase. (d) LTEM images of an FeGe NW obtained at 95 K shows a skyrmion chain state desired for racetrack memory application. (e) Magnetic phase diagram of a $Fe_{0.97}Co_{0.03}Ge$ nanoplates mapped using three different detection techniques, which supports the LTEM observation of (f) helimagnetic and (g) skyrmion lattice phase formation. Real space observation of skyrmion spin texture via electron holography conducted on $Fe_{0.5}Co_{0.5}Si$ thin film shows (h) surface plot of the absolute phase shift in the vicinity of the skyrmion. (i) Electron phase shifts of the helimagnetic and skyrmion lattice phase as a function of sample thickness (experiments carried out in 300 kV and 1000 kV microscopes) with the schematic inset showing the three-dimensional spin structure of a skyrmion. (j-m) Electron holography imaging experiments conducted on a $Fe_{0.75}Co_{0.25}Si$ NW sample: Magnetic phase contrast images show (j) helimagnetic and (k) skyrmion phase in $Fe_{0.75}Co_{0.25}Si$ NW. The skyrmion enclosed in the rectangle in (k) in the forms of (l) its color-coded display (using the color wheel) and (m) magnetic phase contrast map. Scale bar in (j,k) is 50 nm and (l,m) is 30 nm. [Panel a-d are reproduced with permission from Nano Lett. **17**, 508 (2017), Copyright 2017 ACS. Panel e-f are reproduced with permission from Adv. Funct. Mater. **29**, 1805418 (2019), Copyright 2019 Wiley-VCH. Panel h, i are reproduced with permission from Nat. Nanotechnol. **9**, 337 (2014), Copyright 2015 Springer Nature Limited, Panel j-m are reproduced with permission from ACS Nano **13**, 7833 (2019), Copyright 2019 ACS]. 17

Figure 1.6 : Cantilever magnetometry of a MnSi NW (a) Experimental cantilever setup with the NW in green attached to a Si cantilever. (b) Representative field sweep with the different magnetic states outlined. The change in the resonance frequency of the cantilever, Δf, is directly related to change in magnetization of the NW. (c) Temperature dependence of the frequency shifts in the experiment. The strong dips related to the skyrmion phase exist only in the region where a

skyrmion lattice has been previously shown to form. This figure is reproduced with permission from Nano Lett. **15**, 4839 (2015), Copyright 2015 ACS. 21

Figure 1.7 : Real space LTEM and EH imaging studies of different nanostructures of the FeGe made by FIB fabrication techniques (a) LTEM images of FeGe nanoribbons with different width highlighting the transformation of skyrmion lattice to single chain of skyrmions with varying width at 220 K. (b) Magnetic phase diagram for the nanoribbons of different widths, showing the ability of the thin ribbons to stabilize a single skyrmion chain. (c) EH imaging of an FeGe nanowedge that allows for visualization of change in magnetic texture with varying width and magnetic field, scale bar is 150 nm. The skyrmions squeeze to fit in at smaller widths while at larger widths and lower fields the skyrmions elongate along the width direction. These images also highlight the formation of skyrmions from the helical turns. (d) SEM image and schematic illustration of the fabrication of an FeGe nanodisk using FIB milling. The inset in (d) shows a TEM bright-field image of the cross -section of the nanodisk. (e) Magnetic field dependence of the in-plane magnetization of a target skyrmion stabilized in FeGe nanodisk. (f) The FIB fabricated wedge shaped FeGe structure used for real space visualization of chiral bobbers via EH. (g) Schematic representation of the spin structures for a magnetic chiral bobber and a skyrmion tube. (h) Electron holography image on the wedge shaped FeGe with red arrows indicating weak contrast objects that are identified as chiral bobbers. (i) Phase-shift profiles as a function of position that correspond to the bands of the same color marked in (h). [Panel a, b are reproduced with permission from Nat. Commun. **6**, 8504 (2015), Copyright 2015 Springer Nature Limited. Panel c is reproduced with permission from Nat. Commun. **8**, 15569 (2017), Copyright 2017 Springer Nature Limited. Panel d, e are reproduced with permission from Phys. Rev. Lett. **119**, 197205 (2017), Copyright 2017 Americal Physical Society. Panel f-i are reproduced with permission from Nat. Nanotechnol. **13**, 451 (2018), Copyright 2018 Springer Nature Limited]. 23

Figure 1.8 : Magnetotransport measurements on NWs of B20 skyrmion hosting materials. Magnetoresistance (MR) of a 400 nm diameter MnSi NW (inset a) in a parallel configuration (a) Constant applied field MR measurement with a sweeping temperature highlight the helimagnetic transition. (b) Isothermal MR field sweeps that are used to identify the magnetic transition critical fields. (c) Offset MR-H isotherms between 10-36 K of an $Fe_{0.81}Co_{0.19}Si$ NW in parallel configuration. (d) Second order derivatives of the MR-H isotherms in panel (c) more clearly reveals the critical magnetic state transitions. The black arrows (H_{C1}) and red arrows (H_{C2}) highlight the critical fields for the magnetic state transitions at different temperatures. Values for increasing and decreasing field strength are denoted by the superscripts "+" and "-", respectively. e) The observed quantized transitions of MR of a MnSi NW with a diameter of ~ 40 nm and f) the corresponding illustration of the calculated spin states of the various skyrmion cluster states. [Panel a, b are reproduced with permission from Nano Lett. **14**, 2026 (2014), Copyright 2014 ACS. Panel c, d are reproduced with permission from ACS Nano **13**, 7833 (2019), Copyright 2019 ACS. Panel e, f are reproduced with permission from Nat. Commun. **6**, 7637 (2015), Copyright 2015 Springer Nature Limited]..... 27

Figure 1.9 : Skyrmion detection and electrodynamics via THE measurements of nanostructures. (a) SEM image of a $Fe_{0.97}Co_{0.03}Ge$ nanoplate with metal contacts fabricated as a Hall device setup

shown in the schematic in panel (b). (c) Extracted THE signal of the $Fe_{0.97}Co_{0.03}Ge$ nanoplate obtained from isothermal field sweeps at various temperatures with the corresponding (d) heat map representation of the extracted THE resistivity as a function of the temperature and magnetic field. (e) Extracted THE signal obtained from the Hall device fabricated on a MnSi NW shown in the inset of (e). (g) Maximum THE signal obtained from a MnSi NW as a function of current density that can be fitted as exponential function to estimate the skyrmion drift velocity, vd. (h) Skyrmion drift velocity as a function of current density in a MnSi NW. Extrapolation of a linear fit allows for the estimation of the critical current density, jc, required for skyrmion motion in MnSi NWs. [Panel a,c,d are reproduced with permission from Adv. Funct. Mater. 29, 1805418 (2019), Copyright 2019 Wiley-VCH. Panel b,e-f are reproduced with permission from Nat. Commun. 6, 8217 (2015), Copyright 2015 Springer Nature Limited]. 31

Figure 2.1 : Topological crystalline defects. (a) Illustration of a hollow cylinder cut along the plane *S* and long the define line ξ_0. Linear defects such as (b,c) edge and (d) screw dislocations marked with respective Burgers vector *b*. (e,f,g) Twist defects shown as disclinations marked with Frank vector ω. (h) Schematic of a dislocation incorporated inside a loop marked with yellow trace known as Burgers circuit. (i) The topological invariant, b , is independent of the shape of the Burgers circuit if it incorporates the dislocation. Panels a-g are reproduced with permission from *Nature* **2014**, *507*, 51. Copyright 2014 Springer Nature Limited. Panels h,1 are reproduced with permission from *J. Phys. Condens. Matter* **2019**, *31*, 083001. Copyright 2019 IOP Publishing. 47

Figure 2.2: SDD growth of spiral nanoplates. (a) Growth rate (R) dependence on supersaturation (σ). Progression of screw dislocation nucleation originating from two adjacent individual 2D layers. Propagation of screw dislocation by acting as a nucleation site for atoms, growing as a spiral nanoplate. Panel a is reproduced with permission from *Science* **2010**, *328,* 476. Copyright 2010 AAAS. Panel b is reproduced with permission from *ACS Nano* **2014**, *8*, 11543. Copyright 2014 ACS. Panel c is reproduced with permission *Nano Lett.* **2014**, *14*, 6418. Copyright 2014 ACS. 48

Figure 2.3 : Stacking configuration of SDD grown WS_2 nanoplates (a) AFM image of the triangular spiral as represented in schematic in panel (b). (c) Layer stacking of triangular spiral nanoplate showing AbA order of noncentrosymmetric 2H layers marked by + stacking of individual layer. (d) AFM image of the hexagonal spiral formed by two triangular spirals stacked after 60° rotation represented in schematic in panel (e). (f) Layer stacking of hexagonal spiral nanoplate AbA stacking and BaB (marked by -) stacking of adjacent layers resulting a centrosymmetric structure. (g) AFM image of the mixed spiral formed by three triangular spirals where two triangular spirals and one triangular stacked after 60° rotation represented in schematic in panel (h). (i) Layer stacking of mixed spiral nanoplate 2 AbA (++) layers and BaB (-) stacked together resulting a non-centrosymmetric structure. Shinny grey are W and green atoms are S. Scale bar in a, d and g are 500 nm. Figure 3 is reproduced with permission from *J. Am. Chem. Soc.* **2017**, *139*, 3496. Copyright 2017 ACS..... 49

Figure 3.1 : (a) Representative SEM images of as-synthesized $Fe_{1-x}Co_xSi$ NWs on a Si (100) substrate. The magnified inset image reveals the cross-section of the thick NWs. (b) Powder X-

ray diffraction pattern of the $Fe_{1-x}Co_xSi$ as-grown NWs in comparison with both FeSi (red) and CoSi (blue) standard patterns reproduced from JCPDS PDF#00-038-1397 and JCPDS PDF#00-008-362, respectively. The inset clearly shows the two most intense peaks of $Fe_{1-x}Co_xSi$ NWs lie between the standard peaks of FeSi and CoSi. (c) SEM-EDS elemental mapping of $Fe_{1-x}Co_xSi$ NWs on reacted Si substrate. (d) Low magnification HAADF-STEM image taken on an 85 nm thick NW, SEM image of which is shown in the inset. (e) High magnification HAADF-STEM image of the (111) crystallographic plane confirmed by the SAED pattern shown in the inset. (f) Low magnification ABF-STEM image at the edge of the NW with inset image of FFT pattern reveals the growth direction of the NW along [110] crystallographic axis. 57

Figure 3.2 : Magnetic phase contrast (φ_{MAG}) images of the $Fe_{0.75}Co_{0.25}Si$ NW obtained *via* off-axis EH observations. (a-c) φ_{MAG} images at 10, 20, and 30 K with no applied magnetic field. (d-f) φ_{MAG} images at 10, 20, and 30 K with an out-of-plane applied magnetic field of 100 Oe. (g-i) φ_{MAG} images at 10, 20, and 30 K with an out-of-plane applied magnetic field of 200 Oe. Upper and lower panels display the φ_{MAG} distribution in the forms of color-coded $\nabla\varphi_{MAG}$ and $\cos(300\varphi_{MAG})$, respectively. Color hue and brightness represent $\text{atan2}(\nabla\varphi_{MAG})$ and $|\nabla\varphi_{MAG}|$; refer to the color wheel given at the bottom right. Scale bar for (a-i) is presented at the bottom right. (j) Magnified images of the red rectangles shown in (i). Scale bar is 30 nm. 61

Figure 3.3 : Temperature dependent MR of different $Fe_{1-x}Co_xSi$ NWs. Temperature dependent resistivity of (a) NW1 (sample A; inset shows a SEM image of a representative four probe device), (b) NW2 and NW3 (Sample B). Temperature dependent MR of NW3 with applied magnetic field (c) $H_{\parallel}$ and (d) $H_{\perp}$ 65

Figure 3.4 : $H_{\parallel}$ MR-H isotherms and critical field assessment for NW3. (a) Offset MR-H isotherms between 10-36K, (b) The specific MR-H isotherm at 20K, and its first (dMR/dH) and second order (d^2MR/dH^2) derivative with respect to forward (bold color) and backward (faded color) field sweep direction. The dashed lines mark the peaks on d^2MR/dH^2 curve which represent critical fields for the magnetic transitions. (c) Offset second order derivatives of the MR-H isotherms in panel (a). The black arrows (H_{C1}) and red arrows (H_{C2}) highlight the critical fields for the magnetic state transitions at different temperatures. Values for increasing and decreasing field strength are denoted by the superscripts "+" and "-", respectively. 68

Figure 3.5 : Summary magnetic phase diagram. H_{C1} (black squares) and H_{C2} (red stars) are critical fields for magnetic state transitions as determined by magnetotransport measurements of NW3 ($Fe_{0.81}Co_{0.19}Si$) 70

Figure 4.1 : Anomalous and anisotropic magnetotransport features of the FeGe NW in the parallel configuration. (a) SEM image of a representative four-probe device of NW1 with labelled current and voltage probes used in the transport measurements. The dashed black box marks the probing area of the NW between the voltage leads. Scale bar is 4 μm. (b) MR- $H_{||}$ curves in the temperature range of 10 – 290 K with bold and faded color corresponding to decreasing and increasing field sweeps, respectively. MR-$H_{||}$ curves are offset for clarity. (c) MR-H curves at 10 K showing strong anisotropic MR response in the parallel configuration in comparison with the MR-H curve in the

perpendicular configuration. (d) Enlarged inset of MR-$H_{||}$ curve at 10 K with increasing (top panel) and decreasing (middle panel) field sweeps (represented by black arrows) highlighting the apparent hysteresis, with the corresponding $dMR/dH_{||}$ curve (bottom panel) of the latter with critical fields H_{C1}, H_{C2} and H_{sat} indicated as vertical lines. Values for increasing and decreasing field strength are denoted by the superscripts "+" and "-", respectively. 83

Figure 4.2 : Illustration of the interconversions of various magnetic states in NWs revealed by representative MR responses. The dependence of MR signal in the (a) parallel magnetic field configuration for a FeGe NW with the orientation of chiral modulation vector (Q) of non-collinear spin textures: (b-d) the schematics of spin textures and its 2D projection of chiral domains with the corresponding Q in the parallel configuration of FeGe NW shown for (b) helical, (c) SkS and (d) conical phase. The schematic shown in (b-d) depicts a ~ 90° flipping of the Q during the transformation of spin states with increasing and decreasing field strength. Selected MR responses of NW1 in decreasing field sweeps plotted as MR-$H_{||}$ curves with the corresponding $dMR/dH_{||}$ curves at (e) 60 K, (f) 120 K, and (g) 180 K for the assessment of the critical fields (H_{C1}, H_{C2} and H_{sat}) that are marked as vertical lines..... 85

Figure 4.3 : LTEM imaging of a $Fe_{0.95}Co_{0.05}Ge$ NPL. (a) Bright-field TEM image and SAED pattern (inset) of the single-crystal $Fe_{0.95}Co_{0.05}Ge$ NPL, with its two edges along the crystallographic direction (110) making an angle of 60°. (b) EELS thickness profile indicates uniformly thin NPL. LTEM images collected under (c) 0 Oe (230 K) and (d) $H_{\perp}$~300 Oe (240 K) show ground state helical stripe pattern and hexagonal SkL, respectively. (e) Schematic of the LTEM configuration for imaging magnetic spin textures such as SkS, where $H_{||}$ and incident e-beam are parallel and perpendicular to the NPL basal plane, respectively. SkS are aligned parallel to $H_{||}$ with the spin texture modulation vector (Q_{SkS}) in the plane perpendicular to $H_{||}$. (f) Schematic free-energy landscape for the transformation of metastable SkS, generated by rapid field cooling at 230 K and 150 K while holding constant $H_{||} = -230$ Oe. A series of defocused-LTEM images shown at 150 K (g-k) and 230 K (l-p). The increase of $H_{||}$ from − 200 Oe to 200 Oe at T = 230 K stimulated a field-driven transformation of metastable stable SkS (g) to the helical phase (h-i) and back to the thermodynamically stable SkS (k). At 150 K, the metastable SkS (l) show clear signature of flexible bending (m,n) away from the edges of the NPL before it reaches the transition state of disordered helical phase (o) upon which the metastable SkS annihilate and transform to a multi-Q helical phase (p). The $H_{||}$ direction is ~10° from the long edge of the NPL as marked in g, j. All scale bars are 500 nm..... 89

Figure 4.4 : Summary $H_{||}$-T plots of FeGe nanostructures. The critical fields for the magnetic phase transitions (H_{C1}, H_{C2} and $H_{||\,sat}$) were inferred from the MR measurements under $H_{||}$ on FeGe NW1 and $Fe_{0.97}Co_{0.03}Ge$ NPL below T_c ~ 280 K. The vertical red lines represent the temperature above which the conical phase tends to destabilize as detected by MR measurements. The critical fields displayed are averaged (with error bars) for positive and negative applied magnetic fields with increasing and decreasing field sweeps. 93

Figure 5.1 : Structural characterization of $Ni_{1-x}Co_xPS3$ ($0 \leq x < 0.5$) NS. a, Crystal structure model of bilayer $Ni_{1-x}Co_xPS_3$ with one pair of neighboring octahedral coordination units (bottom). b,

Powder X-ray diffraction patterns of various $Ni_{1-x}Co_xPS3$ NS samples in comparison with the standard monoclinic $NiPS_3$ (PDF# 33-0952) and $CoPS_3$ (PDF #78-0498). The broad peak at $2\theta \sim 26^o$ in all PXRD patterns comes from the carbon cloth. **c,** Energy dispersive spectroscopy (EDS) mapping and **d**, the corresponding spectrum of a $Ni_{0.68}Co_{0.32}PS_3$ NS show uniform distribution of constituent elements. **e,** HAADF-STEM image of a $Ni_{0.68}Co_{0.32}PS_3$ nanosheet collected from the $Ni_{0.68}Co_{0.32}PS_3$ NS sample on carbon cloth shown in the inset SEM image. **f,** SAED pattern of the $Ni_{0.68}Co_{0.32}PS_3$ nanosheet along the [001] zone axis. **g,** Atomic force microscopy image of a $Ni_{0.68}Co_{0.32}PS_3$ NS transferred onto Si/SiO_2 substrate, showing a thickness ~ 5.6 nm. **h**, Raman spectra of various $Ni_{1-x}Co_xPS_3$ ($0 \leq x < 0.5$) NS..... 105

Figure 5.2 : Structural characterization by *X*-ray absorption spectroscopy (XAS) and electron spin resonance (ESR) spectroscopy of various $Ni_{1-x}Co_xPS_3$ samples. a-b, Ni *K*-edge (a) and Co *K*-edge (b) XANES spectra of $Ni_{0.68}Co_{0.32}PS_3$ NS and single crystals together with NiO, Ni foil, and Co foil, pyrite-type CoS_2, Co_3O_4, where pre-edge peak represents 1s → 3d (e_g*) transition. c, First-shell fitting (Ni-S) of Fourier transform of EXAFS spectra for $NiPS_3$ NS, $Ni_{0.68}Co_{0.32}PS_3$ NS and single-crystals. The decreased coordination number around Ni site was obtained in $Ni_{0.68}Co_{0.32}PS_3$ NS. EXAFS spectra were fitted using the FEFF code 6.01 based on the optimized $NiPS_3$ and $Ni_5Co_3P_8S_{24}$ structures (inset shows the nearest coordination of Ni site). d, ESR spectra of $Ni_{0.68}Co_{0.32}PS_3$ NS in comparison with the $NiPS_3$ NS and $Ni_{0.68}Co_{0.32}PS_3$ single crystal, measured at 90 K..... 107

Figure 5.3 : Characterization of magnetic properties of selected NS and single crystals of $Ni_{1-x}Co_xPS_3$. a, Temperature dependence of the ZFC magnetization measured at H= 200 Oe on various $Ni_{1-x}Co_xPS_3$ NS (x = 0, 0.32, 0.40) and the $Ni_{0.68}Co_{0.32}PS_3$ single crystal. **b**, *M-H* curves measured at 5 K of various $Ni_{1-x}Co_xPS_3$ NS (x = 0, 0.12, 0.32, 0.40) in comparison with that of $Ni_{0.68}Co_{0.32}PS_3$ single crystal. **c**, *M-H* curves of the $Ni_{0.60}Co_{0.40}PS_3$ NS at different temperatures. Magnetic hysteresis is clearly observed at low temperatures below 100 K..... 110

Figure 5.4 : Theoretical calculations of the electronic structures and spin configurations in $NiPS_3$ with and without *S* vacancy (S_v). a-b, The illustrations of the exchange interactions in a hexagonally arranged lattice of Ni neighbors in $NiPS_3$ mediated *via* S atoms. **c,** Top view of a $NiPS_3$ monolayer with alternating ferromagnetic chains marked with dashed black boxes, coupled antiferromagnetically throughout the crystal lattice. **d, f,** Spin-polarized projected density of state (PDOS) and (**e, g**) the corresponding illustrations of the magnetic moment distribution of antiferromagnetic $NiPS_3$ without S vacancy (**d,e**) and $NiPS_3$ with S vacancy (**f, g**). Fermi energy is set to zero. 112

Figure 6.1 : Crystal structure of NiX_2 (a) Crystal model of NiX_2 oriented normal to c-axis. (b) Spin arrangement of layered antiferromagnetic NiX_2 with trigonal unit cell drawn by blue dashed line. 126

Figure 6.2 : Controllable growth of spiral NiX_2 (a) Schematic of the physical vapor deposition set up for NiX_2 NPL synthesis. (b) Overview optical microscopy image of $NiBr_2$ nanoplates growing flat all over the freshly cleaved mica substrate. (c) Powder X-ray diffraction pattern of $NiBr_2$

(PDF# 03-0580) nanoplates on mica substrate with only high intensity (00*l*) peaks. (d) Overview optical microscopy image of NiI_2 nanoplates growing vertically and flat over the Si substrate. (e) Powder X-ray diffraction pattern of NiI_2 (PDF# 03-0473) on Si substrate reveals growth of phase pure NiI_2 nanoplates..... 127

Figure 6.3 : Topography and stacking of spiral NiX_2 (a) OM image of a spiral $NiBr_2$ nanoplate on mica substrate. (b) Corresponding AFM characterization shows a triangular topology of the spiral. (c) The step heigh profile reveals monolayer spiral growth as represented in a schematic in panel (d). (e) OM image of a spiral NiI_2 nanoplate on Si/SiO_2 substrate. (f) Corresponding AFM characterization shows hexagonal topology of the spiral. (g) The step heigh profile reveal formation of two multilayer spiral sharing a single dislocation core as represented in a schematic in panel (h)..... 129

Figure 6.4 : (a) $NiBr_2$ nanoplate (OM image in the inset) with two spirals with same handedness separately growing from two dislocation core. (b) $NiBr_2$ nanoplate (OM image in the inset) with no apparent spiral growth. Scale bar in both images shown in the inset of panel a,b is 50 μm. 130

List of Tables

Table 1.1 : Summary of bulk materials known to host skyrmion and skyrmion-like spin textures. The following columns of the table provide information including the space group, ordering temperature (T_c), skyrmion domain size, as well as the skyrmion type..... 10

Table 2.1: Summary of magnetic ordering of antiferromagnetic transition metal phosphorus trichalcogenides, MPX_3. The following columns of the table provide information including the antiferromagnetic spin arrangement and ordering temperature (T_N) 46

Chapter 1 : Magnetic Skyrmions in Nanostructures of Non-centrosymmetric Materials*

1.1 Introduction

Understanding the role of topology plays in materials science and condensed matter physics has become an exploding field of research in the last few decades. A new page in this field was turned in 2009 with the experimental discovery of a topologically protected particle-like spin texture known as magnetic skyrmions found in a single crystal of cubic B20 noncentrosymmetric magnetic material.[1-5] This name originates from the Skyrme model that was developed in nuclear physics to describe configurations of stable localized particle-like excitations in field theory.[3] Skyrmions are exotic vortex-like magnetic spin textures in which the central spin is anti-aligned and the outer spins are aligned with the externally applied magnetic field (Figure 1.1a). The non-collinear spin structures, such as helimagnetic, conical (Figure 1.1b) and skyrmion orderings, are most commonly a result of a direct thermodynamic competition between the ferromagnetic exchange interaction and the Dzyaloshinskii-Moriya exchange interaction (DMI).[4] The arrangement of spins within a single skyrmion can wrap a sphere, which is generally characterized with non-zero topological charge known as the skyrmion winding number (w) defined by

$$w = \frac{1}{4\pi}\int n.\left(\frac{\partial}{\partial x}n \times \frac{\partial}{\partial y}n\right) d^2r;\ \ n = m/|m| \qquad (1)$$

where m is the local magnetic moment.[5] Based on the integral value of the skyrmion number and symmetry of crystal structure, topologically non-trivial spin textures including magnetic skyrmions could have different internal spin arrangements.[2,5] A skyrmion lattice and nanometer

*This chapter is written in collaboration with Stolt, M. J. and Jin, S.

size skyrmion domain was first reported for a Bloch-type skyrmion which was experimentally found in metal monosilicides with non-centrosymmetric B20 crystal structure (Figure 1.1c).[5,6]

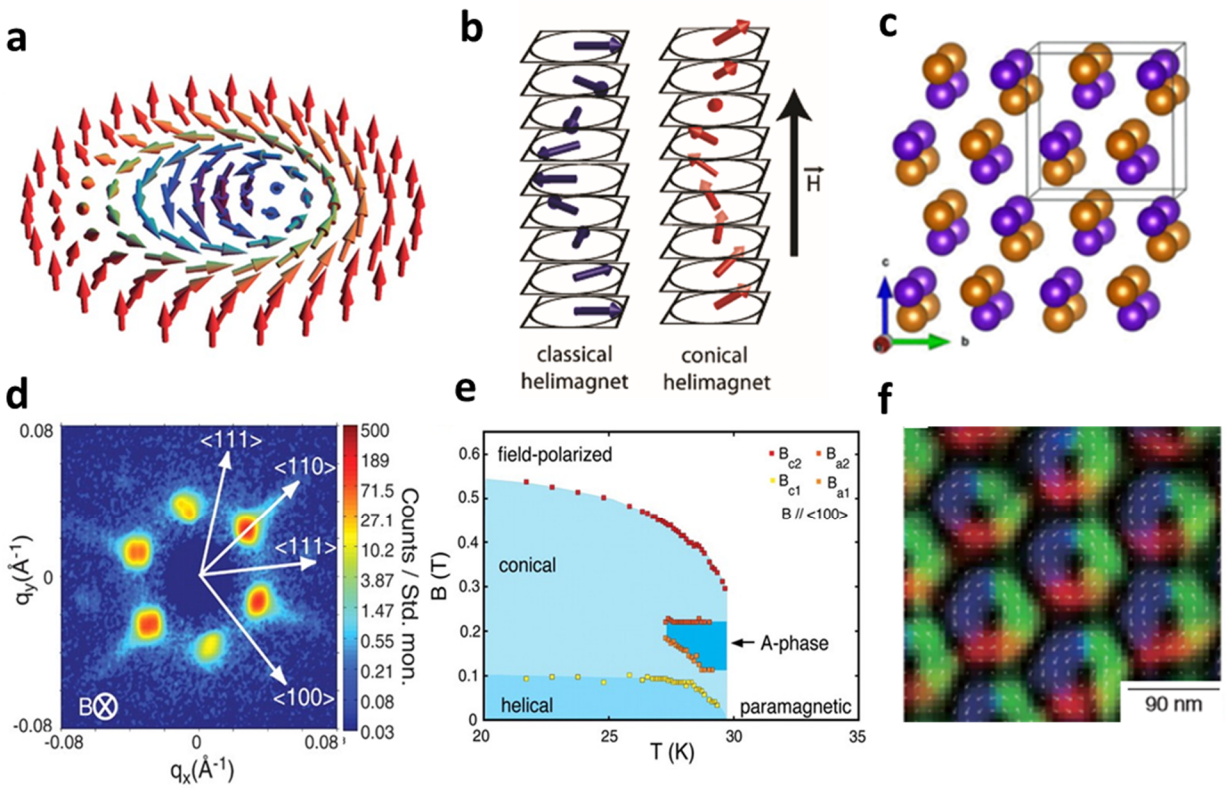

Figure 1.1 : An introduction to magnetic skyrmions in the cubic B20 phase. (a) Magnetic moment vector map of a Bloch-type magnetic skyrmion. (b) Other spin structures present in cubic B20 structures such as the ground state helimagnetic phase and field polarized conical phase. (c) The cubic B20 crystal structure with single unit cell outlined as a box. (d) SANS diffraction pattern of a MnSi single crystal revealing magnetic skyrmion lattice phase (e) Magnetic phase diagram of MnSi mapped out using SANS. (f) LTEM image of skyrmion lattice structure under a weak magnetic field (50 mT) applied perpendicular to the $Fe_{0.5}Co_{0.5}Si$ thin film. [Panel b is reproduced with permission from Nano Lett. 10, 1605 (2010), Copyright 2010 ACS. Panel c is reproduced with permission from Phys. Rev. Lett. 120, 217201 (2018), Copyright 2018 American Physical Society. Panel d,e are reproduced with permission from Science 323, 915 (2009), Copyright 2009 AAAS. Panel f is reproduced with permission from Nature 465, 901 (2010), Copyright 2010 Springer Nature Limited].

This first experimental observation of magnetic skyrmions was in a single crystal of MnSi with the cubic B20 crystal structure using small angle neutron scattering (SANS).[5] These experiments revealed scattering patterns with 6-fold symmetry in the temperature and magnetic

field region of the so-called "A-phase" (magnetic skyrmion phase) of MnSi (Figure 1.1d). The circular domains of magnetic skyrmions arrange into a hexagonal lattice, which leads to this scattering pattern with 6-fold symmetry. SANS experiments at different applied magnetic field and temperatures allowed for the mapping of the entire magnetic phase diagram of MnSi below the helimagnetic transition temperature, T_c. The magnetic phase diagram of MnSi, like other skyrmion hosting materials, includes many complex magnetic phases including the helimagnetic, conical, field-polarized, as well as the magnetic skyrmion (Figure 1.1e).

The periodicity of the non-collinear spin texture is defined by the ratio of the ferromagnetic exchange and DMI strengths, where an increasing DMI will lead to a shorter spin structure periodicity.[7] However, for a non-zero DMI to exist, the material at hand must lack inversion symmetry.[8] Non-centrosymmetric B20 cubic crystal structure (space group: $P2_13$) such as the metal monosilicides, monogermanides and their alloys that include MnSi,[5,9,10] $Fe_{1-x}Co_xSi$,[6] FeGe,[11,12] MnGe,[13] fulfil this requirement due to their atomic arrangements (Figure 1.1c). The intrinsic DMI produced by the non-centrosymmetric crystal structure due to spin-orbit interaction, also known as bulk DMI, gives rise to a relatively large DMI strength which leads to periodicity of less than 100 nm for both the helimagnetic and skyrmion phases. The overall symmetry of the crystal system leads to the formation of a chiral Bloch-type skyrmion with a vortex-like spin structure that can be visualized in real space using magnetic contrast imaging techniques such as Lorentz transmission electron microscopy (LTEM) (Figure 1.1f).[6] However, the window of applied magnetic field and temperature where the skyrmions exist is drastically different in the various cubic B20 compounds.[5,9] These stability windows in each of the magnetic phase diagrams of each known skyrmion material have been mapped using some combination of SANS, magnetic contrast imaging and/or magnetic susceptibility measurements as discussed later.

The domain size of skyrmions formed by the bulk DMI is generally less than 100 nm and down to 3 nm depending on the material. The ability of the magnetic skyrmion domain to form in such small sizes compared to ferromagnetic domains is likely tied to the topology of the spin structure that prevents them from being destroyed by small variations in applied magnetic field and temperature. The topological protection, thermal stability and small magnetic domain of the skyrmion is of interest to magnetic information storage research. Therefore, the skyrmion domain size, a_{sk}, provide an opportunity to break the so-called super paramagnetic limit of magnetic storage using ferromagnetic domains.[14] Superparamagnetism is common in most magnetic nanoparticles and results in ferromagnetic materials losing their ability to maintain the permanent magnetization required for non-volatile magnetic information storage devices.[15] In addition to their small domain size, the long-range modulation of the spins within the skyrmion relative to the underlying atomic lattice allow these quasiparticles to effectively decouple from the lattice so that they can move under small applied electric currents and/or thermal gradients.[2] These advantages makes skyrmions promising candidates for the replacement of ferromagnetic domains in the magnetic memory design known as magnetic racetrack memory.[16-19]

In a conventional racetrack memory device, the ferromagnetic domains are translated as bits along a track by electric current from “write” to “read” *via* a spin transfer torque mechanism (Figure 1.2a).[16] This memory design can be utilized to pattern a high density of information that can be accessed quickly with smaller power consumption (like the dynamic random access memory devices) compared to current technologies such as magnetic hard disk drive (HDD) and FLASH memory.[15,19] However, the current density needed to move the magnetic domains is very high (10^{10}-10^{11} A m^{-2}) which generally causes nanoscale device failure due to Joule heating. The magnetic skyrmions in B20 materials require about ~4 orders of magnitude less current density

(10^6-10^7 A m^{-2}) to translate than their ferromagnetic domain counterpart, therefore they could solve this issue while also shrinking the domain size considerably.[17,19-21] In addition, the emergent magnetic field generated by skyrmion texture can give rise to a unique electronic signature for skyrmions known as the topological Hall effect (THE) (Figure 1.2b) which can be detected by a classical Hall bar device architecture. [2,22-24] Even with all the advantages, before the application of skyrmions could be realized in any envisioned magnetic storage device such as the magnetic racetrack memory device design shown in Figure 1.2c, there are still many scientific and technological challenges that need to be solved.

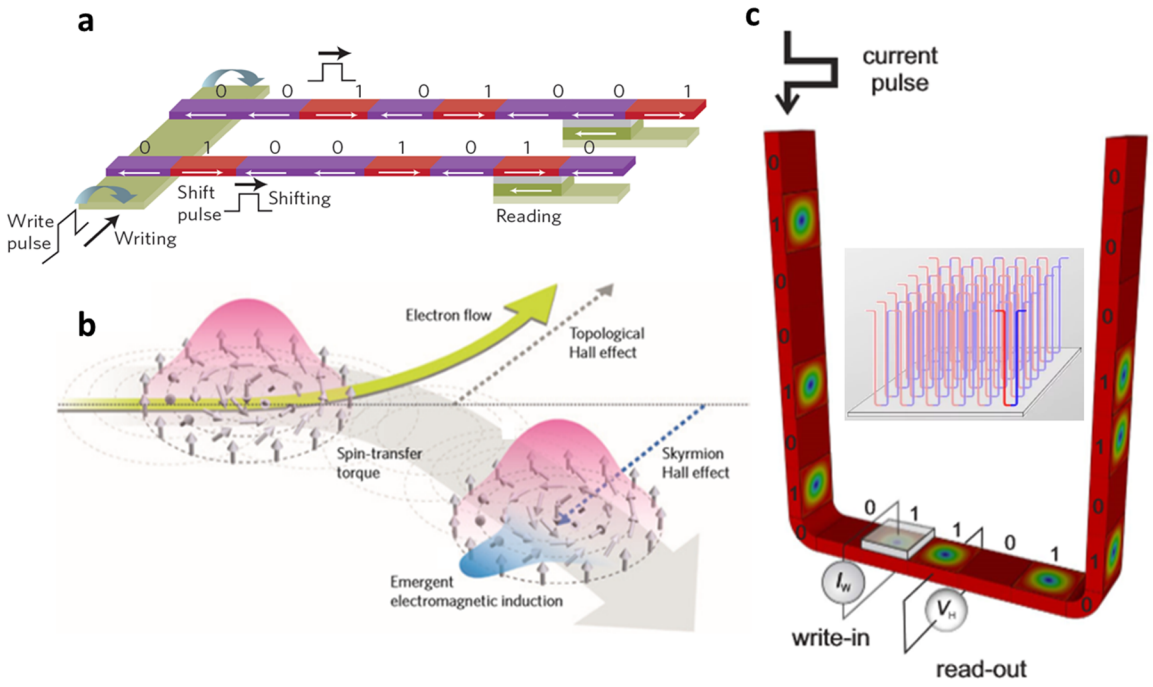

Figure 1.2 : Schematic of a magnetic racetrack memory device design. (a) Example of a magnetic racetrack memory device with ferromagnetic domains as the information bits. (b) Cartoon representation of electron flow in the presence of emergent magnetic field of magnetic skyrmions which results in THE and skyrmion motion under spin transfer torque. (c) An envisioned design of magnetic racetrack memory device where skyrmion are binary information bits and spin current moves the domains along the racetrack. The inset shows the array of racetracks arranged in three dimensions for high density memory storage application. [Panel a is reproduced with permission Nat. Mater. 11, 372 (2012), Copyright 2012 Springer Nature Limited. Panel b is reproduced with permission from Nat. Nanotechnol. 8,

899 (2013), Copyright 2013 Springer Nature Limited. Panel c is reproduced with permission from Sci. Rep. 5, 15773 (2015). Copyright 2015 Springer Nature Limited].

To explore skyrmions for potential magnetic storage, the study of the stability and dynamics of skyrmions in nanoscale skyrmion-hosting systems is crucial. Nanowires (NWs) have many advantages over bulk crystals or thin films — most important of which is that a NW geometry should stabilize the skyrmion phase more so than in the bulk and thin film systems which was experimentally shown in MnSi (Figure 1.3a-c) and other B20 system.[9] As the dimension of the system approaches the size of the skyrmion domains, the conical magnetic configuration will be destabilized energetically compared to the skyrmion state.[25] Along with the confinement stabilization of the skyrmion phase, a NW can also acts as a natural "racetrack" and waveguide for the skyrmion motion and presents a convenient geometry for prototype device work. Moreover, NW's small cross-section could facilitate the study of these prototype devices and emergent electrodynamics of skyrmions at much larger current densities. Therefore, NW systems can be utilized to study the skyrmion dynamics and manipulate skyrmions on even faster timescales.[2, 18, 24, 26]

To investigate the interesting skyrmion physics in materials, solid-state chemistry has proven instrumental in developing synthesis techniques for skyrmion hosting materials. Chemical methods for synthesizing skyrmion hosting single-crystal NWs and other nanostructures of metal silicides and germanides has been developed over the last 15 years.[27-35] Chemical vapor deposition (CVD) and chemical vapor transport (CVT) synthesis have proven successful in growing nanostructures of the skyrmion-hosting B20 monosilicides such as MnSi,[36-38] and alloys of FeSi, CoSi, such as $Fe_{1-x}Co_xSi$ (Figure 1.3d-g).[39-43] These NWs feature rhombohedral cross-sections split by a merohedral twin plane that partitions the NW into two parts of opposite chirality (left and

right handiness) with NW growth along [110] crystallographic direction (Figure 1.3e-g) which is characteristic of chiral B20 crystal system (space group $P2_13$).[30,36,38,43] Nanostructures of B20 germanides such FeGe[12] and their alloys with controllable amount of cobalt doping (e.g., $Fe_{1-x}Co_xGe$) have been synthesized using CVD techniques as well (Figure 1.3h-k).[44] These synthetic methods generally can also produce unconventional shapes of geometrically confine nanostructures such as nanorods, nanoplates and nano-octahedra which can provide unique opportunities to observe the evolution of spin textures in skyrmion hosting systems. Of course, nanostructures can also be top-down fabricated using focused-ion beam (FIB) from bulk crystals (as discussed in Section 4.2) or MBE growth thin films.[45-48] However, further processing is still needed for making 1D racetracks or other low-dimensional nanostructures.

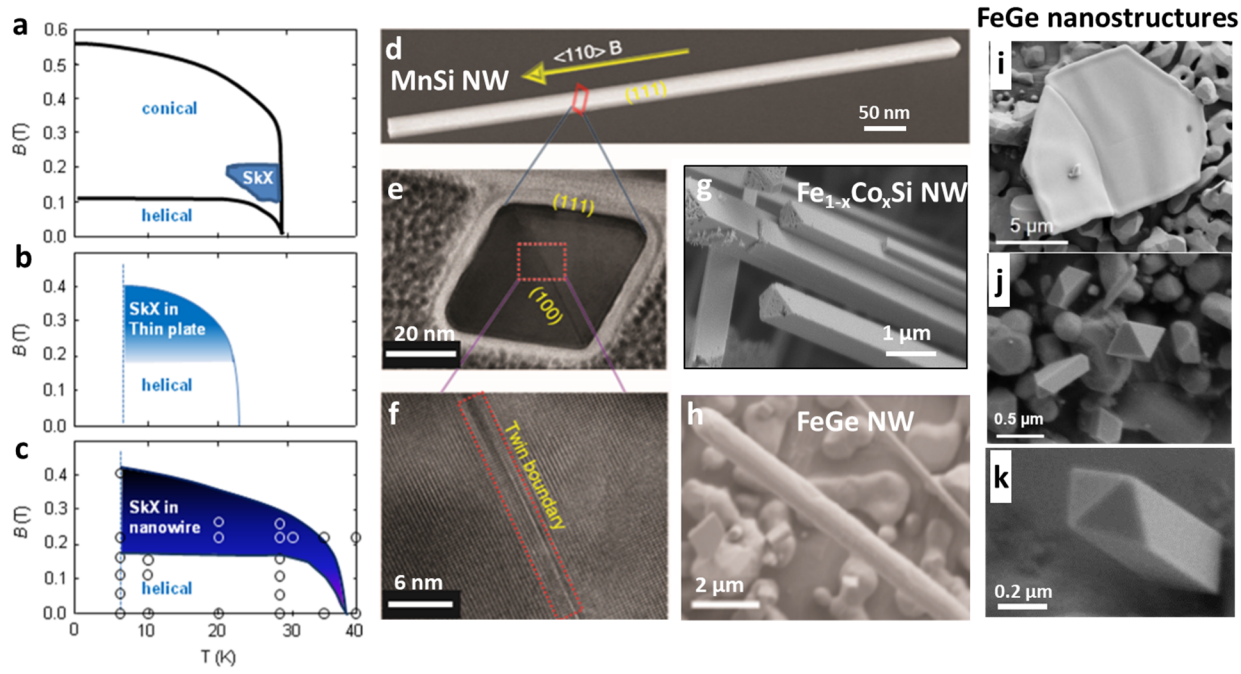

Figure 1.3 : Magnetic skyrmion stability in B20 nanostructures and the crystal morphology of B20 NWs and various bottom-up synthesized nanostructures grown via CVD growth. (a) Magnetic phase diagrams showing skyrmion phase stability (a) bulk crystals (b) thin plate, and (c) nanowire samples of MnSi, respectively. (d) SEM image of a MnSi NW with a smooth (111) surface and <110> growth direction. (e) A cross-sectional TEM image of the MnSi NW with a merohedral twin boundary, where the (001) twin plane is parallel to the <110> growth direction. (f) High-resolution

TEM image of the cross-section at the twin boundary. CVD grown (g) well faceted $Fe_{1-x}Co_xSi$ microwire along the <110> growth direction and (h) FeGe NW along the <111> growth direction. Non-conventional morphology such as (i) nanoplates, (j) nano-octahedra, (k) nanorod of FeGe B20 nanostructures grown using CVD process. [Panel a-c are reproduced with permission from Nano Lett. **13**, 3755 (2013), Copyright 2013 ACS. Panel d-f are reproduced with permission from Nat. Commun. **6**, 7637 (2015), Copyright 2015 Springer Nature Limited, Panel g is reproduced with permission from ACS Nano **13**, 7833 (2019), Copyright 2019 ACS. Panel h, j, k are reproduced with permission from Nano Lett. **17**, 508 (2017), Copyright 2017 ACS. Panel i is reproduced with permission from Adv. Funct. Mater. **29**, 1805418 (2019), Copyright 2019 Wiley-VCH].

In this chapter, we highlight the recent progress in the studies of magnetic skyrmions in NWs and other nanostructures of non-centrosymmetric B20 materials. We first discuss the methods of observation and detection of skyrmion in chiral B20 materials with bulk DMI. We do not attempt to discuss in detail the magnetic skyrmions formed by interfacial DMI in various multilayer thin films, which is available in previously published reviews.[49-51] For an overview related to general transport studies of skyrmions in bulk B20 materials we refer to Ref [2,52]. Here, we focus on the importance of skyrmions in B20 nanostructures, which is conducive for studies related to geometric confinement and stability of skyrmions. We summarize the knowledge on the impact of morphology and dimensionality of skyrmion hosting materials in stabilizing isolated magnetic skyrmions in confined geometry and the benefits for implementation in magnetic memory applications. This chapter also brings attention to detection of individual or clusters of confined skyrmions by solely electrical means which could be integrated with writing and reading device components for prototypes of the envisioned skyrmion-based racetrack memory devices.

1.2 Spin Textures and Crystal Symmetry

There exists a unique relationship between the interaction of atomic spin and crystal symmetry. Of all the known compounds with the cubic B20 crystal structure, only MnSi,[5,9,10,37,38,53] $Fe_{1-x}Co_xSi$,[6,43,54] FeGe,[11,12,55,56] MnGe,[13,57] $Cu2OSeO_3$,[58] and their alloys[44,59-61] have been

identified as materials that can host Bloch-type magnetic skyrmions. Other materials with non-zero DMI due to polar symmetry breaking by the asymmetric layer stacking arrangement of thin film systems,[18,49,51,62,63] can lead to interfacial DMI and the formation of Néel-type skyrmions which has been reported in multilayer thin films with heavy-metal/ferromagnetic interfaces,[26,64-67] ferromagnetic/topological insulator hetrostructures,[68] heavy-metal/ magnetic insulator,[69] and recently found ABO_3 perovskite bilayers.[70-72] Néel skyrmions were also discovered in single crystals of GaV_4S_8 material. GaV_4S_8 has a non-centrosymmetric crystal structure like the B20 compounds, however, its crystal symmetry is of the *R*3*m* space group instead of the $P2_13$ space group, and this leads to the formation of Néel instead of Bloch skyrmions.[73] More recently, other skyrmion hosting materials with bulk DMI have also been identified. For example, the Co-Zn-Mn family of compounds with the *β*-Mn structure (space group $P4_132$ *or* $P4_332$*)* host traditional Bloch-type skyrmions well above room temperature with a $T_c > 300$ K, including some examples with T_c up to around 400K [74] Other *β*-Mn structure of alloy $Fe_xCo_{1-x}Rh_{0.5}Mo_3N$ also host Bloch-type skyrmions which are stable up to ~ 115 K.[75] Magnetic skyrmions with slightly varying, but still topologically protected spin textures can also be formed when the ferromagnetic exchange interaction competes with magnetic interactions other than the DMI. Interestingly, Fe_3Sn_2, with a kagome lattice structure, has centrosymmetric crystal symmetry and therefore no bulk DMI, but it able to form skyrmions through long range dipole-dipole interactions, which end up producing skyrmions with a ring-like state with high ordering temperature, 630 K.[76] Like Fe_3Sn_2, Mn-Ni-Ga alloys (space group $P6_3/mmc$) also form skyrmions through long range dipole-dipole interactions, but Mn-Ni-Ga alloys host type-II bubble domains instead of ring skyrmions, they are comprised of two skyrmions of opposite helicity merged together which are stable up to ~350 K in Mn-Ni-Ga alloys.[77] In both cases, the lack of bulk DMI as the source of skyrmion formation results in

quite large magnetic domain sizes >100 nm. The most recent discovery in the skyrmion field is of anti-skyrmions hosted by tetragonal Heusler alloys with D_{2d} crystal symmetry of $Mn_{1.4}Pt_{0.9}Pd_{0.1}Sn$ (space group, $I\text{-}42m$)[78] which are stable up to ~400 K and have a non-trivial topological spin texture completely unique to the anti-skyrmion state. However, in these systems the relatively weak dipole-dipole interaction also leads to a slow periodic rotation of neighboring spins, resulting in skyrmions with sizes between ~100s to 1000s nm, much larger than the skyrmions typically found in B20 materials. These materials are summarized in Table 1.1. Apart from skyrmion spin textures in B20 materials, other 3D spin textures like hedgehog lattice state and chiral bobbers are also observed in MnGe[13,57] and FeGe,[79] respectively. After the theoretical understanding of the role atomic arrangement in a crystal lattice and various spin interactions plays in stability of non-collinear spin textures in these materials, development of different detection techniques has proven instrumental in their experimental discovery.

Table 1.1 : Summary of bulk materials known to host skyrmion and skyrmion-like spin textures. The following columns of the table provide information including the space group, ordering temperature (T_c), skyrmion domain size, as well as the skyrmion type

Material	Space Group (C=Centrosymmetric, NC=Non-Centrosymmetric)	T_c (K)	Skyrmion Domain Size (nm)	Skyrmion Type
MnSi[9]	$P2_13$ (NC)	28	18	Bloch
$Fe_{0.5}Co_{0.5}Si$[6]	$P2_13$ (NC)	36	90	Bloch
FeGe[12]	$P2_13$ (NC)	278	78	Bloch
MnGe[13]	$P2_13$ (NC)	150	~5.5	Bloch (3D hedgehog)
Cu_2OSeO_3[58]	$P2_13$ (NC)	59	62	Bloch

$Co_8Zn_8Mn_4$[74]	$P4_132$ (NC)	318	120	Bloch
$Fe_xCo_{1-x}Rh_{0.5}Mo_3N$[75]	$P4_132$ (NC)	~115	~110	Bloch
Fe_3Sn_2[76]	R-3m (C)	630	~150	Bloch (Ring-Type)
Mn-Ni-Ga Alloys[77]	$P6_3/mmc$ (C)	~350	~90	Type-II Bubble
GaV_4S_8[73]	$R3m$ (NC)	12.7	~22	Neel
$Mn_{1.4}Pt_{0.9}Pd_{0.1}Sn$[78]	I-42m (NC)	~400	~150	Anti-Skyrmion

1.3 Evolution of Detection Techniques of Magnetic Skyrmions in B20 Materials

The experimental discovery of skyrmion has led to the exploration of skyrmion hosting materials and techniques to detect skyrmion phase. Development of instrumentation to observe skyrmions is a key aspect which led the skyrmion research to flourish in the basic sciences. In this section, we discuss the common skyrmion detection techniques on well-known skyrmion hosting B20 materials.

1.3.1 Reciprocal Space Detection of Magnetic Skyrmions in Bulk Crystals

As previously mentioned, magnetic skyrmions were first experimentally discovered in a ~1 mm single crystal of MnSi using SANS.[5] Since this initial discovery, SANS has been used to positively identify magnetic skyrmion lattices in a number of different cubic B20 magnetic materials including FeGe,[80,81] MnGe,[60] and $Fe_{1-x}Co_xSi$.[82-84] This technique is commonly used to analyze bulk crystals and more recently thin film samples. In most B20 materials, upon application of a small applied field (~0.1 T), the helimagnetic spin state rotates to align its periodic wave vector, Q, along the axis of the applied magnetic field resulting in the formation of the conical state.[5] At temperatures just below T_c, there exists a small window of applied magnetic field where the conical state will transform into a skyrmion lattice shown in the magnetic phase diagram in

Figure 1.1e.[5] Both the conical and helimagnetic states are known as single *Q* states since only one wave vector is required to describe their periodicity. In a SANS experiment, the transition from the helimagnetic to conical state is typically inferred from the disappearance of the diffraction spots associated with the helimagnetic phase since the periodicity of the conical state is in the direction of the incident beam.[5,83] The emergence of the skyrmion phase as a function of temperature for any random orientations of the applied magnetic field charaterized by observation of six Bragg reflections on a regular hexagon that is strictly perpendicular to the magnetic field (Figure 1.1d).[5] The skyrmion lattice is describe as a triple *Q* state since three wave vectors are now required to describe the packing of the skyrmion lattice state.[2] Increasing the applied magnetic field results in a reemergence of the conical state from the skyrmion lattice phase, which will then finally transform into a fully field polarized state. SANS has proven to be a powerful tool to study the complex magnetism intrinsic to these skyrmion hosting materials. However, the large crystal size required for SANS experiments makes studying confined systems such as thin films exceedingly difficult, or impossible in the case of single nanostructures.

A surface sensitive technique known as resonant elastic X-ray scattering (REXS) unambiguously identifies the helical, conical, and skyrmion lattice states in various B20 compounds and combines element-selectivity with extremely fast time resolution.[85-89] When probing a skyrmion lattice, X-rays acquire the momentum transferred directly from the periodicities of the long-range magnetic order of spin structures. Therefore, the scattering form factors for the helical and skyrmion orders are significantly different in REXS, unlike the case in SANS, where they are almost the same.[85] This makes REXS a powerful technique that can uniquely identify skyrmion structure as compared to SANS. Typical REXS data of different magnetic phases in a single crystal are obtained from scattering of incident polarized soft X-rays

scattered from the samples and collected using a CCD camera to produce reciprocal space maps (RSMs).[85, 88] However, it's a surface- sensitive technique that requires high quality single crystals with well-defined and smooth facets to increase the signal to noise ratio of scattered X-ray with magnetic phase information.

1.3.2 Magnetic Susceptibility and Spectroscopy Detection of Skyrmions

Almost all magnetic materials are thoroughly studied through magnetization and magnetic susceptibility measurements, and skyrmion hosting materials are no exception. Direct current (DC) magnetization measurements are used to determine the T_c and saturation magnetization of these weakly ferromagnetic materials. However, DC techniques yield little information about the skyrmion phase. To probe the skyrmion phase, alternating current magnetic susceptibility (ACMS) experiments are necessary.[90] Previous field sweep studies in several skyrmion materials, including MnSi,[61,91,92] FeGe[59,93] and MnGe,[60, 94] have revealed a distinct broad dip in magnetization curves at critical fields related to the formation and destruction of the skyrmion lattice, or the so-called "A-phase" in reports before magnetic skyrmions were understood. For instance, ACMS experiments were carried out for the $Fe_{0.95}Co_{0.05}Ge$ system (T_c ~ 276 K) at a low excitation amplitude of 0.1 mT and an excitation frequency of 10 Hz to reveal the stability of skyrmion phase, where AC moment is plotted as a function of applied magnetic field as shown in Figure 1.4a.[59] For all temperatures below T_c, an increased value of the AC moment was observed for magnetic fields between ~250 Oe and ~ 450 Oe. The two inflection points of this broad dip reveal mark the formation and the destruction of the skyrmion lattice in $Fe_{0.95}Co_{0.05}Ge$ and are marked H_{b1} and H_{b2}, respectively.[59, 93] Upon destruction of the skyrmion lattice, these skyrmion materials are known to return to the conical state before finally transitioning into the fully field polarized state or ferromagnetic state.[5] These magnetic measurements are useful for not only indirectly probing the

skyrmion phase stability regime (Figure 1.4b), but also for understanding all of the complex magnetic states inherent to skyrmion materials which could be critical for determining how skyrmion phase interact with other magnetic states.

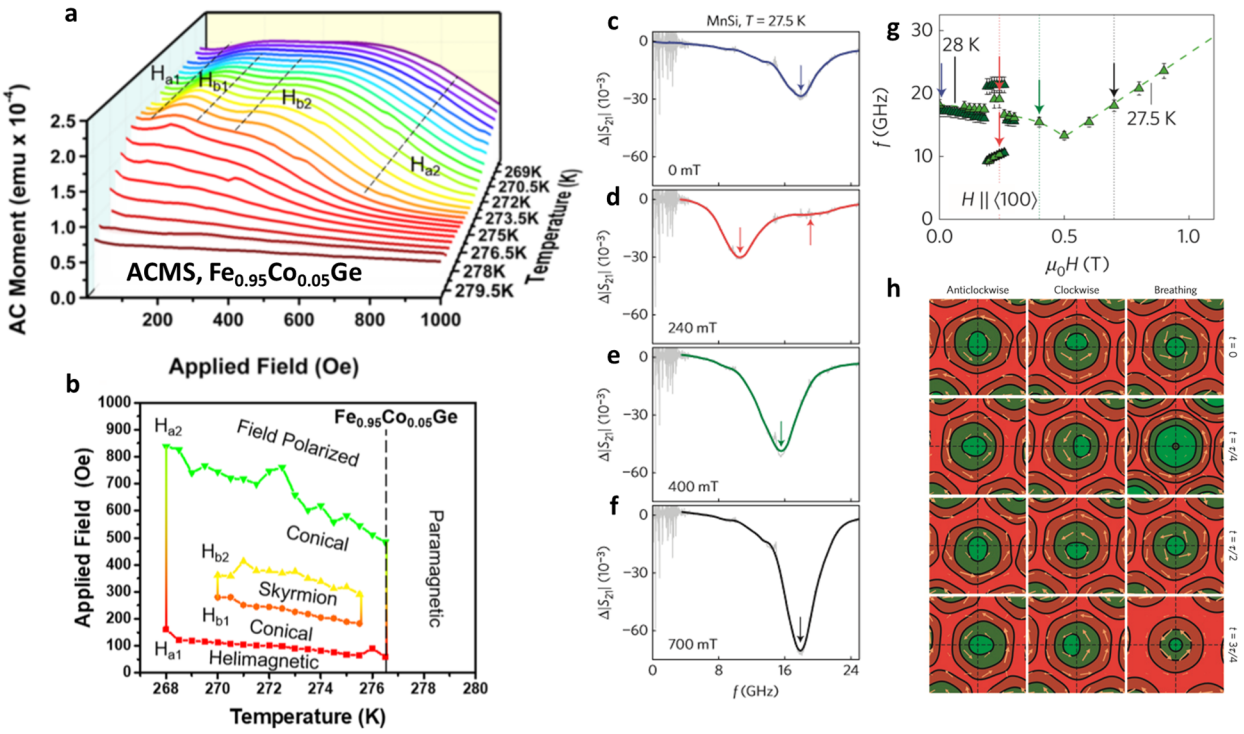

Figure 1.4. Magnetic phase determination using magnetic susceptibility and spectroscopy measurements. (a) Magnetic susceptibility measurements of bulk $Fe_{0.95}Co_{0.05}Ge$ powder using ACMS shows transitions in the AC field sweeps that are characteristic of a skyrmion phase, and the relevant magnetic phase transitions have been highlighted with dashed lines used to plot (b) the magnetic phase diagrams for $Fe_{0.95}Co_{0.05}Ge$ illustrating the stability for the skyrmion phase as well as the existence of other relevant magnetic phases such as helimagnetic, conical, field polarized, and paramagnetic states. (c-f) All-electrical broadband spectroscopy spectra $\Delta|S_{21}|$ for MnSi at various magnetic fields at T = 27.5 K. (g) The corresponding resonance frequencies (marked by arrows) as a function of applied magnetic field calculated for different temperature (below T_c). (h) Illustration of the anticlockwise and clockwise gyration modes as well as the breathing mode of the skyrmion lattice phase at different times t during a period τ. [Panel a, b are reproduced with permission from Chem. Mater. **30**, 1146 (2018), Copyright 2018 ACS. Panel c-h are reproduced with permission from Nat. Mater. **14**, 478 (2015), Copyright 2015 Springer Nature Limited]

ACMS measurements could help us to determine the stability regime of the skyrmion phase in bulk crystals, however the signals are not unique to skyrmion phases. In contrast, recently,

microwave absorption spectroscopy (MAS) has been used as a powerful tool for identifying and studying the spin dynamics in skyrmion hosting materials as it provides a specific resonance response associated with all magnetic phases (field polarized, conical, helical, and skyrmion phases).[95] The combination of MAS, micromagnetic simulations, and analytical theory has been used to identify the various magnetic phases associated with cubic B20 materials such as FeGe,[96] MnSi,[97] $Fe_{1-x}Co_xSi$[97] and Cu_2OSeO_3.[97,98] For example, the electrical broadband spectra were calculated with MAS measurement device setup with a disc shaped sample of MnSi (Figure 1.4c-f), where the relative amplitude of scattering parameter is plotted with absolute frequency.[97] The spectra are dominated by a broad minimum that is accompanied by weaker signals where the skyrmion phase is predicted to be stable (marked by arrows). The magnetic resonances of the skyrmion lattice phase and other magnetic phases have been simulated and quantitively identified with varying applied magnetic field in MAS measurements. The resonances consist of a clockwise and an anti-clockwise gyration mode of the skyrmion cores, as well as of a single breathing mode which are plotted with respect to varying applied field (Figure 1.4g) and compared with theoretical studies (Figure 1.4h). The characteristic changes in the spectra coincide with the magnetic phase boundaries determined for the same samples from ACMS measurements.[91, 97]

1.3.3 Real Space Observation of Magnetic Skyrmions

To overcome the sample size limitations using techniques discussed in the section above and to provide real space visualization of these exotic spin textures, different types of magnetic contrast imaging techniques have been utilized to study the skyrmion phase, especially in nanostructures, including Lorentz transmission electron microscopy (LTEM),[6,9-13,44] electron holography,[43,54-56,79] and magnetic force microscopy (MFM).[99] By far the most popular imaging technique is LTEM due to its relative ease of use and high sample throughput. LTEM of

$Fe_{0.5}Co_{0.5}Si$ thin film was the first example for real-space observation of magnetic skyrmion lattice (Figure 1.1f).[6] In situ observation of magnetic constant is performed with the sample in a field-free region in the TEM column by turning off the main objective lens and using another lens known as the Lorentz lens placed below the sample as the imaging lens.[100] The resolution of the LTEM is significantly lower (~2 - 5 nm) because of this objective lens modification compared to traditional TEM techniques, but for many magnetic spin structures, like skyrmions, this resolution is sufficient. For example, the real space observation of the cubic skyrmion lattice in a helimagnet MnGe with a periodicity ~ 3 nm has been successfully imaged with LTEM imaging.[13] The magnetic contrast is seen only in over and under focused images (Figure 1.5a-c), and it is produced by the Lorentz force of the in-plane magnetization of the sample. The magnetic contrast of skyrmions appears as circular spots as shown in case of an FeGe NW (Figure 1.5d).[12]

LTEM technique not only provides information regarding spin texture of skyrmion but also enables the observation of the nucleation and fusion processes and the distortion of skyrmions with varying applied magnetic field and temperature. Adjusting the temperature and magnetic field in the LTEM allowed for the mapping of the magnetic phase diagram, for example, as shown in case of the $Fe_{0.97}Co_{0.03}Ge$ nanoplate (Figure 1.5e).[44] The helimagnetic phase generates helical stripe pattern (Figure 1.5f) and skyrmion lattice apperas as hexagonally arranged spots (Figure 1.5g) across the whole $Fe_{0.97}Co_{0.03}Ge$ nanoplate.[44] The real space observation of skyrmions via LTEM serves as an important piece of evidence for supporting skyrmion detection from magnetotransport measurements.[38,44] Similar experiments have been used to map out the magnetic phase diagrams of several skyrmion hosting materials with the cubic B20 nanostructures.[2]

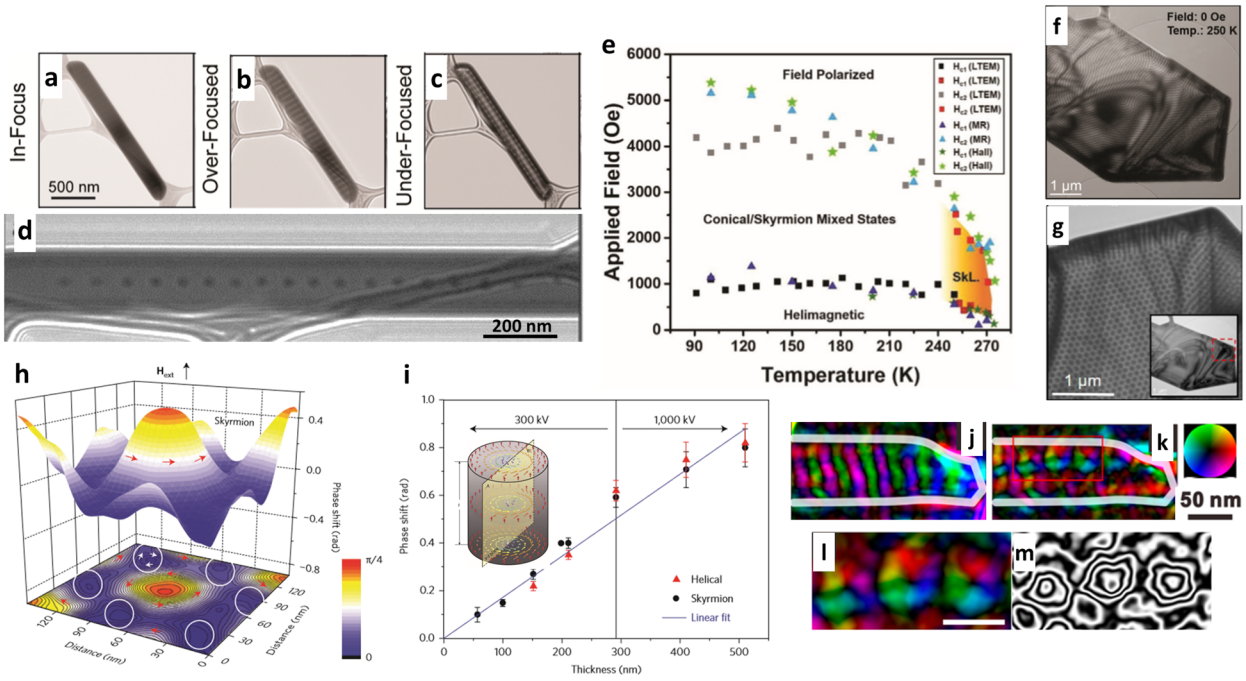

Figure 1.5 : Real space observation of magnetic skyrmion in B20 nanostructures using LTEM and EH. LTEM observation of B20 FeGe NW show no magnetic contrast in zero magnetic field for (a) In-focus, (b) over-focused, and (c) under-focused LTEM images of the NW with zero magnetic field, showing the striped magnetic contrast corresponding to the helical phase. (d) LTEM images of an FeGe NW obtained at 95 K shows a skyrmion chain state desired for racetrack memory application. (e) Magnetic phase diagram of a $Fe_{0.97}Co_{0.03}Ge$ nanoplates mapped using three different detection techniques, which supports the LTEM observation of (f) helimagnetic and (g) skyrmion lattice phase formation. Real space observation of skyrmion spin texture via electron holography conducted on $Fe_{0.5}Co_{0.5}Si$ thin film shows (h) surface plot of the absolute phase shift in the vicinity of the skyrmion. (i) Electron phase shifts of the helimagnetic and skyrmion lattice phase as a function of sample thickness (experiments carried out in 300 kV and 1000 kV microscopes) with the schematic inset showing the three-dimensional spin structure of a skyrmion. (j-m) Electron holography imaging experiments conducted on a $Fe_{0.75}Co_{0.25}Si$ NW sample: Magnetic phase contrast images show (j) helimagnetic and (k) skyrmion phase in $Fe_{0.75}Co_{0.25}Si$ NW. The skyrmion enclosed in the rectangle in (k) in the forms of (l) its color-coded display (using the color wheel) and (m) magnetic phase contrast map. Scale bar in (j,k) is 50 nm and (l,m) is 30 nm. [Panel a-d are reproduced with permission from Nano Lett. **17**, 508 (2017), Copyright 2017 ACS. Panel e-f are reproduced with permission from Adv. Funct. Mater. **29**, 1805418 (2019), Copyright 2019 Wiley-VCH. Panel h, i are reproduced with permission from Nat. Nanotechnol. **9**, 337 (2014), Copyright 2015 Springer Nature Limited, Panel j-m are reproduced with permission from ACS Nano **13**, 7833 (2019), Copyright 2019 ACS].

While LTEM has become a ubiquitous technique for studying magnetic skyrmions in real space, it has some limitations that can be overcome using a more in-depth and time intensive

microscopy technique known as electron holography (EH).[101-104] One of the major drawbacks of LTEM is that the magnetic contrast can be imaged at over and under focused TEM mode due to magnetic induction between electron beam and in-plane magnetic components of the target magnets, leading to Fresnel fringes obscuring all magnetic contrast near the edges of the sample.[105] In thin films and nanostructures, these fringes can potentially blur the entire area of interest especially when the size of the nanostructure approaches sub 100 nm length scale. In contrast, the EH technique uses in-focus imaging to produce magnetic contrast, overcomes this issue. During the experiment, the incident electron beam is split via a biprism into two beams: one travels through the sample (sample beam) and other travels through the vacuum (reference beam).[104] At the detector, the two beams converge and produce an interference pattern (a hologram) that can be used to calculate the phase shift of the sample beam over the entire image. This phase shift includes two separate components: a thickness or mean inner potential (MIP) component and a magnetic component. The MIP phase shift can be easily removed by taking a phase shift image above the magnetic transition temperature, T_c. Above the T_c, the image should contain only the MIP phase shift as the sample is in a paramagnetic state, and this MIP phase shift can be subtracted from all future phase shift images taken below T_c.[103] Removal of the MIP phase shift results in a pure magnetic phase shift image that is sensitive to in-plane magnetization and contains three-dimensional information regarding skyrmion structure.[54,79,106] Initially, EH technique was used on a thin sample of $Fe_{0.5}Co_{0.5}Si$ to produce the first real space imaging evidence of skyrmions with quantification of absolute phase shift associated with skyrmion spin structure and its vicinity as shown in Figure 1.5h.[54] The linear correlation with the thickness of thin film sample with absolute phase shift (Figure 1.5i) results in image reconstruction of the long tube-like 3D skyrmion structure exist in cubic B20 materials (Figure 1.5i inset).[54] Since then, several other skyrmion materials have

been studied with EH technique,[43,79,106] but more importantly, it has been utilized to further understand the details of three-dimensional spin textures in confined systems, including when the skyrmion tubes terminate as a magnetic singularity (see more discussion later in Section 4.2).[79] Recently, one-dimensional skyrmion lattice arrangement was found and imaged in a $Fe_{0.75}Co_{0.25}Si$ NW using EH.[43] Helimagnetic stripe pattern (Figure 1.5j) and skyrmion phase (Figure 1.5k) are clearly visualized in a NW without performing any mechanical processing (ion milling or deposition of PtC_x layer) or other treatments on the NW. This study demonstrates the technical capability of EH to image weak-phase object like a skyrmion even in sub-100 nm sized nanostructures.

1.4 Skyrmions in Nanostructured Geometry

As discussed previously, in bulk samples such as large single crystals and polycrystalline powders, magnetic skyrmions exist only in a small pocket of temperature and applied field region just below T_c of the material.[5, 83] This poses a challenge for the utilization of magnetic skyrmions in proposed magnetic information storage applications, as small variations in temperature or applied magnetic field could cause the destruction of the skyrmion phase. However, it has been shown theoretically that geometrical confinement of magnetic skyrmion phase in a nanostructure can increase the stability of the skyrmion phase via destabilization of conical phase.[9,11,107-109] The stabilization of the skyrmions in nanoscale systems was also theoretically predicted by the introduction of large anisotropy energy[110] and experimentally confirmed from skyrmion phase stability in a MnSi NW (Figure 1.3a-c).[9] Due to the miniaturization of real memory devices, it is also crucial to understand the stability and electrodynamics of skyrmions in confined geometries. In this section, we highlight the detection of skyrmion stability regime and current dynamics in

single-crystal nanostructures made by bottom-up synthesis and FIB fabricated nanostructures of B20 materials.

1.4.1 Detection of Skyrmion Stability in NW Morphology using Cantilever Magnetometry

In addition to the clear real space observation of magnetic skyrmion in MnSi NWs[9] and FeGe NWs[12] using LTEM, the experimental mechanism behind skyrmion stabilization for the NW morphology has also studied in a rather unique way using cantilever magnetometry.[110] Cantilever magnetometry gives insight into the magnetization of a *single* nanostructure and yields similar results to bulk magnetic susceptibility data albeit with more time intensive data acquisition and processing. Furthermore, this technique also enables detection of magnetic phases when the applied magnetic field is parallel to NW axis which is not possible for previously discussed magnetic contrast imaging. Cantilever magnetometry technique achieve its nanostructure sensitivity by directly bonding the magnetic NW to a non-magnetic cantilever (Figure 1.6a) and monitoring the resonance frequency, f, of the cantilever as a function applied field, Δf, with any change in the magnetization of the NW (Figure 1.6b)**.** Dips in the resonance frequency similar to AC susceptibility measurements of a MnSi single crystal can be seen in the region where a skyrmion lattice is expected to exist (Figure 1.6c). Using this technique, the skyrmion stability region for the MnSi NW can be mapped out on a magnetic phase diagram and is in good agreement with the LTEM experiments.[9] These experiments were then repeated on MnSi NWs with different aspect ratios to study potential stability difference caused by shape anisotropy, but the results were inconclusive. Likely, different aspects of a NW play a role in the stabilization of the skyrmion phase such as uniaxial anisotropy due to the NW shape.[107]

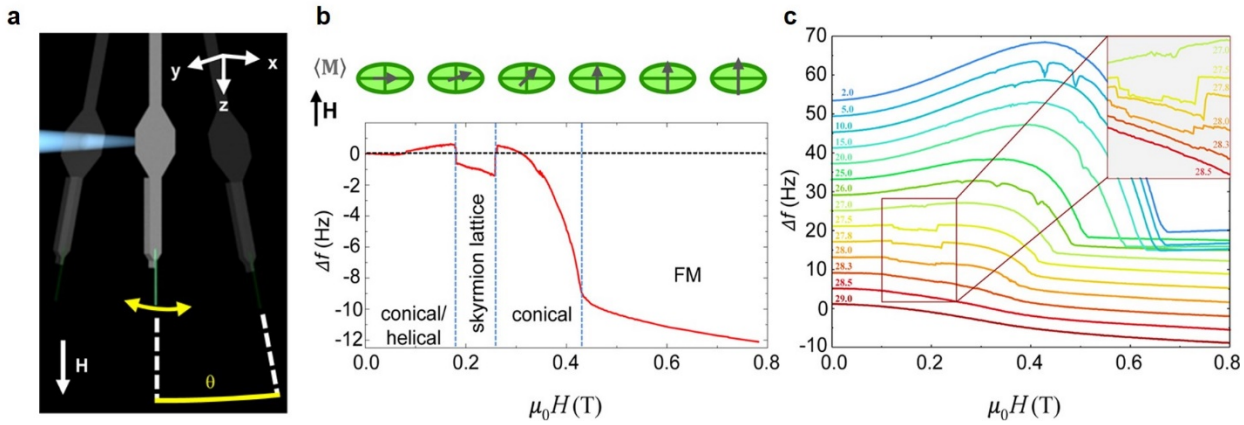

Figure 1.6 : Cantilever magnetometry of a MnSi NW (a) Experimental cantilever setup with the NW in green attached to a Si cantilever. (b) Representative field sweep with the different magnetic states outlined. The change in the resonance frequency of the cantilever, Δf, is directly related to change in magnetization of the NW. (c) Temperature dependence of the frequency shifts in the experiment. The strong dips related to the skyrmion phase exist only in the region where a skyrmion lattice has been previously shown to form. This figure is reproduced with permission from Nano Lett. **15**, 4839 (2015), Copyright 2015 ACS.

1.4.2 Magnetic Skyrmions in Various Nanostructure Morphologies

Initial studies of magnetic skyrmions in nanostructures made clear that the nanostructure geometry plays a large role in stabilizing skyrmion phase. Therefore, much progress has been made in the study of skyrmions in confined geometries, and researchers have begun studying nanostructures with varying geometrical shapes beyond simple 1D or 2D geometry. Since the skyrmion field is relatively young, the control over nanostructure geometries that can be produced *via* bottom-up synthesis is limited. FIB technique has been successfully used to carve out different nanostructured geometries with good control from large crystalline domains of skyrmion hosting materials, despite the low throughput and high cost. FIB deposition of a PtC_x layer *insitu* on the surface of the nanostructure has been found to greatly decrease Frensel fringing allowing for these FIB fabricated nanostructures to be studied more readily with LTEM and EH.[55,105,111] FeGe is by far the most well studied material using these FIB methods, and it was first studied in a FIB fabricated nanoribbon geometry (Figure 1.7a-c).[105,111] When the width of the nanoribbon was

reduced to below two times the skyrmion domain size (a_{sk}) of FeGe (~70 nm), only a single skyrmion chain would form at all temperatures. However, when the width of the nanoribbon was larger than ~150 nm, the skyrmions would exist as a lattice above ~200 K, and below 200 K the skyrmions would exist in a distorted skyrmion chains.[105] This low temperature region of FeGe is known as the "sparse skyrmion regime" which is unique to nanostructures of FeGe.[56] This skyrmion phase information is represented in the magnetic phase diagram (Figure 1.7b) mapped out using LTEM, which show the control over skyrmion packing with respect to varying width of FeGe nanoribbon.[105] Furthermore, a FIB fabricated nanowedge of FeGe was studied using EH technique to observe the effects of a thickness gradient on skyrmions.[111] As shown in Figure 1.7c, skyrmions can form unhindered until the wedge thickness was well below a_{sk}. At intermediate thicknesses (~2*a_{sk}) and lower applied magnetic fields (~2000 Oe), the skyrmions distort and elongate to fill the gap. Application of a stronger magnetic field (~3000 Oe) causes the distorted skyrmions to transition into a "zig-zag" skyrmion lattice. Moreover, each single turn of the helix in the helimagnetic state would directly form into the skyrmion upon application of the magnetic field, which is marked by the white arrows in Figure 1.7c. This study yields new insights into the transformation of magnetic spin structures with respect to geometrical confinement of the skyrmion hosting nanostructures.

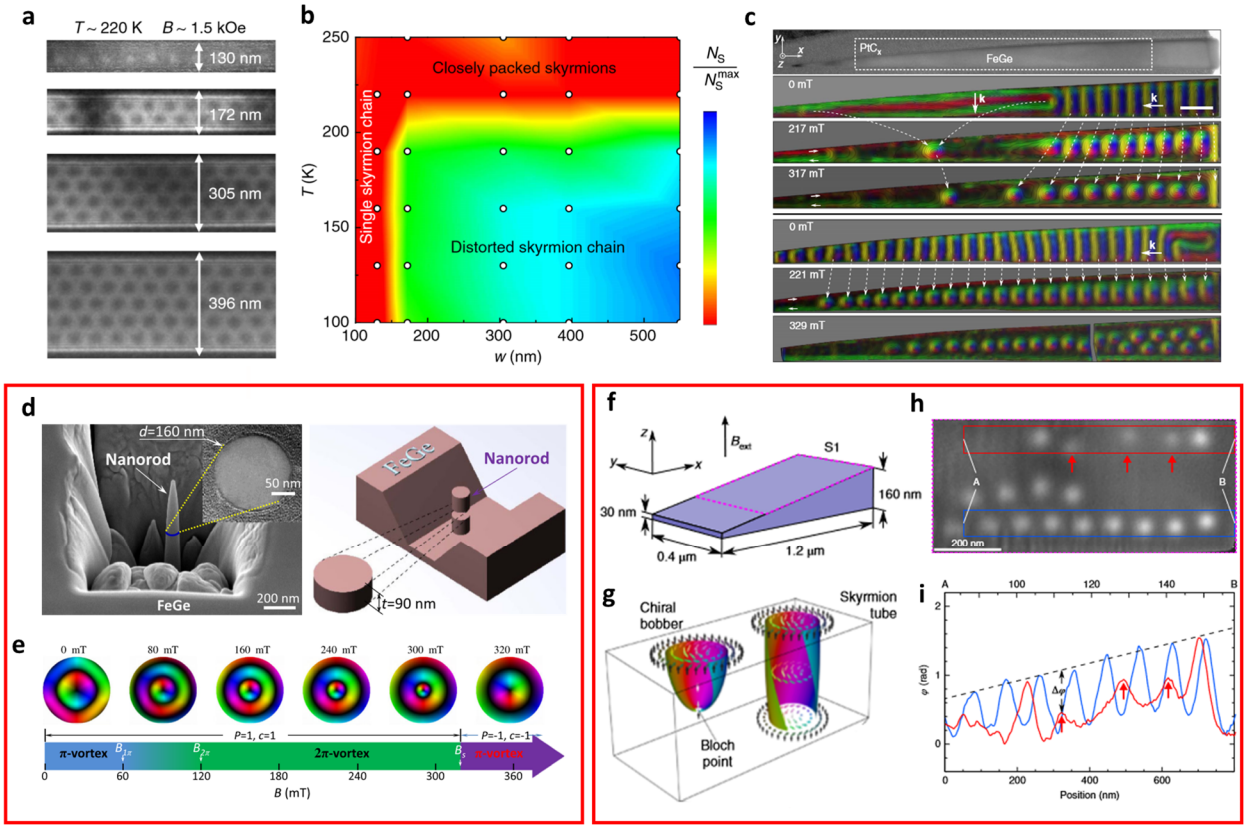

Figure 1.7 : Real space LTEM and EH imaging studies of different nanostructures of the FeGe made by FIB fabrication techniques (a) LTEM images of FeGe nanoribbons with different width highlighting the transformation of skyrmion lattice to single chain of skyrmions with varying width at 220 K. (b) Magnetic phase diagram for the nanoribbons of different widths, showing the ability of the thin ribbons to stabilize a single skyrmion chain. (c) EH imaging of an FeGe nanowedge that allows for visualization of change in magnetic texture with varying width and magnetic field, scale bar is 150 nm. The skyrmions squeeze to fit in at smaller widths while at larger widths and lower fields the skyrmions elongate along the width direction. These images also highlight the formation of skyrmions from the helical turns. (d) SEM image and schematic illustration of the fabrication of an FeGe nanodisk using FIB milling. The inset in (d) shows a TEM bright-field image of the cross -section of the nanodisk. (e) Magnetic field dependence of the in-plane magnetization of a target skyrmion stabilized in FeGe nanodisk. (f) The FIB fabricated wedge shaped FeGe structure used for real space visualization of chiral bobbers via EH. (g) Schematic representation of the spin structures for a magnetic chiral bobber and a skyrmion tube. (h) Electron holography image on the wedge shaped FeGe with red arrows indicating weak contrast objects that are identified as chiral bobbers. (i) Phase-shift profiles as a function of position that correspond to the bands of the same color marked in (h). [Panel a, b are reproduced with permission from Nat. Commun. **6**, 8504 (2015), Copyright 2015 Springer Nature Limited. Panel c is reproduced with permission from Nat. Commun. **8**, 15569 (2017), Copyright 2017 Springer Nature Limited. Panel d, e are reproduced with permission from Phys. Rev. Lett. **119**, 197205 (2017), Copyright 2017 Americal Physical Society. Panel f-i are reproduced with permission from Nat. Nanotechnol. **13**, 451 (2018), Copyright 2018 Springer Nature Limited].

Increasing confinement of skyrmions from the 1D systems like the nanoribbons and nanowedges to a pseudo 0D system such as a nanodisk has been theoretically predicted to stabilize the skyrmion phase further. With sufficiently strong confinement, the skyrmions are predicted to become the ground magnetic state of the system as a "target skyrmion",[56, 112] which gets its name from the two rings of opposite chirality that form concentric ring "target" without an applied magnetic field. EH study of an FeGe nanodisks with a diameter of 160 nm and thickness of 90 nm (Figure 1.7d) revealed a target skyrmion (2π-vortex) as magnetic ground state at 95 K (Figure 1.7e), which was the first evidence for the confinement induced magnetic skyrmion ground state (60 – 320 mT).[112]

Moreover, a FIB fabricated nanowedge with well controlled and specific dimensions (Figure 1.7f) was used to perform real space observation of 3-D spin structures stabilized in FeGe system known as the chiral bobber (ChB).[47,79] These ChB coexist with regular lattice of skyrmion-tube like structures in FeGe system (Figure 1.7g).[79] However, the penetration depth of the spin modulation of chiral bobbers is limited along the direction of applied field due to formation of magnetic singularity and occupy lesser volume in comparison to lattice of skyrmion tubes. EH technique proved beneficial to identify ChBs in the vicinity of skyrmion tube lattice (Figure 1.7h). This is possible due to the corresponding weak phase shift of ChB as compared to the average value from skyrmion spin textures, which is represented as the phase shift profile of skyrmion and ChB (Figure 1.7i).[79]

1.5 Electrical Detection of Skyrmions and Skyrmion Dynamics in Nanowires

The techniques described above can allow the observation and detection of skyrmions in bulk and/or nanostructures, but none of these methods can be implemented as a practical detection method in information storage devices such as racetrack memory.[19] They also do not address the

interesting electron-skyrmion interactions that are likely to stem from the skyrmion's non-trivial topology. For these reasons, transport studies are critical for understanding the fundamental electron-skyrmion interactions, as well as for developing a technology that could be reliably detect magnetic skyrmions in an information storage device. The implementation of purely electrical detection of skyrmion is crucial as it reveal the presence/absence of skyrmions which enables the reading process of information in a racetrack memory device architecture.[113-115] Most studies on skyrmions in nanostructures have been primarily carried out using magnetic imaging, while electrical measurements of skyrmion hosting nanostructures is limited.

1.5.1 Magnetoresistance Measurement for Determination of Skyrmion Stability Regime

Transport studies of magnetic materials including skyrmion materials usually begin with magnetoresistance (MR) measurements as they are facile to conduct and yield important information about the conduction electrons interactions with different magnetic phases.[37,38] MR measurements study the change in electrical resistance as a function of applied magnetic field relative to zero field (Equation 2), allowing for different magnetic phases to be electrically probed.

$$\mathrm{MR\%} = (\mathrm{R}(H) - \mathrm{R}(0))/\mathrm{R}(0)*100 \quad (2)$$

where R(H) and R(0) are the resistance at a specific applied magnetic field and zero field, respectively. For example, in the MR experiments on a MnSi NW (inset of Figure 1.8a) set up in the parallel configuration, where the direction of applied magnetic field is parallel to the NW's long axis,[37] the temperature was swept while applying a constant magnetic field (Figure 1.8a). This measurement allows for the identification of the T_c, which is seen as a large dip (~4%) in the MR signal at ~32 K (higher than reported for bulk MnSi, $T_c \sim 28$ K).[37,91] The spin structure evolution in NWs can be represented by plotting field-driven isotherms (MR-H) by sweeping the applied magnetic field at a constant temperature. For MnSi NWs, the MR results under the parallel

configuration do not vary greatly from those under the perpendicular configuration, however, in both cases, a more stabilized skyrmion regime relative to bulk crystals or thin films was observed.[9] This large difference in signal change between the two configurations is common in magnets with large aspect ratios where the magnet will have an easy and a hard axis of magnetization resulting in anisotropic MR (AMR) signal.[107] In the case of a magnetic NW, the easy axis is expected to be along the long axis of the NWs barring any large crystalline effects. AMR gives the MR measurements under parallel configuration a signal boost that can be beneficial for detection of the different magnetic phases.[37,43] After determination of T_c, isothermal MR experiments (Figure 1.8b) can be used to determine the critical fields for each subsequent applied magnetic field induced magnetic transition. As the applied magnetic field along the long axis of NWs increases, small kinks and jumps in the MR signal were observed, denoted as H_{A1} and H_{A2} in Figure 1.8b. H_{A1} appears at the applied magnetic field position where the transition from the helimagnetic to the skyrmion phase is expected to take place, while H_{A2} appears at the applied magnetic field where the skyrmion phase was observed to transition into the fully field polarized state. In combination with previous LTEM observations,[9] these critical fields can be assigned to the transitions between each of the magnetic phases. Similarly, $Fe_{1-x}Co_xSi$ NW devices were studied in parallel MR configuration to study field driven spin modulation along the NW axis.[43] However, the magnitude of the MR signal for $Fe_{1-x}Co_xSi$ NWs is an order of magnitude smaller than MnSi NWs.[37] Therefore, the apparent MR signature of magnetic state transitions such as kinks in MR-H curves were not discernable as shown in case of an $Fe_{0.81}Co_{0.19}Si$ NW (Figure 1.8c). However, the second derivative of MR-H curves (Figure 1.8d) for temperatures below T_c of $Fe_{0.81}Co_{0.19}Si$ NWs enabled the further assessment of critical field for magnetic state transitions.[43]

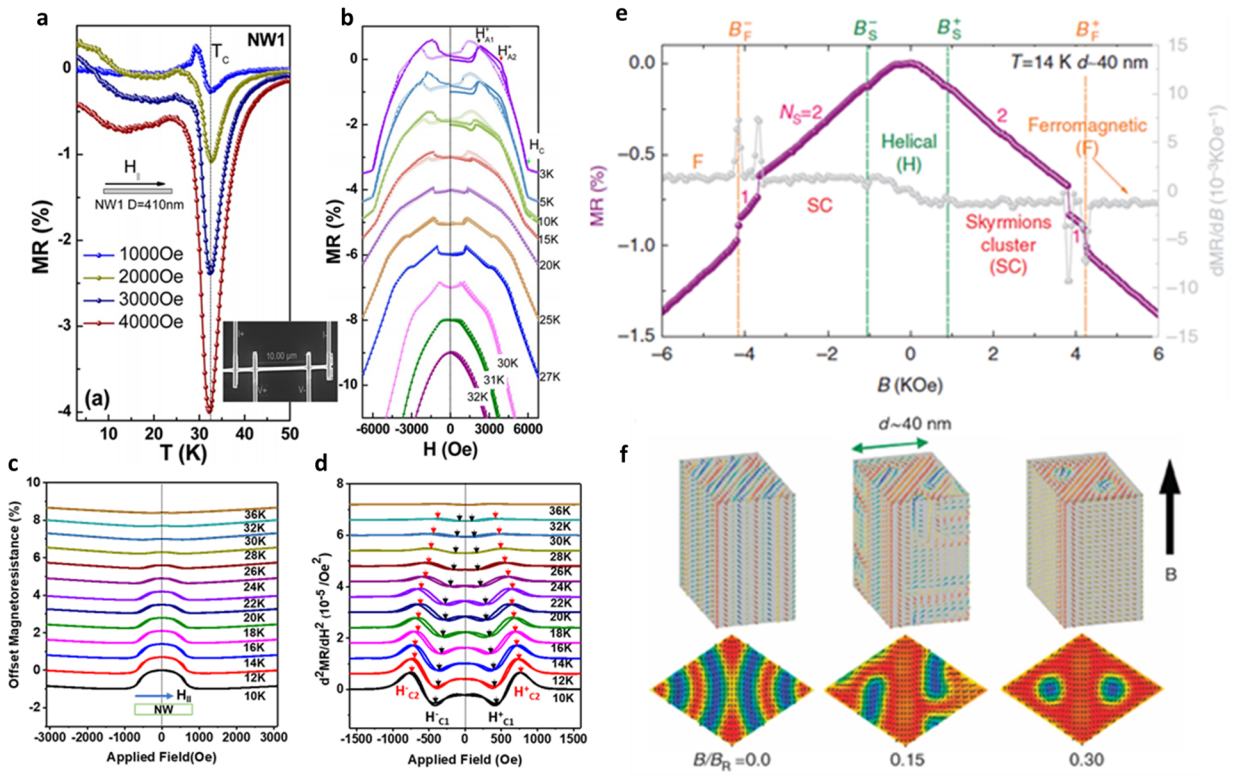

Figure 1.8 : Magnetotransport measurements on NWs of B20 skyrmion hosting materials. Magnetoresistance (MR) of a 400 nm diameter MnSi NW (inset a) in a parallel configuration (a) Constant applied field MR measurement with a sweeping temperature highlight the helimagnetic transition. (b) Isothermal MR field sweeps that are used to identify the magnetic transition critical fields. (c) Offset MR-H isotherms between 10-36 K of an $Fe_{0.81}Co_{0.19}Si$ NW in parallel configuration. (d) Second order derivatives of the MR-H isotherms in panel (c) more clearly reveals the critical magnetic state transitions. The black arrows (H_{C1}) and red arrows (H_{C2}) highlight the critical fields for the magnetic state transitions at different temperatures. Values for increasing and decreasing field strength are denoted by the superscripts "+" and "-", respectively. e) The observed quantized transitions of MR of a MnSi NW with a diameter of ~ 40 nm and f) the corresponding illustration of the calculated spin states of the various skyrmion cluster states. [Panel a, b are reproduced with permission from Nano Lett. **14**, 2026 (2014), Copyright 2014 ACS. Panel c, d are reproduced with permission from ACS Nano **13**, 7833 (2019), Copyright 2019 ACS. Panel e, f are reproduced with permission from Nat. Commun. **6**, 7637 (2015), Copyright 2015 Springer Nature Limited].

1.5.2 Quantized Magnetoresistance Transitions of Isolated Skyrmion in Nanowires

Detection of individual or isolated skyrmions by electrical means is crucial for accessing skyrmion as individual information bits. In B20 materials, the skyrmions tend to form a hexagonal lattice structure, hence in order to achieve stability of isolated skyrmions, nanostructuring has

proven beneficial.[12,105] CVD grown NWs have shown a large variation in diameter, which makes parallel configuration of the MR experiments on MnSi NWs advantageous for probing a small number (<10) of skyrmions at a time easily.[38] In a MnSi NW sample (Figure 1.3d-f), below T_c ~ 32K, skyrmions were found to exist with a domain size that is roughly ~17 nm. Therefore, a NW with a diameter of 40 nm should only host roughly 2 skyrmions of opposite chirality and these skyrmion 3D tubes run along the long axis of the NW on both sides of the merohedral twinning boundary that runs through the length of the NW. Figure 1.8e shows the magnetic field-driven cascading quantized transitions of skyrmion cluster states in this 40 nm MnSi NW using refined magneto-transport measurements. By tracking the size dependence on the number of quantized jumps in MR-H curves of the skyrmions assembled into cluster states, the stability of the number of skyrmions can be tuned solely with applied magnetic field, which was also corroborated by the Monte Carlo simulations (Figure 1.8f).[38] These studies clearly demonstrate that skyrmions can exist in discrete numbers from single to several skyrmions and simple MR measurement can enable an electric reading of the number of skyrmions in the cluster states. It is feasible to acquire real space images of magnetic spin texture in in-plane applied magnetic field using techniques like scanning transmission X-ray microscopy and X-ray holography since the probing particles are unperturbed by magnetic fields, in contrast to LTEM and EH measurements. However, further development in these techniques are required to conduct experiments on a NW morphology at cryogenic temperatures. While fundamentally interesting, these MR measurements are not directly applicable to racetrack memory devices as these tubular skyrmions cannot be moved along the long axis of the NW.

1.5.3 Topological Hall Effect Detection and Skyrmions Dynamics in B20 Nanostructures

While the MR measurements proved effective for identifying the critical fields for magnetic phase transitions, the measurements cannot reveal anything else about the skyrmion state and do not uniquely confirm the skyrmion phase. Understanding the skyrmion time-dependent dynamics is also needed to track or predict the positions of skyrmions along a racetrack device. Imaging technique such as LTEM has been used to observe skyrmion motion under applied current.[116,117] However, the experimental apparatus is very complicated and costly, and it is nearly impossible to observe short-time dynamics due to the image blurring. One of the prominent characteristics of skyrmion spin structure is its emergent magnetic field.[22,23,118] This is because when a conduction electron passes through a topologically non-trivial spin texture, the spin of the conduction electron adiabatically couples to the local spins and acquires a quantum-mechanical Berry phase that can be re-formulated in terms of an effective magnetic field, which deflects the conduction electrons perpendicular to the current direction (Figure 1.2b).[2,23] The manifestation of this emergent magnetic field is known as the topological Hall effect (THE), which is known as an electronic signature of skyrmion which can be measured in a Hall device setup (Figure 1.9a). The total Hall signal is comprised of three parts (Equation 3) that will each individually add to the total signal, ρ_{xy}: 1) the normal Hall effect (NHE) (Equation 4), 2) The anomalous Hall effect (AHE) (Equation 5**)**, and 3) the THE, where μ_0 stands for vacuum permeability, R_0 is normal Hall coefficient, M is magnetization of the sample and H is applied magnetic field.

$$\rho_{xy}=\rho_{NHE}+\rho_{AHE}+\rho_{THE} \tag{3}$$

$$\rho_{NHE} = R_0\mu_0 H \tag{4}$$

$$\rho_{AHE} = [\alpha\rho_{xx} + \beta\rho_{xx}^2 + b\rho_{xx}^2]\mu_0 M(H) \tag{5}$$

The linear dependence of ρ_{AHE} on magnetization (M) is convenient for the fitting process that can be used to extract the THE signal. For example, in the case of FeGe thin films[11,108,119] and large microcrystals,[120] the AHE can be effectively calculated and removed in conjunction with magnetization measurements. However, for nanostructure samples, such as MnSi NWs and $Fe_{1-x}Co_xGe$ nanoplates (Figure 1.9a), the magnetization cannot be measured easily. This means that the magnetization and therefore the AHE is assumed to act similarly to the bulk MnSi and $Fe_{1-x}Co_xGe$ systems.[59,93] For the $Fe_{0.97}Co_{0.03}Ge$ nanoplates example, to effectively remove the AHE contribution from the total Hall signal, a fitting and subtraction method was employed by assuming that the AHE behaves as a smoothly varying linear function. Fitting the linear function to the data above the critical field and subtracting the fit across the whole asymmetric component of the Hall signal yields the deviation from a smoothly varying function. As previously stated, the AHE and NHE signals should be smoothly varying and therefore any deviation can be accurately described as the THE signal. The extraction process can then be reproducibly carried out on the measurements at various temperatures (Figure 1.9c). Plotting the THE signal as a function of temperature and applied magnetic field as a heat map (Figure 1.9d) creates a form of a magnetic phase diagram that represents the region in which the skyrmion phase is stable in the $Fe_{0.97}Co_{0.03}Ge$ nanoplate.

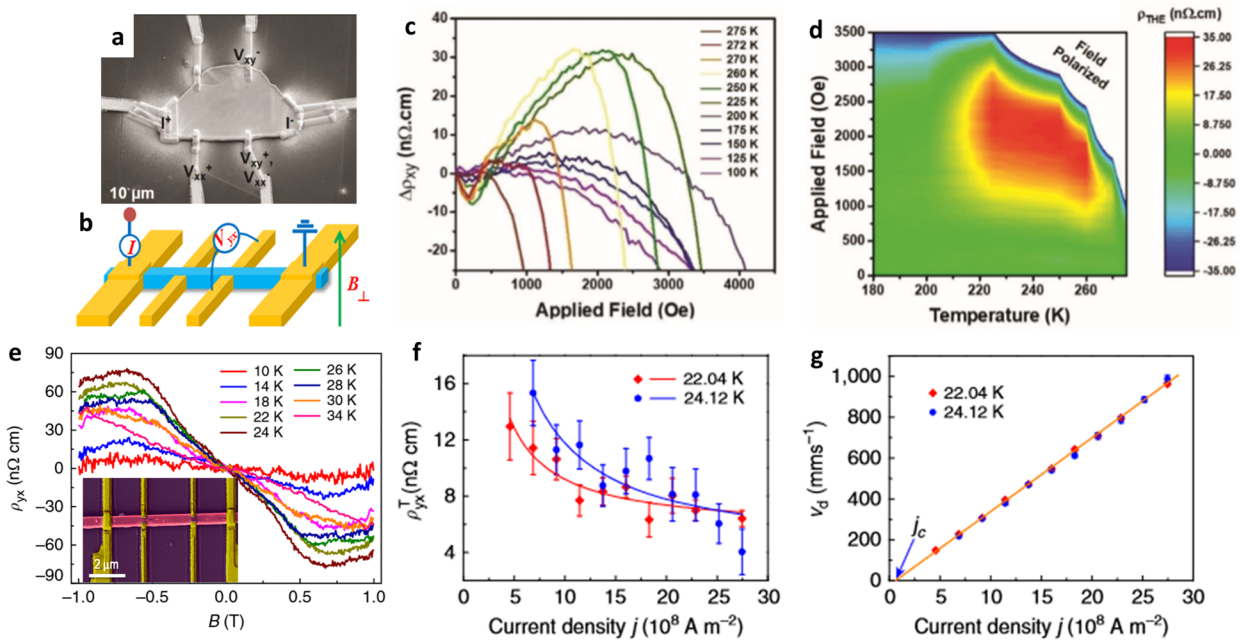

Figure 1.9 : Skyrmion detection and electrodynamics via THE measurements of nanostructures. (a) SEM image of a $Fe_{0.97}Co_{0.03}Ge$ nanoplate with metal contacts fabricated as a Hall device setup shown in the schematic in panel (b). (c) Extracted THE signal of the $Fe_{0.97}Co_{0.03}Ge$ nanoplate obtained from isothermal field sweeps at various temperatures with the corresponding (d) heat map representation of the extracted THE resistivity as a function of the temperature and magnetic field. (e) Extracted THE signal obtained from the Hall device fabricated on a MnSi NW shown in the inset of (e). (g) Maximum THE signal obtained from a MnSi NW as a function of current density that can be fitted as exponential function to estimate the skyrmion drift velocity, vd. (h) Skyrmion drift velocity as a function of current density in a MnSi NW. Extrapolation of a linear fit allows for the estimation of the critical current density, jc, required for skyrmion motion in MnSi NWs. [Panel a,c,d are reproduced with permission from Adv. Funct. Mater. 29, 1805418 (2019), Copyright 2019 Wiley-VCH. Panel b,e-f are reproduced with permission from Nat. Commun. 6, 8217 (2015), Copyright 2015 Springer Nature Limited].

Once the THE signal, and therefore the skyrmion phase, has been positively identified (which can be further corroborated with real space imaging as discussed in Section 3.3), the current dynamics of the skyrmion phase can be studied. The THE signal, which is unique to the skyrmion phase, is dependent on several factors, including the skyrmion domain size (a_{sk}), the normal Hall coefficient, as well as the skyrmion lattice packing (Equation 6),[2,53,121]

$$\rho_{THE} = n \times P \times R_0 \times B_{eff} \quad (6)$$

where n is the skyrmion packing density, P is the spin polarization of charge carriers and B_{eff} is the emergent magnetic field associated with one skyrmion. In addition, the magnitude of the THE signal is also affected by the motion of skyrmion and its drift velocity.[23,121,122] Both SANS[17] and magnetic imaging[117] experiments have shown that skyrmions will begin to move under small applied currents (~1×10^{-6} A/m^2) in a B20 skyrmion hosting material through a spin transfer torque mechanism (Figure 1.2b).[2] Once the skyrmions begin to depin from the lattice and translate, the effective magnetic field, B_{eff}, that is responsible for the THE will begin to produce an emergent electric field, E_{eff}, through Faraday's law of induction.[23, 121] This E_{eff} is oriented opposite to the electric field produced by the electrons deflected due to the THE, which results in a decrease of the THE signal as the skyrmions move. As the current is increased further, the skymion velocity increases, so does the E_{eff} resulting in an ever diminishing THE signal. For this reason, current density dependent Hall effect measurements should give insight into the dynamics of the skyrmion phase and allow for the current density dependent drift velocity, v_d, of the skyrmions to be calculated.

The observation of reduced THE signal due to the emergent field of moving skyrmions was first made on a single crystal of MnSi[23] and then on MnSi NW in perpendicular configuration (inset of Figure 1.9e).[53] However, the fabrication of Hall devices on a single NW is much more challenging that those on thin films and nanoplates morphology.[123-124] In Figure 1.9e, a decay in the THE signal of the MnSi NW was observed with increasing current density. This maximum THE signal at each current density can be determined and plotted (Figure 1.9f). Fitting this decay data to an exponential function (Figure 1.9g) allows for the current density dependent v_d of the skyrmion phase to be determined and extrapolation of the v_d to 0 estimates the critical current density, j_c.[53] This is the current density required for the skyrmions to de-pin and to begin to

translate. In the case of MnSi NWs the j_c was found to be ~ 4×10^7 A/m^2, which is roughly 1 order of magnitude higher than that found in the bulk crystals of MnSi (~2×10^6 A/m^2).[17] In comparison to MnSi bulk crystals, the skyrmions are stabilized and moving in the NWs over a much larger temperature and field window, in which they are not expected to be stable in bulk.

Similar Hall measurements have been implemented to FIB fabricated FeGe nanostrips that successfully acquired quantized THE signal from cluster of individual skyrmion.[125] These THE measurements are important for understanding the electrical dynamics of the skyrmion phase, but the overall signals are quite small (10s of nΩ cm) and the THE measurements are quite challenging. In most cases the THE signal is less than 10% of the total Hall signal. $\rho_{yx}^{T} \propto B_{eff} \propto 1/a_{sk}^{2}$. For reliable electrical detection of the skyrmion phase via THE, fabrication of Hall devices with high signal-to-noise ratio is crucial. The total THE signal is expected to decrease at higher temperatures with the reduction of spin polarization of a materials at elevated temperatures.[44,120] For low temperature measurements, design of novel Hall-bar NW device configuration could be beneficial for creation and THE detection of "metastable" skyrmions by all electrical means.[126-127] Furthermore, reducing the skyrmion domain size *via* chemical alloying could lead to larger THE signal. The future of skyrmion-based memory devices demands more and better selective and sensitive detection technique for skyrmions in magnetic materials.

1.6 Summary and Outlook

Nanostructures of non-centrosymmetric B20 materials have enabled the studies and exploration of magnetic skyrmions in confined magnetic materials which have shed new scientific insights on the confinement and evolution of magnetic skyrmions and laid a solid foundation for skyrmion-based memory and information technology. An overview of the discovery of the

magnetic skyrmion as well as the experimental methods used to detect these exotic magnetic textures in non-centrosymmetric materials either in bulk or as nanostructures is presented in this chapter. Significant progress in the field of skyrmion research has led to the determination of enhanced stability, electrical detection and current-driven dynamics of skyrmions, especially in nanostructures of metal silicide and germanides with B20 crystal structure, using several measurement techniques as discussed herein. These detection methods are discussed in a way that illustrates how each technique can study the magnetic skyrmions with its strengths and weaknesses. Developing more sensitive and accurate methods, especially those methods purely based on electrical transport measurements, to reliably detect skyrmions (including isolated skyrmions) is critical for the realization of skyrmion-based memory devices. Recently, tunneling anisotropic magnetoresistance (TAMR) signal to probe skyrmion domains was acquired via scanning tunneling microscopy.[129-131] This detection technique may be further extended to giant magnetoresistance (GMR) like device design for skyrmion detection, similar to reading elements in HDD for ferromagnetic domains.[65,132,133] Visualizing the fine details of the internal spin structures of skyrmions with novel high resolution magnetic imaging technique such as 4D Lorentz scanning transmission electron microscopy (STEM) could be helpful for further understanding the dynamics of skyrmion motion and their detection.[134] As always, discovery of new materials that can host skyrmions at room temperatures and wider magnetic field range could facilitate the eventual applications of skyrmions, even though this challenge is not unique to nanostructures of skyrmions hosting materials. Apart from magnetic skyrmion stability in non-centrosymmetric B20 materials, recent observation of chiral fermions in B20 materials, stems out curiosity towards understanding of unique topological quantum properties in this class of materials and their implementation in electronic devices.[135-138] The development of purely electrical detection

techniques to detect skyrmions would lay the groundwork for the utilizing nanostructures of these B20 non-centrosymmetric nanostructures as prototypes for the implementation in next generation spintronic devices.

1.7 Contribution to the research field from this work

The research work presented in this thesis primary focus on exploring material platforms that develop a better understanding of topological magnetism in nanostructures. The application of stable topological spin textures in future spintronic devices with high memory densities, necessitates their study of stability, transformation, and detection in nanostructured morphology. We have targeted two key issues in the field of skyrmion-based electronics by investigating magnetic skyrmion in confined geometries of nanostructures: 1) easy accessibility of magnetic skyrmion phase in the presence of other competing non-collinear structures (helical/conical), 2) developing purely electrical and highly sensitivity detection techniques of magnetic skyrmion phase that could be easily implementable in device architectures. Over the past decade, the Song Jin group (UW Madison) has developed the research niche of CVD grown magnetic skyrmion hosting nanostructures. The detailed characterization of the magnetic spin textures on these unique nanostructure samples discussed in this thesis was made possible due to the fruitful research collaboration both nationally and internationally. In collaboration with Dr. Matthew J. Stolt (Song Jin group, UW Madison), we have conducted a detailed analysis of magnetotransport measurements on FeGe nanostructures presented in this thesis. The preliminary magnetotransport measurements on FeGe nanowires initially started at High Magnetic Field lab (Hefei, P.R. China) in Prof. Haifeng Du and Prof Mingliang Tian Lab research group which further motivate the purely electrical of detection of magnetic skyrmions in FeGe nanostructures here at UW-Madison. To corroborate our magnetotransport measurements on these unique nanostructured magnetic

skyrmion samples, the real space imaging of magnetic skyrmion and other spin textures was performed in the research facility at RIKEN (Japan) supervised by Prof. Yoshinori Tokura and Dr. Xiuzhen Yu. Dr Kodai Niitsu (RIKEN, Japan) has performed the challenging task of visualizing the magnetic skyrmion *via* electron holography measurements on well-faceted and unprocessed (no mechanical processing or other modifications) $Fe_{1-x}Co_xSi$ NWs. The real space imaging of three-dimensional structure of magnetic skyrmion strings was carried out by Dr. Fehmi S. Yasin (RIKEN, Japan) on a thin $Fe_{0.95}Co_{0.05}Ge$ nanoplate using an unconventional LTEM imaging setup under an in-plane applied magnetic field at National Institute for Materials Science (NIMS), Japan. With the support of these fruitful research collaborations, we have developed a complete toolkit (transport studies and magnetic imaging) to comprehend the enhanced stability, field driven transformations and electrical detection of magnetic skyrmions in confined sample geometries which can be further extended to material platforms other than cubic B20 materials.

The figures and introduction presented in this chapter have been published in the journal *APL Materials*. Reference as follows: Mathur, N.; Stolt, M. J.; Jin, S., Magnetic skyrmions in nanostructures of non-centrosymmetric materials. *APL Materials* **2019**, 7, 120703.

References

1 U. K. Rößler, A. N. Bogdanov, and C. Pfleiderer, Nature **442**, 797 (2006).
2 N. Nagaosa and Y. Tokura, Nat. Nanotechnol. **8**, 899 (2013).
3 T. H. R. Skyrme, Nucl. Phys. **31**, 556 (1962).
4 T. Moriya, Phys. Rev. **120**, 91 (1960).
5 S. Mühlbauer, B. Binz, F. Jonietz, C. Pfleiderer, A. Rosch, A. Neubauer, R. Georgii, and P. Böni, Science **323**, 915 (2009).
6 X. Z. Yu, Y. Onose, N. Kanazawa, J. H. Park, J. H. Han, Y. Matsui, N. Nagaosa, and Y. Tokura, Nature **465**, 901 (2010).
7 A. Bogdanov and A. Hubert, J. Magn. Magn. Mater. **138**, 255 (1994).
8 I. Dzyaloshinsky, J. Phys. Chem. Solids **4**, 241 (1958).

[9] X. Yu, J. P. DeGrave, Y. Hara, T. Hara, S. Jin, and Y. Tokura, Nano Lett. **13**, 3755 (2013).

[10] A. Tonomura, X. Yu, K. Yanagisawa, T. Matsuda, Y. Onose, N. Kanazawa, H. S. Park, and Y. Tokura, Nano Lett. **12**, 1673 (2012).

[11] X. Z. Yu, N. Kanazawa, Y. Onose, K. Kimoto, W. Z. Zhang, S. Ishiwata, Y. Matsui, and Y. Tokura, Nat. Mater. **10**, 106 (2010).

[12] M. J. Stolt, Z.-A. Li, B. Phillips, D. Song, N. Mathur, R. E. Dunin-Borkowski, and S. Jin, Nano Lett. **17**, 508 (2017).

[13] T. Tanigaki, K. Shibata, N. Kanazawa, X. Yu, Y. Onose, H. S. Park, D. Shindo, and Y. Tokura, Nano Lett. **15**, 5438 (2015).

[14] V. Skumryev, S. Stoyanov, Y. Zhang, G. Hadjipanayis, D. Givord, and J. Nogués, Nature **423**, 850 (2003).

[15] C. Chappert, A. Fert, and F. N. Van Dau, Nat. Mater. **6**, 813 (2007).

[16] A. Brataas, A. D. Kent, and H. Ohno, Nat. Mater. **11**, 372 (2012).

[17] F. Jonietz, S. Mühlbauer, C. Pfleiderer, A. Neubauer, W. Münzer, A. Bauer, T. Adams, R. Georgii, P. Böni, R. A. Duine, K. Everschor, M. Garst, and A. Rosch, Science **330**, 1648 (2010).

[18] J. Sampaio, V. Cros, S. Rohart, A. Thiaville, and A. Fert, Nat. Nanotechnol. **8**, 839 (2013).

[19] S. S. P. Parkin, M. Hayashi, and L. Thomas, Science **320**, 190 (2008).

[20] M. D. Stiles and A. Zangwill, Phys. Rev. B **66**, 014407 (2002).

[21] D. C. Ralph and M. D. Stiles, J. Magn. Magn. Mater. **320**, 1190 (2008).

[22] A. Neubauer, C. Pfleiderer, B. Binz, A. Rosch, R. Ritz, P. G. Niklowitz, and P. Böni, Phys. Rev. Lett. **102**, 186602 (2009).

[23] T. Schulz, R. Ritz, A. Bauer, M. Halder, M. Wagner, C. Franz, C. Pfleiderer, K. Everschor, M. Garst, and A. Rosch, Nat. Phys. **8**, 301 (2012).

[24] S. Zhang, A. A. Baker, S. Komineas, and T. Hesjedal, Sci. Rep. **5**, 15773 (2015).

[25] D. Morikawa, K. Shibata, N. Kanazawa, X. Z. Yu, and Y. Tokura, Phys. Rev. B **88**, 024408 (2013).

[26] A. Fert, V. Cros, and J. Sampaio, Nat. Nanotechnol. **8**, 152 (2013).

[27] A. Pokhrel, J. P. DeGrave, D. Liang, J. M. Higgins, and S. Jin, in *Semiconductor Nanowires: From Next-Generation Electronics to Sustainable Energy* (The Royal Society of Chemistry, 2015), pp. 312.

[28] A. L. Schmitt, L. Zhu, D. Schmeiβer, F. J. Himpsel, and S. Jin, J. Phys. Chem. B **110**, 18142 (2006).

[29] A. L. Schmitt, M. J. Bierman, D. Schmeisser, F. J. Himpsel, and S. Jin, Nano Lett. **6**, 1617 (2006).

[30] J. R. Szczech and S. Jin, J. Mater. Chem. **20**, 1375 (2010).

[31] J. M. Higgins, A. L. Schmitt, I. A. Guzei, and S. Jin, J. Am. Chem. Soc. **130**, 16086 (2008).

[32] J. R. Szczech, A. L. Schmitt, M. J. Bierman, and S. Jin, Chem. Mater. **19**, 3238 (2007).

[33] Y. Song, A. L. Schmitt, and S. Jin, Nano Lett. **7**, 965 (2007).

[34] C. Yan, J. M. Higgins, M. S. Faber, P. S. Lee, and S. Jin, ACS Nano **5**, 5006 (2011).

[35] A. L. Schmitt, J. M. Higgins, J. R. Szczech, and S. Jin, J. Mater. Chem. **20**, 223 (2010).

[36] J. M. Higgins, R. Ding, J. P. DeGrave, and S. Jin, Nano Lett. **10**, 1605 (2010).

[37] H. Du, J. P. DeGrave, F. Xue, D. Liang, W. Ning, J. Yang, M. Tian, Y. Zhang, and S. Jin, Nano Lett. **14**, 2026 (2014).

[38] H. Du, D. Liang, C. Jin, L. Kong, M. J. Stolt, W. Ning, J. Yang, Y. Xing, J. Wang, R. Che, J. Zang, S. Jin, Y. Zhang, and M. Tian, Nat. Commun. **6**, 7637 (2015).

[39] J. In, K. S. K. Varadwaj, K. Seo, S. Lee, Y. Jo, M.-H. Jung, J. Kim, and B. Kim, J. Phys. Chem. C **112**, 4748 (2008).

[40] A. L. Schmitt, J. M. Higgins, and S. Jin, Nano Lett. **8**, 810 (2008).

[41] J. P. DeGrave, A. L. Schmitt, R. S. Selinsky, J. M. Higgins, D. J. Keavney, and S. Jin, Nano Lett. **11**, 4431 (2011).

[42] J. M. Higgins, P. Carmichael, A. L. Schmitt, S. Lee, J. P. Degrave, and S. Jin, ACS Nano **5**, 3268 (2011).

[43] N. Mathur, M. J. Stolt, K. Niitsu, X. Yu, D. Shindo, Y. Tokura, and S. Jin, ACS Nano **13**, 7833 (2019).

[44] M. J. Stolt, S. Schneider, N. Mathur, M. J. Shearer, B. Rellinghaus, K. Nielsch, and S. Jin, Adv. Funct. Mater. **29**, 1805418 (2019).

[45] S. L. Zhang, R. Chalasani, A. A. Baker, N.-J. Steinke, A. I. Figueroa, A. Kohn, G. v. d. Laan, and T. Hesjedal, AIP Adv. **6**, 015217 (2016).

[46] Y. Li, N. Kanazawa, X. Z. Yu, A. Tsukazaki, M. Kawasaki, M. Ichikawa, X. F. Jin, F. Kagawa, and Y. Tokura, Phys. Rev. Lett. **110**, 117202 (2013).

[47] A. S. Ahmed, J. Rowland, B. D. Esser, S. R. Dunsiger, D. W. McComb, M. Randeria, and R. K. Kawakami, Phys. Rev. Mater. **2**, 041401 (2018).

[48] A. S. Ahmed, B. D. Esser, J. Rowland, D. W. McComb, and R. K. Kawakami, J. Cryst. Growth **467**, 38 (2017).

[49] R. Wiesendanger, Nat. Rev. Mater. **1**, 16044 (2016).

[50] A. Fert, N. Reyren, and V. Cros, Nat. Rev. Mater. **2**, 17031 (2017).

[51] K. Everschor-Sitte, J. Masell, R. M. Reeve, and M. Kläui, J. Appl. Phys. **124** (24), 240901 (2018).

[52] N. Kanazawa, S. Seki, and Y. Tokura, Adv. Mater. **29**, 1603227 (2017).

[53] D. Liang, J. P. DeGrave, M. J. Stolt, Y. Tokura, and S. Jin, Nat. Commun. **6**, 8217 (2015).

[54] H. S. Park, X. Yu, S. Aizawa, T. Tanigaki, T. Akashi, Y. Takahashi, T. Matsuda, N. Kanazawa, Y. Onose, D. Shindo, A. Tonomura, and Y. Tokura, Nat. Nanotechnol. **9**, 337 (2014).

[55] D. Song, Z.-A. Li, J. Caron, A. Kovács, H. Tian, C. Jin, H. Du, M. Tian, J. Li, J. Zhu, and R. E. Dunin-Borkowski, Phys. Rev. Lett. **120**, 167204 (2018).

[56] X. Zhao, C. Jin, C. Wang, H. Du, J. Zang, M. Tian, R. Che, and Y. Zhang, Proc. Natl. Acad. Sci. U.S.A **113**, 4918 (2016).

[57] N. Kanazawa, Y. Onose, T. Arima, D. Okuyama, K. Ohoyama, S. Wakimoto, K. Kakurai, S. Ishiwata, and Y. Tokura, Phys. Rev. Lett. **106**, 156603 (2011).

[58] T. Adams, A. Chacon, M. Wagner, A. Bauer, G. Brandl, B. Pedersen, H. Berger, P. Lemmens, and C. Pfleiderer, Phys. Rev. Lett. **108**, 237204 (2012).

[59] M. J. Stolt, X. Sigelko, N. Mathur, and S. Jin, Chem. Mater. **30**, 1146 (2018).

[60] Y. Fujishiro, N. Kanazawa, T. Nakajima, X. Z. Yu, K. Ohishi, Y. Kawamura, K. Kakurai, T. Arima, H. Mitamura, A. Miyake, K. Akiba, M. Tokunaga, A. Matsuo, K. Kindo, T. Koretsune, R. Arita, and Y. Tokura, Nat. Commun. **10**, 1059 (2019).

[61] C. Dhital, M. A. Khan, M. Saghayezhian, W. A. Phelan, D. P. Young, R. Y. Jin, and J. F. DiTusa, Phys. Rev. B **95**, 024407 (2017).

[62] A. Crépieux and C. Lacroix, J. Magn. Magn. Mater. **182**, 341 (1998).

[63] A. N. Bogdanov and U. K. Rößler, Phys. Rev. Lett. **87**, 037203 (2001).

[64] S. Heinze, K. von Bergmann, M. Menzel, J. Brede, A. Kubetzka, R. Wiesendanger, G. Bihlmayer, and S. Blügel, Nat. Phys. **7**, 713 (2011).

[65] N. Romming, C. Hanneken, M. Menzel, J. E. Bickel, B. Wolter, K. von Bergmann, A. Kubetzka, and R. Wiesendanger, Science **341**, 636 (2013).

[66] C. Moreau-Luchaire, C. Moutafis, N. Reyren, J. Sampaio, C. A. F. Vaz, N. Van Horne, K. Bouzehouane, K. Garcia, C. Deranlot, P. Warnicke, P. Wohlhüter, J. M. George, M. Weigand, J. Raabe, V. Cros, and A. Fert, Nat. Nanotechnol. **11**, 444 (2016).

[67] O. Boulle, J. Vogel, H. Yang, S. Pizzini, D. de Souza Chaves, A. Locatelli, T. O. Menteş, A. Sala, L. D. Buda-Prejbeanu, O. Klein, M. Belmeguenai, Y. Roussigné, A. Stashkevich, S. M. Chérif, L. Aballe, M. Foerster, M. Chshiev, S. Auffret, I. M. Miron, and G. Gaudin, Nat. Nanotechnol. **11**, 449 (2016).

[68] K. Yasuda, R. Wakatsuki, T. Morimoto, R. Yoshimi, A. Tsukazaki, K. S. Takahashi, M. Ezawa, M. Kawasaki, N. Nagaosa, and Y. Tokura, Nat. Phys. **12**, 555 (2016).

[69] Q. Shao, Y. Liu, G. Yu, S. K. Kim, X. Che, C. Tang, Q. L. He, Y. Tserkovnyak, J. Shi, and K. L. Wang, Nat. Electron. **2**, 182 (2019).

[70] J. Matsuno, N. Ogawa, K. Yasuda, F. Kagawa, W. Koshibae, N. Nagaosa, Y. Tokura, and M. Kawasaki, Sci. Adv. **2**, e1600304 (2016).

[71] L. Wang, Q. Feng, Y. Kim, R. Kim, K. H. Lee, S. D. Pollard, Y. J. Shin, H. Zhou, W. Peng, D. Lee, W. Meng, H. Yang, J. H. Han, M. Kim, Q. Lu, and T. W. Noh, Nat. Mater. **17**, 1087 (2018).

[72] S. Das, Y. L. Tang, Z. Hong, M. A. P. Gonçalves, M. R. McCarter, C. Klewe, K. X. Nguyen, F. Gómez-Ortiz, P. Shafer, E. Arenholz, V. A. Stoica, S. L. Hsu, B. Wang, C. Ophus, J. F. Liu, C. T. Nelson, S. Saremi, B. Prasad, A. B. Mei, D. G. Schlom, J. Íñiguez, P. García-Fernández, D. A. Muller, L. Q. Chen, J. Junquera, L. W. Martin, and R. Ramesh, Nature **568**, 368 (2019).

[73] I. Kézsmárki, S. Bordács, P. Milde, E. Neuber, L. M. Eng, J. S. White, H. M. Rønnow, C. D. Dewhurst, M. Mochizuki, K. Yanai, H. Nakamura, D. Ehlers, V. Tsurkan, and A. Loidl, Nat. Mater. **14**, 1116 (2015).

[74] Y. Tokunaga, X. Z. Yu, J. S. White, H. M. Rønnow, D. Morikawa, Y. Taguchi, and Y. Tokura, Nat. Commun. **6**, 7638 (2015).

[75] W. Li, C. Jin, R. Che, W. Wei, L. Lin, L. Zhang, H. Du, M. Tian, and J. Zang, Phys. Rev. B **93**, 060409 (2016).

[76] Z. Hou, W. Ren, B. Ding, G. Xu, Y. Wang, B. Yang, Q. Zhang, Y. Zhang, E. Liu, F. Xu, W. Wang, G. Wu, X. Zhang, B. Shen, and Z. Zhang, Adv. Mater. **29**, 1701144 (2017).

[77] J. C. Loudon, A. C. Twitchett-Harrison, D. Cortés-Ortuño, M. T. Birch, L. A. Turnbull, A. Štefančič, F. Y. Ogrin, E. O. Burgos-Parra, N. Bukin, A. Laurenson, H. Popescu, M. Beg, O. Hovorka, H. Fangohr, P. A. Midgley, G. Balakrishnan, and P. D. Hatton, Adv. Mater. **31**, 1806598 (2019).

[78] A. K. Nayak, V. Kumar, T. Ma, P. Werner, E. Pippel, R. Sahoo, F. Damay, U. K. Rößler, C. Felser, and S. S. P. Parkin, Nature **548**, 561 (2017).

[79] F. Zheng, F. N. Rybakov, A. B. Borisov, D. Song, S. Wang, Z.-A. Li, H. Du, N. S. Kiselev, J. Caron, A. Kovács, M. Tian, Y. Zhang, S. Blügel, and R. E. Dunin-Borkowski, Nat. Nanotechnol. **13**, 451 (2018).

[80] N. Kanazawa, J. S. White, H. M. Rønnow, C. D. Dewhurst, Y. Fujishiro, A. Tsukazaki, Y. Kozuka, M. Kawasaki, M. Ichikawa, F. Kagawa, and Y. Tokura, Phys. Rev. B **94**, 184432 (2016).

[81] E. Moskvin, S. Grigoriev, V. Dyadkin, H. Eckerlebe, M. Baenitz, M. Schmidt, and H. Wilhelm, Phys. Rev. Lett. **110**, 077207 (2013).

[82] K. Ishimoto, Y. Yamaguchi, J. Suzuki, M. Arai, M. Furusaka, and Y. Endoh, Phys. B (Amsterdam, Neth.) **213-214**, 381 (1995).

[83] W. Münzer, A. Neubauer, T. Adams, S. Mühlbauer, C. Franz, F. Jonietz, R. Georgii, P. Böni, B. Pedersen, M. Schmidt, A. Rosch, and C. Pfleiderer, Phys. Rev. B **81**, 041203 (2010).

[84] S. V. Grigoriev, V. A. Dyadkin, D. Menzel, J. Schoenes, Y. O. Chetverikov, A. I. Okorokov, H. Eckerlebe, and S. V. Maleyev, Phys. Rev. B **76**, 224424 (2007).

[85] S. L. Zhang, A. Bauer, D. M. Burn, P. Milde, E. Neuber, L. M. Eng, H. Berger, C. Pfleiderer, G. van der Laan, and T. Hesjedal, Nano Lett. **16**, 3285 (2016).

[86] S. L. Zhang, G. van der Laan, W. W. Wang, A. A. Haghighirad, and T. Hesjedal, Phys. Rev. Lett. **120**, 227202 (2018).

[87] M. C. Langner, S. Roy, S. K. Mishra, J. C. T. Lee, X. W. Shi, M. A. Hossain, Y. D. Chuang, S. Seki, Y. Tokura, S. D. Kevan, and R. W. Schoenlein, Phys. Rev. Lett. **112**, 167202 (2014).

[88] S. L. Zhang, A. Bauer, H. Berger, C. Pfleiderer, G. van der Laan, and T. Hesjedal, Phys. Rev. B **93**, 214420 (2016).

[89] S. Zhang, G. van der Laan, J. Müller, L. Heinen, M. Garst, A. Bauer, H. Berger, C. Pfleiderer, and T. Hesjedal, Proc. Natl. Acad. Sci. U.S.A **115**, 6386 (2018).

[90] C. V. Topping and S. J. Blundell, J. Phys. Condens. Matter **31**, 013001 (2018).

[91] A. Bauer and C. Pfleiderer, Phys. Rev. B **85**, 214418 (2012).

[92] E. Karhu, S. Kahwaji, T. L. Monchesky, C. Parsons, M. D. Robertson, and C. Maunders, Phys. Rev. B **82**, 184417 (2010).

[93] H. Wilhelm, M. Baenitz, M. Schmidt, U. K. Rößler, A. A. Leonov, and A. N. Bogdanov, Phys. Rev. Lett. **107**, 127203 (2011).

[94] J. F. DiTusa, S. B. Zhang, K. Yamaura, Y. Xiong, J. C. Prestigiacomo, B. W. Fulfer, P. W. Adams, M. I. Brickson, D. A. Browne, C. Capan, Z. Fisk, and J. Y. Chan, Phys. Rev. B **90**, 144404 (2014).

[95] M. Garst, J. Waizner, and D. Grundler, J. Phys. D **50**, 293002 (2017).

[96] E. Turgut, M. J. Stolt, S. Jin, and G. D. Fuchs, J. Appl. Phys. **122**, 183902 (2017).

[97] T. Schwarze, J. Waizner, M. Garst, A. Bauer, I. Stasinopoulos, H. Berger, C. Pfleiderer, and D. Grundler, Nat. Mater. **14**, 478 (2015).

[98] Y. Okamura, F. Kagawa, M. Mochizuki, M. Kubota, S. Seki, S. Ishiwata, M. Kawasaki, Y. Onose, and Y. Tokura, Nat. Commun. **4**, 2391 (2013).

[99] P. Milde, D. Köhler, J. Seidel, L. M. Eng, A. Bauer, A. Chacon, J. Kindervater, S. Mühlbauer, C. Pfleiderer, S. Buhrandt, C. Schütte, and A. Rosch, Science **340**, 1076 (2013).

[100] M. De Graef, in *Experimental Methods in the Physical Sciences*, edited by Marc De Graef and Yimei Zhu (Academic Press, 2001), Vol. 36, pp. 27.

[101] A. Tonomura, Rev. Mod. Phys. **59**, 639 (1987).

[102] H. Lichte, Ultramicroscopy **20**, 293 (1986).

[103] H. Lichte and M. Lehmann, Rep. Prog. Phys **71**, 016102 (2007).

[104] P. A. Midgley and R. E. Dunin-Borkowski, Nat. Mater. **8**, 271 (2009).

[105] H. Du, R. Che, L. Kong, X. Zhao, C. Jin, C. Wang, J. Yang, W. Ning, R. Li, C. Jin, X. Chen, J. Zang, Y. Zhang, and M. Tian, Nat. Commun. **6**, 8504 (2015).

[106] S. Schneider, D. Wolf, M. J. Stolt, S. Jin, D. Pohl, B. Rellinghaus, M. Schmidt, B. Büchner, S. T. B. Goennenwein, K. Nielsch, and A. Lubk, Phys. Rev. Lett. **120**, 217201 (2018).

[107] A. B. Butenko, A. A. Leonov, U. K. Rößler, and A. N. Bogdanov, Phys. Rev. B **82**, 052403 (2010).

[108] S. X. Huang and C. L. Chien, Phys. Rev. Lett. **108**, 267201 (2012).

[109] S. D. Yi, S. Onoda, N. Nagaosa, and J. H. Han, Phys. Rev. B **80**, 054416 (2009).

[110] A. Mehlin, F. Xue, D. Liang, H. F. Du, M. J. Stolt, S. Jin, M. L. Tian, and M. Poggio, Nano Lett. **15**, 4839 (2015).

[111] C. Jin, Z.-A. Li, A. Kovács, J. Caron, F. Zheng, F. N. Rybakov, N. S. Kiselev, H. Du, S. Blügel, M. Tian, Y. Zhang, M. Farle, and R. E. Dunin-Borkowski, Nat. Commun. **8**, 15569 (2017).

[112] F. Zheng, H. Li, S. Wang, D. Song, C. Jin, W. Wei, A. Kovács, J. Zang, M. Tian, Y. Zhang, H. Du, and R. E. Dunin-Borkowski, Phys. Rev. Lett. **119**, 197205 (2017).

[113] K. Hamamoto, M. Ezawa, and N. Nagaosa, Appl. Phys. Lett. **108**, 112401 (2016).

[114] D. Maccariello, W. Legrand, N. Reyren, K. Garcia, K. Bouzehouane, S. Collin, V. Cros, and A. Fert, Nat. Nanotechnol. **13**, 233 (2018).

[115] S. Wang, J. Tang, W. Wang, L. Kong, M. Tian, and H. Du, J. Low Temp. Phys. (2019).

[116] M. Nagao, Y.-G. So, H. Yoshida, M. Isobe, T. Hara, K. Ishizuka, and K. Kimoto, Nat. Nanotechnol. **8**, 325 (2013).

[117] X. Z. Yu, N. Kanazawa, W. Z. Zhang, T. Nagai, T. Hara, K. Kimoto, Y. Matsui, Y. Onose, and Y. Tokura, Nat. Commun. **3**, 988 (2012).

[118] N. Nagaosa and Y. Tokura, Phys. Scr. **T146**, 014020 (2012).

[119] N. A. Porter, J. C. Gartside, and C. H. Marrows, Phys. Rev. B **90**, 024403 (2014).

[120] M. Leroux, M. J. Stolt, S. Jin, D. V. Pete, C. Reichhardt, and B. Maiorov, Sci. Rep. **8**, 15510 (2018).

[121] J. Iwasaki, M. Mochizuki, and N. Nagaosa, Nat. Nanotechnol. **8**, 742 (2013).

[122] J. Zang, M. Mostovoy, J. H. Han, and N. Nagaosa, Phys. Rev. Lett. **107**, 136804 (2011).

[123] J. P. DeGrave, D. Liang, and S. Jin, Nano Lett. **13** (6), 2704 (2013).

[124] K. Storm, F. Halvardsson, M. Heurlin, D. Lindgren, A. Gustafsson, P. M. Wu, B. Monemar, and L. Samuelson, Nat. Nanotechnol. **7**, 718 (2012)

[125] N. Kanazawa, M. Kubota, A. Tsukazaki, Y. Kozuka, K. S. Takahashi, M. Kawasaki, M. Ichikawa, F. Kagawa, and Y. Tokura, Phys. Rev. B **91**, 041122 (2015).

[126] H. Oike, A. Kikkawa, N. Kanazawa, Y. Taguchi, M. Kawasaki, Y. Tokura, and F. Kagawa, Nat. Phys. **12**, 62 (2015).

[127] D. Liang, M. J. Stolt, and S. Jin, Nat. Phys. **12**, 25 (2016).

[128] F. Kagawa, H. Oike, W. Koshibae, A. Kikkawa, Y. Okamura, Y. Taguchi, N. Nagaosa, and Y. Tokura, Nat. Commun. **8**, 1332 (2017).

[129] C. Hanneken, F. Otte, A. Kubetzka, B. Dupé, N. Romming, K. von Bergmann, R. Wiesendanger, and S. Heinze, Nat. Nanotechnol. **10**, 1039 (2015).

[130] D. M. Crum, M. Bouhassoune, J. Bouaziz, B. Schweflinghaus, S. Blügel, and S. Lounis, Nat. Commun. **6**, 8541 (2015).

[131] M. Hervé, B. Dupé, R. Lopes, M. Böttcher, M. D. Martins, T. Balashov, L. Gerhard, J. Sinova, and W. Wulfhekel, Nat. Commun. **9**, 1015 (2018).

[132] X. Zhang, W. Cai, X. Zhang, Z. Wang, Z. Li, Y. Zhang, K. Cao, N. Lei, W. Kang, Y. Zhang, H. Yu, Y. Zhou, and W. Zhao, ACS Appl. Mater. Interfaces **10**, 16887 (2018).

[133] N. E. Penthorn, X. Hao, Z. Wang, Y. Huai, and H. W. Jiang, Phys. Rev. Lett. **122**, 257201 (2019).

[134] Z. Chen, E. Turgut, Y. Jiang, K. X. Nguyen, G. C. Correa, M. J. Stolt, S. Jin, D. C. Ralph, G. D. Fuchs, and D. A. Muller, Microsc. Microanal. **25**, 32 (2019).

[135] P. Tang, Q. Zhou, and S.-C. Zhang, Phys. Rev. Lett. **119**, 206402 (2017).

[136] Z. Rao, H. Li, T. Zhang, S. Tian, C. Li, B. Fu, C. Tang, L. Wang, Z. Li, W. Fan, J. Li, Y. Huang, Z. Liu, Y. Long, C. Fang, H. Weng, Y. Shi, H. Lei, Y. Sun, T. Qian, and H. Ding, Nature **567**, 496 (2019).

[137] D. Takane, Z. Wang, S. Souma, K. Nakayama, T. Nakamura, H. Oinuma, Y. Nakata, H. Iwasawa, C. Cacho, T. Kim, K. Horiba, H. Kumigashira, T. Takahashi, Y. Ando, and T. Sato, Phys. Rev. Lett. **122**, 076402 (2019).

[138] D. S. Sanchez, I. Belopolski, T. A. Cochran, X. Xu, J.-X. Yin, G. Chang, W. Xie, K. Manna, V. Süß, C.-Y. Huang, N. Alidoust, D. Multer, S. S. Zhang, N. Shumiya, X. Wang, G.-Q. Wang, T.-R. Chang, C. Felser, S.-Y. Xu, S. Jia, H. Lin, and M. Z. Hasan, Nature **567**, 500 (2019).

Chapter 2 : Defects in Two-Dimensional Magnetic Van Der Waals Materials

2.1 Introduction

Since the realization of monolayer graphene, the field of two-dimensional (2D) van der Waals (vdW) materials have shown remarkable progress that could be beneficial to fabricate next generation nanodevices.[1-3] The recent discovery of 2D vdW magnetic materials enables the possibility of stable long-range magnetic spin order down to a single atomic layer of atoms.[4, 5] The presence of long-range intrinsic magnetic ordering in some 2D vdW magnetic monolayers alleviate the limitations imposed by Mermin-Wagner theorem. This emerging field of research promotes investigations towards the understanding of magnetic phase transitions and emergent phenomena in vertically stacked layered arrangements of 2D vdW magnets.[4, 6] The measurements needed to acquire the layer-dependent magnetic response of 2D vdW magnets are routinely conducted by exfoliating as-grown bulk crystals down to few layers in inert environment and further encapsulating with graphene or/and hexagonal boron nitride (h-BN) layers to prevent exposure from moisture and oxygen.[7-9] However, the mechanical exfoliation process might bring extrinsic disorders and defects such as remaining polymer residue between the layers or wrinkled/broken layers during the transfer process of stacked layers.[10-14] Improvements in exfoliation processes are required to address these shortcomings to further study the novel properties in 2D vdW magnets. Apart from the emerging extrinsic defects during the transfer process, intrinsic disorders such as point defects, that are often unavoidable during growth process and strongly influence the key physical properties of 2D vdW materials. Minimizing points defect in 2D vdW magnets are always advantages for the examination of intrinsic magnetic ordering. However, the comprehensive understanding of well-characterized crystalline defects and their

correlation to the intrinsic magnetic ordering could also enable exploration of defect-tunable magnetism in 2D vdW magnets.

2.2 Vacancy Defects in Correlated Magnetic Van Der Waals Materials

Due to low formation energy, the atomic vacancies are commonly found during the synthesis process of 2D vdW materials as shown in case of many transition metal dichalcogenides (TMDs).[12-14] Furthermore, both anion and cation vacancies shown to occur in TMDs which depends on the synthesis route undertaken for the growth of the crystal.[13] Like TMDs, we expect that the presence of vacancy defects in 2D vdW magnets might perturb the intrinsic magnetic ordering, particularly, when the strong magnetic correlation involved with neighboring magnetic atoms. The family of antiferromagnetic transition metal phosphorus trichalcogenides, MPX_3, exhibiting strong correlation between electronic (charge) and magnetic (spin) structure that results from long-range superexchange interactions mediated by sulfur atoms.[15-17] Bulk crystals of MPX_3 are characterized by monoclinic structure (space group: C 2/m) where the transition metal (M) cations are generally 3d elements (Mn, Fe, Co, Ni etc.) surrounded by an octahedral cage formed by six $[P_2X_6]^{4-}$ (S or Se) bipyramids forming a 2D graphene-like honeycomb lattice arrangement with neighboring metal ions.[18] MPX_3 compounds exhibit various types of antiferromagnetic ordering such as zig-zag, Neel, and stripy-pattern below their respective Néel temperature (T_N) (Table 2.1) resulting from long-range anion-mediated magnetic exchange interactions.[15, 19-21] Exploring chemical synthesis methods with comprehensive structure and magnetic characterization of MPX_3 materials could assist in understanding the role of vacancy defects in defect-mediated magnetism.

Table 2.1: Summary of magnetic ordering of antiferromagnetic transition metal phosphorus trichalcogenides, MPX_3. The following columns of the table provide information including the antiferromagnetic spin arrangement and ordering temperature (T_N)

Material	Antiferromagnetic ordering	T_N (K)	Spin arrangement
$FePS_3$ [19]	out-of-plane anisotropy	118	Zig-Zag
$MnPS_3$ [20]	out-of-plane anisotropy	78	Neel, isotropic
$NiPS_3$ [21]	In-plane anisotropy	155	Zig-Zag with slight out of plane tilt
$CoPS_3$[22]	In-plane anisotropy	120	Zig-Zag

2.3 Topological Defects in 2D Van Der Waals Materials

Apart from commonly found atomic vacancy defects in 2D vdW materials during synthesis process, defects like dislocation in materials are distinguishable from other lattice imperfections as these are characterized by topological invariant known as Burgers vector (b).[23] Thus, they fall under the category of topological crystalline defects. These crystalline defects exist in materials as three prototypes: 1) edge dislocations, 2) screw dislocation and 3) disclinations, where both edge and screw dislocation defined by translational displacement of plane near the defect line (ξ_0) while disclinations involve rotational displacement vector (ω) as shown in Figure 2.1a-g.[24] Mathematically, topological nature of these defects is illustrated by Burgers circuits formed by an arbitrary loop (L) encompassing the dislocation and taking a line integral of displacement vector u defined as the difference between the atomic location R in a dislocated crystal and the atomic

location R_0 in the corresponding pristine crystal arrangement, i.e., $u \equiv R - R_0$ (Figure 2.1h). The value of the line integral gives a topological invariant parameter as b of the dislocation which remains the same irrespective of the shape of Burgers circuits encompassing the dislocation (Figure 2.1i).

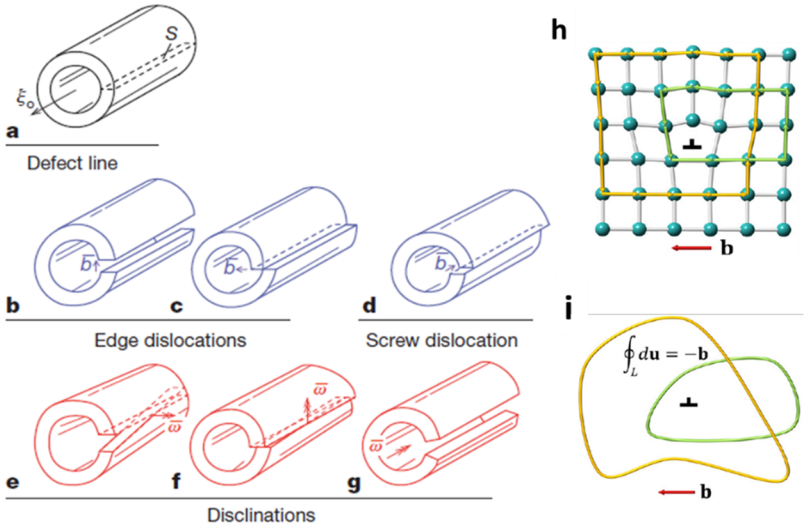

Figure 2.1 : Topological crystalline defects. (a) Illustration of a hollow cylinder cut along the plane S and long the define line ξ_0. Linear defects such as (b,c) edge and (d) screw dislocations marked with respective Burgers vector b. (e,f,g) Twist defects shown as disclinations marked with Frank vector ω. (h) Schematic of a dislocation incorporated inside a loop marked with yellow trace known as Burgers circuit. (i) The topological invariant, b , is independent of the shape of the Burgers circuit if it incorporates the dislocation. Panels a-g are reproduced with permission from *Nature* **2014**, *507*, 51. Copyright 2014 Springer Nature Limited. Panels h,1 are reproduced with permission from *J. Phys. Condens. Matter* **2019**, *31*, 083001. Copyright 2019 IOP Publishing.

2.3.1 Screw Dislocation Driven Growth of Spiral 2D Van Der Waals Nanoplates

Besides the unquie topological nature of these crystal defects, dislocations play a key role as an active nucleation site for the growth of 2D vdW materials. [25-27] Particularly, screw dislocation driven growth mechanism adopted by 2D layered materials allow them to grow in a spiral topology that can create a complex layer stacking rather than conventional layer-by-layer growth mechanism. The layer-by-layer growth in conventional bulk crystals and nanoplates of 2D layered materials require high supersaturation (μ) of growth precursors to overcome the energy barrier for

the formation of new stacked layers (μ is defined by μ = ln (c/c*), where c and c* are represented by precursor's concentration and its equilibrium concentration, respectively). In contrast, the growth driven by dislocation step edge can be achieved at a low supersaturation (Figure 2.2a) of precursors described by Burton-Cabrera-Frank (BCF) crystal field growth theory.[28] Therefore, setting the parameters that allow low μ of precursors is crucial for the synthesis and growth control of layered spiral nanoplates. The initial introduction of screw dislocation for the SDD growth of

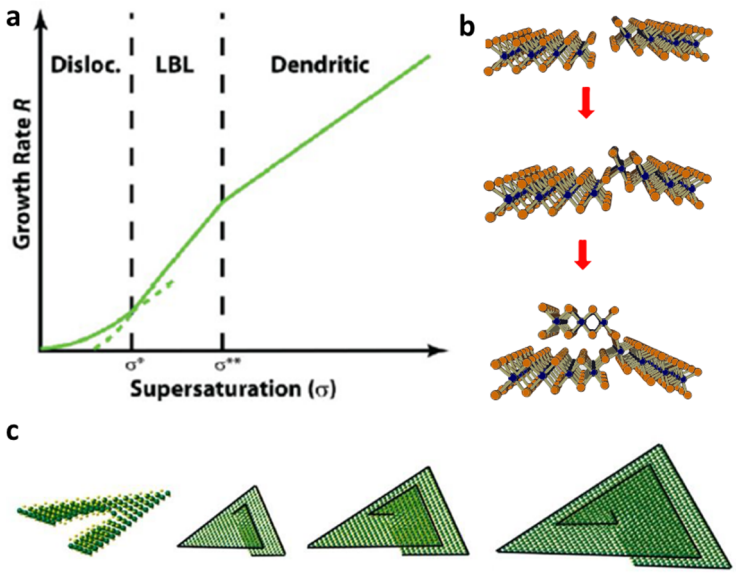

Figure 2.2: SDD growth of spiral nanoplates. (a) Growth rate (R) dependence on supersaturation (σ). Progression of screw dislocation nucleation originating from two adjacent individual 2D layers. Propagation of screw dislocation by acting as a nucleation site for atoms, growing as a spiral nanoplate. Panel a is reproduced with permission from *Science* **2010**, *328,* 476. Copyright 2010 AAAS. Panel b is reproduced with permission from *ACS Nano* **2014**, *8*, 11543. Copyright 2014 ACS. Panel c is reproduced with permission *Nano Lett.* **2014**, *14*, 6418. Copyright 2014 ACS.

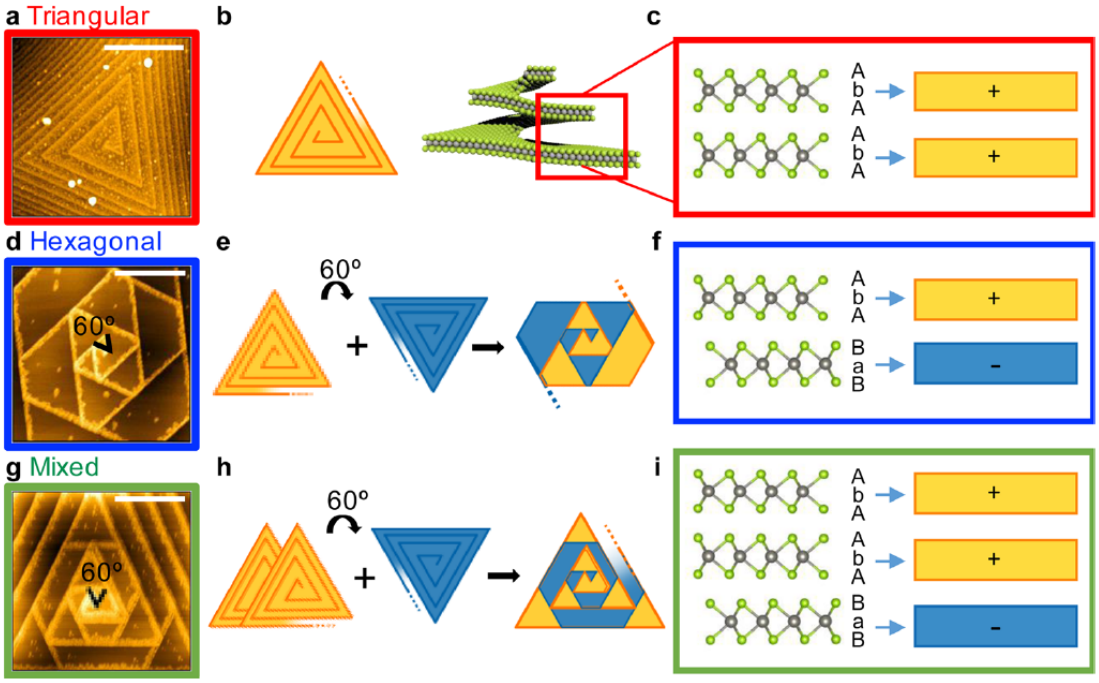

Figure 2.3 : Stacking configuration of SDD grown WS_2 nanoplates (a) AFM image of the triangular spiral as represented in schematic in panel (b). (c) Layer stacking of triangular spiral nanoplate showing AbA order of noncentrosymmetric 2H layers marked by + stacking of individual layer. (d) AFM image of the hexagonal spiral formed by two triangular spirals stacked after 60° rotation represented in schematic in panel (e). (f) Layer stacking of hexagonal spiral nanoplate AbA stacking and BaB (marked by -) stacking of adjacent layers resulting a centrosymmetric structure. (g) AFM image of the mixed spiral formed by three triangular spirals where two triangular spirals and one triangular stacked after 60° rotation represented in schematic in panel (h). (i) Layer stacking of mixed spiral nanoplate 2 AbA (++) layers and BaB (-) stacked together resulting a non-centrosymmetric structure. Shinny grey are W and green atoms are S. Scale bar in a, d and g are 500 nm. Figure 3 is reproduced with permission from *J. Am. Chem. Soc.* **2017**, *139*, 3496. Copyright 2017 ACS.

spiral vdW nanoplates might occur because of the mismatch in the growth rate between the two nearby layers (Figure 2.2b, c). [29, 30] In addition, the other external factors such as uneven topography of the growth substate and microparticle inclusions could also be responsible for the initial introduction of screw dislocation growth sites. The dimensions of the spiral vdW nanoplates are determined by the growth rate in both vertical (direction of screw axis) and lateral directions. Interestingly, the 2D nanoplates grown via multiple screw dislocation create a complex layer stacking as shown in case of CVD-synthesized WS_2 spiral nanoplates (Figure 2.3).[31] The

dislocated nanoplates of MX_2 formed by a single screw dislocation appear as a triangular-shaped spiral (Figure 2.3a-c). The spiral created by two triangular shaped screw dislocations stacked after 60° rotation form a hexagonal spiral (Figure 2.3d-f). Further, the three-dislocation spiral with two stacked triangular spirals with no rotation and a triangular spiral stacked after 60° rotation form a mixed spiral stacking (Figure 2.3g-i). The result of the crystal symmetry breaking manifested by these complex stacking of screw dislocated plates has directly impacted the optical properties of WS_2 spiral nanoplates. More recently, it has been reported that the growth of screw dislocated nanoplates on curved surfaces (non-Euclidean) such as gold/oxide nanoparticles enables consistent twisting of individual layers, forming a twisted spiral structure (like a spiral staircase).[32] This direct growth of twisted spiral structures provides a prefect alterative to stacked twisted multilayers (>2) which could be an extremely cumbersome task when performed mechanically.

2.4 Contribution to the research field from this work

Magnetism mediated by symmetry breaking is ubiquitous in condensed matter systems including the 2D vdW magnets. Crystal defects, often unavoidable during the growth processes, break the lattice symmetry of the crystal in the vicinity of the defect site and strongly influence the magnetic properties of the material. The role of crystalline defects is extensively studied in 2D vdW materials like graphene, TMDs including their influence on the key fundamental properties that could hinder or improve the device performance. We expect that the presence of crystalline defects in 2D vdW magnets could directly affect the intrinsic magnetic ordering of the system and well-characterized defects in crystals could enable another knob for tuning 2D magnetism. I have conducted a comprehensive structural and magnetic characterization of $Ni_{1-x}Co_xPS_3$ nanosheets and bulk single crystals in collaboration with Dr. Fengmei Wang (CAS Key Laboratory of Nanosystem and Hierarchical Fabrication, P.R. China) and these findings are further supported by

theoretical calculations performed by Dr. Aurora N. Janes (UW Madison, Schmidt group). The detailed analysis of magnetic correlations in the presence of sulfur vacancy defects reveal the phenomenon of defect mediated ferromagnetism in $NiPS_3$ antiferromagnets and promote future exploration of other competing correlated states and magnetic spin textures by defect engineering in 2D antiferromagnets. We further developed a method for the synthesis of 2D vdW magnets with topological defects *via* SDD growth of vdW materials that fall right into the Song Jin group's area of expertise. These unique nanostructures could provide a new material platform to explore and understand the microscopic picture of dislocation-spin interaction that are governed by the principle of topology.

References

[1] K. S. Novoselov, A. K. Geim, S. V. Morozov, D. Jiang, Y. Zhang, S. V. Dubonos, I. V. Grigorieva, A. A. Firsov, *Science* **2004**, *306*, 666.

[2] K. F. Mak, C. Lee, J. Hone, J. Shan, T. F. Heinz, *Phys. Rev. Lett.* **2010**, *105*, 136805.

[3] A. K. Geim, I. V. Grigorieva, *Nature* **2013**, *499*, 419.

[4] B. Huang, G. Clark, E. Navarro-Moratalla, D. R. Klein, R. Cheng, K. L. Seyler, D. Zhong, E. Schmidgall, M. A. McGuire, D. H. Cobden, W. Yao, D. Xiao, P. Jarillo-Herrero, X. Xu, *Nature* **2017**, *546*, 270.

[5] C. Gong, L. Li, Z. Li, H. Ji, A. Stern, Y. Xia, T. Cao, W. Bao, C. Wang, Y. Wang, Z. Q. Qiu, R. J. Cava, S. G. Louie, J. Xia, X. Zhang, *Nature* **2017**, *546*, 265.

[6] B. Huang, M. A. McGuire, A. F. May, D. Xiao, P. Jarillo-Herrero, X. Xu, *Nat. Mater.* **2020**, *19*, 1276.

[7] Y. Huang, Y.-H. Pan, R. Yang, L.-H. Bao, L. Meng, H.-L. Luo, Y.-Q. Cai, G.-D. Liu, W.-J. Zhao, Z. Zhou, L.-M. Wu, Z.-L. Zhu, M. Huang, L.-W. Liu, L. Liu, P. Cheng, K.-H. Wu, S.-B. Tian, C.-Z. Gu, Y.-G. Shi, Y.-F. Guo, Z. G. Cheng, J.-P. Hu, L. Zhao, G.-H. Yang, E. Sutter, P. Sutter, Y.-L. Wang, W. Ji, X.-J. Zhou, H.-J. Gao, *Nat. Commun.* **2020**, *11*, 2453.

[8] B. Huang, G. Clark, D. R. Klein, D. MacNeill, E. Navarro-Moratalla, K. L. Seyler, N. Wilson, M. A. McGuire, D. H. Cobden, D. Xiao, W. Yao, P. Jarillo-Herrero, X. Xu, *Nat. Nanotechnol.* **2018**, *13*, 544.

[9] T. Song, X. Cai, M. W.-Y. Tu, X. Zhang, B. Huang, N. P. Wilson, K. L. Seyler, L. Zhu, T. Taniguchi, K. Watanabe, M. A. McGuire, D. H. Cobden, D. Xiao, W. Yao, X. Xu, *Science* **2018**, *360*, 1214.

[10] M. Yi, Z. Shen, *Journal of Materials Chemistry A* **2015**, *3*, 11700.

[11] J. Hong, Z. Hu, M. Probert, K. Li, D. Lv, X. Yang, L. Gu, N. Mao, Q. Feng, L. Xie, J. Zhang, D. Wu, Z. Zhang, C. Jin, W. Ji, X. Zhang, J. Yuan, Z. Zhang, *Nat. Commun.* **2015**, *6*, 6293.

[12] D. Rhodes, S. H. Chae, R. Ribeiro-Palau, J. Hone, *Nat. Mater.* **2019**, *18*, 541.
[13] Z. Lin, B. R. Carvalho, E. Kahn, R. Lv, R. Rao, H. Terrones, M. A. Pimenta, M. Terrones, *2D Materials* **2016**, *3*, 022002.
[14] J. Jiang, T. Xu, J. Lu, L. Sun, Z. Ni, *Research* **2019**, *2019*, 4641739.
[15] S. Y. Kim, T. Y. Kim, L. J. Sandilands, S. Sinn, M.-C. Lee, J. Son, S. Lee, K.-Y. Choi, W. Kim, B.-G. Park, C. Jeon, H.-D. Kim, C.-H. Park, J.-G. Park, S. J. Moon, T. W. Noh, *Phys. Rev. Lett.* **2018**, *120*, 136402.
[16] K. Kim, S. Y. Lim, J.-U. Lee, S. Lee, T. Y. Kim, K. Park, G. S. Jeon, C.-H. Park, J.-G. Park, H. Cheong, *Nat. Commun.* **2019**, *10*, 345.
[17] S. Kang, K. Kim, B. H. Kim, J. Kim, K. I. Sim, J.-U. Lee, S. Lee, K. Park, S. Yun, T. Kim, A. Nag, A. Walters, M. Garcia-Fernandez, J. Li, L. Chapon, K.-J. Zhou, Y.-W. Son, J. H. Kim, H. Cheong, J.-G. Park, *Nature* **2020**, *583*, 785.
[18] F. Wang, T. A. Shifa, P. Yu, P. He, Y. Liu, F. Wang, Z. Wang, X. Zhan, X. Lou, F. Xia, J. He, *Adv. Funct. Mater.* **2018**, *28*, 1802151.
[19] J.-U. Lee, S. Lee, J. H. Ryoo, S. Kang, T. Y. Kim, P. Kim, C.-H. Park, J.-G. Park, H. Cheong, *Nano Lett.* **2016**, *16*, 7433.
[20] Y.-J. Sun, Q.-H. Tan, X.-L. Liu, Y.-F. Gao, J. Zhang, *The Journal of Physical Chemistry Letters* **2019**, *10*, 3087.
[21] N. Chandrasekharan, S. Vasudevan, *J. Phys. Condens. Matter* **1994**, *6*, 4569.
[22] A. R. Wildes, V. Simonet, E. Ressouche, R. Ballou, G. J. McIntyre, *J. Phys. Condens. Matter* **2017**, *29*, 455801.
[23] M. Li, *J. Phys. Condens. Matter* **2019**, *31*, 083001.
[24] P. Cordier, S. Demouchy, B. Beausir, V. Taupin, F. Barou, C. Fressengeas, *Nature* **2014**, *507*, 51.
[25] F. Meng, S. A. Morin, A. Forticaux, S. Jin, *Accounts of Chemical Research* **2013**, *46*, 1616.
[26] R. Chen, J. Cao, S. Gee, Y. Liu, J. Yao, *MRS Advances* **2020**, *5*, 3437.
[27] S. A. Morin, M. J. Bierman, J. Tong, S. Jin, *Science* **2010**, *328*, 476.
[28] W. K. Burton, N. Cabrera, F. C. Frank, *Nature* **1949**, *163*, 398.
[29] L. Zhang, K. Liu, A. B. Wong, J. Kim, X. Hong, C. Liu, T. Cao, S. G. Louie, F. Wang, P. Yang, *Nano Lett.* **2014**, *14*, 6418.
[30] L. Chen, B. Liu, A. N. Abbas, Y. Ma, X. Fang, Y. Liu, C. Zhou, *ACS Nano* **2014**, *8*, 11543.
[31] M. J. Shearer, L. Samad, Y. Zhang, Y. Zhao, A. Puretzky, K. W. Eliceiri, J. C. Wright, R. J. Hamers, S. Jin, *J. Am. Chem. Soc.* **2017**, *139*, 3496.
[32] Y. Zhao, C. Zhang, D. D. Kohler, J. M. Scheeler, J. C. Wright, P. M. Voyles, S. Jin, *Science* **2020**, *370*, 442.

Chapter 3 : Electron Holography and Magnetotransport Measurements Reveal Stabilized Magnetic Skyrmions in $Fe_{1-x}Co_xSi$ Nanowires*

3.1 Abstract

Magnetic skyrmions are topological spin textures that have shown promise for future non-volatile memory devices. Herein, we report on the stability of magnetic skyrmions in alloyed cubic B20 $Fe_{1-x}Co_xSi$ nanowires (NWs) determined using off-axis electron holography and magnetotransport measurements. This study presents the real space observation of one-dimensional skyrmion lattice in a NW of $Fe_{1-x}Co_xSi$ which shows that the skyrmion phase in a $Fe_{0.75}Co_{0.25}Si$ NW exists at lower applied magnetic fields (200 Oe) with a reduced domain size (28 ± 2 nm) in comparison to bulk and thin film samples. Magnetotransport measurements were used to observe the helimagnetic transition temperature dependence on the cobalt concentration in the $Fe_{1-x}Co_xSi$ NWs. Field-dependent magnetoresistance measurements of $Fe_{1-x}Co_xSi$ NWs under applied magnetic field parallel to the NW axis and their second derivative plots reveal the critical fields for the magnetic state transition at different temperatures. A representative magnetic phase diagram constructed with the results from transport measurements of a $Fe_{0.81}Co_{0.19}Si$ NW clearly shows expanded stability region for magnetic skyrmions in the $Fe_{1-x}Co_xSi$ NWs.

3.2 Introduction

Topologically stable spin textures known as magnetic skyrmions have garnered interest recently due to their potential applications in high density and energy efficient memory devices at the nanoscale.[1, 2] Magnetic skyrmions are known to exist in structures that lack inversion symmetry such as B20 chiral magnets,[1, 3] β-Mn-type Co-Zn-Mn alloys[4] and ferromagnetic (FM) thin film

* This chapter is written in collaboration with Stolt, M. J.; Niitsu, K.; Yu, X.; Shindo, D.; Tokura, Y.; Jin, S

multilayers.[2] In non-centrosymmetric crystal structures, such as the cubic B20 structure, the lack of inversion symmetry gives rise to the antisymmetric exchange interaction known as the Dzyaloshinskii-Moriya interaction (DMI).[1, 5, 6] DMI then competes with the FM exchange interaction, which results in the formation of skyrmions when the applied magnetic field is perpendicular to DMI vector.[1] The compound with the cubic B20 crystal structure such as MnSi, $Fe_{1-x}Co_xSi$, and FeGe can host skyrmions that have domain sizes typically less than 100 nm, and are stable below their helimagnetic transition temperature (T_c).[1, 3, 7-10] These materials can serve as the models to study skyrmion physics and also be utilized for prototype magnetic memory devices, partially because the nanometer-sized magnetic skyrmions can be driven at ultra-low current densities ($\sim 10^6 A/m^2$).[11-13]

Apart from material selection, previous theoretical and experimental studies show that the effect of geometrical confinement, such as that induced by a nanostructure, hinders the formation of a conical phase in chiral B20 magnets and favors skyrmion phase stability.[14] Lorentz transmission electron microscopy (LTEM) studies of both MnSi and FeGe nanowires (NWs) showed a stabilization of the skyrmion phase to a larger temperature and applied magnetic field window in comparison to both thin films and bulk crystals.[3, 15, 16] In addition to enhanced stability of the magnetic skyrmion phase due to nanostructuring, one-dimensional (1D) NWs act as skyrmion waveguides and restrict the domains lateral drift, which is advantageous for the magnetic memory architecture known as racetrack memory (RM).[17] These advantages make NWs a promising platform for skyrmion device research, however nanodevice work has been limited in the skyrmion field partially due to the difficulty in fabricating nanostructured devices.[12, 18]

To date, the stability of the skyrmion phase in thin films and nanostructures has been primarily explored with real space observation using microscopy techniques such as LTEM.[8-10, 15]

However, the magnetic contrast of a LTEM image is easily blurred by surface roughness and Fresnel fringing due to the required out-of-focus imaging, both of which are prevalent while imaging nanostructures. Therefore, it is increasingly difficult to achieve high magnetic contrast using LTEM in a skyrmion hosting NW as the diameter is continually reduced.[10, 19] In contrast, another technically more sophisticated TEM-based magnetic imaging technique known as off-axis electron holography (EH) overcomes these issues *via* in-focus imaging.[20, 21] EH captures the phase information coming from the electric and magnetic potential of materials. The former is the unwanted electrostatic contribution that can be mostly eliminated by subtracting the same data set captured above T_c.[22, 23] Recently, the EH technique has shown its ability to visualize weak magnetic phase objects like skyrmions with variation in sample thickness which was carried out on a wedge-shaped FeGe strip of variable width ~ 45 - 150 nm.[24] Detection of skyrmion phase with real space observation is extremely useful for confirming the robustness of skyrmion phase in nanostructures, even though imaging observation is not suitable for electronic device applications.

Purely electrical detection of the skyrmion phase is required to integrate magnetic skyrmions into racetrack memory (RM) or other spintronic devices. Nanostructured skyrmion hosting materials typically exhibit anisotropic magnetoresistance (AMR), which may be exploited to electrically detect the skyrmion phase stability with respect to NW orientation.[25-27] Magnetoresistance (MR) detection of skyrmion cluster states has been demonstrated in ultra-thin MnSi NWs, when applied magnetic field is parallel to NW long axis.[27] However, the small skyrmion size in the MnSi system (~18 nm) makes the device fabrication process challenging to achieve quantized detection of isolated skyrmions. Interestingly, the cubic B20 silicide alloys, $Fe_{1-x}Co_xSi$, can host skyrmions with a range of domain sizes from ~ 40 nm to 230 nm by controlling the cobalt alloying composition (higher Co concentrations leads to larger skyrmion sizes) below

their respective T_c (below ~50 K).[1, 28] Selection of the appropriate composition and dimension could enable $Fe_{1-x}Co_xSi$ NWs to host a single chain of skyrmions. This would require a synthetic process that produces $Fe_{1-x}Co_xSi$ NWs with a wide range of Co alloying composition and appropriate dimensions to host skyrmions.

Chemical vapor deposition (CVD) has proven itself a powerful synthetic technique for the growth of high quality, single crystalline NWs of several B20 metal silicide and germanide, such as MnSi,[29] FeGe[16] and $Fe_{1-x}Co_xSi$.[30-32] The composition of the $Fe_{1-x}Co_xSi$ NWs can be further tuned by controlling the vapor pressure of the individual precursors during the CVD reaction. These CVD reactions also produce a high yield of NWs with a large variation in their thickness and length, which is advantageous for geometrical dependent skyrmion device studies.

In this chapter, we present a study on the skyrmion stability in CVD grown $Fe_{1-x}Co_xSi$ NW systems using both off-axis EH and MR measurements. We report real space observation of a skyrmion phase in a NW of $Fe_{1-x}Co_xSi$ ($x \sim 0.25$). The EH observations were employed to visualize and confirm the skyrmion hosting nature of these $Fe_{1-x}Co_xSi$ NWs. Then the critical fields for various magnetic phase transitions were identified from MR measurements of a $Fe_{0.81}Co_{0.19}Si$ NW, with the assistance of the information from the EH observations. Integrating the information of all measurements led to the development of a representative magnetic phase diagram for the $Fe_{1-x}Co_xSi$ NWs.

3.3 Results and Discussion

3.3.1 Synthesis and Characterization of $Fe_{1-x}Co_xSi$ NWs

We synthesized single-crystal alloyed $Fe_{1-x}Co_xSi$ NWs using CVD reactions with metal iodide precursors (FeI_2 and CoI_2) on Si (100) substrates coated with 100 nm silicon oxide by modifying from previous reports (see details in Experimental Section and Figure A1.1 in the Supporting

Information).[30-32, 33] Here, we used two separate small cylindrical alumina crucible to facilitate independent control over the relative vapor

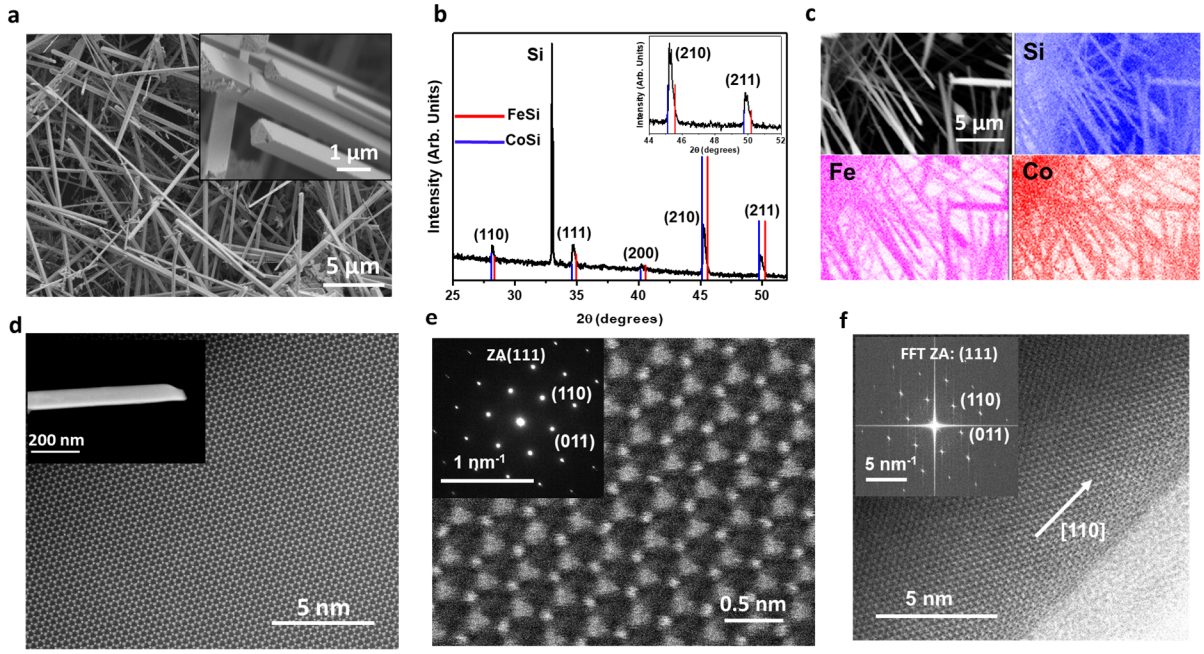

Figure 3.1 : (a) Representative SEM images of as-synthesized $Fe_{1-x}Co_xSi$ NWs on a Si (100) substrate. The magnified inset image reveals the cross-section of the thick NWs. (b) Powder X-ray diffraction pattern of the $Fe_{1-x}Co_xSi$ as-grown NWs in comparison with both FeSi (red) and CoSi (blue) standard patterns reproduced from JCPDS PDF#00-038-1397 and JCPDS PDF#00-008-362, respectively. The inset clearly shows the two most intense peaks of $Fe_{1-x}Co_xSi$ NWs lie between the standard peaks of FeSi and CoSi. (c) SEM-EDS elemental mapping of $Fe_{1-x}Co_xSi$ NWs on reacted Si substrate. (d) Low magnification HAADF-STEM image taken on an 85 nm thick NW, SEM image of which is shown in the inset. (e) High magnification HAADF-STEM image of the (111) crystallographic plane confirmed by the SAED pattern shown in the inset. (f) Low magnification ABF-STEM image at the edge of the NW with inset image of FFT pattern reveals the growth direction of the NW along [110] crystallographic axis.

pressure of each metal iodide precursor, which enables synthesis of wide composition range of the $Fe_{1-x}Co_xSi$ NWs (Figure A1.2). A representative scanning electron microscope (SEM) image of the as-grown $Fe_{1-x}Co_xSi$ NWs on a silicon substrate (Figure 3.1a) shows high density of NWs that were from 50 nm up to 1 μm in thickness and 4 to 15 μm in length. The observed rhombohedral tip morphology (Figure 3.1a inset) of the NW (more clearly seen in thicker wires) is characteristic of B20 NWs and has been previously observed in NWs of both isostructural MnSi[27] and FeSi.[34]

This rhombohedral shaped feature of chiral B20 crystal system (space group $P2_13$) is split by a merohedral twin plane[27, 34] which partitions the NW into two parts of opposite chirality (left and right handiness).

Powder X-ray diffraction (PXRD) patterns (Figure 3.1b) obtained from an area of dense $Fe_{1-x}Co_xSi$ NWs on the silicon substrate, confirmed the alloying of isostructural B20 cubic FeSi and CoSi system. The inset in Figure 3.1b shows that the two most intense PXRD peaks lie between the peak positions from the standard patterns of FeSi and CoSi, suggesting successful alloying of $Fe_{1-x}Co_xSi$ NWs. We further utilized SEM energy dispersive spectroscopy (EDS) to analyze the composition of NW bunches because the magnetic properties of the NWs are so heavily dependent on their compositions. SEM-EDS elemental mapping (Figure 3.1c) shows a homogenous distribution of Fe, Co and Si in these NWs. As PXRD averages over a large area, and not sensitive to individual nanostructures, we employed high angle annular dark/bright field scanning electron microscopy (HAADF/ABF-STEM) imaging and selected area electron diffraction (SAED) to study the structure of the individual NW shown in the inset of Figure 3.1d. Low magnification HAADF-STEM image (Figure 3.1d) clearly demonstrates that the observed region has well-organized crystallinity without any segregations/precipitations. High magnification HAADF-STEM image (Figure 3.1e) displays the atomic arrangement of Si and Fe/Co atom in the crystallographic plane. SAED pattern (Figure 3.1e inset) is indexed to the B20 cubic structure along the (111) zone axis and shows the single crystalline nature of the NW. Low magnification ABF-STEM image (Figure 3.1f) was taken at the edge of the NW to determine the NW growth direction. The corresponding Fast Fourier transform (FFT) pattern of the image confirms the growth direction is along the [110] crystallographic axis, which agrees with previous

reports on B20 silicide NWs that exhibited merohedral twinning and grown *via* CVD technique.[27, 34]

Because CVD synthesis yields nanostructures with wide range of chemical compositions and dimensions, we further used SEM-EDS to investigate the variation in compositions from two different NW reaction samples (sample A and sample B) obtained from similar CVD syntheses after transferring the NWs to clean Si substrates. The results of the SEM-EDS analysis of the cobalt substitution, x, for 15 individual $Fe_{1-x}Co_xSi$ NWs each from sample A and sample B are represented in the form of a histogram (Figure A1.2a-c). The cobalt substitution in the $Fe_{1-x}Co_xSi$ NWs from both samples ranges from $0.1 < x < 0.5$ and the average Co% alloying from sample A (B) is 33% (22%). However, there might be a possibility of slight inhomogeneity in Co% alloying within a single NW which is beyond the detection capability of standard less EDS. Note that the typical quantitative error for standard less EDS analysis is approximately 5% [35] and the statistical standard deviation in the atomic percent of each element for sample A (B) is 6.6% (4.2%). Given the direct influence of alloy composition (x) on skyrmion size and stability, these CVD syntheses yielded $Fe_{1-x}Co_xSi$ NWs that can host skyrmions within an expected size range of ~ 40-90 nm below their respective T_c's (below ~50 K).[28, 36]

3.3.2 Real Space Observation of Magnetic Structures in $Fe_{0.75}Co_{0.25}Si$ NW

We chose the tip region of the NW shown in Figure 3.1d-f for the EH observations. The region of interest has ~85 nm average width and average composition of $x \sim 0.25$ with sufficient chemical homogeneity (see TEM-EDS details in Figure A1.3). Besides, according to the φ_{MIP} (phase shift due to the mean inner potential) distribution taken at 60 K (Figure A1.4), the NW consists of flat facets forming a rhombohedral cross-section similarly to the NWs shown in the inset of Figure 3.1a, which is advantageous to capture the φ_{MAG} (phase shift due to the in-plane magnetic flux)

undulation by the subtraction processes. The off-axis EH observations were carried out at different temperatures (T) of 10, 20, 30, and 60 K, and under the out-of-plane magnetic fields (H) of 0, 100, and 200 Oe using an interferometry of double biprism (see Experimental Section for data collection and processing details).[37] Note that we observed no apparent magnetic contrast at or above 40 K at zero applied magnetic field which implies that the T_c of the NW lies in the range of 30-40 K.

The resultant φ_{MAG} distributions are summarized in Figure 3.2a-i in the forms of color-coded $\nabla\varphi_{MAG}$ and $\cos(300\varphi_{MAG})$. At $H = 0$ Oe, we can see the helical magnetic stripes with the periodicity of ~30 nm and the nearly [110] propagation vector which coincides with the NW's growth direction. According to previous SANS and LTEM studies on bulk and thin film $Fe_{1-x}Co_xSi$ systems, the preferred orientation of helical propagation axis is along the [100] direction for all compositions.[9, 38, 39] This contradiction is also found in B20 MnSi NW system where the direction of helical propagation axis in NWs differs from preferred orientation in bulk systems.[40] This is likely caused by the shape anisotropy intrinsic to the NW geometry. Note that we often encountered staggered or branched helices from the middle of the NW (for example, see Figure 3.2a). We suspect this may be caused by the (100) merohedral twin which divides the rhombohedral cross-section into two triangles.[27, 34] If the merohedral twin divides the NW into two crystallographic subsections, helices might be independently formed within the subsections and can merge with each other forming long-range ordering but may also form mazed helices when the bumped helices have different magnetic phases. Similar magnetic structure is robust even at H

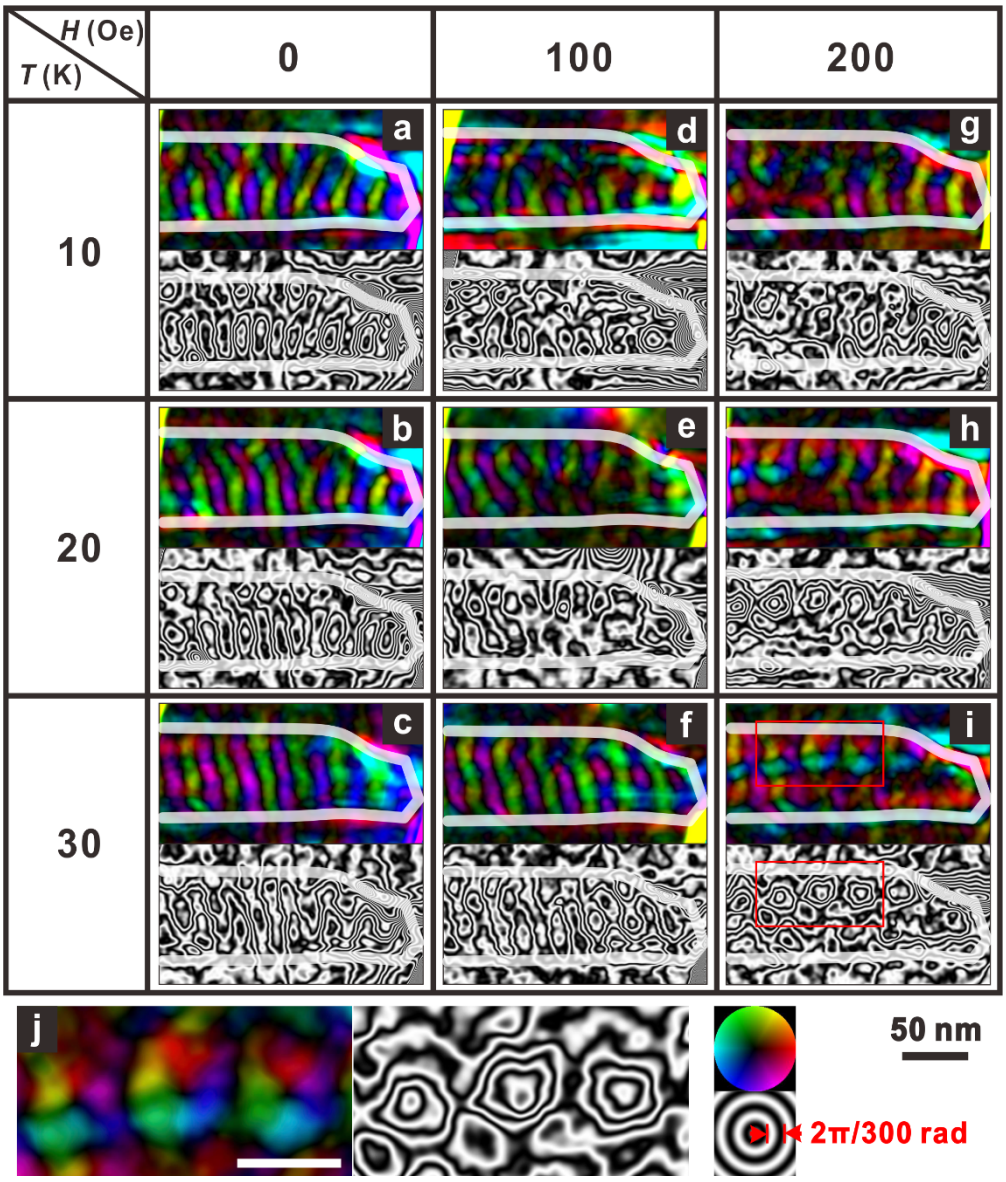

Figure 3.2 : Magnetic phase contrast (φ_{MAG}) images of the $Fe_{0.75}Co_{0.25}Si$ NW obtained *via* off-axis EH observations. (a-c) φ_{MAG} images at 10, 20, and 30 K with no applied magnetic field. (d-f) φ_{MAG} images at 10, 20, and 30 K with an out-of-plane applied magnetic field of 100 Oe. (g-i) φ_{MAG} images at 10, 20, and 30 K with an out-of-plane applied magnetic field of 200 Oe. Upper and lower panels display the φ_{MAG} distribution in the forms of color-coded $\nabla\varphi_{MAG}$ and $\cos(300\varphi_{MAG})$, respectively. Color hue and brightness represent $\text{atan2}(\nabla\varphi_{MAG})$ and $|\nabla\varphi_{MAG}|$; refer to the color wheel given at the bottom right. Scale bar for (a-i) is presented at the bottom right. (j) Magnified images of the red rectangles shown in (i). Scale bar is 30 nm.

= 100 Oe (Figure 3.2 d- f). In contrast, when H = 200 Oe is applied, the robustness of the helices dramatically decays (Figure 3.2g-i). While the helices seem to be still persistent at 10 K, a few

skyrmions with ~28 nm size start to coexist alongside the upper edge at 20 K. At 30 K, skyrmions in a 1D chain configuration are formed (Figure 3.2i).

As an advantage of EH observations, the $\nabla\varphi_{MAG}$ map variation allows us to quantitatively estimate the spatial distribution of in-plane magnetic flux. Magnified images (Figure 3.2j) of the rectangles shown in Figure 3.2i clarify the 1D-arrayed skyrmions with the phase shift 0.070 ± 0.005 rad from core to periphery, which is sufficiently larger than the phase resolution of 0.025 rad for the present EH setup (Figure A1.5-6). According to the previous EH study on $Fe_{0.5}Co_{0.5}Si$ thin film,[22] phase shift of 0.14 rad is obtained with the sample thickness of 85 nm for a 90-nm size skyrmion. Taking the bulk crystal composition (x) dependence on magnetic moment (m_x) of $m_{0.25}/m_{0.50}$ = 1.88 [41] or 1.09 [28, 42] into account, the phase shift of a ~28-nm size skyrmion with x = 0.25 and 85-nm thick NW could be estimated to be 0.08 or 0.05 rad, respectively. Therefore, the measured phase shift is in good agreement with the estimation.

On the basis of these EH observations, the skyrmion phase is identified to be stable at a slightly lower applied field in the $Fe_{0.75}Co_{0.25}Si$ NW sample in comparison to previously reported results on a $Fe_{0.7}Co_{0.3}Si$ bulk sample (~280 Oe).[43] Interestingly, the size of the skyrmion observed in NW is 28 ± 2 nm (the error reflects the slight variations in the observed skyrmion size in Figure 3.2j) and the measured helical pitch is ~ 30 nm which is much smaller than that has been previously reported for any composition of $Fe_{1-x}Co_xSi$.[1, 9, 22] We expected to observe a single chain of skyrmions (domain size ~ 50-60 nm) in 85-nm thick $Fe_{0.75}Co_{0.25}Si$ NW sample according to previous reports correlating helical period with x in $Fe_{1-x}Co_xSi$ system.[28] The real space observation of reduced skyrmion size in the NW is not studied in detail in this study. However, for B20 skyrmion-hosting materials, this reduced size of skyrmion has been reported previously in $Fe_{0.8}Co_{0.2}Si$ single crystal system where helical period is ~ 34 nm[44] and MnSi thin film system

where helical period is ~ 8.5 nm.[45] This discrepancy likely originates from different exchange coupling strengths, because helical period is determined by the ratio J/D, where J and D are the Heisenberg and Dzyaloshinskii Moriya exchange couplings, respectively. One common issue in all these studies including ours is the lack of long-range order that avoids formation of a skyrmion hexagonal lattice packing. Possible reasons for the irregular arrangement of skyrmions are the geometrical confinement in the NW and the crystallographic separation by the merohedral twinning plane.[27, 34] These conditions might force the skyrmions to adjust their shape; such similar skyrmion size adjustment has been previously reported for FIB fabricated nanostructured FeGe wedges.[24] Another possible reason could be the presence of compositional disorder preventing consistent long-range crystalline packing in a single crystal which leads to hierarchical nature of skyrmion formation. Nevertheless, Figure 3.2i is the evidence for the robust nature of skyrmion formation against disorder in a sort of one-dimensional lattice formation and clearly confirms the presence of a skyrmion phase in a 1D $Fe_{1-x}Co_xSi$ NW. The imaging experiment conducted for this NW is challenging and shows the capabilities of EH technique as we can clearly visualize weak phase object like skyrmion in sub-100-nm thick NW without performing any mechanical processing or other modifications to the NW samples, such as ion milling or deposition of PtC_x layer (which could impart additional sources of impurities and might affect the magnetic properties of this doped $Fe_{0.75}Co_{0.25}Si$ NW). According to the previous reports for FIB fabricated NWs, magnetic edge twists play a key role in stabilizing confined skyrmions in the NWs.[24, 46] We guess this argument might be applicable for the present unprocessed NW. However, since the observed NW seems to have tilted facets with respect to the projection as well as suffers from abrupt change in traversing thickness at the edges, visualizing surface magnetic states is still challenging by the current observation setup.

3.3.3 Temperature Dependent Magnetotransport Behavior of $Fe_{1-x}Co_xSi$ NW of Different Compositions

With the observation of the skyrmion phase, we then studied the magnetotransport behaviors as a function of Co substitution (x) in the $Fe_{1-x}Co_xSi$ NWs. We will focus on three NW devices as examples: NW1 was selected from sample A and has a diameter of 169 nm with a composition of $Fe_{0.63}Co_{0.37}Si$; NW2 has a diameter of ~395 nm with a composition of $Fe_{0.79}Co_{0.21}Si$ and NW3 had a diameter of ~180 nm with a composition of $Fe_{0.81}Co_{0.19}Si$; both NW2 and NW3 were obtained from sample B (Figure A1.7 and Table A1 for SEM images and compositional analysis). The average room temperature resistivity of these three NW devices is ~0.55±0.14 mΩ.cm, which is close to the value reported for bulk $Fe_{1-x}Co_xSi$ crystals (~0.2-0.4 mΩ.cm), suggesting good quality of metal electrode contact with the NWs. Zero field cooling (ZFC) curves shows characteristic variations of resistivity with temperature for NW1 from sample A (Figure 3.3a) as well as for NW2 and 3 from sample B (Figure 3.3b). These are qualitatively similar to ZFC results of the bulk and thin film systems with compositions close to these NW samples.[36, 47] To elucidate the composition dependent magnetotransport behaviors, we carried out field cooling (FC) experiments and measure magnetoresistance [MR (%) = $(R(H) - R(0))/R(0) \times 100$, where $R(H)$ and $R(0)$ are the resistance at a specific applied magnetic field and zero field, respectively] as a function of temperature for NW1,2 (Figure A1.8) and NW3 (Figure 3.3c,d). The maxima in the FC curves represents the T_c of NW1 (~65 K), NW2 (~35 K) and NW3 (~30 K), which are expected to vary with the Co composition in the $Fe_{1-x}Co_xSi$ NWs.[36] For NW1, T_c is higher than the maximum value reported for the bulk $Fe_{1-x}Co_xSi$ crystal (50 K, $x = 0.4$).[43] However, there is also the possibility of a slight elevation in the value of T_c due to potential confinement effects of NW morphology, which have previously been seen in MnSi NWs.[8] FC curves obtained from NW3 when the direction of applied

magnetic field is parallel (H∥) to the long axis of the NW (Figure 3.3c), also yields a T_c close to 30 K. For measurements under H∥, the NW long axis was aligned under an optical microscope to within a ~10° deviation during the process of mounting the NW device. However, there is discernable variation in the FC curves with different configurations (H⊥ and H∥) below T_c which could be attributed to magnetic anisotropy expected with a NW morphology.[14, 40]

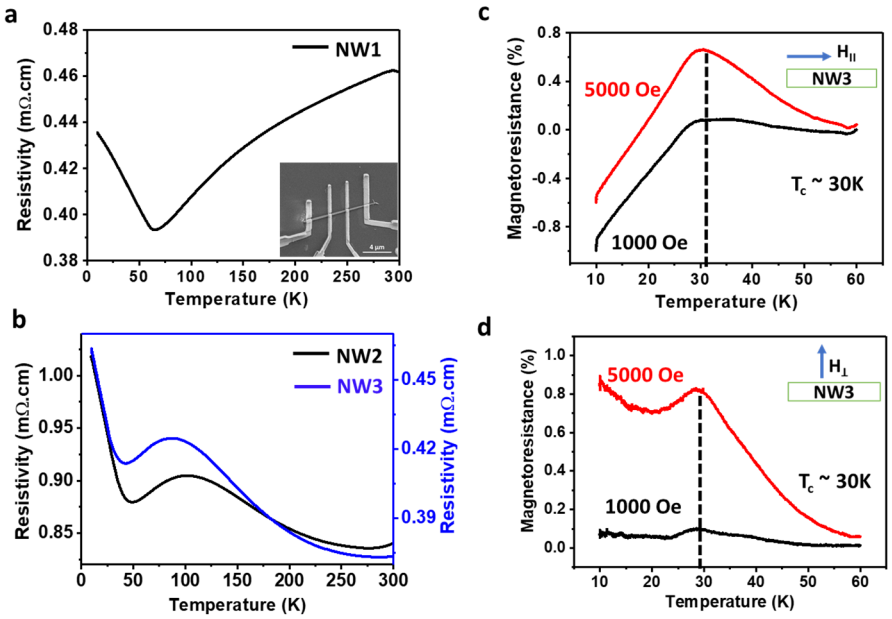

Figure 3.3 : Temperature dependent MR of different $Fe_{1-x}Co_xSi$ NWs. Temperature dependent resistivity of (a) NW1 (sample A; inset shows a SEM image of a representative four probe device), (b) NW2 and NW3 (Sample B). Temperature dependent MR of NW3 with applied magnetic field (c) H∥ and (d) H⊥.

3.3.4 Assessment of the Critical Field for Magnetic Phase Transition from Magnetotransport Measurements

As previously discussed, in B20 helimagnets such as $Fe_{1-x}Co_xSi$ and MnSi, the evolution of different spin structures under varying applied magnetic field below T_c could be electrically detected by field-dependent MR measurements. The origin of the MR is attributed to the coupling

of conduction electrons with the chiral modulations.[27] The study of field-driven spin structure evolution in NWs can be represented by plotting field-driven isotherms (MR-H); which are obtained by sweeping the applied magnetic field at a constant temperature. The 1D morphology of NWs presents an opportunity to study spin modulation along the long axis of the NW. In previous studies on B20 MnSi NW system,[40] the critical field of each magnetic transition is marked by easily discernible kinks in MR-H isotherms under H∥. To further highlight the magnetic transition states, the first derivatives of the MR-H isotherms at different temperatures were taken to reveal sharp peaks at different critical fields. The implementation of a similar approach with the $Fe_{1-x}Co_xSi$ NW devices is more difficult because the magnitude of MR signal is significantly lower (~1 order of magnitude) than that of the MnSi NW devices. Therefore, these experiments require the highest signal-to-noise ratio (S/N) of fabricated NW devices. For this reason, we focus on NW3's MR-H experiments in the following discussion due to its highest S/N. However, all three measured NWs showed comparable results.

We conducted MR measurements on NW3 in the parallel configuration between 10-36 K with H∥ swept at a rate of 10 Oe/sec from -3000 Oe to 3000 Oe with the applied current density kept in the range of ~10^8 A/m^2. Representative field-driven MR-H isotherms (Figure 3.4a) show different variation in MR signal under high and low applied magnetic field ranges. At high fields (H∥ >1000 Oe), a positive MR signal linearly increases as a function of applied magnetic field which is consistent with previous reports on $Fe_{1-x}Co_xSi$ systems.[31, 36, 48] MR-H isotherms in the low field regions (H∥ <1000 Oe) show a humplike feature that fades away as we increase temperature closer to T_c. This magnetotransport behavior strongly correlates the low field region of MR-H isotherms to the evolution of magnetic spin textures (only helical and skyrmion phase) we observed *via* EH imaging in the $Fe_{0.75}Co_{0.25}Si$ NW and previously reported imaging results on

$Fe_{0.5}Co_{0.5}Si$ thin film samples.[9, 22] To see this relation, we further analyze MR-H isotherms to assess the critical fields for each of the magnetic state transitions at different temperatures in NW3.

To determine the critical fields for each of the magnetic state transitions, we evaluate the second order derivatives of MR-H isotherms under H∥. Enough though, there is no theoretical underpinning in differentiating MR-H isotherm for critical field analysis, this results in a more sensitive graphical representation of the critical field for magnetic transitions. The MR signal in $Fe_{1-x}Co_xSi$ is an order of magnitude less than that in MnSi, which makes it more difficult to determine the critical field as no apparent kinks could be seen in MR-H isotherms. Mathematically, a kink is just a deviation from a smooth curve or rather seen as a point of maximum curvature (minimum radius of curvature) in a subset of connecting data points in the vicinity. This can be more accurately represented as maxima/minima by plotting d^2MR/dH^2 vs H and could be associated with the critical field for magnetic state transitions at different temperatures. To further illustrate this analysis, Figure 3.4b shows stacked plots of the specific MR-H isotherm for NW3 at 20 K with its first (dMR/dH) and second order (d^2MR/dH^2) derivative as a function of forward (bold color) and backward (faded color) field sweeps. In contrast to the MnSi NWs,[40] for the $Fe_{1-x}Co_xSi$ NW here, the kinks are difficult to visualize in the MR-H isotherm at 20 K and there are no apparent sharp peaks manifested in the dMR/dH curve. But there are clearly two peaks in the d^2MR/dH^2 curve arising from kinks in MR-H isotherm at 20K, which are marked with dashed lines (averaged for forward and backward sweeps) and correspond to the lower and upper critical fields driving the system into and out of the skyrmion state. The hysteresis loop in the MR-H isotherms corresponds to the dependence of magnetic spin state stability with history of field sweep. A similar hysteresis was also observed in MnSi NWs when applied magnetic field is along its growth direction, <110>.[40] The hysteresis feature appears to be dominant in the field range where

skyrmion stability is expected. The reasons for the hysteresis feature in the MR-H isotherms are not clear at the present, but it does not significantly affect the assessment of various magnetic transitions.

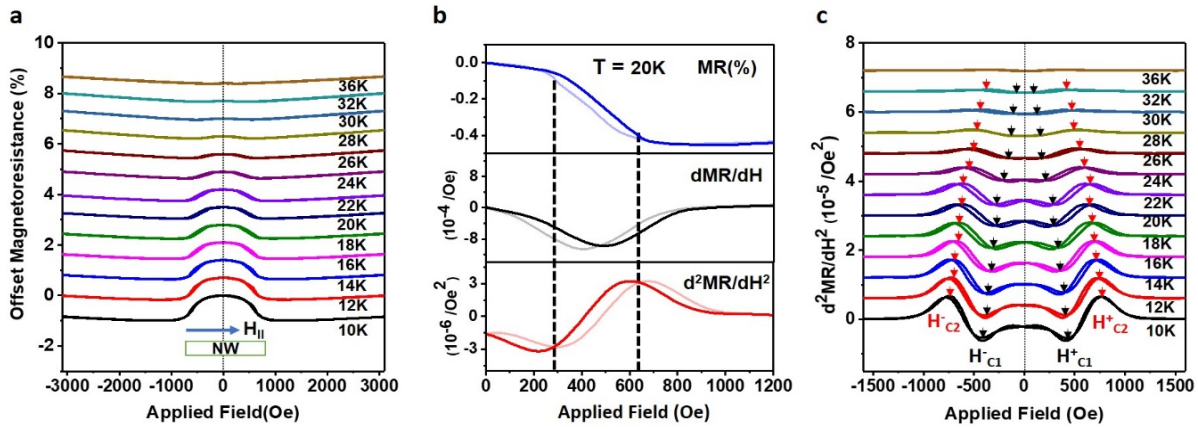

Figure 3.4 : $H_{\parallel}$ MR-H isotherms and critical field assessment for NW3. (a) Offset MR-H isotherms between 10-36K, (b) The specific MR-H isotherm at 20K, and its first (dMR/dH) and second order (d^2MR/dH^2) derivative with respect to forward (bold color) and backward (faded color) field sweep direction. The dashed lines mark the peaks on d^2MR/dH^2 curve which represent critical fields for the magnetic transitions. (c) Offset second order derivatives of the MR-H isotherms in panel (a). The black arrows (H_{C1}) and red arrows (H_{C2}) highlight the critical fields for the magnetic state transitions at different temperatures. Values for increasing and decreasing field strength are denoted by the superscripts "+" and "-", respectively.

Furthermore, we plotted d^2MR/dH^2 curves at various temperatures from 10-36 K to determine the stability regime more accurately for the different magnetic spin structures in NW3. Figure 3.4c highlights the critical fields as H_{C1} (peaks marked with black arrows) indicating the helimagnetic to skyrmion state transition, and H_{C2} (peaks marked with red arrows) indicating the skyrmion to field polarized state transition. The critical field values for positive and negative applied magnetic field are denoted by the superscripts "+" and "−", respectively. At $H > H_{C2}$, the destruction of skyrmion lattice is presumed to occur by transition into intermediate conical state and eventually into the fully polarized ferromagnetic state. However, the critical field for the magnetic transition between these two field polarized (conical and ferromagnetic) states is difficult

to determine accurately from our analysis, as no additional peak was visible in the d^2MR/dH^2 curves. We are still able to observe these peaks in d^2MR/dH^2 curves at 32 K, which is slightly above the T_c determined by the FC experiments (close to 30 K for NW3), but no discernable peaks are seen at or above 36 K, where the system is likely in a paramagnetic state. The peaks in d^2MR/dH^2 curves are found to be broad and convoluted near critical fields which might be due to the stability of transitional mixed magnetic phase in $Fe_{1-x}Co_xSi$ system. Real space imaging evidence for coexistence of mixed states of helical (field polarized) and skyrmions was previously reported for $Fe_{0.5}Co_{0.5}Si$ thin film samples and by our EH imaging experiment (Figure 3.2), although both imaging experiments were conducted in field perpendicular configuration ($H_\perp$).[9, 22]

We also conducted field-driven magnetotransport measurements in a perpendicular applied field configuration ($H_\perp$). We found that the FC curves for NW3 (Figure 3.3d) shows a T_c around 30 K under $H_\perp$ which is expected to be similar to the T_c determined under $H_\parallel$. It is apparent from the perpendicular MR (Figure A1.9) that the magnetic state transitions are not as pronounced in comparison to the parallel MR data. The MR-H curves evidently show detectable signs of H_{C2}. We assumed there would also be abrupt changes in the slope of MR-H curves caused by H_{C1}. However, H_{C1} is likely not resolvable under $H_\perp$ due to the decrease in signal caused by the AMR intrinsic to the NW morphology. The lack of clear MR signatures of skyrmion state was also seen in MnSi NWs.[40] Our electron holography experiments already confirmed that both helical and skyrmion states are stable under $H_\perp$, therefore, electrical detection of spin structure under $H_\perp$ might require other techniques such as topological Hall effect measurements[12] to relate electrical signatures to the skyrmion stability in $Fe_{1-x}Co_xSi$ NWs.

3.3.5 Representative Magnetic Phase Diagram

Summarizing the magnetotransport results on the skyrmion hosting $Fe_{1-x}Co_xSi$ NW, we have plotted a representative magnetic phase diagram (H-T plot) inferred from magnetotransport measurements on NW3 ($Fe_{0.81}Co_{0.19}Si$) under $H_{\parallel}$ (Figure 3.5). We plotted the critical fields (H_{C1} and H_{C2}, averaged for positive and negative applied magnetic fields) for magnetic state transitions

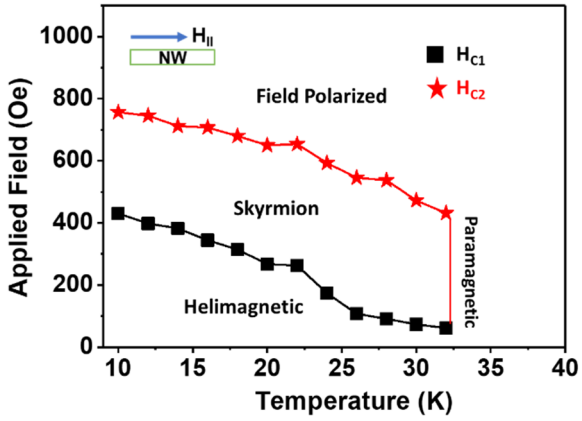

Figure 3.5 : Summary magnetic phase diagram. H_{C1} (black squares) and H_{C2} (red stars) are critical fields for magnetic state transitions as determined by magnetotransport measurements of NW3 ($Fe_{0.81}Co_{0.19}Si$).

to determine the phase boundary between different spin-states in the H-T plot. The real space observation of skyrmion lattice in a NW with a slightly different composition of $Fe_{0.75}Co_{0.25}Si$ *via* EH allows us to confidently attribute the transition observed in MR-H isotherms. Both analyses confirm the stability of skyrmion phase at lower applied magnetic field in comparison to previous reports on bulk $Fe_{1-x}Co_xSi$ samples with similar compositions.[39, 43] Because of the different cobalt compositions (x) in $Fe_{1-x}Co_xSi$ NWs examined in electron holography and MR measurements, along with the effect of NW induced shape anisotropy, we anticipate shifts in helical to skyrmion critical magnetic transition fields inferred from these two techniques.[39, 40] Therefore, we can only qualitatively support our magnetotransport observations with the EH imaging experiment since the applied magnetic field configurations were along different axes of the NW in these experiments. However, the critical fields for each magnetic phase transition in previously studied MnSi NWs

did not show any significant difference in LTEM studies under $H_{\perp}$ and in MR measurements under $H_{\parallel}$.[8, 40, 49] Hence, our experimental studies provide a conservative estimate of the stability regime of helimagnetic and skyrmion state in $Fe_{1-x}Co_xSi$ NWs.

3.4 Conclusion

In conclusion, we presented a study on the real space observation and magnetotransport measurements of the skyrmion stability regime in $Fe_{1-x}Co_xSi$ NWs. Using off-axis electron holography, we observed the formation of 1D skyrmion lattice in a single-crystal $Fe_{0.75}Co_{0.25}Si$ NW which has clearly demonstrated the technical capability of EH technique to visualize skyrmions in NWs with sub-100 nm thickness without performing any mechanical processing or other treatments on the NW. Magnetotransport measurements enabled us to compare the helimagnetic transitions temperatures of $Fe_{1-x}Co_xSi$ NWs with different compositions under applied fields in different configurations ($H_{\perp}$ and $H_{\parallel}$). Furthermore, second order derivative analysis of MR-H isotherms enabled the detection of magnetic spin structure transition and a conservative estimate of the skyrmion stability regime under $H_{\parallel}$ of a $Fe_{0.81}Co_{0.19}Si$ NW. This approach can be extended to other skyrmion hosting systems that suffer from low MR signal. These findings confirm the enhanced stability of magnetic skyrmions in $Fe_{1-x}Co_xSi$ NWs and lay the foundation for future studies to understand skyrmion stability in confined geometries, and will be beneficial for exploitation of magnetic skyrmions for spintronic nanodevices.

3.5 Experimental Section

3.5.1 Chemical Vapor Deposition Synthesis of $Fe_{1-x}Co_xSi$ Nanowires

Single-crystal $Fe_{1-x}Co_xSi$ alloyed nanowires (NWs) were synthesized *via* chemical vapor deposition (CVD) technique using metal iodide precursors (FeI_2 and CoI_2) and Si (100) wafers

with 100 nm silicon oxide coating as reaction substrate. NW synthesis were carried out in a custom-built CVD reactor comprised of a 1-inch fused silica tube placed in a single-zone tube furnace (Lindberg\BlueM) (see details in Figure A1.1). The sealed tube was equipped with pressure and gas flow controls (argon as carrier gas) and a liquid nitrogen trap before the vacuum pump. The temperature of central heating zone was maintained at ~900 ºC where the Si substrate was placed. These CVD reactions were typically carried out for 20 min under a steady Ar flow rate of 190 sccm at a pressure of 500 Torr. Two small cylindrical alumina boats (diameter ~ 4 mm, height ~ 6.5 mm) were used to contain ~50 mg of two metal precursors separately at different location in the tube furnace to allow control over the relative vapor pressure of each metal iodide precursor. After determining the temperature gradient in the single zone tube furnace, metal precursor alumina boats were placed close to their respective melting temperature upstream of the hot zone.

3.5.2 Structural Characterization and Elemental Compositional Analysis

Powder X-ray Diffraction (PXRD) patterns were collected on a Bruker D8 Advance diffractometer with Ni-filtered Cu Kα radiation (λ = 1.5418 Å). To confirm the phase of $Fe_{1-x}Co_xSi$ NWs, selected area electron diffraction (SAED) patterns were obtained using a FEI Tecnai TF-12 transmission electron microscopy (TEM) operated at 120 keV on individual NWs. Elemental compositional analysis was carried out using energy dispersive spectroscopy (EDS) on a LEO 1530 scanning electron microscope (SEM) equipped with an EDS detector (Noran System Seven, Thermo-Fisher) at an accelerating voltage of 20 keV. The high angle annular dark/bright field scanning transmission electron microscopy (HAADF/ABF-STEM) images were collected using a Cs-corrected 200 kV TEM (JEM-ARM200F, JEOL) with a HAADF detector angle of 90-170 mrad.

3.5.3 Electron holography of $Fe_{1-x}Co_xSi$ Nanowires

For conducting electron holography observations**,** a 300-kV TEM (Hitachi, HF-3300S) was used with double-biprism interferometry.[37] Electron holograms were recorded using a slow-scan charge-coupled-device (CCD) camera (Gatan UltraScan4000) with a pixel size of 4,096×4,096 (15 μm/pixel). A batch of ~100-300 holograms was captured consecutively at every temperature and magnetic field. They were averaged into one phase image after drift compensation and reconstruction processes to achieve the phase resolution required to capture the magnetic phase shift from a weak phase object like a skyrmion. The optical conditions are provided in Figure A1.5. Fringe contrast and pitch are 33.72% and 2.4 nm, respectively. The spatial resolution of one hologram and field of view (hologram band width) are 4.74 nm and ~200 nm, respectively. The phase resolution defined by the standard deviation in vacuum is 0.097 rad for one reconstructed phase image. This value is reduced to 0.025 rad after averaging a batch of reconstructed phase images. Applied magnetic fields are estimated by extrapolating linear relationship between injected current in the superconductive coil and the measured magnetic fields.

In principle, the reconstructed phase φ can be decomposed into the components brought about by the in-plane magnetic flux (φ_{MAG}) and the mean inner potential (φ_{MIP}). With the reasonable assumption that the latter would be independent of temperature change, the φ_{MIP} can be removed by subtracting the phase image obtained at temperatures above T_C, enabling to capture the residual φ_{MAG} distribution.[21] In the present observations, however, faint artefacts of the undersubtracted/oversubtracted φ_{MIP} and Fresnel fringe contrasts hamper us to capture the magnetic structures clearly. To make them discernable, further image processing was carried out for the subtracted phase images, the detailed procedures of which is given in Figure A1.6, and the resultant dataset is displayed in Figure 3.2.

3.5.4 Magnetotransport measurements of $Fe_{1-x}Co_xSi$ Nanowires

Standard four-probe devices were fabricated on individual NWs using electron beam lithography techniques and electron beam assisted metal evaporation of Ti/Au for metal contacts to the NWs (see ESI for details on the device fabrication process). The transport measurements were carried out in a Physical Property Measurement System (PPMS, Quantum Design Inc.) with a 9 T superconducting magnet. The DC current was supplied by a Keithley 6221 current source and the voltage was monitored by a Keithley 2182A nanovoltmeter.

The results from this chapter have been published in the journal *ACS Nano*. Reference as follows:

Mathur, N.; Stolt, M. J.; Niitsu, K.; Yu, X.; Shindo, D.; Tokura, Y.; Jin, S., Electron Holography and Magnetotransport Measurements Reveal Stabilized Magnetic Skyrmions in $Fe_{1-x}Co_xSi$ Nanowires. *ACS Nano* **2019,** 13, 7833-7841.

Appendix 1 in this thesis contains supporting information and additional figures of this chapter

References

1. Nagaosa, N.; Tokura, Y., Topological Properties and Dynamics of Magnetic Skyrmions. *Nat. Nanotechnol.* **2013,** *8*, 899-911.
2. Sampaio, J.; Cros, V.; Rohart, S.; Thiaville, A.; Fert, A., Nucleation, Stability and Current-Induced Motion of Isolated Magnetic Skyrmions in Nanostructures. *Nat. Nanotechnol.* **2013,** *8*, 839.
3. Mühlbauer, S.; Binz, B.; Jonietz, F.; Pfleiderer, C.; Rosch, A.; Neubauer, A.; Georgii, R.; Böni, P., Skyrmion Lattice in a Chiral Magnet. *Science* **2009,** *323*, 915.
4. Tokunaga, Y.; Yu, X. Z.; White, J. S.; Rønnow, H. M.; Morikawa, D.; Taguchi, Y.; Tokura, Y., A New Class of Chiral Materials Hosting Magnetic Skyrmions Beyond Room Temperature. *Nat. Commun.* **2015,** *6*, 7638.

5. Moriya, T., Anisotropic Superexchange Interaction and Weak Ferromagnetism. *Phys. Rev.* **1960,** *120*, 91-98.

6. Dzyaloshinsky, I., A Thermodynamic Theory of "Weak" Ferromagnetism of Antiferromagnetics. *J. Phys. Chem. Solids* **1958,** *4*, 241-255.

7. Jin, C.-M.; Du, H.-F., Real-Space Observation of Individual Skyrmions in Helimagnetic Nanostripes. *Chin. Phys. B* **2015**, 24, 12850.

8. Yu, X.; DeGrave, J. P.; Hara, Y.; Hara, T.; Jin, S.; Tokura, Y., Observation of the Magnetic Skyrmion Lattice in a MnSi Nanowire by Lorentz TEM. *Nano Lett.* **2013,** *13*, 3755-3759.

9. Yu, X. Z.; Onose, Y.; Kanazawa, N.; Park, J. H.; Han, J. H.; Matsui, Y.; Nagaosa, N.; Tokura, Y., Real-Space Observation of a Two-Dimensional Skyrmion Crystal. *Nature* **2010,** *465*, 901.

10. Yu, X. Z.; Kanazawa, N.; Onose, Y.; Kimoto, K.; Zhang, W. Z.; Ishiwata, S.; Matsui, Y.; Tokura, Y., Near Room-Temperature Formation of a Skyrmion Crystal in Thin-Films of the Helimagnet FeGe. *Nat. Mater.* **2010,** *10*, 106.

11. Jonietz, F.; Mühlbauer, S.; Pfleiderer, C.; Neubauer, A.; Münzer, W.; Bauer, A.; Adams, T.; Georgii, R.; Böni, P.; Duine, R. A.; Everschor, K.; Garst, M.; Rosch, A., Spin Transfer Torques in MnSi at Ultralow Current Densities. *Science* **2010,** *330*, 1648.

12. Liang, D.; DeGrave, J. P.; Stolt, M. J.; Tokura, Y.; Jin, S., Current-Driven Dynamics of Skyrmions Stabilized in MnSi Nanowires Revealed by Topological Hall Effect. *Nat. Commun.* **2015,** *6*, 8217.

13. Schulz, T.; Ritz, R.; Bauer, A.; Halder, M.; Wagner, M.; Franz, C.; Pfleiderer, C.; Everschor, K.; Garst, M.; Rosch, A., Emergent Electrodynamics of Skyrmions in a Chiral Magnet. *Nat. Phys.* **2012,** *8*, 301.

14. Butenko, A. B.; Leonov, A. A.; Rößler, U. K.; Bogdanov, A. N., Stabilization of Skyrmion Textures by Uniaxial Distortions in Noncentrosymmetric Cubic Helimagnets. *Phys. Rev. B* **2010,** *82*, 052403.

15. Tonomura, A.; Yu, X.; Yanagisawa, K.; Matsuda, T.; Onose, Y.; Kanazawa, N.; Park, H. S.; Tokura, Y., Real-Space Observation of Skyrmion Lattice in Helimagnet MnSi Thin Samples. *Nano Lett.* **2012,** *12*, 1673-1677.

16. Stolt, M. J.; Li, Z.-A.; Phillips, B.; Song, D.; Mathur, N.; Dunin-Borkowski, R. E.; Jin, S., Selective Chemical Vapor Deposition Growth of Cubic FeGe Nanowires That Support Stabilized Magnetic Skyrmions. *Nano Lett.* **2017,** *17*, 508-514.

17. Parkin, S. S. P.; Hayashi, M.; Thomas, L., Magnetic Domain-Wall Racetrack Memory. *Science* **2008,** *320*, 190.

18. Kanazawa, N.; Kubota, M.; Tsukazaki, A.; Kozuka, Y.; Takahashi, K. S.; Kawasaki, M.; Ichikawa, M.; Kagawa, F.; Tokura, Y., Discretized Topological Hall Effect Emerging from Skyrmions in Constricted Geometry. *Phys. Rev. B* **2015,** *91*, 041122.

19. Du, H.; Che, R.; Kong, L.; Zhao, X.; Jin, C.; Wang, C.; Yang, J.; Ning, W.; Li, R.; Jin, C.; Chen, X.; Zang, J.; Zhang, Y.; Tian, M., Edge-Mediated Skyrmion Chain and its Collective Dynamics in a Confined Geometry. *Nat. Commun.* **2015,** *6*, 8504.

20. Lichte, H., Electron Holography Approaching Atomic Resolution. *Ultramicroscopy* **1986,** *20*, 293-304.

21. Tonomura, A., Applications of Electron Holography. *Rev. Mod. Phys.* **1987,** *59*, 639-669.

22. Park, H. S.; Yu, X.; Aizawa, S.; Tanigaki, T.; Akashi, T.; Takahashi, Y.; Matsuda, T.; Kanazawa, N.; Onose, Y.; Shindo, D.; Tonomura, A.; Tokura, Y., Observation of the Magnetic Flux and Three-Dimensional Structure of Skyrmion Lattices by Electron Holography. *Nat. Nanotechnol.* **2014,** *9*, 337.

23. Midgley, P. A.; Dunin-Borkowski, R. E., Electron Tomography and Holography in Materials Science. *Nat. Mater.* **2009,** *8*, 271.

24. Jin, C.; Li, Z.-A.; Kovács, A.; Caron, J.; Zheng, F.; Rybakov, F. N.; Kiselev, N. S.; Du, H.; Blügel, S.; Tian, M.; Zhang, Y.; Farle, M.; Dunin-Borkowski, R. E., Control of Morphology and Formation of Highly Geometrically Confined Magnetic Skyrmions. *Nat. Commun.* **2017,** *8*, 15569.

25. Huang, S. X.; Fei, C.; Jian, K.; Jiadong, Z.; Shu, G. J.; Chou, F. C.; Chien, C. L., Unusual Magnetoresistance in Cubic B20 $Fe_{0.85}$ $Co_{0.15}Si$ Chiral Magnets. *New J. Phys.* **2016,** *18*, 065010.

26. Kang, J.; Zang, J., Transport Theory of Metallic B20 Helimagnets. *Phys. Rev. B* **2015,** *91*, 134401.

27. Du, H.; Liang, D.; Jin, C.; Kong, L.; Stolt, M. J.; Ning, W.; Yang, J.; Xing, Y.; Wang, J.; Che, R.; Zang, J.; Jin, S.; Zhang, Y.; Tian, M., Electrical Probing of Field-Driven Cascading Quantized Transitions of Skyrmion Cluster States in MnSi Nanowires. *Nat. Commun.* **2015,** *6*, 7637.

28. Beille, J.; Voiron, J.; Roth, M., Long Period Helimagnetism in the Cubic B20 $Fe_xCo_{1-x}Si$ and $Co_xMn_{1-x}Si$ alloys. *Solid State Commun.* **1983,** *47*, 399-402.

29. Higgins, J. M.; Ding, R.; DeGrave, J. P.; Jin, S., Signature of Helimagnetic Ordering in Single-Crystal MnSi Nanowires. *Nano Lett.* **2010,** *10*, 1605-1610.

30. In, J.; Varadwaj, K. S. K.; Seo, K.; Lee, S.; Jo, Y.; Jung, M.-H.; Kim, J.; Kim, B., Single-Crystalline Ferromagnetic $Fe_{1-x}Co_xSi$ Nanowires. *J. Phys. Chem. C* **2008,** *112*, 4748-4752.

31. Schmitt, A. L.; Higgins, J. M.; Jin, S., Chemical Synthesis and Magnetotransport of Magnetic Semiconducting $Fe_{1-x}Co_xSi$ Alloy Nanowires. *Nano Lett.* **2008,** *8*, 810-815.

32. DeGrave, J. P.; Schmitt, A. L.; Selinsky, R. S.; Higgins, J. M.; Keavney, D. J.; Jin, S., Spin Polarization Measurement of Homogeneously Doped $Fe_{1-x}Co_xSi$ Nanowires by Andreev Reflection Spectroscopy. *Nano Lett.* **2011,** *11*, 4431-4437.

33. Pokhrel, A.; DeGrave, J. P.; Liang, D.; Higgins, J. M.; Jin, S. Growth of Metal Silicide Nanowires and Their Spintronic and Renewable Energy Applications. In *Semiconductor Nanowires: From Next-Generation Electronics to Sustainable Energy*; Lu, W., Xiang, J., Eds.; Royal Society of Chemistry (RSC): Cambridge, U.K., 2015; pp 312-362.

34. Szczech, J. R.; Jin, S., Epitaxially-Hyperbranched FeSi Nanowires Exhibiting Merohedral Twinning. *J. Mater. Chem.* **2010,** *20*, 1375-1382.

35. Newbury, D. E.; Swyt, C. R.; Myklebust, R. L., "Standardless" Quantitative Electron Probe Microanalysis with Energy-Dispersive X-ray Spectrometry: Is It Worth the Risk? *Anal. Chem.* **1995,** *67*, 1866-1871.

36. Onose, Y.; Takeshita, N.; Terakura, C.; Takagi, H.; Tokura, Y., Doping Dependence of Transport Properties in $Fe_{1-x}Co_xSi$. *Phys. Rev. B* **2005,** *72*, 224431.

37. Harada, K.; Tonomura, A.; Togawa, Y.; Akashi, T.; Matsuda, T., Double-Biprism Electron Interferometry. *Appl. Phys. Lett.* **2004,** *84*, 3229-3231.

38. Ishimoto, K.; Yamaguchi, Y.; Suzuki, J.; Arai, M.; Furusaka, M.; Endoh, Y., Small-Angle Neutron Diffraction from the Helical Magnet $Fe_{0.8}Co_{0.2}Si$. *Phys. B (Amsterdam, Neth.)* **1995,** *213-214*, 381-383.

39. Münzer, W.; Neubauer, A.; Adams, T.; Mühlbauer, S.; Franz, C.; Jonietz, F.; Georgii, R.; Böni, P.; Pedersen, B.; Schmidt, M.; Rosch, A.; Pfleiderer, C., Skyrmion Lattice in the Doped Semiconductor $Fe_{1-x}Co_xSi$. *Phys. Rev. B* **2010,** *81*, 041203.

40. Du, H.; DeGrave, J. P.; Xue, F.; Liang, D.; Ning, W.; Yang, J.; Tian, M.; Zhang, Y.; Jin, S., Highly Stable Skyrmion State in Helimagnetic MnSi Nanowires. *Nano Lett.* **2014,** *14*, 2026-2032.

41. Mazurenko, V. V.; Shorikov, A. O.; Lukoyanov, A. V.; Kharlov, K.; Gorelov, E.; Lichtenstein, A. I.; Anisimov, V. I., Metal-Insulator Transitions and Magnetism in Correlated Band Insulators: FeSi and $Fe_{1-x}Co_xSi$. *Phys. Rev. B* **2010,** *81*, 125131.

42. Ishimoto, K.; Yamaguchi, Y.; Mitsuda, S.; Ishida, M.; Endoh, Y., Stability and Winding of the Long Period Helical Spin Structure in $Fe_{1-x}Co_xSi$. *J. Magn. Magn. Mater.* **1986,** *54-57*, 1003-1004.

43. Ou-Yang, T. Y.; Shu, G. J.; Hu, C. D.; Chou, F. C., Dynamic Susceptibility Study on the Skyrmion Phase Stability of $Fe_{0.7}Co_{0.3}Si$. *J. Appl. Phys.* **2015,** *117*, 123903.

44. Schwarze, T.; Waizner, J.; Garst, M.; Bauer, A.; Stasinopoulos, I.; Berger, H.; Pfleiderer, C.; Grundler, D., Universal Helimagnon and Skyrmion Excitations in Metallic, Semiconducting and Insulating Chiral Magnets. *Nat. Mater.* **2015**, 14, 478.

45. Li, Y.; Kanazawa, N.; Yu, X. Z.; Tsukazaki, A.; Kawasaki, M.; Ichikawa, M.; Jin, X. F.; Kagawa, F.; Tokura, Y., Robust Formation of Skyrmions and Topological Hall Effect Anomaly in Epitaxial Thin Films of MnSi. *Phys. Rev. Lett.* **2013,** *110*, 117202.

46. Song, D.; Li, Z.-A.; Caron, J.; Kovács, A.; Tian, H.; Jin, C.; Du, H.; Tian, M.; Li, J.; Zhu, J.; Dunin-Borkowski, R. E., Quantification of Magnetic Surface and Edge States in an FeGe Nanostripe by Off-Axis Electron Holography. *Phys. Rev. Lett.* **2018,** *120*, 167204.

47. Sinha, P.; Porter, N. A.; Marrows, C. H., Strain-Induced Effects on the Magnetic and Electronic Properties of Epitaxial $Fe_{1-x}Co_xSi$ Thin Films. *Phys. Rev. B* **2014,** *89*, 134426.

48. Manyala, N.; Sidis, Y.; DiTusa, J. F.; Aeppli, G.; Young, D. P.; Fisk, Z., Magnetoresistance from Quantum Interference Effects in Ferromagnets. *Nature* **2000,** *404*, 581.

49. Mehlin, A.; Xue, F.; Liang, D.; Du, H. F.; Stolt, M. J.; Jin, S.; Tian, M. L.; Poggio, M., Stabilized Skyrmion Phase Detected in MnSi Nanowires by Dynamic Cantilever Magnetometry. *Nano Lett.* **2015,** *15*, 4839-4844.

Chapter 4 : In-Plane Magnetic Field-Driven Creation and Annihilation of Magnetic Skyrmion Strings in Nanostructures*

4.1 Abstract

In bulk chiral crystals, three-dimensional structures of magnetic skyrmions form topologically-protected skyrmion strings (SkS) that have shown potential as magnonic nano-waveguides for information transfer. Although SkS stability is expected to be enhanced in nanostructures of skyrmion-hosting materials, experimental observation and detection of SkS in nanostructures under an applied in-plane magnetic field has been difficult. Here, we show temperature-dependent magnetic field-driven creation and annihilation of SkS in B20 FeGe nanostructures (nanowires and nanoplates) under in-plane magnetic field ($H_{\parallel}$) and explain the mechanisms behind these transformations. Unusual asymmetric and hysteretic magnetoresistance (MR) features are observed but previously unexplained during magnetic phase transitions within the SkS stability regime when $H_{\parallel}$ is along the nanostructure's long edge, which increase the sensitivity of MR detection. Lorentz transmission electron microscopy of the SkS and other magnetic textures under $H_{\parallel}$ in corroboration with the analysis of the anisotropic MR responses elucidates the field-driven creation and annihilation processes of SkS responsible for such hysteretic MR features and reveals an unexplored stability regime in nanostructures.

4.2 Introduction

The realization of faster information transfer and denser storage capacity using magnetic materials has become a major topic in condensed matter physics.[1, 2] Nanoscale topological spin textures like magnetic skyrmions are promising for potential applications in high density and

* This chapter is written in collaboration with Yasin, F. S.; Stolt, M. J.; Nagai, T.; Kimoto, K.; Du, H.; Tian, M.; Tokura, Y.; Yu, X.; Jin, S.

energy efficient memory nanodevices.[1-4] Although magnetic skyrmions are commonly illustrated as two-dimensional spin textures,[5-7] they naturally possess a three-dimensional structure resembling elongated strings extending throughout the thickness of the sample up to several millimeters in length which align along the direction of the applied magnetic field.[8-12] These three-dimensional spin textures known as magnetic skyrmion strings (SkS) are analogous to the vortex lines in superfluids[13] and type II superconductors,[14] manifest current-induced non-linear dynamics and characteristics of magnonic nano-waveguides.[9, 10] The broken inversion symmetry in the crystal lattice induces a Dzyaloshinskii-Moriya interaction (DMI) energy term that stabilizes SkS. Their string-like shape is robust enough to resist transformation, but flexible enough to bend; and the creation and annihilation of SkS proceeds with formation of magnetic singularities known as Bloch points.[8, 11, 15] The actualization of these unique topological features in real materials has pushed the investigation towards the less explored dimension along the length of SkS. [8-12]

Crystals of chiral helimagnets with the non-centrosymmetric cubic B20 crystal structure can host SkS and form a periodic hexagonal lattice arrangement in a narrow and restricted window of applied magnetic field and temperature in the magnetic phase diagram (H-T plot) just below their respective Curie temperature, T_c.[1, 5, 11, 15-18] Nanostructures of skyrmion-hosting materials have been shown to thermodynamically stabilize SkS phase more easily than bulk and thin film systems.[18-23] Moreover, the presence of intrinsic shape-induced anisotropy, edge-mediated nucleation, and chiral edge twist states could result in extended stability of the SkS in nanostructures.[11, 22, 24-26] However, real space imaging of skyrmion textures is traditionally limited to an out-of-plane applied field configuration (field oriented parallel to the imaging axis). The rarity of both pure in-plane applied field configuration and cryogenic capabilities in commercial transmission electron microscopes (TEMs), as well as the low signal intrinsic to nanosized objects,

makes the detection of SkS (oriented perpendicular to imaging axis) in confined geometries challenging. A recent real-space observation of SkS under an in-plane applied magnetic field employed scanning transmission X-ray microscopy (STXM) to image fabricated thin lamella of FeGe (~ 120 nm) at 100 K.[11]

On the other hand, electrical transport detection of skyrmion states has been successfully implemented on nanostructures over a large range of temperatures and applied magnetic fields.[18] However, the topological Hall effect (THE), usually taken as the electronic signature of skyrmions, can only be implemented with an out-of-plane applied field configuration required for the experimental setup.[27-30] Magnetoresistance (MR) detection is more natural under in-plane applied magnetic field for skyrmion-hosting nanostructures and effectively yields information about the interaction of conduction electrons with chiral modulations of spin textures.[18, 21, 24, 29] Here we report a comprehensive magnetotransport study of FeGe nanowires (NWs) and $Fe_{1-x}Co_xGe$ (with ≤ 5% Co doping) nanoplates (NPLs) with an externally applied in-plane magnetic field to explore the extended temperature-dependent stability and field-driven magnetic phase transformations of SkS from T_c ~ 280 K down to 10 K. We further employed defocused Lorentz TEM (LTEM) under pure in-plane magnetic field to image the temperature-dependent creation and annihilation of metastable SkS in a $Fe_{0.95}Co_{0.05}Ge$ NPL and understand the mechanism(s) behind the field-driven transformation processes adopted by topologically stable SkS and explain the unusual MR features uniquely observed in nanostructures.

4.3 Results and Discussion

4.3.1 Anisotropic and Sensitive In-Plane Magnetotransport Response in FeGe NWs during Magnetic Phase Transitions

We conducted magnetotransport measurements on single-crystal FeGe NWs grown *via* a chemical vapor deposition (CVD) process.[20] While the MR results discussed in this chapter are mainly from NW1 (thickness ~ 760 nm), NW2 (thickness ~ 400 nm) qualitatively shows similar MR features (Figure A2.1). The magnitude of MR ($[R(H) - R(0)]/R(0)$, where $R(H)$ and $R(0)$ are the resistance at a specific applied magnetic field and zero field, respectively) generated by FeGe NWs (~ 0.1%) is significantly lower than NWs of other isostructural cubic B20 materials, such as MnSi [24, 29] and $Fe_{1-x}Co_xSi$ (~1%).[21] Therefore, these experiments require high signal-to-noise ratio (S/N) with good metallic contact (Figure A2.1a and Figure A2.2a) of the fabricated NW devices (see experimental section for detailed device fabrication process). The field-driven evolution of spin textures in the FeGe NW1 device (Figure 4.1a) was studied by measuring isothermal magnetic field sweep (MR-H) curves which were obtained by sweeping the applied magnetic field (increasing and decreasing) at a constant temperature in parallel (magnetic field $H_{||}$ || current density (J) or NW axis) and perpendicular configurations ($H_{\perp} \perp J$) and measuring the resistance across the voltage probes as shown in the Figure 4.1a (see Figures A2.2b-g and experimental section for more details regarding magnetotransport measurements and asymmeterization process).

Figure 4.1b shows MR-$H_{||}$ curves over selected temperatures in the range of 10 - 290 K. The field-dependent MR signal disappears for the paramagnetic state measured above $T_c \sim 280$ K. Anomalous MR signature accompanied by appreciable hysteresis was observed at low temperatures (below 100 K) which is marked by a sharp change in the MR signal when $|H_{||}|$ is

below the saturation field. Qualitatively similar low temperature MR features under $H_{||}$ were also observed (but not explained) in the FeGe NPL (with 3% Co doping) devices,[28] but not in FeGe bulk[31] and thin film systems,[32] which makes these anomalous MR features unique to nanostructures. The strong anisotropic response of MR signal obtained in the parallel MR configuration stands in clear contrast to the smooth MR curve in the perpendicular configuration (see a specific comparison at 10 K in Figure 4.1c), suggesting an in-plane magnetic anisotropy. Moreover, there is no sign of the anomalous MR signal in the perpendicular configuration at any temperature below T_c (Figures A2.2d,e). The NW's orientation and morphology manifest as a magnetic hard-axis perpendicular to the NW with a higher saturation field and less-pronounced MR features corresponding to the magnetic phase transitions (Figures A2.2f, g).

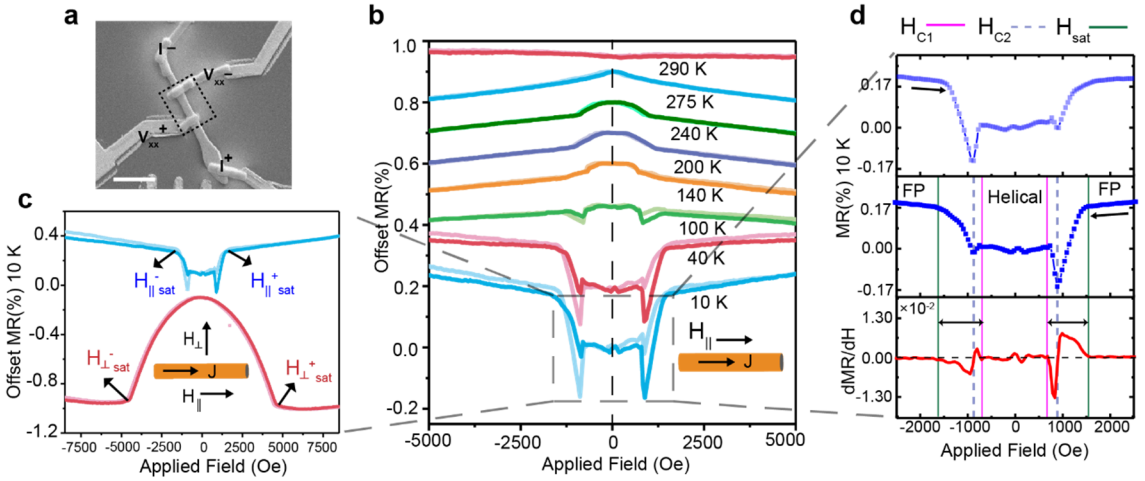

Figure 4.1 : Anomalous and anisotropic magnetotransport features of the FeGe NW in the parallel configuration. (a) SEM image of a representative four-probe device of NW1 with labelled current and voltage probes used in the transport measurements. The dashed black box marks the probing area of the NW between the voltage leads. Scale bar is 4 µm. (b) MR- $H_{||}$ curves in the temperature range of 10 – 290 K with bold and faded color corresponding to decreasing and increasing field sweeps, respectively. MR-$H_{||}$ curves are offset for clarity. (c) MR-H curves at 10 K showing strong anisotropic MR response in the parallel configuration in comparison with the MR-H curve in the perpendicular configuration. (d) Enlarged inset of MR-$H_{||}$ curve at 10 K with increasing (top panel) and decreasing (middle panel) field sweeps (represented by black arrows) highlighting the apparent hysteresis, with the corresponding $dMR/dH_{||}$ curve (bottom panel) of the latter with critical fields H_{C1}, H_{C2} and H_{sat} indicated as vertical lines. Values for increasing and decreasing field strength are denoted by the superscripts "+" and "-", respectively.

The effective uniaxial anisotropy of the FeGe NW could be estimated by the difference of the saturation field between the parallel ($H_{\parallel\,sat}$) and perpendicular ($H_{\perp\,sat}$) configuration, which is ~ 3000 Oe at 10 K. The shape-induced uniaxial anisotropy in magnetic NWs generally originates from the anisotropic demagnetization effect in the sample which favors the magnetic easy-axis along the length of the NW that could result in enhanced stability of SkS even at low temperatures. In MnSi thin films, the presence of strain-induced uniaxial anisotropy enables the formation of elliptically distorted SkS extended over a large region of the magnetic phase diagram, which was further confirmed by the planar Hall effect and magnetization measurements even down to 2 K.[33, 34] However, such effect has not been observed in bulk skyrmion-hosting B20 materials. To elucidate the field-driven transformations of different spin textures at low temperatures, we plotted the MR-$H_{\parallel}$ curves at 10 K with increasing and decreasing field separately (Figure 4.1d), which highlight the clear hysteresis between the increasing versus decreasing field sweeps as a hallmark of the first-order phase change, or possibly of the topological transition. Together with the first derivative ($dMR/dH_{\parallel}$) curve of the decreasing field sweep (Figure 4.1d bottom panel), the critical fields of each magnetic phase transition can be detected by the slope change in the MR-$H_{\parallel}$ curves and marked as H_{C1}, H_{C2} and H_{sat}.

4.3.2 Analysis of SkS Stability and Magnetotransport Features under In-Plane Magnetic Field in FeGe Nanostructures

The origin of the MR is attributed to the coupling of conduction electrons with the chiral modulations of non-collinear spin textures. The progression of magnetic phase transformations and orientation of chiral modulation vector (Q) in FeGe NWs under $H_{\parallel}$ (Figure 4.2a) are illustrated in Figures 4.2b-d. In contrast to bulk systems, $Q_{helical}$ aligns itself along the NW axis due to the shape-induced anisotropy which was also previously reported for NWs of cubic B20 materials

including FeGe.[19-21] The formation of conical domains leads to the alignment of the $Q_{conical}$ in the direction of $H_{||}$ like the helical phase. Note that Q_{SkS} (Figure 4.2c) is the simplified representation of the 3Q skyrmion state in the plane perpendicular to the $H_{||}$.[5] In principle, there should not be any chiral modulations along the length of the SkS. The transformation of aligned SkS to the helical/conical phase requires a ~ 90° flipping of the Q in NWs. This contrasts with the smooth transformation between the helical and the conical phase with aligned Q, previously shown in the case of epitaxially grown FeGe thin films.[32] Moreover, in the helical or conical state with the Q being parallel to the NW edge and hence to the J, which should result in more scattering of the conducting electrons and thus a higher resistance state in MR measurements when compared to SkS.[34, 35] These factors could contribute to the more sensitive MR detection under $H_{||}$ during the magnetic phase transformations, especially at low temperature where collective spin dynamics are restricted due to low thermal energy.

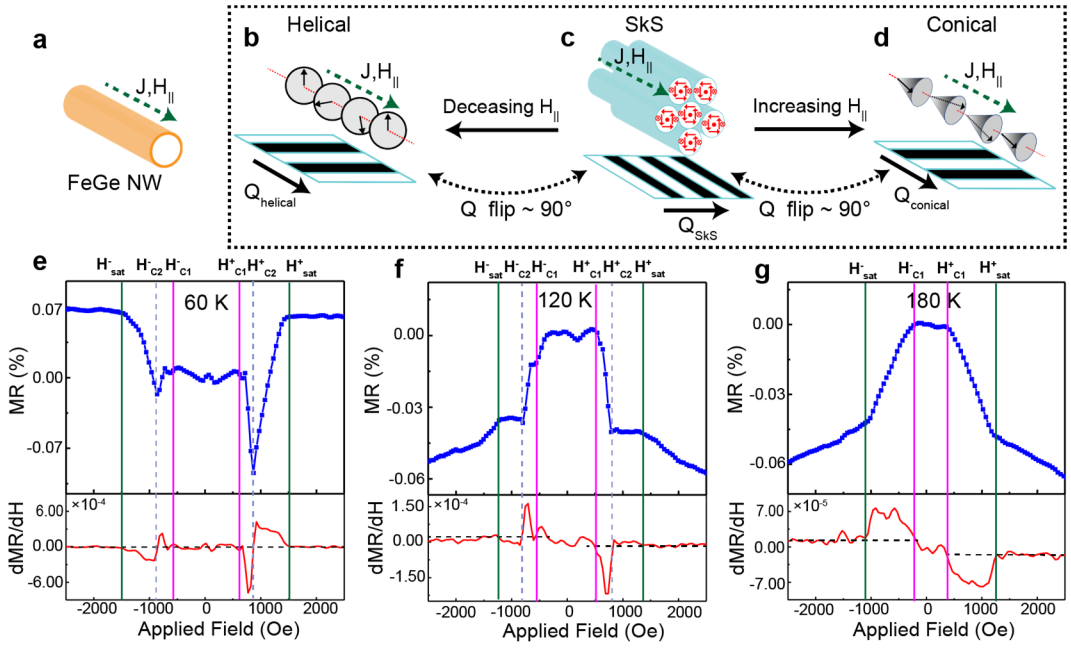

Figure 4.2 : Illustration of the interconversions of various magnetic states in NWs revealed by representative MR responses. The dependence of MR signal in the (a) parallel magnetic field configuration for a FeGe NW with the orientation of chiral modulation vector (Q) of non-collinear spin textures: (b-d) the schematics of spin textures and its

2D projection of chiral domains with the corresponding Q in the parallel configuration of FeGe NW shown for (b) helical, (c) SkS and (d) conical phase. The schematic shown in (b-d) depicts a ~ 90° flipping of the *Q* during the transformation of spin states with increasing and decreasing field strength. Selected MR responses of NW1 in decreasing field sweeps plotted as MR-$H_{||}$ curves with the corresponding dMR/d$H_{||}$ curves at (e) 60 K, (f) 120 K, and (g) 180 K for the assessment of the critical fields (H_{C1}, H_{C2} and H_{sat}) that are marked as vertical lines.

To determine the stability regime of the magnetic phases in FeGe NW1, we resort to temperature-dependent field-driven creation and annihilation of chiral spin textures. Figures 4.2e-f show the field-driven responses of the MR-$H_{||}$ curves for NW1 at 60 K, 120 K, and 180 K, with the corresponding dMR/d$H_{||}$ curves (see Figure A2.3 for the complete data in the temperature range of 20 – 275 K). At 60 K (Figure 4.2e), the anomalous MR signal in the applied field range of $H_{C1} < H_{||} < H_{sat}$ sharply rises and falls, indicating the creation or annihilation of SkS and the ~ 90° *Q* rotation. However, after the transformation from helical to SkS state at H_{C1}, SkS should remain stable over a large applied field range due to their topological protection. Therefore, the sharp rise in the MR signal above H_{C2} indicates the formation of competing high-resistance conical state that could coexist with the SkS.[11] Anisotropic MR is proportional to the spatial modulation of spin textures averaged over a cross-section of the NW.[36] The sharp increase in the MR signal above H_{C2} points towards a larger volume occupancy of the conical phase in comparison to SkS at low temperatures, where SkS could arrange in a sparse regime rather than occupying the whole cross-section of the NW.[25] This could be further understood by increasing the temperature where conical phase destabilizes due to thermal fluctuations and effects of the confined geometry.[5, 28, 33, 37] At 120 K (Figure 4.2f), the abrupt change in the MR ($H_{C1} < H_{||} < H_{C2}$) due to the transformation of helical to SkS phase persists, but the steep rise above H_{C2} wanes with increasing $H_{||}$ (Figures A2.3a-g). Furthermore, the MR-$H_{||}$ curve at 180 K (Figure 4.2g) shows no observable transition at H_{C2} and the stability window of the SkS extends over the mixed phase (SkS + conical) regime due to destabilization of the conical phase. This field-driven response of the MR signal remains

consistent until the temperature approaches T_c (Figures A2.3h-l), suggesting the presence of closed-packed SkS lattice arrangement extended throughout the NW at high temperatures like in bulk systems.[38]

Apart from the sensitive MR under $H_{||}$, the strong hysteretic MR features are apparent below ~ 100 K in FeGe NWs, especially in the SkS stability regime as revealed by the MR measurements. At low temperatures, the MR signal changes sharply between $H_{C1} < H_{||} < H_{sat}$ and increases in intensity when the field-driven transformation of spin textures starts with a conical phase rather than a helical ground state, forming a hysteretic MR feature in the MR-$H_{||}$ curves. (Figures 4.1b, d and Figures A2.1b, c). This apparent difference in MR signal between the increasing and decreasing field sweeps might originate from the dissimilarity in SkS packing densities, which in turn are caused by the temperature-dependent energy barrier for SkS formation from the various initial spin states (helical vs. conical).[15, 26] These hysteretic MR features appear to be unique to the nanostructure morphology of various skyrmion-hosting B20 materials but were previously not explained;[21, 24] such hysteresis features were significantly enchanced in FeGe NWs in its SkS stability regime in comparision to NWs of other cubic B20 metal silicide materials with slighly different morphology and even higher overall MR signal.[21, 24] This suggests that the temperature-dependent energy barrier for SkS creation and annihilation could also depend on the shape and magnetic anisotropy of the nanostructures. These results clearly demonstrate the sensitivity of in-plane magnetotransport response to reveal field-driven transformations, stability and arrangement of spin textures in FeGe NWs, even though the magnitude of the MR signal is quite low (~ 0.1%).

The key driving force behind the low-temperature stability of SkS in FeGe NWs seems to be the shape-induced uniaxial anisotropy. Other factors that influence the evolution of spin textures

at low temperatures include magneto-crystalline anisotropy, which is considerably small compared to the exchange energy of the FeGe system.[39] To validate this stabilization mechanism of SkS in other nanostructure morphologies, we further investigated and conducted detailed analysis of the magnetotransport data acquired from the FeGe NPL with 3% cobalt doping, in which skyrmion phase exists with minimal change in skyrmion size and T_c from pure FeGe (see Figure A2.4, Figure A2.5 and Figure A2.6 and Supporting information for detailed analysis).[28,40] The voltage probes were fabricated near the edge of the NPL with an average thickness ~ 640 nm (Figures A2.4a-d), where SkS are more likely to nucleate as shown previously for thin FeGe lamella.[11] The anomalous and hysteresis features observed in the MR- $H_{||}$ curves of the $Fe_{0.97}Co_{0.03}Ge$ NPL at low temperatures might be due to enhanced anisotropic effects, revealed by the quantitative analysis of MR data in comparison with NWs (Figure A2.5). Moreover, a decreasing gradient in the MR-$H_{||}$ ($H_{C2} < H_{||} < H_{sat}$) was observed with increasing temperature (Figures A2.6d-l) which may be interpreted as a destabilization of the conical phase, reminiscent of the results for FeGe NWs. These magnetotransport measurements further highlight the importance of edge-induced stability of SkS in nanostructures. [11, 22]

4.3.3 Real Space Observation of SkS and its Magnetic Phase Transformations under Purely In-Plane Magnetic Field

To further confirm the evolution of SkS and other magnetic textures, we conducted real-space imaging using LTEM under an in-plane applied magnetic field to capture the length-wise view of the SkS. Defocused-LTEM on NWs is very challenging due to effect of Fresnel fringes around the samples' edges that hinder the visualization and interpretation of magnetic contrast images. However, since the MR responses of NW and NPL above are very similar in both stability and field-driven transformation of spin textures**,** we chose to image a uniformly thin $Fe_{0.95}Co_{0.05}Ge$

NPL with an average thickness ~ 150 nm and basal plane perpendicular to the zone axis (ZA) of (111) (Figures 4.3a,b). We observed a helical ground state with $Q_{helical}$ aligned along the long edge

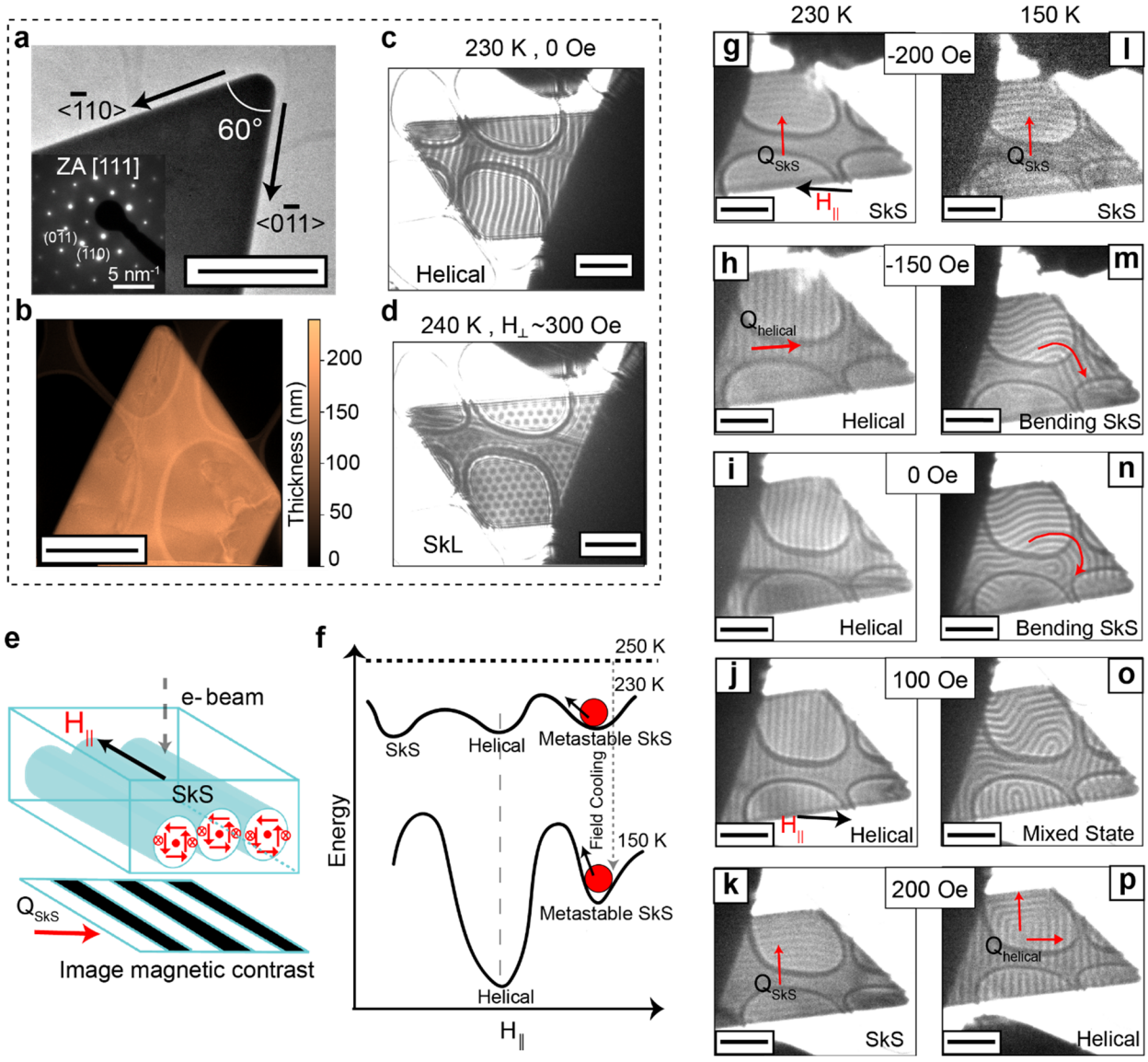

Figure 4.3 : LTEM imaging of a $Fe_{0.95}Co_{0.05}Ge$ NPL. (a) Bright-field TEM image and SAED pattern (inset) of the single-crystal $Fe_{0.95}Co_{0.05}Ge$ NPL, with its two edges along the crystallographic direction (110) making an angle of 60°. (b) EELS thickness profile indicates uniformly thin NPL. LTEM images collected under (c) 0 Oe (230 K) and (d) $H_{\perp}$~300 Oe (240 K) show ground state helical stripe pattern and hexagonal SkL, respectively. (e) Schematic of the LTEM configuration for imaging magnetic spin textures such as SkS, where $H_{||}$ and incident e-beam are parallel and perpendicular to the NPL basal plane, respectively. SkS are aligned parallel to $H_{||}$ with the spin texture modulation

vector (Q_{SkS}) in the plane perpendicular to $H_{||}$. (f) Schematic free-energy landscape for the transformation of metastable SkS, generated by rapid field cooling at 230 K and 150 K while holding constant $H_{||} = -230$ Oe. A series of defocused-LTEM images shown at 150 K (g-k) and 230 K (l-p). The increase of $H_{||}$ from − 200 Oe to 200 Oe at T = 230 K stimulated a field-driven transformation of metastable stable SkS (g) to the helical phase (h-i) and back to the thermodynamically stable SkS (k). At 150 K, the metastable SkS (l) show clear signature of flexible bending (m,n) away from the edges of the NPL before it reaches the transition state of disordered helical phase (o) upon which the metastable SkS annihilate and transform to a multi-Q helical phase (p). The $H_{||}$ direction is ~10° from the long edge of the NPL as marked in g, j. All scale bars are 500 nm.

of the NPL (<110> crystallographic direction) and skyrmion lattice (SkL) with periodicity ~ 80 nm (Figures 4.3c,d) when applying $H_{\perp} \sim 300$ Oe. To generate SkS along the NPL's long axis requires $H_{||}$ perpendicular to the optical axis. Using a external solenoid apparatus integrated into a Lorentz TEM (Hitachi, HF-3000L), we applied a pure in-plane magnetic field ($H_{||}$) and acquired defocused images of the emergent SkS (Figure 4.3e). However, due to the technical limitation of microscope optics and image aberration correction, the $H_{||}$ is limited to a range of ± 250 Oe. To explore the field-driven spin evolution process at low temperatures where SkS are stable at $H_{||}$ higher than the microscope field limit, we generated metastable SkS by rapid field cooling, a process in which an $H_{||}$ of − 230 Oe was held constant as the sample was rapidly cooled to the desired temperature. [8, 41]

Next, we decreased $H_{||}$ and then reversed the field direction, which stimulated the transformation of the metastable SkS to a helical phase (Figure 4.3f) and the periodicity of magnetic spin textures was extracted from the experimental data (Figure A2.7). Figure 4.3g shows that the SkS align parallel to $H_{||}$ (~ 10° off the long edge of the NPL) and therefore have magnetic contrast distinct from the helical domains at zero field where the $Q_{helical}$ tends to align along the long axis of the NPL (Figure 4.3c). At 230 K, the metastable SkS were completely transformed to

the helical phase by decreasing field strength from $H_{||} = -200$ Oe (Figure 4.3g) to – 150 Oe (Figure 4.3h). We observed ~ 90° flipping of Q during the transformation process as predicted for the nanostructure morphology (as illustrated in Figure 4.2b, c). After reaching zero field and then increasing $H_{||}$ in the opposite direction, the helical phase was again transformed to aligned SkS (Figures 4.3i-k). This suggests that the SkS phase is thermodynamically stable at 230 K below 250 Oe. Although we were unable to image the conical phase due to field limitation, $Q_{conical}$ should align in the direction of $H_{||}$ like the helical domains.[11]

In contrast to the evolution of the spin textures above 200 K (Figures 4.3g-k and more LTEM images at 200 K shown in Figures A2.8a-d), at 150 K, the magnetization dynamics of the transformation of metastable SkS to the helical phase is significantly slower. At 150 K, the SkS near the center of the NPL undergoes flexible bending which increases with decreasing $H_{||}$ (Figures 4.3l-n). With increasing $H_{||}$ in the opposite direction, the system realizes a disordered mixed state (Figure 3o) which could be related to the destruction of a topological state before transforming to a multi-Q helical phase (Figure 4.3p). This multi-Q helical state might be a result of significant contribution of anisotropic demagnetization (stray) field at the low temperatures present in the NPL, which easily transforms to a stable single-Q helical state by increasing $H_{||}$ by ~ 100 Oe above zero field (Figures A2.8e-h).[42, 43] In principle, the transformation of topologically protected SkS to the helical phase is facilitated by the dynamics of Bloch points in the material. In earlier studies [15, 44, 45], the transformation of SkS to the helical phase proceeds with the merging of SkS to the formation of Bloch points that travel across the material. The bending of SkS during the transformation process might indicate that there exists a linear potential (like tension in a string) holding a SkS with two Bloch points across the ends of the SkS, which eases with decreasing $H_{||}$.[15] We further conducted the micromagnetic simulations on confined rectangular (NPL) and wire

(NW) geometries of FeGe under in-plane magnetic field as shown in Figure A2.9 (see simulation details in the experimental section). The simulation results show that the SkS stabilized in NPL geometry bend freely within the x-y plane (in-plane) which is in agreement with the LTEM results, but the NW geometry confines the SkS more rigidly. This could perhaps explain the difference in MR- $H_{||}$ isotherms during magnetic phase transitions between the two geometries (Figure 4.1b and Figure A2.5c) as there is an extra geometric degree of freedom available for the SkS to move and initiate a transformation event in the NPL. Moreover, the thermal activation barrier for the nucleation/annihilation of Bloch points and their impurity pinning in the material are key factors that could affect the transformation of SkS to a non-topological phase and warrants future investigation.

4.3.4 Representative Magnetic Phase Diagram of FeGe Nanostructures under In-Plane Magnetic Field

Finally, we plotted a representative magnetic phase diagram ($H_{||}$-T plot) inferred from the magnetotransport measurements in the parallel configuration conducted on FeGe NW1 and $Fe_{0.97}Co_{0.03}Ge$ NPL (Figure 4.4). The specific data points on the $H_{||}$-T plot are critical fields for magnetic phase transitions (H_{C1}, H_{C2}, $H_{|| sat}$) below $T_c \sim 280$ K, indicating the stability regime of various spin textures (SkS, SkL, helical, conical) in these FeGe nanostructures. The coexistence of SkS and conical phase ($H_{C2} < H_{||} < H_{|| sat}$) at low temperatures might be a consequence of inhomogeneous distribution of demagnetizing field in the nanostructures with rounded morphology.[43] The vertical red dash lines at 140 K for the FeGe NW and 200 K for the

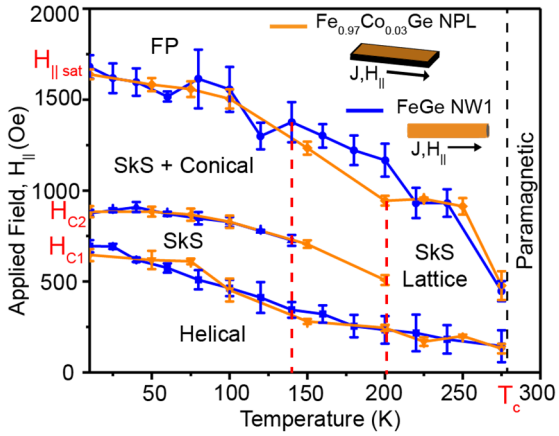

Figure 4.4 : Summary $H_{||}$-T plots of FeGe nanostructures. The critical fields for the magnetic phase transitions (H_{C1}, H_{C2} and $H_{||\ sat}$) were inferred from the MR measurements under $H_{||}$ on FeGe NW1 and $Fe_{0.97}Co_{0.03}Ge$ NPL below $T_c \sim$ 280 K. The vertical red lines represent the temperature above which the conical phase tends to destabilize as detected by MR measurements. The critical fields displayed are averaged (with error bars) for positive and negative applied magnetic fields with increasing and decreasing field sweeps.

$Fe_{0.97}Co_{0.03}Ge$ NPL on the $H_{||}$-T plot, mark the temperature above which the conical phase destabilizes as detected by MR measurements. Interestingly, most of the magnetic phase boundaries in this $H_{||}$ -T plot resemble those in the $H_{||}$-T plot for the thin FeGe lamella (120 nm) investigated using magnetic X-ray diffraction (Figure A2.10),[11] providing additional support for our conclusions. However, in that study, magnetic X-ray diffraction was unable to detect SkS when measuring in the parallel configuration. They suggest that while their apparatus was limited in probing at the center of the micron size lamella, edge effects may help to nucleate and stabilize SkS as also demonstrated for these FeGe nanostructures.

4.4 Conclusion

In conclusion, we investigated field-driven creation and annihilation of SkS in FeGe nanostructures using magnetotransport measurements and LTEM imaging under an applied in-plane field ($H_{||}$). The anomalous MR signal observed at low temperatures is ascribed to the combination of ~ 90° flipping of the Q during magnetic phase transitions and the phase coexistence between the SkS and the conical state. Unusual MR hysteresis features previously not seen in bulk

B20 materials are observed in the SkS stability regime of FeGe nanostructures and could be associated with different field-driven transformations of SkS starting from helical or conical phase. These unique and prominent MR features in nanostructures enable the sensitive detection of thermodynamically stable SkS over a wide range of temperatures which is most likely the effect of shape-induced anisotropy. Furthermore, LTEM imaging in conjunction with micromagnetic simulations in confined geometries of FeGe nanostructures under $H_{||}$ reveal that the SkS adopt a bending mechanism during the transformation between metastable SkS and helical phase at low temperatures. The in-plane magnetotransport measurements in corroboration with the real-time visualization of magnetic textures present a complete toolkit to understand the field driven transformations of SkS and other magnetic textures as elucidated in this study. These findings provide new understanding of in-plane field-driven transformations and stability of SkS in nanostructures and demonstrate nanostructures as a model system to explore the dynamics of topological defects, SkS magnonics, and non-linear dynamics of a single SkS for future spintronic devices.

4.5 Experimental Section

4.5.1 Synthesis and Structural Characterization of FeGe Nanostructures

Single crystal FeGe NWs and $Fe_{1-x}Co_xGe$ NPL samples used in this work were synthesized *via* CVD technique.[20, 28] The difference between the synthesis of NPL vs. NWs is the addition of cobalt precursor to form slightly Co-doped (a few percent) FeGe product, which also results in the morphology change.[28] The $Fe_{0.95}Co_{0.05}Ge$ NPL used for defocused LTEM imaging under in-plane applied magnetic field was first transferred to a Cu TEM grid by gently dragging the Cu grid over the surface of the reacted CVD substrate. TEM imaging and selected area electron diffraction (SAED) were carried out on the NPL using a Hitachi HF-3000L electron microscope operated at

300 kV. Thickness profile of the NPL was determined using electron energy loss spectroscopy (EELS) Gatan-GIF system attached on a commercial TEM (JEM2800, JEOL).

4.5.2 Device fabrication for electrical measurements

Magnetoresistance (MR) devices based on single-crystal FeGe NWs[20] and NPL[28] were fabricated using a combination of electron-beam (e-beam) and focused ion beam (FIB) lithography. FeGe nanostructures were transferred to Si (100) wafers coated with a 600 nm silicon oxide layer by gently scraping the Si substrate over the reacted CVD substrate. Then, two polymer e-beam resist layers of methyl methacrylate (MMA, MicroChem) and one layer of poly-MMA (PMMA, MicroChem) were sequentially spin coated onto the Si substrates and cured after each coating by baking the substrate on a 180 °C hotplate for 5 min. Nano-Pattern Generation System (NPGS) software was used to define large metal lead patterns using e-beam lithography, carried out on a LEO 1530 SEM operating at 30 keV, then the defined patterns were developed in a MIBK (Methyl isobutyl ketone) /isopropanol (IPA) solution for 30 s. Ti (75 nm)/ Au (100 nm) metals were evaporated at a deposition rate of 1.0 Å/sec using an e-beam metal evaporator (Angstrom Engineering) with post-deposition lift-off using acetone. These lithographic steps were used to make Ti/Au metal leads that ended ~1 μm away from the selected nanostructures. Finally, the metal contact to the nanostructures was made by Pt directly deposited in a Zeiss Auriga FESEM Focused Ion Beam (FIB) system equipped with a Ga^+ beam operating at 30 keV and 20 pA current. The distances between different Pt leads were kept at a few μm away which is significantly larger than the 10s nm of the penetration depth and radial spread of Ga^+ beam generally reported in materials.[46] The longitudinal resistivity (ρ_{xx}) of the FeGe NWs at room temperature (~ 0.4 mΩ cm) that is close to the value reported for bulk FeGe crystals (~ 0.2 mΩ cm)[30] and the high value

of residual resistance ratio (RRR~ 9) confirm good metallic contact with NWs (Figure A2.1a and Figure A2.2a).

4.5.3 Magnetotransport measurements

The fabricated NW (or NPL) devices were wire-bonded into a chip carrier and measured in a Quantum Design physical property measurement system (PPMS) 6000 equipped with a 9T magnet using a Keithley 6220 DC current source and a Keithley 2182A nanovoltmeter for the magnetotransport measurements. Both the in-plane applied magnetic field ($H_{\parallel}$) and current density (*J*) were along the long axis of the NW to obtain the MR- $H_{\parallel}$ curves in the parallel configuration for detection of the SkS (Figure A2.1b, Figure A2.1c and Figure A2.3). To interpret the anisotropic magnetotransport features under $H_{\parallel}$, we also conducted MR measurements in the perpendicular configuration (where the applied magnetic field is out of plane to the NW, H ⊥ J) shown in Figure A2.2. To mount the NW device into the chip carrier for measurements under $H_{\parallel}$, the nanostructures' long axis was aligned under an optical microscope to within a ~10° deviation. We conducted MR measurements on FeGe NWs in the range of 10 - 290 K with the applied magnetic field swept at a rate of 20 Oe/sec from −10000 Oe to 10000 Oe and the applied current density (*J*) kept in the range of ~10^8 A/m^2. The critical field for magnetic phase transitions was determined by analyzing the abrupt changes in the derivative of MR with respect to the applied field (dMR/dH) shown in Figure A2.3. MR asymmeterization of individual MR-H curve results in separation of symmetric (true MR signal) and asymmetric (arises due to strong Hall effect of FeGe) component by applying a simple mathematical equation (1):

$$R_{asym} = \frac{R_{xx}(H^+) - R_{xx}(H^-)}{2} \quad (1)$$

where H^+ and H^- represents applied magnetic field in positive and negative branch of a MR-H curve, respectively.

4.5.4 LTEM measurements

The imaging of magnetic domain structures was carried out at a low magnification mode of a transmission electron microscope (TEM) (Hitachi HF-3000L) with a cold-field-emission electron gun configured at an acceleration voltage of 300 kV. The TEM is equipped with an external solenoid apparatus capable of generating external in-plane magnetic field (−250 - 250 Oe). The in-plane magnetizations can be indirectly imaged as bright or dark contrast in a defocused (under- or over-focus) image plane due to the deflections of incident electrons *via* a Lorentz force. The dark contrast that appears as geometric shapes near the borders of the image in the LTEM images are other thick NPLs present on the TEM grid in the vicinity of the observed $Fe_{0.95}Co_{0.05}Ge$ NPL. To obtain quantitative information of in-plane magnetizations such as periodicity of the SkS or helical domains (Figure A2.7), we used a software package QPt (HREM Co.) to calculate the phase imparted onto the electron from the magnet, which is based on the transport-of-intensity equation (TIE).[47]

4.5.5 Micromagnetic Simulations

We used MuMax3 to perform Landau-Lifshitz-Gilbert equation-based micromagnetic simulations to study the effect of sample geometry on the stability of skyrmion strings. We used typical values for material parameters including exchange stiffness constant A_{ex} = 8.78 pJ/m, bulk DMI D_{bulk} = 1.58 mJ/m^2, saturation magnetization M_{sat} = 384 kA/m and Gilbert damping constant $\alpha = 0.3$. The two mesh sizes were 128 pix x 64 pix x 20 pix = 1024 nm x 512 nm x 120 nm for the nanoplate (NPL) and 128 pix x 16 pix x 16 pix = 1024 nm x 128 nm x 128 nm for the nanowire (NW). The skyrmion string initial states shown in Figure A2.9 were obtained by applying an in-plane magnetic

field sweep from -2 kOe to +2.5 kOe for the NPL and -1.5 kOe to +2 kOe for the NW, with each starting from a random magnetization state.

The results from this chapter have been published in the journal *Advanced Functional Materials*. Reference as follows:

Mathur, N.; Yasin, F. S.; Stolt, M. J.; Nagai, T.; Kimoto, K.; Du, H.; Tian, M.; Tokura, Y.; Yu, X.; Jin, S., In-Plane Magnetic Field-Driven Creation and Annihilation of Magnetic Skyrmion Strings in Nanostructures. *Adv. Funct. Mater.* **2021**, 31, 2008521

Appendix 2 in this thesis contains supporting information and additional figures of this chapter

References

[1] N. Nagaosa, Y. Tokura, *Nat. Nanotechnol.* **2013**, *8*, 899.

[2] S. S. P. Parkin, M. Hayashi, L. Thomas, *Science* **2008**, *320*, 190.

[3] J. Sampaio, V. Cros, S. Rohart, A. Thiaville, A. Fert, *Nat. Nanotechnol.* **2013**, *8*, 839.

[4] C. Back, V. Cros, H. Ebert, K. Everschor-Sitte, A. Fert, M. Garst, T. Ma, S. Mankovsky, T. L. Monchesky, M. Mostovoy, N. Nagaosa, S. S. P. Parkin, C. Pfleiderer, N. Reyren, A. Rosch, Y. Taguchi, Y. Tokura, K. von Bergmann, J. Zang, *J. Phys. D* **2020**, *53*, 363001.

[5] S. Mühlbauer, B. Binz, F. Jonietz, C. Pfleiderer, A. Rosch, A. Neubauer, R. Georgii, P. Böni, *Science* **2009**, *323*, 915.

[6] X. Z. Yu, Y. Onose, N. Kanazawa, J. H. Park, J. H. Han, Y. Matsui, N. Nagaosa, Y. Tokura, *Nature* **2010**, *465*, 901.

[7] X. Z. Yu, N. Kanazawa, Y. Onose, K. Kimoto, W. Z. Zhang, S. Ishiwata, Y. Matsui, Y. Tokura, *Nat. Mater.* **2010**, *10*, 106.

[8] F. Kagawa, H. Oike, W. Koshibae, A. Kikkawa, Y. Okamura, Y. Taguchi, N. Nagaosa, Y. Tokura, *Nat. Commun.* **2017**, *8*, 1332.

[9] T. Yokouchi, S. Hoshino, N. Kanazawa, A. Kikkawa, D. Morikawa, K. Shibata, T.-h. Arima, Y. Taguchi, F. Kagawa, N. Nagaosa, Y. Tokura, *Sci. Adv.* **2018**, *4*, eaat1115.

[10] S. Seki, M. Garst, J. Waizner, R. Takagi, N. D. Khanh, Y. Okamura, K. Kondou, F. Kagawa, Y. Otani, Y. Tokura, *Nat. Commun.* **2020**, *11*, 256.

[11] M. T. Birch, D. Cortés-Ortuño, L. A. Turnbull, M. N. Wilson, F. Groß, N. Träger, A. Laurenson, N. Bukin, S. H. Moody, M. Weigand, G. Schütz, H. Popescu, R. Fan, P. Steadman, J. A. T. Verezhak, G. Balakrishnan, J. C. Loudon, A. C. Twitchett-Harrison, O. Hovorka, H. Fangohr, F. Y. Ogrin, J. Gräfe, P. D. Hatton, *Nat. Commun.* **2020**, *11*, 1726.

[12] X. Yu, J. Masell, F. S. Yasin, K. Karube, N. Kanazawa, K. Nakajima, T. Nagai, K. Kimoto, W. Koshibae, Y. Taguchi, N. Nagaosa, Y. Tokura, *Nano Lett.* **2020**, *20*, 7313.

[13] E. B. Sonin, *Rev. Mod. Phys.* **1987**, *59*, 87.

[14] P. G. De Gennes, J. Matricon, *Rev. Mod. Phys.* **1964**, *36*, 45.

[15] P. Milde, D. Köhler, J. Seidel, L. M. Eng, A. Bauer, A. Chacon, J. Kindervater, S. Mühlbauer, C. Pfleiderer, S. Buhrandt, C. Schütte, A. Rosch, *Science* **2013**, *340*, 1076.

[16] T. Moriya, *Phys. Rev.* **1960**, *120*, 91.

[17] A. Crépieux, C. Lacroix, *J. Magn. Magn. Mater.* **1998**, *182*, 341.

[18] N. Mathur, M. J. Stolt, S. Jin, *APL Mater.* **2019**, *7*, 120703.

[19] X. Yu, J. P. DeGrave, Y. Hara, T. Hara, S. Jin, Y. Tokura, *Nano Lett.* **2013**, *13*, 3755.

[20] M. J. Stolt, Z.-A. Li, B. Phillips, D. Song, N. Mathur, R. E. Dunin-Borkowski, S. Jin, *Nano Lett.* **2017**, *17*, 508.

[21] N. Mathur, M. J. Stolt, K. Niitsu, X. Yu, D. Shindo, Y. Tokura, S. Jin, *ACS Nano* **2019**, *13*, 7833.

[22] H. Du, R. Che, L. Kong, X. Zhao, C. Jin, C. Wang, J. Yang, W. Ning, R. Li, C. Jin, X. Chen, J. Zang, Y. Zhang, M. Tian, *Nat. Commun.* **2015**, *6*, 8504.

[23] C. Jin, Z.-A. Li, A. Kovács, J. Caron, F. Zheng, F. N. Rybakov, N. S. Kiselev, H. Du, S. Blügel, M. Tian, Y. Zhang, M. Farle, R. E. Dunin-Borkowski, *Nat. Commun.* **2017**, *8*, 15569.

[24] H. Du, J. P. DeGrave, F. Xue, D. Liang, W. Ning, J. Yang, M. Tian, Y. Zhang, S. Jin, *Nano Lett.* **2014**, *14*, 2026.

[25] X. Zhao, C. Jin, C. Wang, H. Du, J. Zang, M. Tian, R. Che, Y. Zhang, *Proc. Natl. Acad. Sci. U.S.A* **2016**, *113*, 4918.

[26] T.-H. Kim, H. Zhao, B. Xu, B. A. Jensen, A. H. King, M. J. Kramer, C. Nan, L. Ke, L. Zhou, *Nano Lett.* **2020**, *20*, 4731.

[27] D. Liang, J. P. DeGrave, M. J. Stolt, Y. Tokura, S. Jin, *Nat. Commun.* **2015**, *6*, 8217.

[28] M. J. Stolt, S. Schneider, N. Mathur, M. J. Shearer, B. Rellinghaus, K. Nielsch, S. Jin, *Adv. Funct. Mater.* **2019**, *29*, 1805418.

[29] H. Du, D. Liang, C. Jin, L. Kong, M. J. Stolt, W. Ning, J. Yang, Y. Xing, J. Wang, R. Che, J. Zang, S. Jin, Y. Zhang, M. Tian, *Nat. Commun.* **2015**, *6*, 7637.

[30] M. Leroux, M. J. Stolt, S. Jin, D. V. Pete, C. Reichhardt, B. Maiorov, *Sci. Rep.* **2018**, *8*, 15510.

[31] J. F. DiTusa, S. B. Zhang, K. Yamaura, Y. Xiong, J. C. Prestigiacomo, B. W. Fulfer, P. W. Adams, M. I. Brickson, D. A. Browne, C. Capan, Z. Fisk, J. Y. Chan, *Phys. Rev. B* **2014**, *90*, 144404.

[32] N. Kanazawa, J. S. White, H. M. Rønnow, C. D. Dewhurst, Y. Fujishiro, A. Tsukazaki, Y. Kozuka, M. Kawasaki, M. Ichikawa, F. Kagawa, Y. Tokura, *Phys. Rev. B* **2016**, *94*, 184432.

[33] M. N. Wilson, E. A. Karhu, A. S. Quigley, U. K. Rößler, A. B. Butenko, A. N. Bogdanov, M. D. Robertson, T. L. Monchesky, *Phys. Rev. B* **2012**, *86*, 144420.

[34] T. Yokouchi, N. Kanazawa, A. Tsukazaki, Y. Kozuka, A. Kikkawa, Y. Taguchi, M. Kawasaki, M. Ichikawa, F. Kagawa, Y. Tokura, *J. Phys. Soc. Japan* **2015**, *84*, 104708.

[35] C. H. Marrows, *Adv. Phys.* **2005**, *54*, 585.

[36] S. X. Huang, C. Fei, K. Jian, Z. Jiadong, G. J. Shu, F. C. Chou, C. L. Chien, *New J. Phys.* **2016**, *18*, 065010.

[37] V. Laliena, J. Campo, *Phys. Rev. B* **2017**, *96*, 134420.

[38] H. Wilhelm, M. Baenitz, M. Schmidt, U. K. Rößler, A. A. Leonov, A. N. Bogdanov, *Phys. Rev. Lett.* **2011**, *107*, 127203.

[39] L. Ludgren, O. Beckman, V. Attia, S. P. Bhattacheriee, M. Richardson, *Phys. Scr.* **1970**, *1*, 69.

[40] M. J. Stolt, X. Sigelko, N. Mathur, S. Jin, *Chem. Mater.* **2018**, *30*, 1146.

[41] H. Oike, A. Kikkawa, N. Kanazawa, Y. Taguchi, M. Kawasaki, Y. Tokura, F. Kagawa, *Nat. Phys.* **2015**, *12*, 62.

[42] M. G. Han, J. A. Garlow, Y. Kharkov, L. Camacho, R. Rov, J. Sauceda, G. Vats, K. Kisslinger, T. Kato, O. Sushkov, Y. Zhu, C. Ulrich, T. Söhnel, J. Seidel, *Sci. Adv.* **2020**, *6*, eaax2138.

[43] A. Bauer, C. Pfleiderer, *Phys. Rev. B* **2012**, *85*, 214418.

[44] J. Wild, T. N. G. Meier, S. Pöllath, M. Kronseder, A. Bauer, A. Chacon, M. Halder, M. Schowalter, A. Rosenauer, J. Zweck, J. Müller, A. Rosch, C. Pfleiderer, C. H. Back, *Sci. Adv.* **2017**, *3*, e1701704.

[45] F. Zheng, F. N. Rybakov, A. B. Borisov, D. Song, S. Wang, Z.-A. Li, H. Du, N. S. Kiselev, J. Caron, A. Kovács, M. Tian, Y. Zhang, S. Blügel, R. E. Dunin-Borkowski, *Nat. Nanotechnol.* **2018**, *13*, 451.

[46] L. Zhao, Y. Cui, W. Li, W. A. Khan, Y. Ma, *Appl. Sci.* **2019**, *9*, 5133.

[47] K. Ishizuka, B. Allman, *J Electron Microsc.* **2005**, *54*, 191.

Chapter 5 : Defect-Mediated Ferromagnetism in Correlated Two-Dimensional Transition Metal Phosphorus Trisulfides*

5.1 Abstract

Controlling the magnetic spin states of two-dimensional (2D) van der Waals (vdW) materials with strong electronic or magnetic correlation is important for spintronic applications but challenging. Crystal defects that are often present in 2D materials such as transition metal phosphorus trisulfides (MPS_3) could influence their physical properties. Here we report the effect of sulfur vacancies on the magnetic exchange interactions and spin ordering of few-layered vdW magnetic $Ni_{1-x}Co_xPS_3$ ($0 \leq x < 0.50$) nanosheets. Magnetic and structural characterization in corroboration with theoretical calculations reveal that sulfur vacancies effectively suppress the strong intralayer antiferromagnetic correlation, giving rise to a weak ferromagnetic ground state in $Ni_{1-x}Co_xPS_3$ nanosheets but not in the single crystal counterparts. Notably, the magnetic field required to tune this ferromagnetic state (< 300 Oe) is much lower than the value needed to tune a typical vdW antiferromagnet (> several thousand Oe). The demonstration of tunable magnetic ordering in vdW materials provides a new route for controlling competing correlated states and magnetic ordering by defect engineering.

5.2 Introduction

Two-dimensional (2D) van der Waals (vdW) materials offer a versatile platform to study novel physical properties and explore their potential applications in electronic, optical, and spintronic devices[1-3]. The realization of magnetism in easily exfoliated 2D vdW crystals provide accessibility to control and manipulate magnetic properties at a single atomic layer level[2, 4-12].

* This chapter is written in collaboration with Wang, F.; Janes, A.N.; Sheng, H.; He P.; Zheng, X.; Yu, P.; DeRuiter, A.J.; Schmidt, J.R.; He, J.; Jin, S.

Among various families of magnetic vdW materials, transition metal phosphorus trichalcogenides (MPX_3, X = S or Se, M cations are generally 3*d* elements: Mn, Fe, Co, Ni, etc.)[10, 13] gained recent attention due to their pressure-induced superconductivity[14], optoelectronic[15-17] and catalytic[18-20] properties. Bulk crystals of MPX_3 have a monoclinic crystal structure (space group of C*2/m*) in which the transition metal cations (M) are surrounded by an octahedral cage of $[P_2X_6]^{4-}$ bipyramids and the neighboring metals have a 2D graphene-like honeycomb lattice arrangement[21, 22]. Resulting from long-range anion-mediated magnetic exchange interactions, MPX_3 compounds exhibit various types of antiferromagnetic (AFM) ordering such as zig-zag, Néel, and stripy-pattern below their respective Néel temperatures (T_N)[22-25].

Among magnetic MPX_3, $NiPS_3$ particularly exhibits intriguing quantum properties due to the presence of strong charge-spin correlation effects[15, 22, 26, 27]. It shows zig-zag antiferromagnetism with weak in-plane anisotropy below $T_N \sim 155$ K, in which ferromagnetically arranged spin chains are antiferromagnetically coupled throughout the crystal lattice down to bilayer stacking. The solution to the XXZ Heisenberg spin model of $NiPS_3$ reveals strong AFM exchange coupling between the third nearest neighboring M, while the nearest and second nearest neighboring M exhibit weak ferromagnetic (FM) exchange interaction and hence supports the existence of zig-zag AFM ground state[15, 26-29]. This long-range AFM interaction is mediated through S atoms located in the same chalcogen sub-layer and is governed by super-superexchange mechanism. In addition, $NiPS_3$ behaves as a negative charge transfer (NCT) insulator and adopts a lower energy self-hole doped ground state where S (3*p* orbital) ligand ends up donating an electron to the attached Ni (3*d* orbital) atom[15, 22]. Low temperature optical conductivity measurements revealed that these intersite transitions are allowed only between AFM Ni neighbors and demonstrated strong correlation between electronic and magnetic structure in $NiPS_3$[22].

Notably, $NiPS_3$ is the only known magnetic vdW material that exhibits NCT ground state with a close resemblance to the hole-doped high temperature cuprates superconductors[27].

The control and manipulation of correlated interactions can lead to new and tunable physical properties in vdW materials. Recently, stacking dependent pressure-induced tunability and electrical control over long-range magnetic exchange interactions have enabled the investigation of novel quantum phenomena and magneto-optoelectronics in magnetic vdW materials[4-9, 30, 31], including $NiPS_3$[27]. On the other hand, the incorporation of atomic defects and chemical substitutions in 2D materials could affect and potentially control the electronic and magnetic interactions by altering the local atomic coordination and make non-magnetic 2D materials, such as graphene and molybdenum disulfide, magnetic[32-35]. It is hoped that the vacancy defects in vdW antiferromagnets could be utilized to potentially control intrinsic AFM ordering to manipulate the spin states of the materials at a much lower applied magnetic field compared to the high field spin flop transitions (40-53 kOe for $MnPS_3$[13] layers and 8-9 kOe for CrI_3[9]), and such modulation of magnetic properties could be appealing for spintronic applications[9, 13].

Here, we target the strongly correlated vdW magnets $Ni_{1-x}Co_xPS_3$ ($0 \leq x < 0.50$) (Figure 5.1a) and demonstrate the tuning of magnetism with sulfur vacancy defects (S_v) in $Ni_{1-x}Co_xPS_3$ nanosheets (NS) synthesized through the chemical vapor conversion method. Magnetic characterization, combined with X-ray absorption spectroscopy and electron spin resonance spectroscopy measurements, reveals that the incorporation of S_v in $Ni_{1-x}Co_xPS_3$ NS result in the emergence of a weak ferromagnetic ground state at low temperatures (<100 K) due to the suppression of AFM correlations at a low applied magnetic field range (< 300 Oe), while no such phenomenon is observed in the $Ni_{1-x}Co_xPS_3$ single crystal counterparts. Theoretical calculations suggest that the presence of S_v disrupts anion-mediated antiferromagnetic interactions,

highlighting the magnetic instability of $NiPS_3$. The experimental findings and theoretical calculations demonstrate the concept of tuning defect-mediated magnetic exchange interactions to manipulate magnetism in magnetic vdW materials.

5.3 Results and Discussion

5.3.1 Synthesis and Structural Characterization of $Ni_{1-x}Co_xPS_3$ Nanosheets and Single Crystals

We synthesized $Ni_{1-x}Co_xPS_3$ ($0 \leq x < 0.50$) NS with the lateral dimension of a few μm which are distributed uniformly on the surface of carbon cloth *via* a two-step process (see Methods, Figure A3.1): i) the metal hydroxide precursor NS with various Ni: Co ratios were first synthesized on carbon cloth; ii) then these metal hydroxide precursor NS were converted to the corresponding $Ni_{1-x}Co_xPS_3$ ($0 \leq x < 0.50$) NS through chemical vapor conversion process. During the second vapor conversion step, the ratio of P: S precursors (mixed elemental powders) was adjusted to a value slightly higher than the stoichiometric ratio (1: 3). Figure 5.1b shows the powder X-ray diffraction (PXRD) patterns obtained from different compositions of as-synthesized $Ni_{1-x}Co_xPS_3$ NS on carbon cloth and compared with the standard patterns of $NiPS_3$ and $CoPS_3$ which show no impurity peaks. The slight shift of the most intense (001) diffraction peak highlighted at $2\theta \sim 14^o$ for $Ni_{1-x}Co_xPS_3$ ($0 < x < 0.5$) suggests alloying of Co into the $NiPS_3$ crystal lattice. Energy dispersive spectroscopy (EDS) results represented in the form of histogram (Figure A3.2) yield the average cobalt substitution (x) in these $Ni_{1-x}Co_xPS_3$ NS samples. Furthermore, the elemental mapping results (Figure 5.1c-d and Figure A3.3) show a homogenous distribution of Ni, Co, P and S throughout the $Ni_{1-x}Co_xPS_3$ NS. High-angle annular dark-field scanning transmission electron microscopy (HAADF-STEM) imaging of individual $NiPS_3$ (Figure A3.4a) and $Ni_{0.68}Co_{0.32}PS_3$ NS (Figure 5.1e) reveals the arrangement of atoms on the (001) basal plane with lattice parameters

close to the theoretical values (a = 0.584 nm and b = 1.014 nm) for $NiPS_3$ (Figure A3.4b). The corresponding selected area electron diffraction (SAED) pattern is indexed to the monoclinic crystal structure along the (001) zone axis (Figure 5.1f), further confirming crystallinity of the $Ni_{0.68}Co_{0.32}PS_3$ NS. Atomic force microscopy determines the thickness of few-layered $Ni_{1-x}Co_xPS_3$ NS in the range of ~ 4-11 nm (Figure 5.1g and Figure A3.5). Raman spectra of $Ni_{1-x}Co_xPS_3$ NS (Figure 5.1g**)** show five in-plane E_g and three out-of-plane A_{1g} phonon modes[36]. The A_{1g} modes at higher frequencies are attributed to the intra-molecular vibrations from $(P_2S_6)^{4-}$ bipyramid structures[26]. More importantly, no other phonon modes were observed in the Raman spectra of $Ni_{1-x}Co_xPS_3$ NS, suggesting the absence of Ni or Co-based chemical impurities.

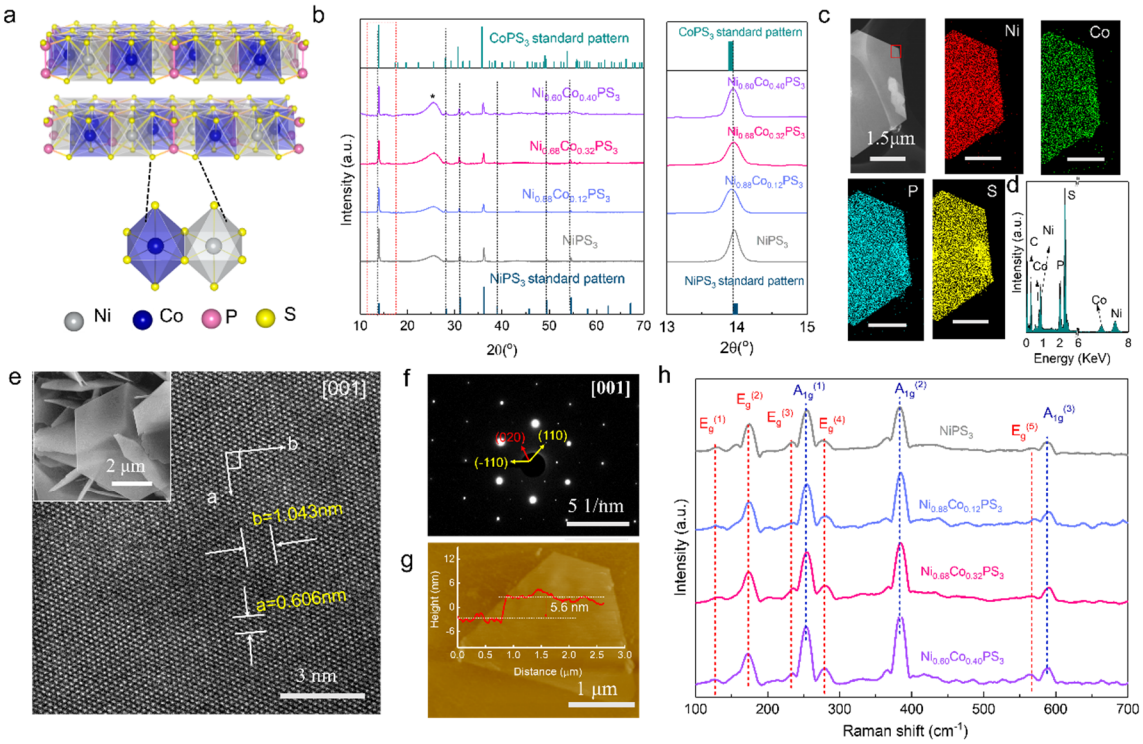

Figure 5.1 : Structural characterization of $Ni_{1-x}Co_xPS3$ ($0 \leq x < 0.5$) NS. a, Crystal structure model of bilayer $Ni_{1-x}Co_xPS_3$ with one pair of neighboring octahedral coordination units (bottom). b, Powder X-ray diffraction patterns of various $Ni_{1-x}Co_xPS3$ NS samples in comparison with the standard monoclinic $NiPS_3$ (PDF# 33-0952) and $CoPS_3$ (PDF #78-0498). The broad peak at 2θ ~ 26° in all PXRD patterns comes from the carbon cloth. **c,** Energy dispersive spectroscopy (EDS) mapping and **d**, the corresponding spectrum of a $Ni_{0.68}Co_{0.32}PS_3$ NS show uniform distribution of

constituent elements. **e,** HAADF-STEM image of a $Ni_{0.68}Co_{0.32}PS_3$ nanosheet collected from the $Ni_{0.68}Co_{0.32}PS_3$ NS sample on carbon cloth shown in the inset SEM image. **f,** SAED pattern of the $Ni_{0.68}Co_{0.32}PS_3$ nanosheet along the [001] zone axis. **g,** Atomic force microscopy image of a $Ni_{0.68}Co_{0.32}PS_3$ NS transferred onto Si/SiO_2 substrate, showing a thickness ~ 5.6 nm. **h**, Raman spectra of various $Ni_{1-x}Co_xPS_3$ ($0 \leq x < 0.5$) NS.

For comparison purposes, we also grew single crystals of $Ni_{1-x}Co_xPS_3$ ($x \approx 0.17, 0.32, 0.50$) with millimeter lateral dimensions (Figure A3.6a-c) using a chemical vapor transport (CVT) method (see Methods for details). Their phase purity was checked using PXRD (Figure A3.6b), which show high intensity peak only for the (00*l*) crystallographic planes - the expected preferential orientation of the $Ni_{1-x}Co_xPS_3$ single crystals. The uniform alloying of constituent elements in $Ni_{1-x}Co_xPS_3$ single crystals is also confirmed through the EDS elemental mapping (Figure A3.6d-e).

5.3.2 Determination of Sulfur Vacancy Defects in $Ni_{1-x}Co_xPS_3$ Samples

To learn more about the local bonding environments, we acquired and analyzed hard X-ray absorption spectra (XAS) for both $Ni_{1-x}Co_xPS_3$ NS and single crystals. Figure 5.2a and Figure A3.7a show the Ni *K*-edge X-ray absorption near edge structure (XANES) spectra for $NiPS_3$, $Ni_{1-x}Co_xPS_3$ NS and single crystals along with their corresponding reference samples. The XANES profiles of these $Ni_{1-x}Co_xPS_3$ NS and single crystals reveal nearly identical Ni valence state of +2, strongly suggesting the same coordination environment around Ni atoms in the crystal and the absence of any Ni-based impurities. The relatively small pre-peaks at ~8331.0 eV further suggest octahedral coordination[37] of Ni with S ligands along with the $1s \rightarrow e_g^*$ (the lowest unoccupied molecular orbital) transition. Similarly, the Co *K*-edge XANES spectra (Figure 5.2b and Figure A3.7b) show a weak pre-edge peak ~7709.0 eV, revealing the same Co oxidation state of +2 and octahedral coordination around Co atoms in $Ni_{0.68}Co_{0.32}PS_3$ NS and single crystals. More importantly, the Co *K*-edge XANES profiles are significantly different from the reference Co-

based compounds such as CoS_2, Co_3O_4, Co foil, which further confirms the chemical purity of as-synthesized $Ni_{0.68}Co_{0.32}PS_3$ NS and single crystals.

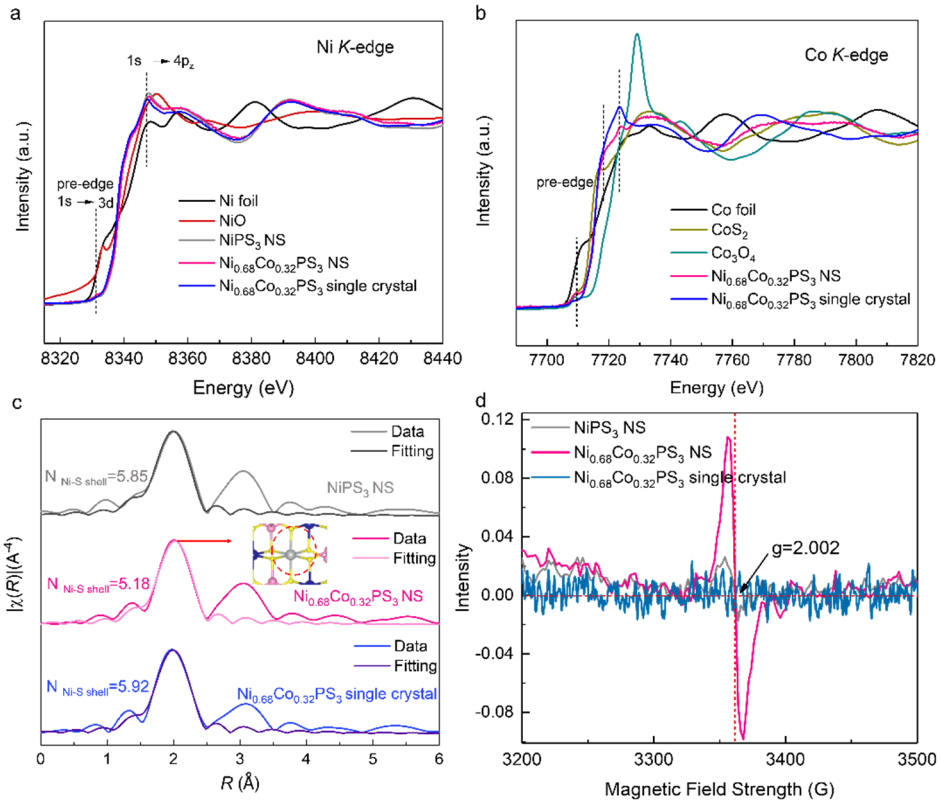

Figure 5.2 : Structural characterization by *X*-ray absorption spectroscopy (XAS) and electron spin resonance (ESR) spectroscopy of various $Ni_{1-x}Co_xPS_3$ samples. a-b, Ni *K*-edge (a) and Co *K*-edge (b) XANES spectra of $Ni_{0.68}Co_{0.32}PS_3$ NS and single crystals together with NiO, Ni foil, and Co foil, pyrite-type CoS_2, Co_3O_4, where pre-edge peak represents 1s → 3d (e_g*) transition. c, First-shell fitting (Ni-S) of Fourier transform of EXAFS spectra for $NiPS_3$ NS, $Ni_{0.68}Co_{0.32}PS_3$ NS and single-crystals. The decreased coordination number around Ni site was obtained in $Ni_{0.68}Co_{0.32}PS_3$ NS. EXAFS spectra were fitted using the FEFF code 6.01 based on the optimized $NiPS_3$ and $Ni_5Co_3P_8S_{24}$ structures (inset shows the nearest coordination of Ni site). d, ESR spectra of $Ni_{0.68}Co_{0.32}PS_3$ NS in comparison with the $NiPS_3$ NS and $Ni_{0.68}Co_{0.32}PS_3$ single crystal, measured at 90 K.

Next, the phase uncorrected extended X-ray absorption fine structure (EXAFS) spectra[38] were collected to understand the chemical coordination environments. The k^3-weighted Fourier transforms of the EXAFS spectra of $NiPS_3$ NS, $Ni_{0.68}Co_{0.32}PS_3$ NS and bulk single crystal samples are well-fitted with the standard monoclinic $NiPS_3$ and $Ni_5Co_3P_8S_{24}$ structures (optimized by

theoretical calculations, see the Methods section for details) and show the identical characteristic features (Figure A3.8a-b). The main peak at approximately 2.01 Å in the k^3-weighted Fourier transform curves at *R* space is attributed to the scattering interaction between the Ni atoms and the first ligand shell (Ni– S), where each Ni atom is coordinated with six *S* atoms shown in the inset of Figure 5.2c. The detailed fitting results of these samples are summarized in Table A3.1. The coordination numbers (CN) of the *S* atom in the first coordination sphere of *Ni* are estimated to be 5.85 and 5.92 in $NiPS_3$ NS and $Ni_{0.68}Co_{0.32}PS_3$ single crystals, respectively. In contrast, a much lower CN of 5.18 is found for $Ni_{0.68}Co_{0.32}PS_3$ NS. This substantial difference from the expected CN of 6 in $Ni_{0.68}Co_{0.32}PS_3$ NS suggests the presence of sulfur vacancy defects (S_v)[19, 39]. Additionally, the increasing Co concentration in $Ni_{1-x}Co_xPS_3$ NS leads to a mild shift to the lower binding energy of Ni^{2+} peak at 855.1 eV of *Ni* 2p3/2 and 162. 9 eV of *S* 2p in X-ray photoelectron spectra (XPS) (Figure A3.9a-b), also suggests the presence of S_v. Furthermore, the very different electron spin resonances (ESR) spectra of the $Ni_{1-x}Co_xPS_3$ NS from the corresponding single crystal counterpart (Figure 5.2d) confirm the presence of S_v in the NS. The *g* value of 2.002 for this observed ESR peak is assigned to the existence of S_v[40, 41]. The ESR signal for $Ni_{0.68}Co_{0.32}PS_3$ NS is substantially higher than that for the pure $NiPS_3$ NS, and no ESR signal observed for the $Ni_{0.68}Co_{0.32}PS_3$ single crystal, which indicates higher concentration of S_v in $Ni_{0.68}Co_{0.32}PS_3$ NS. Moreover, the calculated formation energy (E_v) of single S_v (see Methods for details) shows that, after Co substitution, it is more energetically favorable to incorporate S_v, because E_v is much lower in the case of $Ni_5Co_3P_8S_{24}$ (1.38 eV) than $NiPS_3$ (2.19 eV).

5.3.3 Defect-Mediated Ferromagnetic State in $Ni_{1-x}Co_xPS_3$ Nanosheets.

To study the magnetic properties of as-synthesized $Ni_{1-x}Co_xPS_3$ NS and single crystals, we performed temperature dependent zero-field-cooling (ZFC) and field-cooling (FC) magnetization

measurements using a SQUID magnetometer. The results after subtracting the small diamagnetic background signal from the carbon cloth for these samples are shown in Figure 5.3a (selected samples for the sake of clarity) and Figure A3.10 (full data sets). The ZFC curves reveal a typical AFM behavior for these $Ni_{1-x}Co_xPS_3$ samples with a broad peak ~ 155 K, which corresponds to the T_N [22, 26]. As the x value increases in $Ni_{1-x}Co_xPS_3$, the peak shifts to lower temperature value of T_N for both $Ni_{1-x}Co_xPS_3$ NS and single crystals (inset of Figure 5.3a and Figure A3.11). This is more or less expected with the uniform alloying of Co, because the isostructural and antiferromagnetic $CoPS_3$ has a lower $T_N \sim 120$ K[25]. However, a dramatic increase in the magnetic moment at the low temperatures (< 110 K) is observed in ZFC and FC curves of the $Ni_{1-x}Co_xPS_3$ NS (Fig 3a for $Ni_{0.68}Co_{0.32}PS_3$ and $Ni_{0.60}Co_{0.40}PS_3$ NS, see all NS samples in Figure A3.10 b-c and Figure A3.11). And a slight increase in magnetization of $NiPS_3$ NS at low temperatures (< 25 K) is also shown in Figure 5.3a. In contrast, no such features could be observed in $Ni_{1-x}Co_xPS_3$ single crystal samples even when compared at a similar composition ($x \sim 0.32$). In principle, the chemical alloying of two isostructural compounds ($NiPS_3$ and $CoPS_3$) with the same ground state AFM ordering and minimal difference in lattice parameters should not alter the magnetic arrangements. Here in these $Ni_{1-x}Co_xPS_3$ NS, the AFM ordering is suppressed at the low temperatures, resulting in the emergence of uncompensated magnetic moments below the transition temperature (T^*) ~ 25 K, 61 K, 87 K and 110 K in $NiPS_3$, $Ni_{0.88}Co_{0.12}PS_3$, $Ni_{0.68}Co_{0.32}PS_3$ and $Ni_{0.60}Co_{0.40}PS_3$ NS, respectively. After considering the structural differences between the NS and single crystals of $Ni_{0.68}Co_{0.32}PS_3$, we hypothesize that the presence of S_v in the $Ni_{0.68}Co_{0.32}PS_3$ NS may be responsible for the suppression of long-range AFM correlations while other competing ferromagnetic exchange interactions dominate at low temperatures, creating a magnetically frustrated system. The exchange interactions between the S_v and metal ions, and the local atomic

distortion in the vicinity of defects could also induce robust ferromagnetism, as shown in non-magnetic 2D materials like graphene and molybdenum disulfide[32, 33, 35].

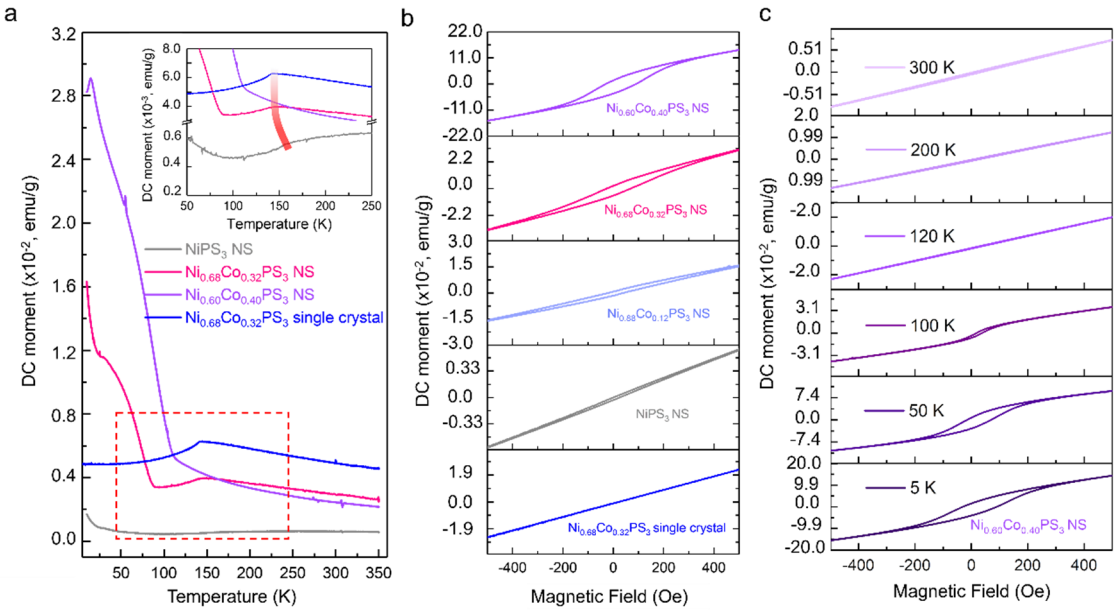

Figure 5.3 : Characterization of magnetic properties of selected NS and single crystals of $Ni_{1-x}Co_xPS_3$. a, Temperature dependence of the ZFC magnetization measured at H= 200 Oe on various $Ni_{1-x}Co_xPS_3$ NS (x = 0, 0.32, 0.40) and the $Ni_{0.68}Co_{0.32}PS_3$ single crystal. **b**, *M-H* curves measured at 5 K of various $Ni_{1-x}Co_xPS_3$ NS (x = 0, 0.12, 0.32, 0.40) in comparison with that of $Ni_{0.68}Co_{0.32}PS_3$ single crystal. **c**, *M-H* curves of the $Ni_{0.60}Co_{0.40}PS_3$ NS at different temperatures. Magnetic hysteresis is clearly observed at low temperatures below 100 K.

Moreover, the field-dependent magnetization (*M-H*) curves of various $Ni_{1-x}Co_xPS_3$ NS (x = 0, 0.12, 0.32, 0.40) at 5 *K* reveal hysteretic feature over a low applied magnetic field range ($|H| < 300$ Oe) and the feature is enhanced as x increases (Figure 5.3b). But there is no hysteretic feature for $Ni_{0.68}Co_{0.32}PS_3$ single crystal in contrast to the NS with the same composition (x = 0.32). The *M-H* curves of various $Ni_{1-x}Co_xPS_3$ NS collected at different temperatures (Figure 5.3c specifically for the $Ni_{0.60}Co_{0.40}PS_3$ NS, and all samples are shown in Figure A3.12) clearly show the well-defined hysteretic feature below their respective T*, further confirming the existence of a weak ferromagnetic ground state arising from uncompensated magnetic moments in AFM system. This soft magnetic behavior (Figure A3.13) is not related to the presence of magnetic impurities such

as the formation of Ni/Co clusters during synthesis, as the measured saturation magnetization of the $Ni_{0.60}Co_{0.40}PS_3$ NS (0.00364 μ_B/formula unit) is around 3 orders of magnitude smaller than expected for Ni/Co metals in a metal cluster (~1-2 μ_B/formula unit). The Co alloying in $NiPS_3$ not only induces the slight shifts in T_N, but also promotes the incorporation of S_v during the synthetic process for $Ni_{1-x}Co_xPS_3$ NS. The contrasting magnetic behaviors observed in $Ni_{1-x}Co_xPS_3$ NS synthesized *via* chemical conversion and single crystals grown by chemical vapor transport, even if they have the same chemical compositions (for example, the $Ni_{0.68}Co_{0.32}PS_3$ highlighted in Figure 5.3a-b), show that the structural difference caused by S_v between these two types of samples is crucial for the weak ferromagnetism observed in the $Ni_{1-x}Co_xPS_3$ NS. Interestingly, the weak ferromagnetic ground state in $Ni_{1-x}Co_xPS_3$ NS emerges at much lower applied magnetic field (< 300 Oe) in comparison to the high field spin flop transitions (> several thousand Oe) in typical 2D vdW antiferromagnets[9, 13]. This suggests that the defect-mediated magnetic ordering in 2D vdW antiferromagnets, such as $Ni_{1-x}Co_xPS_3$, could reduce the applied field requirement for causing the magnetic state transitions in the AFM materials used in spintronic applications.

5.3.4 Governing Mechanism for the Defect-Mediated Magnetism in $Ni_{1-x}Co_xPS_3$ Nanosheets

To understand the underlying mechanism responsible for S_v defect-mediated ferromagnetism in $Ni_{1-x}Co_xPS_3$ ($0 \leq x < 0.5$), it is important to explore the competing electronic and magnetic correlations that could be affected by the presence of S_v. In correlated $NiPS_3$, the half-filled Ni e_g orbitals couples with half-filled *S 3p* orbitals, which mediates the effective electron hopping between neighboring Ni sites[15, 22, 27]. This mechanism is known as the superexchange interaction which is governed by the Goodenough-Kanamori-Anderson rules[42], where the atomic arrangement is the key to effective *Ni-S* orbital overlapping which dictates the strength of the exchange

interaction. The first nearest *Ni* neighbors in NiS_6 octahedra with corner sharing *S* atoms attains ~ 90° Ni-S (*Ni(1)−S(1)−Ni(2)*) orbital overlapping results in a weak FM coupling (J_1), while the second nearest *Ni* neighbors results in weaker FM exchange interaction (J_2) mediated by two S atom (*(Ni(1)−S(1)···S(3)−Ni(3)*) located on different atomic planes and separated by a long distance of ~ 0.4 nm (Figure 5.4a-b) [27]. The magnetic ordering in $NiPS_3$ constitutes of ferromagnetic chains coupled strongly with AFM interaction, forming a zig-zag pattern with alternating chains of anti-aligned Ni atoms (Figure 5.4c) as a consequence of strong third nearest-neighbors (TNN) exchange interaction (J_3 >> J_1, J_2) mediated by two *S* atom located on the same chalcogen sub-layer (*(Ni(1)−S(1)···S(2)−Ni(4)*) (Figure 5.4b). This suggests that the presence of S_v could change the lattice configurations locally and disrupt the long-range effective hopping between two antiferromagnetically aligned TNN, inducing spin fluctuations in the system.

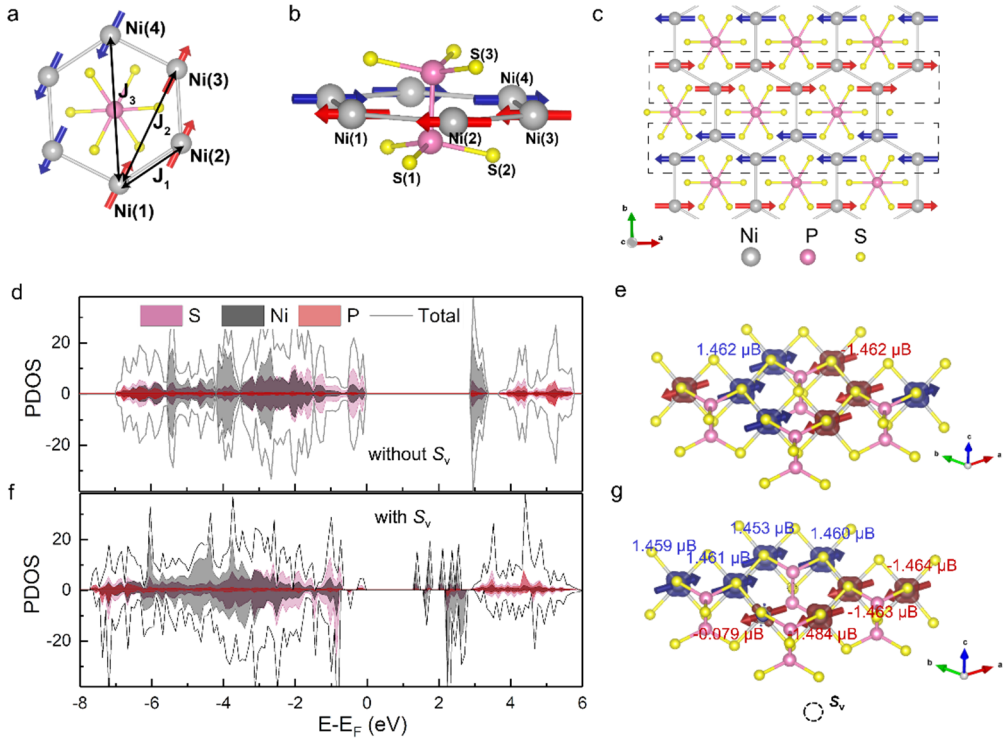

Figure 5.4 : Theoretical calculations of the electronic structures and spin configurations in $NiPS_3$ with and without *S* vacancy (S_v). a-b, The illustrations of the exchange interactions in a hexagonally arranged lattice of Ni neighbors in

$NiPS_3$ mediated *via* S atoms. **c,** Top view of a $NiPS_3$ monolayer with alternating ferromagnetic chains marked with dashed black boxes, coupled antiferromagnetically throughout the crystal lattice. **d, f,** Spin-polarized projected density of state (PDOS) and (**e, g**) the corresponding illustrations of the magnetic moment distribution of antiferromagnetic $NiPS_3$ without S vacancy (**d,e**) and $NiPS_3$ with S vacancy (**f, g**). Fermi energy is set to zero.

After identifying the influence of S_v on the magnetic ordering in $NiPS_3$, we investigate the possible effect on the spin charge density and magnetic structures in the vicinity of S_v using Density Functional Theoretical (DFT) calculations (see Methods for details) on the $NiPS_3$ model system, just to simplify the calculation process. In charge transfer insulator such as $NiPS_3$, the magnetic and electronic properties of the system are dependent on the ease of electron transfer between the anion and cation[22]. In this regard, $NiPS_3$ acquires a "ligand hole-doped" correlated state where the *S* ligand transfer one electron to the half-filled e_g Ni 3*d* orbital and forms a d^9L ground state (*L* represents ligand hole) owing to the low charge-transfer energy[15, 22]. The calculated electronic structure of monolayer $NiPS_3$ also supports this representation of insulating NCT ground state where the projected density of states (PDOS) of occupied S *p*-orbital bands are located closer to the Fermi energy (E_F) than the Ni 3*d* orbital bands (Figure 5.4d). The corresponding spin charge density spectrum of zig-zag AFM $NiPS_3$ with easy in-plane anisotropy shows a reduced magnetic moment (1.462 μB) of individual Ni^{2+} cation (expected value ~ 2.83 μB) due to possible mixed valance state configurations (d^8, d^9L, $d^{10}L^2$) of the NCT state (Figure 5.4e). This NCT state in $NiPS_3$ is expected to dominate between antiferromagnetically aligned neighboring Ni atoms, which is also demonstrated in previous studies *via* optical conductivity measurements[22]. A single S_v created in the $NiPS_3$ supercell within the chalcogen sub-layer disrupts the superexchange interaction between Ni neighbors, and the energetically relaxed structure shows dramatic changes in the characteristically electronic and magnetic properties. The presence of a single S_v shifts the occupied *S* bands away from the E_F, reducing the NCT character (Figure 5.4f). Furthermore, we observe the emergence of unoccupied in-gap like states in the electronic structure which might

arise from local 5-corrdinated environment around *Ni* atoms. These in-gap states could serve as a carrier trap sites[43-45] and hinder the charge transfer process which could further impact the magnetic properties of $NiPS_3$. The charge density distribution of *Ni* orbitals are more affected in the vicinity of S_v site and the equilibrium spin configuration transforms to uncompensated magnetic state with a net magnetic moment of ~ 0.17 μB per formula unit (Figure 5.4g), highlighting the magnetic instability of the AFM arrangement in $NiPS_3$[46]. The incorporation of S_v also increases the concentration of *n*-type carriers in the self-hole doped $NiPS_3$, which was predicted to suppress the long range AFM correlation and might enable other competing correlated states to emerge[27, 47]. This encourages future studies into rich magneto-optical physics of $NiPS_3$ in the presence of point defects as these properties couple strongly with intrinsic magnetic ordering of the crystal[17].

5.4 Conclusion

We demonstrate the effective tuning of magnetic exchange interactions and magnetic ordering in chemically converted nanosheets of vdW magnets $Ni_{1-x}Co_xPS_3$ ($0 \leq x < 0.50$) due to sulfur vacancy defects. X-ray spectroscopy and electron spin resonance spectroscopy confirms the presence of sulfur vacancy defects in $Ni_{1-x}Co_xPS_3$ NS, in contrast to single crystals of the same $Ni_{1-x}Co_xPS_3$ compositions. Magnetic characterization of *S*-deficient $Ni_{1-x}Co_xPS_3$ NS clearly show a weak ferromagnetic ground state at low temperatures (<100 K). Theoretical calculations show that the presence of S_v disrupts the anion-mediated superexchange interaction, i.e., two antiferromagnetically aligned third nearest-neighbors, resulting in effective suppression of the long-range AFM correlation in $NiPS_3$ system. Defect-mediated ferromagnetism emerges at an applied magnetic field (< 300 Oe) that is much smaller than the high field spin flop transition in MPX_3. This result suggests that defect engineering could reduce the high applied field requirement

to tune the magnetic order and make 2D vdW antiferromagnets more attractive for spintronic applications. These findings shed new insights on the magnetic instability in correlated vdW magnetic systems, which could provide new and effective routes to control and manipulate the magnetic spin states of 2D vdW magnets by defect engineering.

5.5 Experimental Methods

5.5.1 Synthesis of $Ni_{1-x}Co_xPS_3$ ($0 \leq x < 0.5$) Nanosheets

The $Ni_{1-x}Co_xPS_3$ NS were synthesized in two steps: i) the metal hydroxide precursor nanosheets containing different Ni: Co ratios were first synthesized on carbon cloth through wet chemical method (see Appendix 3), and then ii) converted in a vapor phase process to make $Ni_{1-x}Co_xPS_3$ ($0 \leq x < 0.5$) NS. A mixed powder (1 g) of phosphorus (red phosphorus, 98.5%, Alfa Aesar) and sulfur (99.5%, Alfa Aesar) with the molar ratio of 2: 5 was placed into the bottom of a custom designed quartz socket tube and the corresponding metal hydroxide precursors were positioned on the other side of the quartz tube.[19] Then, the quartz tube was placed inside a two-zone furnace with P and S powder in the upstream (front zone) and the hydroxide precursor in the downstream (back zone), and evacuated. The two zones were simultaneously heated to 270 ºC (upstream, 9 ºC/min) and 480- 490 ºC (downstream, 16 ºC/min) over 30 min under a flow of 100 sccm Ar gas (99.999%). The ultrathin $Ni_{1-x}Co_xPS_3$ NS evenly covering the surface of the carbon cloth were synthesized over a period of 90 min at 480- 490 ºC. The mass loading of the nanosheets was ~1-3 mg/cm^2.

5.5.2 Growth of $Ni_{1-x}Co_xPS_3$ ($0 < x < 0.5$) Single Crystals

Single crystals of $Ni_{1-x}Co_xPS_3$ were grown using a chemical vapor transport (CVT) method from 1 g mixture of elemental powder precursors of Ni (< 50 μm particle size, 99.7%, Sigma-Aldrich), Co (2 μm particle size, 99.8%, Sigma-Aldrich), P (red phosphorus, 98.5%, Alfa Aesar), and S

(99.98%, Sigma-Aldrich) in stoichiometric ratio plus some excess S powder (~ 50 mg). These powders were transferred to a silica tube with an inner diameter of 6 mm and a length of ~15 cm together with ~ 20 mg of iodine flakes (99.8%, Sigma-Aldrich) as the transport agent. The silica tube was then sealed under a vacuum of < 50 mTorr. For crystal growth, the sealed tube was heated in a 2-zone tube furnace with the source zone set at 625 °C and growth zone at 550 °C for approximately 3 weeks. The $Ni_{1-x}Co_xPS_3$ single crystals appearing as black colored flakes with the lateral size of ~0.1-0.5 cm were found in the center and growth zone of the tube (Figure A3.6a).

5.5.3 Structural characterization

The as-synthesized $Ni_{1-x}Co_xPS_3$ ($0 \leq x < 0.5$) NS and single crystals were characterized with scanning electron microscopy (SEM, Hitachi-SU8220), transmission electron microscopy (TEM, JEM-2100F, 200 kV), energy dispersive spectroscopy (EDS) and powder X-ray diffraction (Bruker D8 Advance X-ray diffractometer equipped with Cu-Ka radiation). High-angle annular dark-field scanning TEM (HAADF-STEM) was conducted on JEM ARM200F with an acceleration voltage of 300 kV. Raman spectroscopy was performed on a confocal Raman microscopy spectrometer (Renishaw Invia) with an excitation laser wavelength of 785 nm. X-ray photoelectron spectroscopy (XPS) data were obtained using an ESCALab250 electron spectrometer from Thermo Fisher Scientific Corporation with a monochromatic 150 W Al K_α radiation and a pass energy for the narrow scan of 30 eV. The binding energies were referenced to the C1*s* line at 284.8 eV from carbon. The thickness of the various nanosheets was measured with an atomic force microscope (Bruker FastScan). Electron spin resonance (ESR) spectroscopy was conducted on a Bruker E500 spectrometer by sweeping the field between 0 and 6000 G at a microwave frequency of 9.420 GHz.

5.5.4 X-ray absorption spectroscopy

Ni and Co K-edge X-ray absorption near edge (XANES) and extended X-ray absorption fine structure (EXAFS) spectra of various $Ni_{1-x}Co_xPS_3$ ($0 \leq x < 0.5$) NS samples on carbon cloth and single crystals were collected using Beamline 10.3.2 at the Advanced Light Source (Berkeley, USA) Beamline 10-BM-B and Beamline 10-ID at the Advanced Photon Source at Argonne National Laboratory (Lemont, USA), respectively. The X-ray wavelength was monochromatized by a Si (111) double-crystal fixed exit monochromator. The intensity of the incident X-ray radiation, I_0, was monitored with a nitrogen filled ionization chamber. All data were collected in fluorescence mode at room temperature with a 7-element Ge detector (Canberra). The spectra were aligned according to a glitch in I_0 near the absorption edge. The XAS spectra were analyzed using ATHENA and ARTEMIS software.[48]

5.5.5 Magnetic measurements

Temperature dependent DC magnetometry measurements of the various $Ni_{1-x}Co_xPS_3$ ($0 \leq x < 0.5$) NS on carbon cloth and single crystals were carried out on a superconducting quantum interference device magnetometer (SQUID, Quantum Design MPMS3) with the zero-field-cooling (ZFC) and field-cooling (FC) modes with a slow cooling rate of 2 *K*/ min. The carbon cloth with NS were cut into pieces and sealed in a gel capsule, which was fixed in a plastic straw for measurement. As a comparison, pure carbon cloth with the same mass was also measured under the same condition. Field dependent magnetization measurement of these samples were performed with an applied magnetic field range of -700 Oe to 700 Oe at the field sweep rate of 14 Oe/s. The hysteresis features shown in *M-H* curves for $Ni_{1-x}Co_xPS_3$ NS is apparent even without subtracting the paramagnetic component of the corresponding magnetization. The magnetization data were collected and compared at different temperatures (5 K - 300 K). Magnetization measurements of individual Ni_{1-}

$_xCo_xPS_3$ ($0< x< 0.5$) single crystals with a size of ~ 0.1-0.2 cm were conducted with the applied magnetic field parallel to the easy plane of magnetization (*ab* plane) for the crystal.

5.5.6 Theoretical calculations

Collinear spin polarized electronic structure calculations were performed using the periodic density function code Vienna ab initio Simulation Package (VASP)[49-52] and interfaced with the Python Environment Atomic Simulation Environment (ASE)[53]. Projector Augmented Wave (PAW) pseudopotentials with a cutoff of 500 eV[54] were used to treat core electrons. Geometry optimizations were carried out using the Perdew-Burke-Ernzehof (PBE) functional[55, 56] to treat correlation and exchange. Single point calculations were then evaluated using the range-separated HSE06 functional and the PBE geometries[57, 58]. The use of HSE06 allows for the accurate description of insulator band gaps compared to PBE which systematically underestimates insulator band gaps. Dispersion was treated using the Tkatchenko-Scheffler method (DFT-TS/HI) with iterative Hirshfeld partitioning[59]. A (2×2) rhombic cell was adopted for $Ni_8P_8S_{24}$ and $Ni_5Co_3P_8S_{24}$ slab with the vacuum spacing set at least 15 Å. The Brillouin zone was sampled with a 8×8×1 Monkhorst Pack Gamma-centered mesh[60]. For geometry optimization, atoms were allowed to relax until forces on them were less than 0.005 eV/Å. The Co substituted cases in the supercell should be screened and confirmed. In general, there are eight Ni sites can be replaced by three Co atoms, which provides $C_8^3 = 56$ substitution cases. Under the constraint of periodic boundary conditions, we screened out three different substitution cases shown in Figure A3.14. We named them as chain substitution case (CS), triangle substitution case (TS) and right-angle substitution (RS) case. After comparing the total energy of the different substitution cases (Table A3.2) , the CS is the stable doping case of $Ni_5Co_3P_8S_{24}$ in ground state. Thus, the lowest energy chain (CS) $Ni_5Co_3P_8S_{24}$ was used for all doped calculations. For sulfur vacancies, calculations were performed

on all possible sulfur vacancies (along with all three initial spin states) and the lowest energy sulfur vacancy systems (geometry and final spin state) are the ones reported. We calculate the vacancy formation energy (E_v) according to the equation (1).

$$E_v = E_d + n\mu_s - E_p \quad (1)$$

where E_p and E_d are the energy of the supercell with and without vacancies, respectively. μ_s and n represent the chemical potential and number of sulfur atoms removed from the surface. The chemical potential of sulfur is calculated from its elemental phase S_8[61].

The results from this chapter have been submitted in a peer reviewed journal. Reference as follows:

Mathur, N.; Wang, F.; Janes, A.N.; Sheng, H.; He P.; Zheng, X.; Yu, P.; DeRuiter, A.J.; Schmidt, J.R.; He, J.; Jin S.; Defect-Mediated Ferromagnetism in Correlated Two-Dimensional Transition Metal Phosphorus Trisulfides. **2020** (Submitted)

Appendix 3 in this thesis contains supporting information and additional figures of this chapter

References

1. Chhowalla, M., Jena, D. & Zhang, H. Two-dimensional semiconductors for transistors. *Nat. Rev. Mater.* **1**, 16052 (2016).
2. Burch, K.S., Mandrus, D. & Park, J.-G. Magnetism in two-dimensional van der Waals materials. *Nature* **563**, 47-52 (2018).
3. Han, W., Kawakami, R.K., Gmitra, M. & Fabian, J. Graphene spintronics. *Nat. Nanotechnol.* **9**, 794-807 (2014).
4. Gong, C. et al. Discovery of intrinsic ferromagnetism in two-dimensional van der Waals crystals. *Nature* **546**, 265-269 (2017).
5. Huang, B. et al. Layer-dependent ferromagnetism in a van der Waals crystal down to the monolayer limit. *Nature* **546**, 270-273 (2017).

6. Deng, Y. et al. Gate-tunable room-temperature ferromagnetism in two-dimensional Fe_3GeTe_2. *Nature* **563**, 94-99 (2018).
7. Jiang, S., Shan, J. & Mak, K.F. Electric-field switching of two-dimensional van der Waals magnets. *Nat. Mater.* **17**, 406-410 (2018).
8. Fei, Z. et al. Two-dimensional itinerant ferromagnetism in atomically thin Fe_3GeTe_2. *Nat. Mater.* **17**, 778-782 (2018).
9. Huang, B. et al. Electrical control of 2D magnetism in bilayer CrI_3. *Nat. Nanotech.* **13**, 544-548 (2018).
10. Wang, F. et al. New Frontiers on van der Waals Layered Metal Phosphorous Trichalcogenides. *Adv. Funct. Mater.* **28**, 1802151 (2018).
11. Meng, L. et al. Anomalous thickness dependence of Curie temperature in air-stable two-dimensional ferromagnetic 1T-$CrTe_2$ grown by chemical vapor deposition. *Nat. Commun.* **12**, 809 (2021).
12. Li, B. et al. Van der Waals epitaxial growth of air-stable $CrSe_2$ nanosheets with thickness-tunable magnetic order. *Nat. Mater.*, https://doi.org/10.1038/s41563-021-00927-2 (2021).
13. Long, G. et al. Persistence of Magnetism in Atomically Thin $MnPS_3$ Crystals. *Nano Lett.* **20**, 2452-2459 (2020).
14. Wang, Y. et al. Emergent superconductivity in an iron-based honeycomb lattice initiated by pressure-driven spin-crossover. *Nat. Commun.* **9**, 1914 (2018).
15. Kang, S. et al. Coherent many-body exciton in van der Waals antiferromagnet $NiPS_3$. *Nature* **583**, 785-789 (2020).
16. Jenjeti, R.N., Kumar, R., Austeria, M.P. & Sampath, S. Field Effect Transistor Based on Layered $NiPS_3$. *Sci. Rep.* **8**, 8586 (2018).
17. Hwangbo, K. et al. Highly anisotropic excitons and multiple phonon bound states in a van der Waals antiferromagnetic insulator. *Nat. Nanotech.* https://doi.org/10.1038/s41565-021-00873-9 (2021).
18. Xue, S., Chen, L., Liu, Z., Cheng, H.-M. & Ren, W. $NiPS_3$ Nanosheet–Graphene Composites as Highly Efficient Electrocatalysts for Oxygen Evolution Reaction. *ACS Nano* **12**, 5297-5305 (2018).
19. Wang, F. et al. Two-dimensional metal phosphorus trisulfide nanosheet with solar hydrogen-evolving activity. *Nano Energy* **40**, 673-680 (2017).
20. Song, B. et al. Tuning Mixed Nickel Iron Phosphosulfide Nanosheet Electrocatalysts for Enhanced Hydrogen and Oxygen Evolution. *ACS Catal.* **7**, 8549-8557 (2017).
21. Brec, R. Review on structural and chemical properties of transition metal phosphorous trisulfides MPS_3. *Solid State Ion.* **22**, 3-30 (1986).
22. Kim, S.Y. et al. Charge-Spin Correlation in van der Waals Antiferromagnet $NiPS_3$. *Phys. Rev. Lett.* **120**, 136402 (2018).

23. Lee, J.-U. et al. Ising-Type Magnetic Ordering in Atomically Thin $FePS_3$. *Nano Lett.* **16**, 7433-7438 (2016).
24. Sun, Y.-J., Tan, Q.-H., Liu, X.L., Gao, Y.-F. & Zhang, J. Probing the Magnetic Ordering of Antiferromagnetic $MnPS_3$ by Raman Spectroscopy. *J. Phys. Chem. Lett.* **10**, 3087-3093 (2019).
25. Wildes, A.R., Simonet, V., Ressouche, E., Ballou, R. & McIntyre, G.J. The magnetic properties and structure of the quasi-two-dimensional antiferromagnet $CoPS_3$. *J. Phys. Condens. Matter* **29**, 455801 (2017).
26. Kim, K. et al. Suppression of magnetic ordering in XXZ-type antiferromagnetic monolayer $NiPS_3$. *Nat. Commun.* **10**, 345 (2019).
27. Gu, Y. et al. Ni-based transition metal trichalcogenide monolayer: A strongly correlated quadruple-layer graphene. *Phys. Rev. B* **100**, 165405 (2019).
28. Chandrasekharan, N. & Vasudevan, S. Magnetism and exchange in the layered antiferromagnet $NiPS_3$. *J. Phys. Condens. Matter* **6**, 4569-4579 (1994).
29. Wildes, A.R. et al. Magnetic structure of the quasi-two-dimensional antiferromagnet $NiPS_3$. *Phys. Rev. B* **92**, 224408 (2015).
30. Li, T. et al. Pressure-controlled interlayer magnetism in atomically thin CrI_3. *Nat. Mater.* **18**, 1303-1308 (2019).
31. Song, T. et al. Switching 2D magnetic states via pressure tuning of layer stacking. *Nat. Mater.* **18**, 1298-1302 (2019).
32. Cai, L. et al. Vacancy-Induced Ferromagnetism of MoS_2 Nanosheets. *J. Am. Chem. Soc.* **137**, 2622-2627 (2015).
33. Lin, Z. et al. Defect engineering of two-dimensional transition metal dichalcogenides. *2D Mater.* **3**, 022002 (2016).
34. Yazyev, O.V. & Helm, L. Defect-induced magnetism in graphene. *Phys. Rev. B* **75**, 125408 (2007).
35. Guguchia, Z. et al. Magnetism in semiconducting molybdenum dichalcogenides. *Sci. Adv.* **4**, eaat3672 (2018).
36. Kuo, C.-T. et al. Exfoliation and Raman Spectroscopic Fingerprint of Few-Layer $NiPS_3$ Van der Waals Crystals. *Sci. Rep.* **6**, 20904 (2016).
37. Ceglia, A. et al. A XANES study of chromophores: the case of black glass. *Anal. Methods* **6**, 2662-2671 (2014).
38. Ravel, B. & Kelly, S.D. The Difficult Chore of Measuring Coordination by EXAFS. *AIP Conference Proceedings* **882**, 150-152 (2007).

39. Kuzmin, A. & Chaboy, J. EXAFS and XANES analysis of oxides at the nanoscale. *IUCrJ* **1**, 571-589 (2014).
40. Wang, X. et al. Single-Atom Vacancy Defect to Trigger High-Efficiency Hydrogen Evolution of MoS_2. *J. Am. Chem. Soc.* **142**, 4298-4308 (2020).
41. Deroide, B., Bensimon, Y., Belougne, P. & Zanchetta, J.V. Lineshapes of ESR signals and the nature of paramagnetic species in amorphous molybdenum sulfides. *J. Phys. Chem. Solids* **52**, 853-857 (1991).
42. Anderson, P.W. eds. F. Seitz & D. Turnbull *Solid State Physics*, **14** 99-214 (1963).
43. Jiang, J., Xu, T., Lu, J., Sun, L. & Ni, Z. Defect Engineering in 2D Materials: Precise Manipulation and Improved Functionalities. *Research* **2019**, 4641739 (2019).
44. Chen, K. et al. Carrier Trapping by Oxygen Impurities in Molybdenum Diselenide. *ACS Appl. Mater. Interfaces* **10**, 1125-1131 (2018).
45. Li, L., Long, R., Bertolini, T. & Prezhdo, O.V. Sulfur Adatom and Vacancy Accelerate Charge Recombination in MoS_2 but by Different Mechanisms: Time-Domain Ab Initio Analysis. *Nano Lett.* **17**, 7962-7967 (2017).
46. Lançon, D., Ewings, R.A., Guidi, T., Formisano, F. & Wildes, A.R. Magnetic exchange parameters and anisotropy of the quasi-two-dimensional antiferromagnet $NiPS_3$. *Phys. Rev. B* **98**, 134414 (2018).
47. Li, Y. et al. Topological superconductivity in Ni-based transition metal trichalcogenides. *Phys. Rev. B* **100**, 214513 (2019).
48. Ravel, B. & Newville, M. ATHENA, ARTEMIS, HEPHAESTUS: data analysis for X-ray absorption spectroscopy using IFEFFIT. *J. Synchrotron Radiat.* **12**, 537-541 (2005).
49. Kresse, G. & Furthmüller, J. Efficient iterative schemes for ab initio total-energy calculations using a plane-wave basis set. *Phys. Rev. B* **54**, 11169-11186 (1996).
50. Kresse, G. & Furthmüller, J. Efficiency of ab-initio total energy calculations for metals and semiconductors using a plane-wave basis set. *Comput. Mater. Sci.* **6**, 15-50 (1996).
51. Kresse, G. & Hafner, J. Ab initio molecular dynamics for liquid metals. *Phys. Rev. B* **47**, 558-561 (1993).
52. Kresse, G. & Hafner, J. Ab initio molecular-dynamics simulation of the liquid-metal--amorphous-semiconductor transition in germanium. *Phys. Rev. B* **49**, 14251-14269 (1994).
53. Hjorth Larsen, A. et al. The atomic simulation environment—a Python library for working with atoms. *J. Phys. Condens. Matter* **29**, 273002 (2017).
54. Blöchl, P.E. Projector augmented-wave method. *Phys. Rev. B* **50**, 17953-17979 (1994).

55. Perdew, J.P., Burke, K. & Wang, Y. Generalized gradient approximation for the exchange-correlation hole of a many-electron system. *Phys. Rev. B* **54**, 16533-16539 (1996).
56. Perdew, J.P., Burke, K. & Ernzerhof, M. Generalized Gradient Approximation Made Simple. *Phys. Rev. Lett.* **77**, 3865-3868 (1996).
57. Heyd, J. & Scuseria, G.E. Assessment and validation of a screened Coulomb hybrid density functional. *J. Chem. Phys.* **120**, 7274-7280 (2004).
58. Krukau, A.V., Vydrov, O.A., Izmaylov, A.F. & Scuseria, G.E. Influence of the exchange screening parameter on the performance of screened hybrid functionals. *J. Chem. Phys.* **125**, 224106 (2006).
59. Bučko, T., Lebègue, S., Hafner, J. & Ángyán, J.G. Improved Density Dependent Correction for the Description of London Dispersion Forces. *J. Chem. Theory Comput.* **9**, 4293-4299 (2013).
60. Monkhorst, H.J. & Pack, J.D. Special points for Brillouin-zone integrations. *Phys. Rev. B* **13**, 5188-5192 (1976).
61. Hu, J., Zhang, Y., Law, M. & Wu, R. First-principles studies of the electronic properties of native and substitutional anionic defects in bulk iron pyrite. *Phys. Rev. B* **85**, 085203 (2012).

Chapter 6 : Growth and Characterization of Two-Dimensional Van Der Waals Magnets with Topological Defects

6.1 Abstract

Manipulation and control of magnetic spin states in two-dimensional (2D) van der Walls (vdW) magnets are key requirements for their future spintronics applications. Topological defects such as screw dislocation influences the physical properties of broad classes of materials. However, there has no report on synthesis that enables the incorporation and growth of screw dislocated nanostructures in 2D vdW magnets. Here we demonstrate a facile physical vapor deposition synthesis of screw dislocation driven synthesis of vdW antiferromagnetic nickel dihalides (NiX_2). Atomic force microscopy characterization reveals monolayer triangular spirals and complex hexagonal spirals in $NiBr_2$ and NiI_2 nanoplates, respectively. Our study presents a novel material platform to investigate dislocation-spin interactions and defect-mediated magnetic tunability of spin textures that are governed by the principles of topology.

6.2 Introduction

The recent discovery of two-dimensional (2D) van der Walls (vdW) magnetic materials enables the possibility of stable long-range magnetic spin ordering down to a single atomic layer of atoms and breaks new grounds with layer-dependent magnetism.[1, 2] The manipulation of intrinsic magnetic ordering and stability of novel spin textures in 2D vdW magnets has been shown in vertically stacked heterostructures fabricated by mechanical exfoliation process.[3-5] However, the overall yield of heterostructures fabricated *via* the mechanical exfoliation process is quite low. In addition, this process might bring extrinsic defects such as remaining polymer residue between the layers or wrinkled/broken layers during the transfer step of stacked layers and the intrinsic point defects could persist in 2D vdW layers and influence key properties of fabricated

heterostructures. [6, 7] These shortcomings warrant further exploration of novel methods of materials synthesis to manipulate spin ordering in 2D vdW magnets.

Topological defects are unique irregularities in crystalline atomic arrangement that are distinguishable from other lattice imperfections as these are characterized by topological invariant known as the Burgers vector.[8] The presence of topological linear defects known as dislocations are crucial in understanding the mechanical behavior and plasticity of materials.[9] Additionally, the introduction of topological defects has shown to strongly influence the electronic,[10, 11] optical,[12-14] and catalytic properties[15, 16] in layered materials and 2D vdW systems. The structural-property relationship in the presence of topological defects is extensively studied in graphene, [17, 18] transition metal dichalcogenides (TMDs) [12, 13, 19] and topological insulators,[20] however, there has been no report on introduction of topological defect in magnetic 2D vdW materials.

The fascinating aspect of dislocations in materials comes from the fact that they can act as active nucleation sites which govern the growth mechanism of nanostructures.[15, 21] Particularly, screw dislocation driven (SDD) growth of 2D materials allow them to grow in spiral topology at a low supersaturation of growth precursors.[15, 22] SDD growth of 2D magnetic layers with strong interlayer coupling can connect multiple layers in a continuous spiral which could affect the spin ordering in the vicinity of the dislocation core.[23, 24] Therefore, these novel material platforms could allow the study into dislocation – spin interactions that are governed by the principles of topology. Here, we demonstrate for the first time SDD growth of 2D vdW layered antiferromagnetic materials, nickel dihalides (NiI_2 and $NiBr_2$). We have successfully able to grow monolayer spiral of$NiBr_2$ and complex multilayer spiral of NiI_2. We hope that the facile growth

process presented in our study could be extended to a broad class of 2D magnets and promote future investigation of magnetic spin coupling with topological singularities in crystals.

6.3 Results and Discussion

6.3.1 NiX_2: a layered antiferromagnet

Nickel dihalides adopt a rhombohedral $CdCl_2$-type crystal structure (space group: R-3m) where

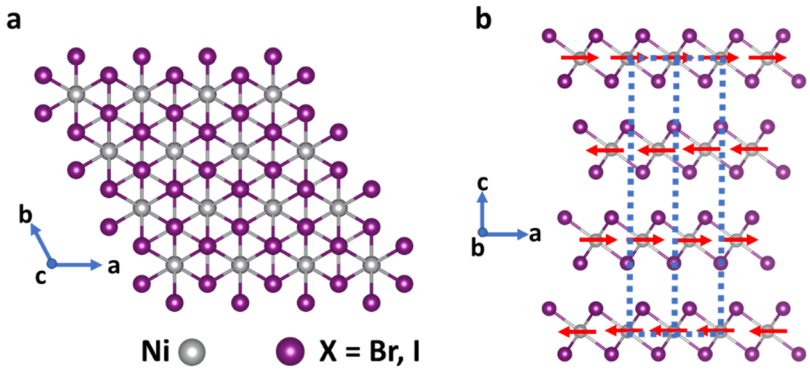

Figure 6.1 : Crystal structure of NiX_2 (a) Crystal model of NiX_2 oriented normal to c-axis. (b) Spin arrangement of layered antiferromagnetic NiX_2 with trigonal unit cell drawn by blue dashed line.

the unit cell consists of three layers of ABC stacking and X anion forms a cubic closed packed arrangement.[25] Figure 6.1a shows a structure of layered NiX_2 crystal that contains triangular nets of Ni atoms octahedrally coordinated with anions (X) and each layer is separated by vdW gaps between X anions. The monolayer of NiX_2 forms a centrosymmetric 1T phase of the trigonal unit cell. Atomically thin NiX_2 is a layered antiferromagnet with in-plane magnetic anisotropy below their respective Néel temperature, T_N (T_N ($NiBr_2$) ~ 52 K[26] and T_N (NiI_2) ~ 75 K[27]), where individual ferromagnetic layers coupled antiferromagnetically with neighboring layers in the stacked arrangement (Figure 6.1b). Additionally, $NiBr_2$ system also show non-collinear spin ordering below T<23 K, resulting from frustrated intralayer magnetic interactions. [25, 26] It could

be an interesting scenario to study the effect of dislocations on both interlayer and intralayer magnetic coupling in NiX_2 layered antiferromagnetic system.

6.3.2 Screw dislocation driven growth of NiX_2

Screw dislocation driven (SDD) growth nanoplates (NPL) of $NiBr_2$ and NiI_2 were synthesized using a facile physical vapor deposition (PVD) technique in a home-built single zone tube furnace. Previous study reported a successful PVD growth of NiI_2 thin NPL down to a monolayer thickness on variety of growth substrates,[28] but growth of spiral NiX_2 NPL has not been reported yet. A

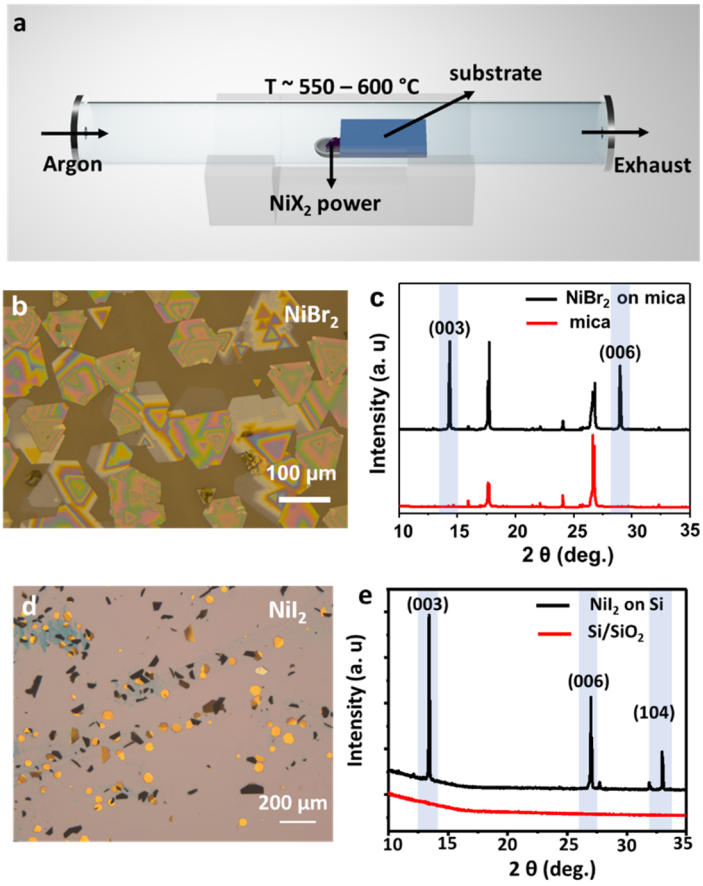

Figure 6.2 : Controllable growth of spiral NiX_2 (a) Schematic of the physical vapor deposition set up for NiX_2 NPL synthesis. (b) Overview optical microscopy image of $NiBr_2$ nanoplates growing flat all over the freshly cleaved mica substrate. (c) Powder X-ray diffraction pattern of $NiBr_2$ (PDF# 03-0580) nanoplates on mica substrate with only high intensity (00*l*) peaks. (d) Overview optical microscopy image of NiI_2 nanoplates growing vertically and flat over the Si substrate. (e) Powder X-ray diffraction pattern of NiI_2 (PDF# 03-0473) on Si substrate reveals growth of phase pure NiI_2 nanoplates.

ceramic boat containing the NiI_2 (Sigma-Aldrich, anhydrous 99.9%) or $NiBr_2$ (Sigma-Aldrich, anhydrous 98%) powders positioned at the center of the heating zone of the furnace. The growth of NiX_2 NPL on mica or Si (001)/SiO_2 substrate was carried out by positioning the substrate at the top of the precursor boat with their respective powder precursor (Figure 6.2a). Before starting the heating process of the reaction, the tube was pumped down to 1 mTorr base pressure and then flushed with continuous flow of 99.99% pure Ar gas to remove oxygen and moisture residue. Further, the tube was filled with Ar gas at a flow rate of 150 sccm to reach the atmosphere pressure which was kept constant throughout the NPL growth process. The furnace was ramped to 550-575 °C and 580-600 °C for the growth of NiI_2 and $NiBr_2$ spiral NPL, respectively and the complete reaction took 5-10 mins. The local supersaturation is the primary factor that influence of the growth of spiral nanostructures;[15] hence the reaction is sensitive to the growth temperature provided for the reaction. After the completion of the reaction, the furnace was rapidly cooled, and substrate was taken out of the reaction tube and quickly transferred to home-built desiccant box. High density $NiBr_2$ spiral NPL grow flat all over the freshly cleaved mica substrate (Figure 6.2b). Powder X-ray diffraction (Figure 6.2c) of as-synthesized $NiBr_2$ NPL on mica substrate clearly show the appearance of high intensity (00*l*) peaks suggesting that the as-grown NPL are well-aligned with the [001] direction normal to the growth substrate. In case of NiI_2 NPL growth on Si/SiO_2 substrate, the majority of the NPL prefer vertical growth found on the substrate (Figure 6.2d) and powder X-ray diffraction pattern reveals growth of phase pure NiI_2 nanoplates (Figure 6.2e).

6.3.3 Topography and complex stacking of spiral NiX_2 nanoplates

Initial selection of spiral NPL amongst all types of nanostructures on the substrate can be done by optical microscopy (OM) images. A representative OM image of a $NiBr_2$ spiral nanoplate (Figure

6.3a) displays triangular-shaped plate with truncated corners. The apparent color gradient due to

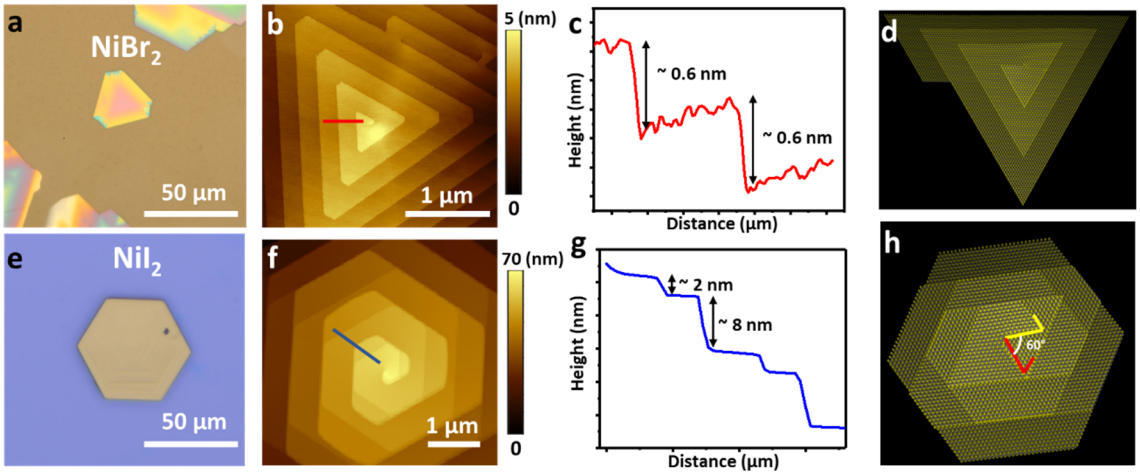

Figure 6.3 : Topography and stacking of spiral NiX_2 (a) OM image of a spiral $NiBr_2$ nanoplate on mica substrate. (b) Corresponding AFM characterization shows a triangular topology of the spiral. (c) The step heigh profile reveals monolayer spiral growth as represented in a schematic in panel (d). (e) OM image of a spiral NiI_2 nanoplate on Si/SiO_2 substrate. (f) Corresponding AFM characterization shows hexagonal topology of the spiral. (g) The step heigh profile reveal formation of two multilayer spiral sharing a single dislocation core as represented in a schematic in panel (h)

the thickness variation starting from the core to the edges of the spiral enables easy identification of dislocated spiral just from OM images. Atomic force microscopy (AFM) characterization of $NiBr_2$ nanoplate shown in Figure 6.3b reveals topography of a triangular shaped spiral with truncated corners, which are correlated with the macroscopic shape of the $NiBr_2$ nanoplate and a clear dislocation spiral hillock is observed. The height profile (Figure 6.3c) of the triangular spiral along the solid red line reveals a 0.6 nm step height of each terrace, which corresponds to the thickness of one layer of $NiBr_2$. This is an example of a monolayer triangular spiral as represented in the schematic in Figure 6.3d. In contrast to $NiBr_2$ growth on mica substrate, OM image (Figure 6.3e) of a spiral NiI_2 plate on Si/SiO_2 substrate appears hexagonal in shape with clear step edges of the spiral topography. AFM images reveal a complex stacking of hexagonal shaped spiral (Figure 6.3f) that has been previously observed in spiral TMDs.[12] The corresponding height profile of the spiral NiI_2 along the solid blue line (Figure 6.3g) reveals two multilayer spirals with step heights of ~ 2 nm and ~ 8 nm, respectively. The overall shape of the hexagonal spiral comes

from the two triangular spirals with the same handedness rotated 60° from each other and originating from a common dislocation core as elucidated in the schematic shown in Figure 6.3h.

We also observed other stacking arrangements of $NiBr_2$ nanoplates grown on same mica substrate. Note that detailed AFM characterization is required to visualize and distinguish the spiral stacking from SDD growth as OM images alone cannot identify these subtle structural differences (see Figure 6.3a and inset images in Figure 6.4). For example, Figure 6.4a shows a

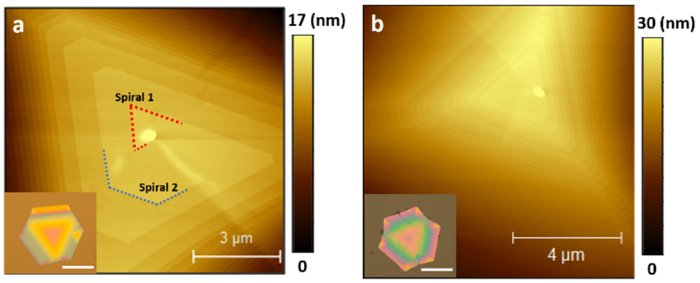

Figure 6.4 : (a) $NiBr_2$ nanoplate (OM image in the inset) with two spirals with same handedness separately growing from two dislocation core. (b) $NiBr_2$ nanoplate (OM image in the inset) with no apparent spiral growth. Scale bar in both images shown in the inset of panel a,b is 50 µm.

$NiBr_2$ nanoplate with two dislocation spirals of same handedness originating from two separate dislocation core. Sometimes the spirals grow with the opposite handedness which intersect to form a Frank-Reed source spiral structure of the NPL. The resulting nanoplate appears as layer-by-layer stacking with no apparent screw dislocations as shown in Figure 6.4b.

6.4 Conclusion

In conclusion, we have developed a facile PVD technique for SDD growth of 2D vdW NiX_2 that could be easily applicable to wide range of 2D vdW magnets. This is a first report on controlled synthetic route for the introduction of topological defects in 2D vdW magnets. We have observed and distinguished the different stackings of NiX_2 spirals by detailed AFM characterization. The microscopic understanding of dislocation-spin interaction in 2D materials warrants future investigation of magnetic properties in these spiral nanoplates. These unquie material platforms

open new avenues to explore magnetic tunability by defects that govern by the principles of topology and their application in novel functional spintronic devices.

References

[1] B. Huang, G. Clark, E. Navarro-Moratalla, D. R. Klein, R. Cheng, K. L. Seyler, D. Zhong, E. Schmidgall, M. A. McGuire, D. H. Cobden, W. Yao, D. Xiao, P. Jarillo-Herrero, X. Xu, *Nature* **2017**, *546*, 270.

[2] C. Gong, L. Li, Z. Li, H. Ji, A. Stern, Y. Xia, T. Cao, W. Bao, C. Wang, Y. Wang, Z. Q. Qiu, R. J. Cava, S. G. Louie, J. Xia, X. Zhang, *Nature* **2017**, *546*, 265.

[3] K. S. Burch, D. Mandrus, J.-G. Park, *Nature* **2018**, *563*, 47.

[4] Y. Deng, Y. Yu, Y. Song, J. Zhang, N. Z. Wang, Z. Sun, Y. Yi, Y. Z. Wu, S. Wu, J. Zhu, J. Wang, X. H. Chen, Y. Zhang, *Nature* **2018**, *563*, 94.

[5] Y. Wu, S. Zhang, J. Zhang, W. Wang, Y. L. Zhu, J. Hu, G. Yin, K. Wong, C. Fang, C. Wan, X. Han, Q. Shao, T. Taniguchi, K. Watanabe, J. Zang, Z. Mao, X. Zhang, K. L. Wang, *Nat. Commun.* **2020**, *11*, 3860.

[6] D. Rhodes, S. H. Chae, R. Ribeiro-Palau, J. Hone, *Nature Materials* **2019**, *18*, 541.

[7] J. Hong, Z. Hu, M. Probert, K. Li, D. Lv, X. Yang, L. Gu, N. Mao, Q. Feng, L. Xie, J. Zhang, D. Wu, Z. Zhang, C. Jin, W. Ji, X. Zhang, J. Yuan, Z. Zhang, *Nat. Commun.* **2015**, *6*, 6293.

[8] M. Li, *J. Phys. Condens. Matter* **2019**, *31*, 083001.

[9] G. I. Taylor, *Proceedings of the Royal Society of London. Series A, Containing Papers of a Mathematical and Physical Character* **1934**, *145*, 362.

[10] R. H. Glaenzer, A. G. Jordan, *Solid-State Electronics* **1969**, *12*, 247.

[11] L. Lu, Y. Shen, X. Chen, L. Qian, K. Lu, *Science* **2004**, *304*, 422.

[12] M. J. Shearer, L. Samad, Y. Zhang, Y. Zhao, A. Puretzky, K. W. Eliceiri, J. C. Wright, R. J. Hamers, S. Jin, *J. Am. Chem. Soc.* **2017**, *139*, 3496.

[13] L. Zhang, K. Liu, A. B. Wong, J. Kim, X. Hong, C. Liu, T. Cao, S. G. Louie, F. Wang, P. Yang, *Nano Lett.* **2014**, *14*, 6418.

[14] R. Suzuki, M. Sakano, Y. J. Zhang, R. Akashi, D. Morikawa, A. Harasawa, K. Yaji, K. Kuroda, K. Miyamoto, T. Okuda, K. Ishizaka, R. Arita, Y. Iwasa, *Nat. Nanotechnol.* **2014**, *9*, 611.

[15] F. Meng, S. A. Morin, A. Forticaux, S. Jin, *Accounts of Chemical Research* **2013**, *46*, 1616.

[16] P. V. Sarma, A. Kayal, C. H. Sharma, M. Thalakulam, J. Mitra, M. M. Shaijumon, *ACS Nano* **2019**, *13*, 10448.

[17] F. Banhart, J. Kotakoski, A. V. Krasheninnikov, *ACS Nano* **2011**, *5*, 26.

[18] O. V. Yazyev, S. G. Louie, *Phys. Rev. B* **2010**, *81*, 195420.

[19] L. Chen, B. Liu, A. N. Abbas, Y. Ma, X. Fang, Y. Liu, C. Zhou, *ACS Nano* **2014**, *8*, 11543.

[20] Y. Ran, Y. Zhang, A. Vishwanath, *Nat. Phys.* **2009**, *5*, 298.

[21] W. K. Burton, N. Cabrera, F. C. Frank, *Nature* **1949**, *163*, 398.

[22] R. Chen, J. Cao, S. Gee, Y. Liu, J. Yao, *MRS Advances* **2020**, *5*, 3437.

[23] B. A. Ivanov, V. E. Kireev, *Journal of Experimental and Theoretical Physics Letters* **2001**, *73*, 188.

[24] T. Nakamura, K. Kawamura, *physica status solidi (b)* **1984**, *122*, 141.

[25] M. A. McGuire, *Crystals* **2017**, *7*, 121.

[26] J. A. Nasser, J. M. Kiat, R. Gabilly, *Solid State Commun.* **1992**, *82*, 49.

[27] S. R. Kuindersma, J. P. Sanchez, C. Haas, *Physica B+C* **1981**, *111*, 231.

[28] H. Liu, X. Wang, J. Wu, Y. Chen, J. Wan, R. Wen, J. Yang, Y. Liu, Z. Song, L. Xie, *ACS Nano* **2020**, *14*, 10544.

Appendix 1 : Supporting Information for Chapter 3*

Electron Holography and Magnetotransport Measurements Reveal Stabilized Magnetic Skyrmions in $Fe_{1-x}Co_xSi$ Nanowires

Additional Figures:

Schematic of chemical vapor deposition synthesis of $Fe_{1-x}Co_xSi$ nanowires

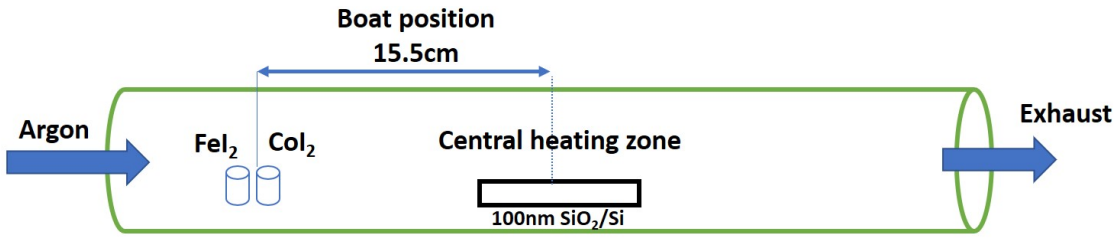

Figure A1.1: Chemical synthesis of $Fe_{1-x}Co_xSi$ alloy nanowires using CVD of two metal iodide precursors. The two precursors were independently vaporized and mixed in gaseous phase and carried downstream in the CVD reactor by argon gas at a flow rate of 190 sccm, where decomposition and silicide nanowire formation occur on silicon substrates coated with thin (~100 nm) silicon oxide placed downstream at 900 ºC.

Compositional analysis of $Fe_{1-x}Co_xSi$ nanowires on silicon substrate

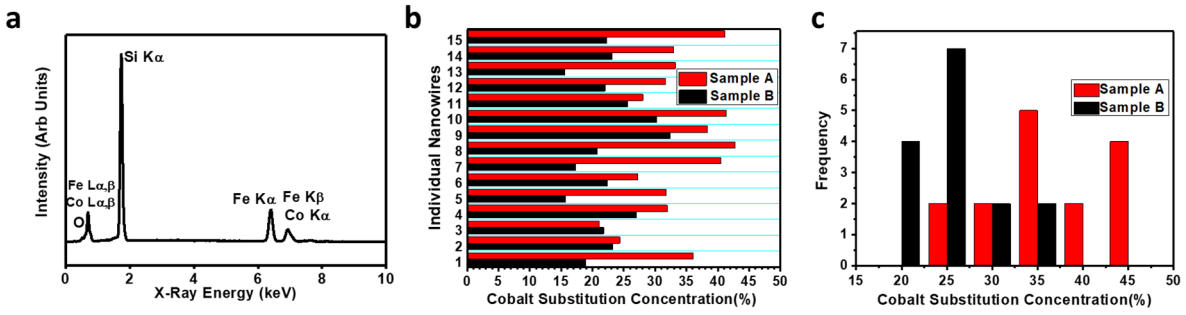

Figure A1.2 : (a) Representative EDS spectrum recorded from the $Fe_{1-x}Co_xSi$ NWs. (b) The results of SEM-EDS analysis of cobalt substitution concentration (x) represented as histograms (c) for 15 nanowires each from sample A (red bars) and sample B (blue bars).

Compositional analysis of the NW sample for electron holography

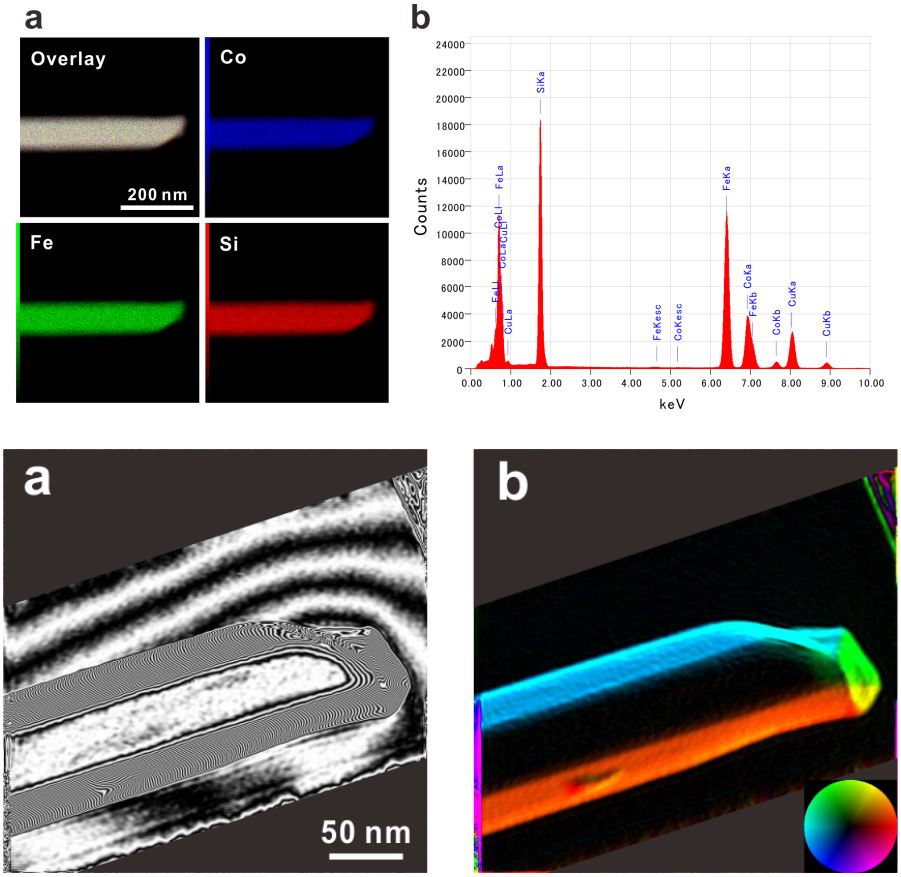

Figure A1.4 : Surface and cross-sectional geometry of the NW sample for electron holography. Reconstructed phase images at $T = 60$ K and $H = 0$ Oe in the forms of (a) $\cos(20\varphi)$ and (b) color-coded $\nabla\varphi$ where the color hue and brightness represent $\text{atan2}(\nabla\varphi)$ and $|\nabla\varphi|$, respectively.

Surface and cross-sectional geometry of the NW sample for electron holography: Above T_C, the phase shift is brought about by the mean inner potential of materials, which is basically responsible for the traversing thickness. Figure A1.4 shows reconstructed phase images at $T = 60$ K and $H = 0$ Oe in the forms of (a) $\cos(20\varphi)$ and (b) color-coded $\nabla\varphi$. These images reveal that the NW consists of flat facets forming a rhombohedral cross-section similarly to the NWs shown in the inset of Figure 3.1a. In addition, we can see phase gradation in vacuum with a summit near the tip of the NW. This is presumably caused by electrical charging due to poor electrical conductivity around the tip. We suspect that the rugged shape of the tip was formed by cleavage fracture. Introduced nano-sized cracks may also depress the surrounding electrical conductivity.

Optical conditions of electron holography observations

Image processing of reconstructed phase images for reducing unwanted artefacts: Figure A1.6a shows the residual phase image at T = 10 K and H = 0 Oe after subtraction by the phase image taken at 60 K and 0 Oe. Broad bands inside the NW running along the long axis are the

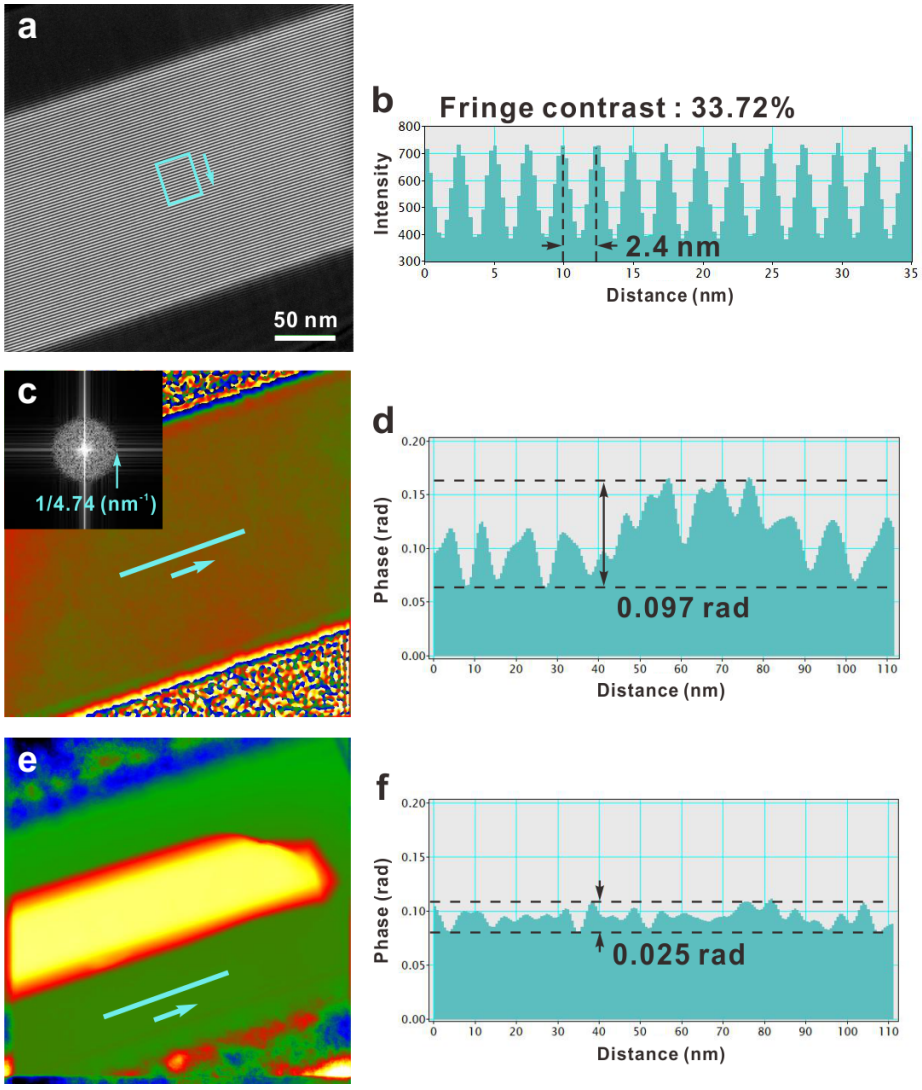

Figure A1.5: Optical conditions of electron holography observations. (a) Representative hologram. (b) Intensity profile of the blue rectangle area marked in (a). (c) Reconstructed phase image of (a). Inset shows Fourier transform pattern. (d) Phase profile of the blue line drawn in (c). (e) Phase image at T = 10 K and H = 0 Oe, wherein 100 reconstructed ones are averaged. (f) Phase profile of the blue line drawn in (e).

undersubtracted/oversubtracted φ_{MIP} components, which are caused by slight geometric misalignment during temperature change. Besides, fine stripes are visible even in vacuum. These

stripes are introduced by the Fresnel diffraction at the lower biprism. The Fresnel fringes should be sufficiently suppressed in the double-biprism interferometry[1] but become apparent if the lower biprism is away from the shade of the upper one. The amplitude of these artefacts is ~0.1 rad, which is less than 1% of the maximum φ_{MIP} (~11.3 rad) but is still comparable to the φ_{MAG} of helices and skyrmions. To remove these unwanted artefacts, we employed additional process which subtracts the phase components that are unchanged along the NW direction. The processed images (Figure A1.6b) can capture the helical stripes more clearly. Finally, the second-order Butterworth filtering[2] was employed to smooth short-range phase undulations and result in Figure A1.6c.

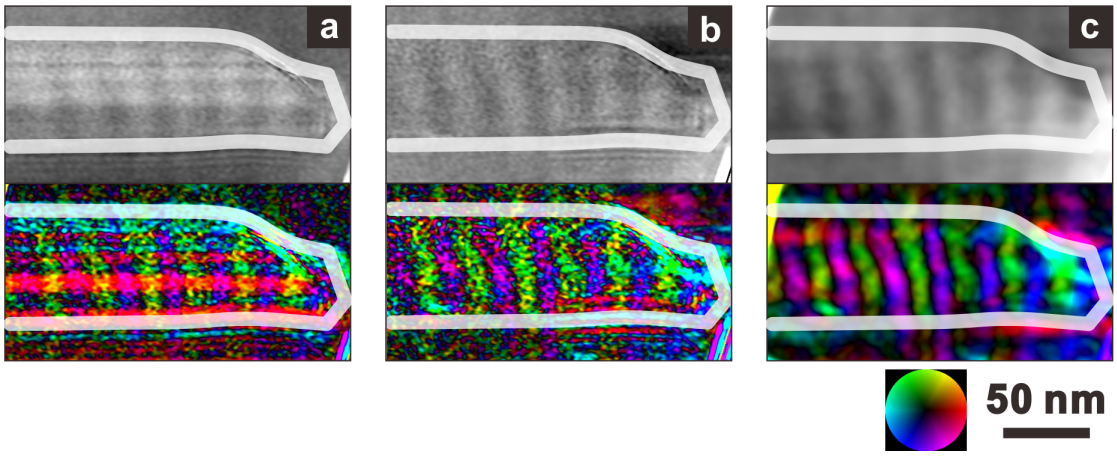

Figure A1.6 : Image processing of reconstructed phase images for reducing unwanted artefacts. (a) Reconstructed phase image at T = 10 K and H = 0 Oe after subtraction by that at T = 60 K and H = 0 Oe. (b) Phase image of (a) after further subtraction by the unchanged components along the NW long axis. (c) Phase image of (b) after the second-order Butterworth filtering. The upper panels are the gray-scale phase (φ) maps, and the lower panels display in the form of $\nabla\varphi$ where the color hue and brightness correspond to atan2($\nabla\varphi$) and $|\nabla\varphi|$, respectively.

Four probe NW device fabrication for magnetoresistance measurements: The $Fe_{1-x}Co_xSi$ NWs from Sample A and B were transferred to Si (100) substrate with a 600 nm silicon oxide coating prior to device fabrication. NWs were dispersed in isopropanol (IPA) solution via ultrasonication and drop casted on the substrates. Photoresist layers of MMA and PMMA was spin coated onto the substrates and the intended areas of PMMA resist were exposed with e-beam lithography using a nano-pattern generation system (NPGS) to fabricate metal electrodes, then the

defined patterns were developed in a MIBK (Methyl isobutyl ketone) /IPA developer solution for

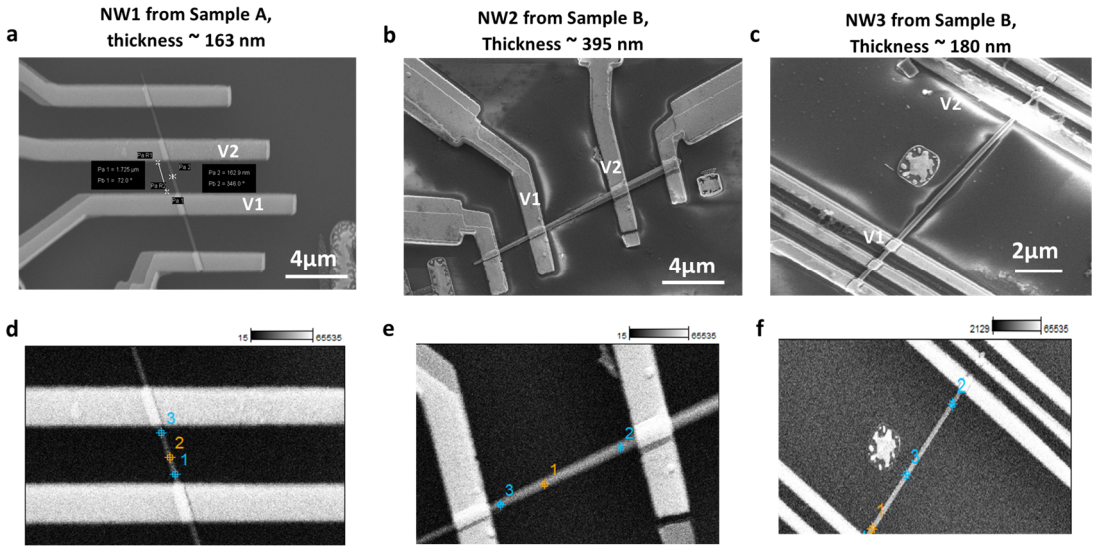

Figure A1.7: The SEM images of four probe device on NW1(a), NW2(b) and NW3(c). V1 and V2 represents voltage leads used for measurement of magnetoresistance. Dimensions were measured from SEM images as shown in (a). (d-f) Magnified images of probing area between the voltage leads of four probe devices on NW 1-3 respectively for SEM-EDS compositional analysis.

30 s. After etching with buffered HF solution for 15 s to remove the silicon oxide layer on the surface of the NW, non-magnetic metallic contacts were fabricated for NW electrodes (~1 µm in width) as a combination of Ti layer covered with Au using e-beam deposition. Importantly, a two-step electrode deposition process was implemented to achieve the most consistent device contact and low S/N ratios. In the first evaporation, the substrate was set perpendicular to the evaporation direction and 50 nm layers of both Ti and Au were evaporated. The second step involves orienting the substrate on a custom-built stage attachment so that the substrate will be angled 45° with respect to the evaporation direction to deposit 70 nm of Ti and 50 nm of Au. The angled evaporation steps allow for better side wall metal contact to the NWs resulting in better S/N devices. The SEM images of the three NW devices measured are shown in Figure A1.5.

Table A1: The average Co% (x) is determined via SEM-EDS conducted at 3 spots between the voltage leads of the fabricated devices for all 3 NWs (Figure A1.7d-f).

	Atomic% Fe_K	Atomic% Co_K	Co substitution
NW1_Spot 1	3.74	2.22	0.37
NW1_Spot 2	3.35	2.26	0.40
NW1_Spot 3	3.86	2.09	0.35
	Average Co substitution (x)	Standard Deviation in x	Standard error in x
	0.37	0.02	0.01

	Atomic% Fe_K	Atomic% Co_K	Co substitution
NW2_Spot 1	7.62	1.82	0.19
NW2_Spot 2	9.75	2.12	0.18
NW2_Spot 3	1.30	0.48	0.27
	Average Co substitution (x)	Standard Deviation in x	Standard error in x
	0.21	0.04	0.02

	Atomic% Fe_K	Atomic% Co_K	Co substitution
NW3_Spot 1	6.02	1.24	0.17
NW3_Spot 2	5.85	1.64	0.22
NW3_Spot 3	6.57	1.31	0.17
	Average Co substitution(x)	Standard Deviation in x	Standard error in x
	0.19	0.02	0.01

Temperature dependent MR for NW1 and NW2 under $H_\perp$

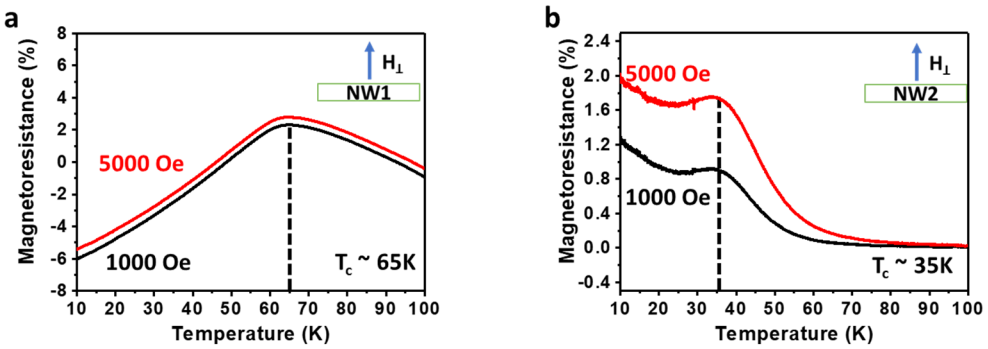

Figure A1.8 : Temperature dependent MR of (a) NW1 and (b) NW2 with perpendicular applied magnetic field, $H_\perp$.

MR-H isotherms between 10-32K under $H_\perp$ for the $Fe_{0.81}Co_{0.19}Si$ NW (NW3)

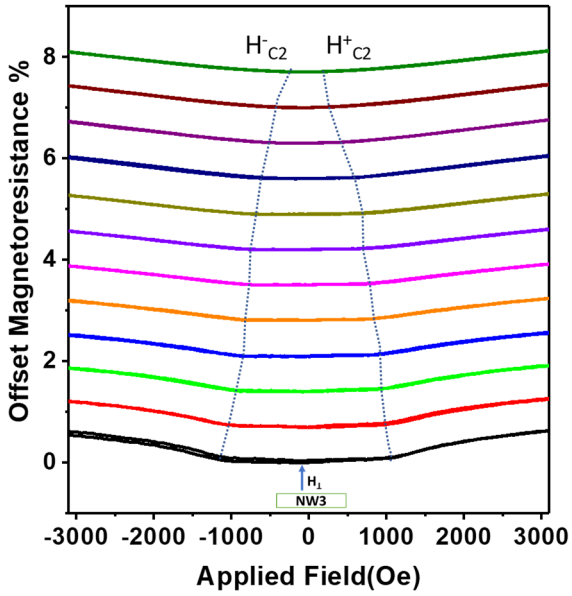

Figure A1.9 : Offset MR-H isotherms between 10-32K under $H_\perp$ for the $Fe_{0.81}Co_{0.19}Si$ NW (NW3). H_{C2} represents critical field for skyrmion to field polarized spin state transition marked by the dotted blue lines on MR-H isotherms.

References:

1. Harada, K.; Tonomura, A.; Togawa, Y.; Akashi, T.; Matsuda, T., Double-Biprism Electron Interferometry. *Appl. Phys. Lett.* **2004,** *84*, 3229-3231

2. Voelkl, E.; Allard, L. F.; Frost, B., Electron Holography: Recent Developments. *Scanning Microsc.* **1997,** *11*, 407-416

Appendix 2: Supporting Information for Chapter 4*

In-Plane Magnetic Field-Driven Creation and Annihilation of Magnetic Skyrmion Strings in Nanostructures

Additional Figures and Discussion:

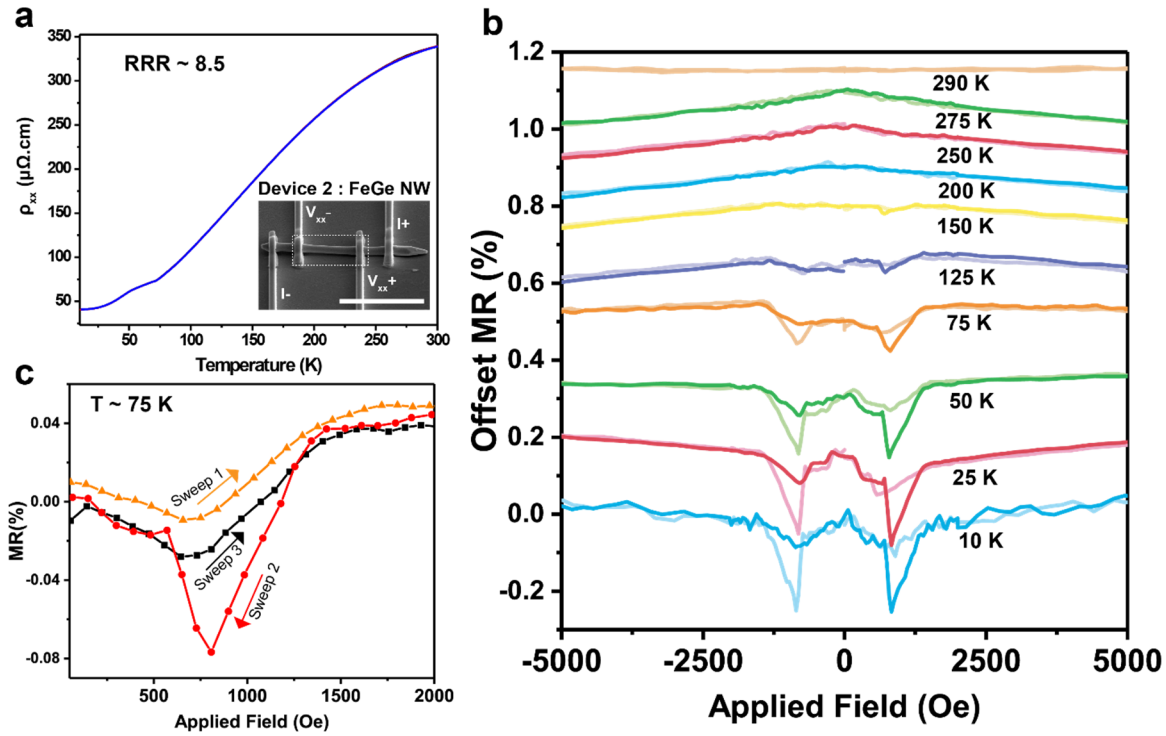

Figure A2.1 : Magnetotrasport measurements conduced on FeGe NW2. (a) Temperature-dependent longitudinal resistivity (ρ_{xx}) of NW2 highlighting the residual resistance ratio (RRR) ~ 8.5, illustrating good metal contact to the FeGe NW. The inset shows the SEM image of NW2 with thickness ~ 400 nm and labelled Pt current and voltage electrodes. The probing area between the voltage leads is marked with dashed white box. Scale bar is 4 μm. (b) MR−$H_{||}$ curves in the temperature range of 10-290 K with the bold and faded color corresponding to the decreasing and increasing field sweeps, respectively. MR−$H_{||}$ curves show the anomalous and strong hysteretic MR features of the FeGe NW at low temperatures. (c) MR− $H_{||}$ curves at 75 K different with sweep order further illustrates that the hysteretic features persist even when the magnetic field sweep starts from zero field.

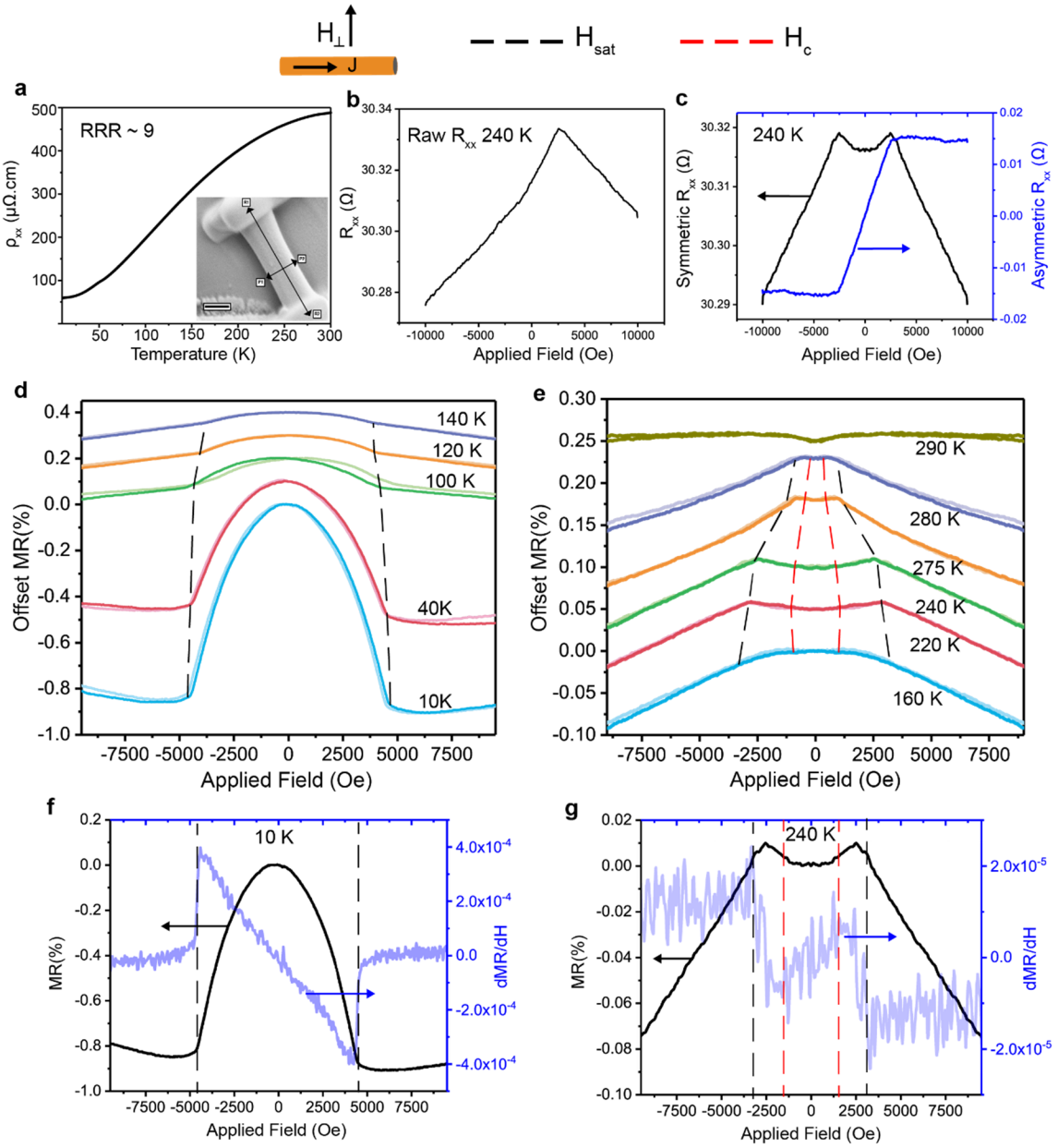

Figure A2.2 : Magnetotransport measurements of FeGe NW1 in the perpendicular field configuration ($H_\perp$). (a) Temperature-dependent longitudinal resistivity (ρ_{xx}) of the NW highlighting the residual resistance ratio (RRR) ~ 9, illustrating good metal contact to the NW. The inset show the SEM image of the probing area between the voltage electrodes (~ 3 μm distance) of the NW1 with thickness ~ 760 nm. Scale bar is 500 nm. (b) Raw R_{xx} signal obtained from the measurements with asymmetric MR component at 240 K as an example. (c) Symmetric MR component considered as the true MR signal after substraction of the asymmetric MR component using equation (1). (d, e) Symmetric MR−$H_\perp$ curves plotted in the temperature range of 10-290 K. MR−$H_\perp$ curves at (f) 10 K and (g) 240 K plotted with the corresponding dMR/d$H_\perp$ curves.

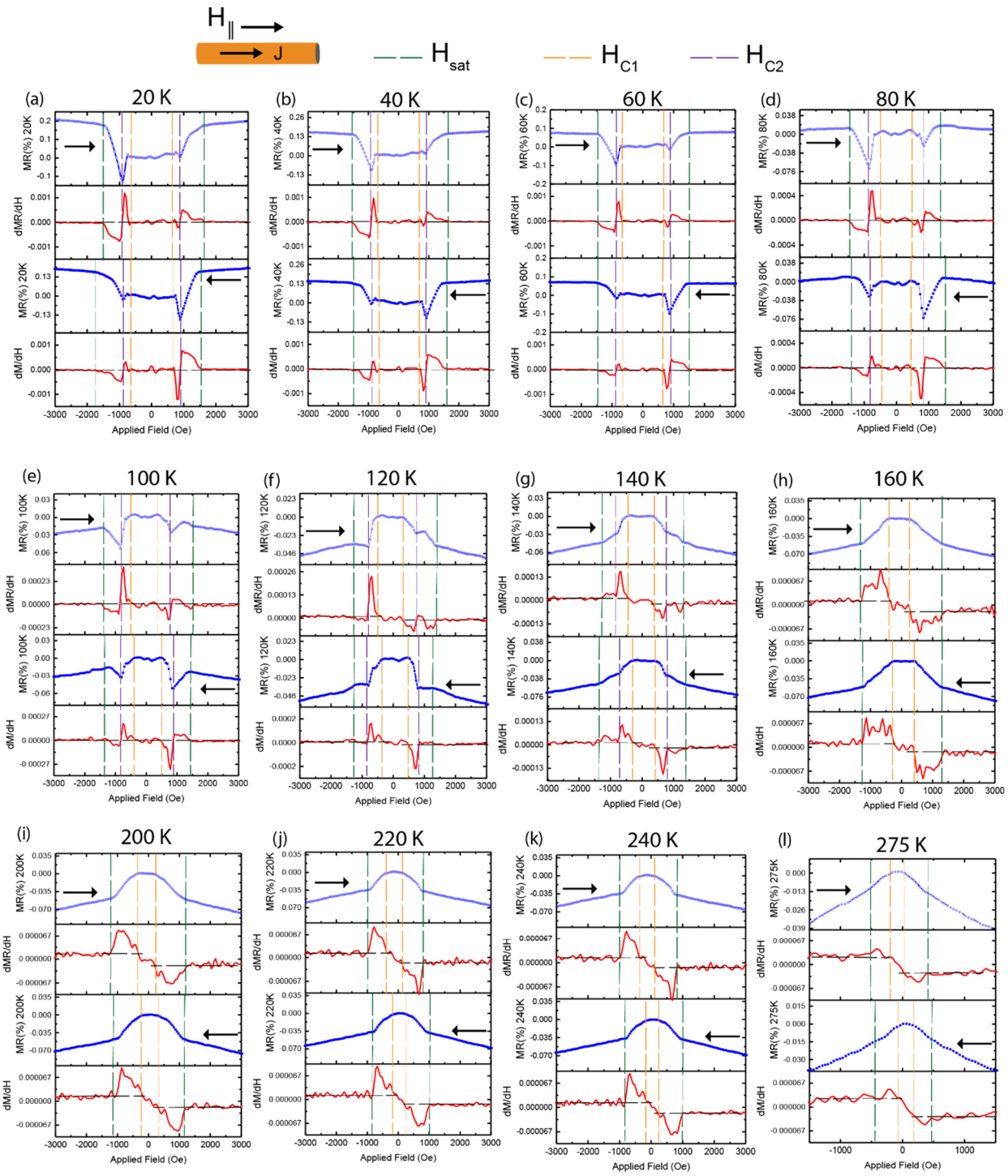

Figure A2.3: The critical field assessments for FeGe NW1 in the parallel field configuration. (a-l) MR– $H_{\parallel}$ curves with increasing or decreasing field (marked by black arrow) with the corresponding dMR/ $H_{\parallel}$ curves. The critical fields (H_{C1} and H_{sat}) are assigned where $dMR/dH_{\parallel}$ abruptly changes and H_{C2} marked at a field where $dMR/H_{\parallel}$ changes sign (sharp increase in MR signal) in the SkS stability region.

Additional discussion on magnetotransport measurements on $Fe_{0.97}Co_{0.03}Ge$ NPL. Previous magnetotransport measurements conducted on $Fe_{0.97}Co_{0.03}Ge$ NPL in the parallel and perpendicular configuration are shown in Figure A2.4, but those results were not understood and discussed in detail.[1] Here, we provide a detailed analysis of the magnetotransport of $Fe_{0.97}Co_{0.03}Ge$ NPL under $H_{||}$ and compare these results with those of FeGe NWs (Figure A2.5 and Figure A2.6). Figure A2.5a shows the enhanced shape induced uniaxial anisotropy present in the FeGe nanostructures ($Fe_{0.97}Co_{0.03}Ge$ NPL and FeGe NW) at low temperatures that could be quantitatively extracted from the difference between $H_{||\ sat}$ and $H_{\perp\ sat}$ (Figures A2.4g,h). The MR-$H_{||}$ curves plotted for the $Fe_{0.97}Co_{0.03}Ge$ NPL at a few selected temperatures (Figure 5b) exhibit close resemblance to the FeGe NW results. However, the anomalous and hysteretic MR features at low temperatures (below ~ 100 K) are less pronounced in the $Fe_{0.97}Co_{0.03}Ge$ NPL in comparison to FeGe NWs. The critical fields for magnetic phase transitions (H_{C1}, H_{C2} and H_{sat}) are marked (Figure A2.6) following the similar procedures for the FeGe NWs (Figure A2.3). We noticed minor contribution of the asymmetric MR in the MR-$H_{||}$ curves. In principle, there should be no asymmetric MR component arising in the parallel configuration, however, the slight misalignment of the NPL with the direction of $H_{||}$ could result in some bleeding of asymmetric MR component into symmetric MR. Although the asymmeterization process can remove the asymmetric MR component from the MR-$H_{||}$ curves, it will also remove the intrinsic asymmetry observed in MR-$H_{||}$ curves with increasing and decreasing field at low temperatures (below ~ 100 K) in the field range of $H_{C1} < H_{||} < H_{sat}$. Nevertheless, the asymmeterization process does not affect the determination of the critical fields for the magnetic phase transitions (Figures A2.6a-c). In contrast to NWs, the conical phase show signs of stability to a slightly higher temperature (~200 K) in NPL

(Figures A2.6d-l). This might be due to increased stability of conical phase away from the NPL edge.

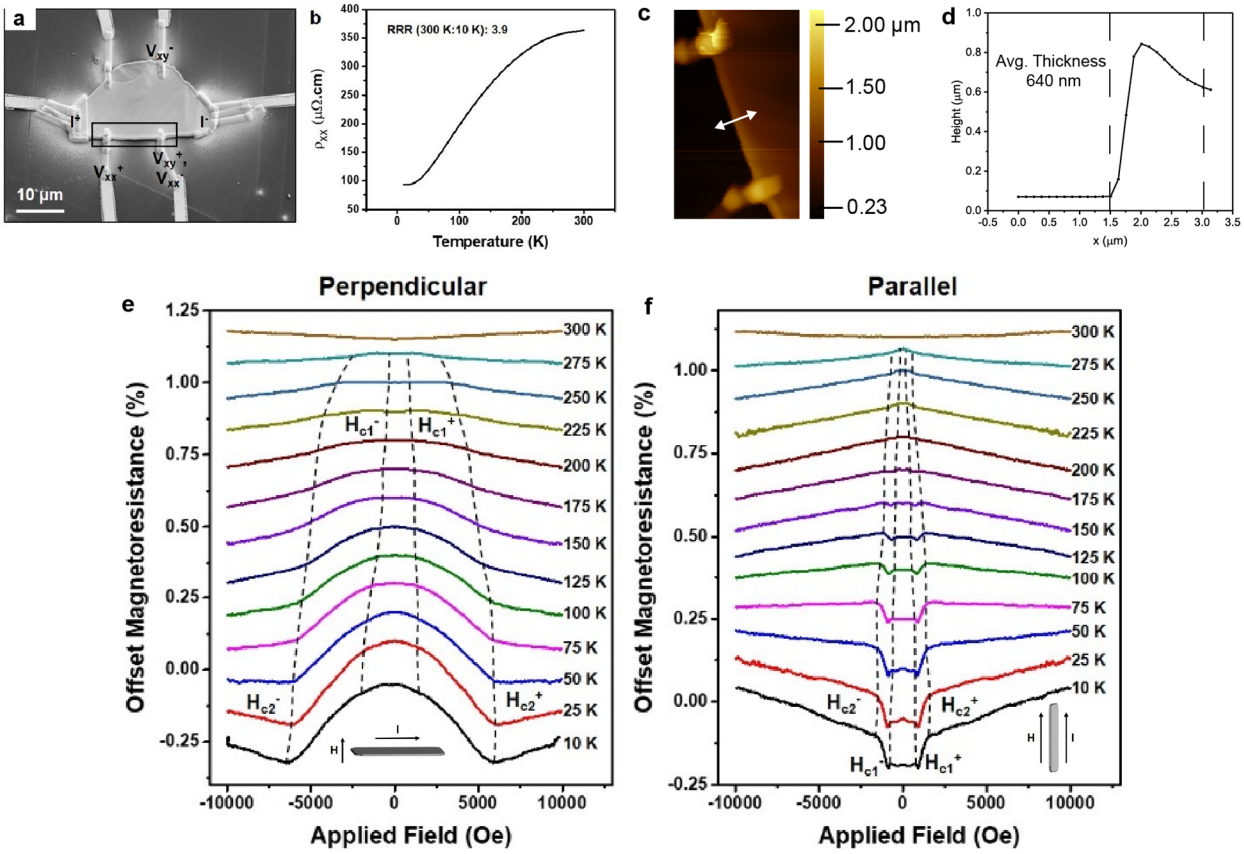

Figure A2.4: Information and magnetotransport of the $Fe_{0.97}Co_{0.03}Ge$ NPL. (a) SEM image of the fabricated NPL nanodevice labelled with current and voltage probes. The black box indicates the probing area and voltage leads used for magnetotransport measurements. (b) Temperature-dependent longitudinal resistivity (ρ_{xx}) with RRR ~ 3.9. (c) Atomic force microscopy (AFM) image of the NPL area shown in the black box in panel (a). (d) Height profile acquired from the AFM image across the probing area enclosed between the black dashed line. Magnetotransport measurements conducted in the perpendicular and parallel configuartion and the corresponding symmetric MR−H curves shown in panel (e) and (f), respectively. The critical fields of H_{C1} and H_{C2} marked in panel (g) and (h) are similar to H_{C1} and H_{sat} shown in this chapter. Panel a,b,e,f are reproduced with permission from Ref [1], Copyright 2019 Wiley-VCH. Data shown in panel c,d are replotted for a $Fe_{0.97}Co_{0.03}Ge$ NPL from Ref [1].

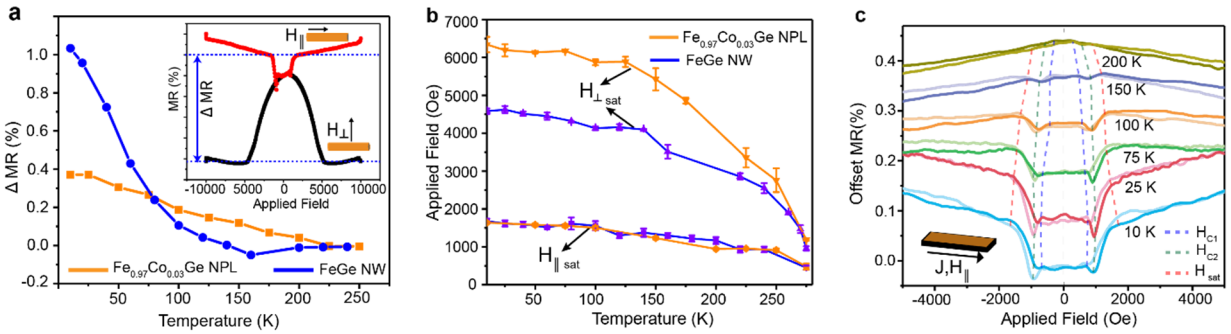

Figure A2.5: Quantitative description of the magnetic anisotropy in FeGe nanostructures and magnetotransport measurements on the $Fe_{0.97}Co_{0.03}Ge$ NPL in more detail. (a) The quantitative analysis of relative AMR effect in FeGe nanostructures extracted by calculating the difference in MR (%) at saturated states (Δ MR(%) = MR($H_{\parallel} = H_{\parallel\ sat}$) – MR ($H_{\perp} = H_{\perp\ sat}$)) and plotted as a function of temperature. The inset shows an example of MR data analysis for the FeGe NW at 10 K when the applied field is parallel (red) and perpendicular (black) to the NW long axis. (b) Demonstration of the effective uniaxial anisotropy present in FeGe nanostructures (comparing $Fe_{0.97}Co_{0.03}Ge$ NPL with FeGe NW) determined from the comparison of the saturated fields found in the parallel and perpendicular MR measurements. (c) MR−$H_{\parallel}$ curves in the parallel configuration acquired from probing near the edge of the $Fe_{0.97}Co_{0.03}Ge$ NPL; bold and faded color correspond to the decreasing and increasing field sweeps. There are also clear hysteretic MR features below 100 K, but they are less pronounced than those observed for FeGe NWs. Data are replotted for a $Fe_{0.97}Co_{0.03}Ge$ NPL device shown in Figure A2.5 from Ref [1].

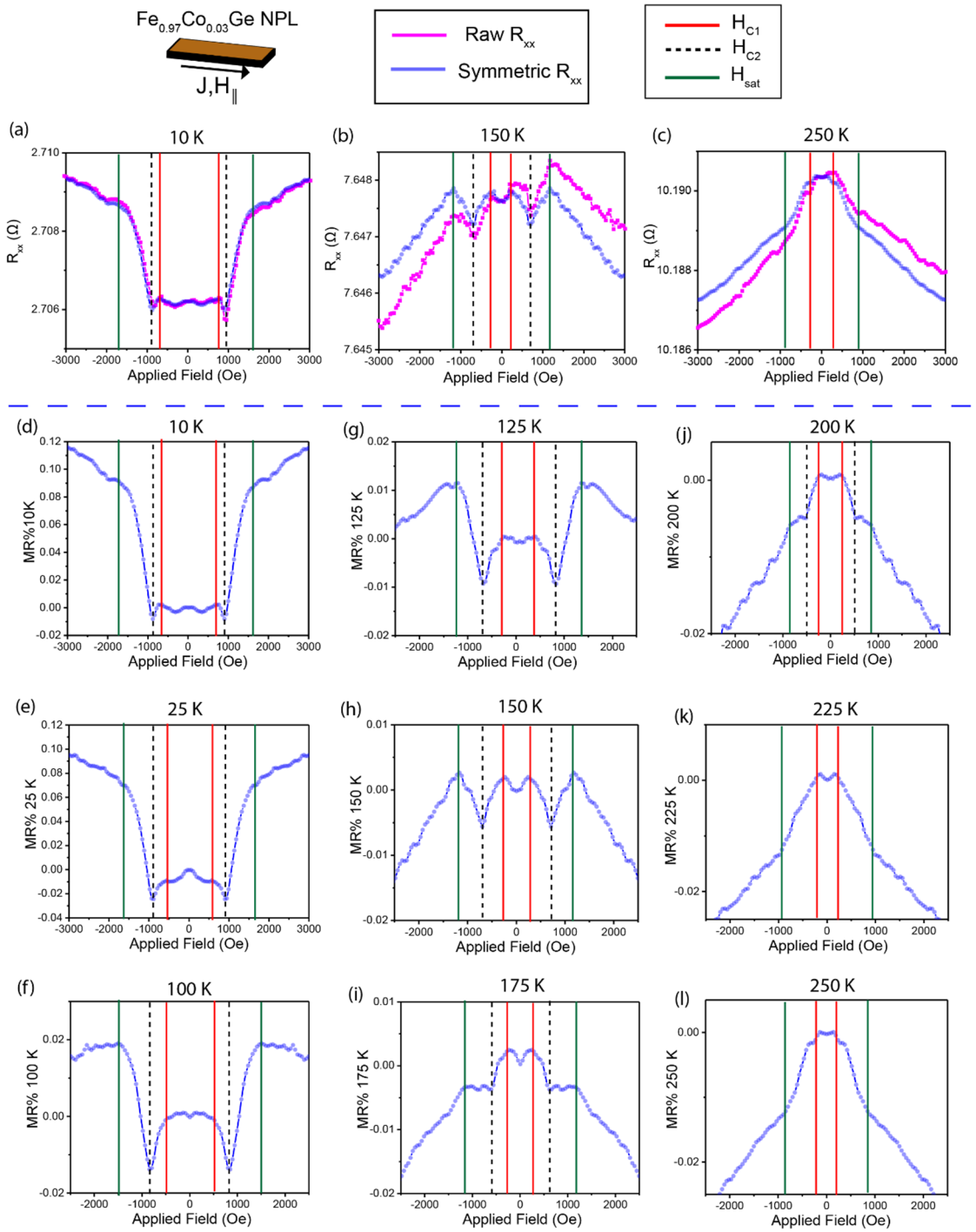

Figure A2.6: Asymmetrization of the MR signal obtained from the $Fe_{0.97}Co_{0.03}Ge$ NPL using equation (1) in the parallel configuration. (a) At low temperature (10 K), asymmetrization process of raw MR signal also removes the asymmetric hysteretic features from the MR−$H_{||}$ curve. However, asymmetrization process does not affect the determination of critical fields for the magnetic phase transition at any temperature shown at (b) 150 K and (c) 250 K as examples. (d-l) Symmetric MR−$H_{||}$ plotted in the temperature range of 10 – 250 K and marked with the critical

fields for magnetic state transitions (H_{C1}, H_{C2} and H_{sat}). Data are replotted for a $Fe_{0.97}Co_{0.03}Ge$ NPL device shown in Figure A2.6 from Ref [1].

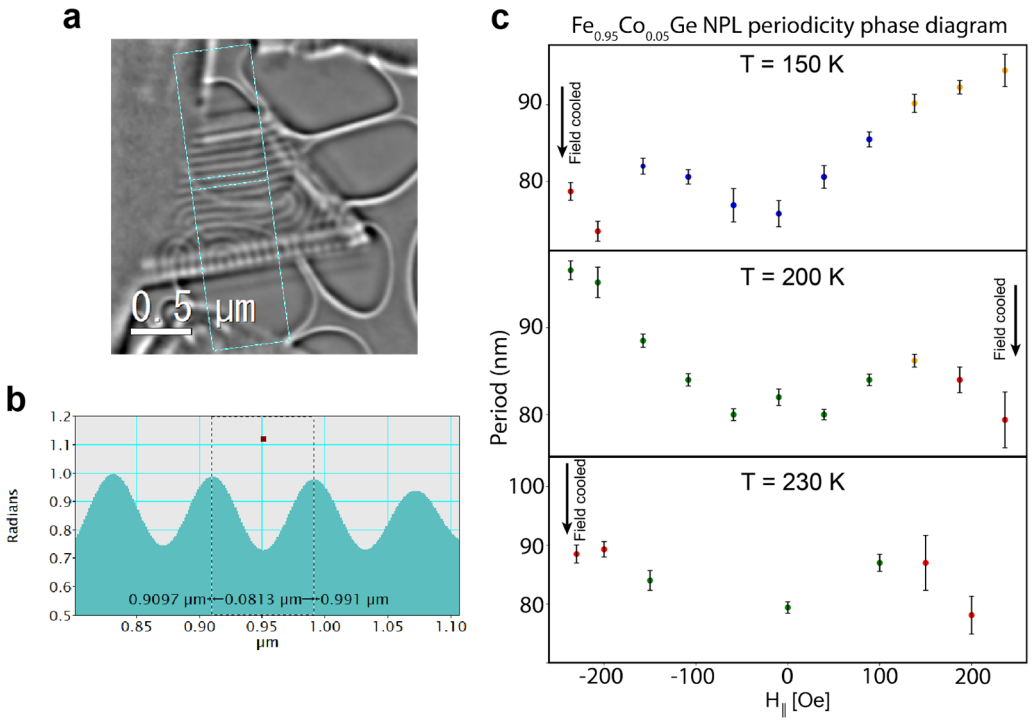

Figure A2.7: Analysis of LTEM image for determining the periodicity of magnetic spin textures. (a) Phase image of $Fe_{0.95}Co_{0.05}Ge$ NPL at 150 K and 50 Oe calculated from an under- and over-focused LTEM. As the phase image is directly mapped onto the magnetization, we can calculate the periodicity of the magnetic domains from this image directly by averaging 500 lines into the 1D profile in (b). (c) Periodicity versus externally applied in-plane magnetic field phase diagram for magnetic textures in $Fe_{0.95}Co_{0.05}Ge$ NPL generated using rapid field cooling with $H_{||} = -230$ Oe (top and bottom panel) and $H_{||} = 230$ Oe (middle panel). Among the various data points in (c), red are measured from SkS aligned parallel to the magnetic field, green from single Q helical states oriented perpendicular to the magnetic field, blue from bending SkS and mixed spin state loosely oriented parallel to the magnetic field, and orange from multi-Q helical states.

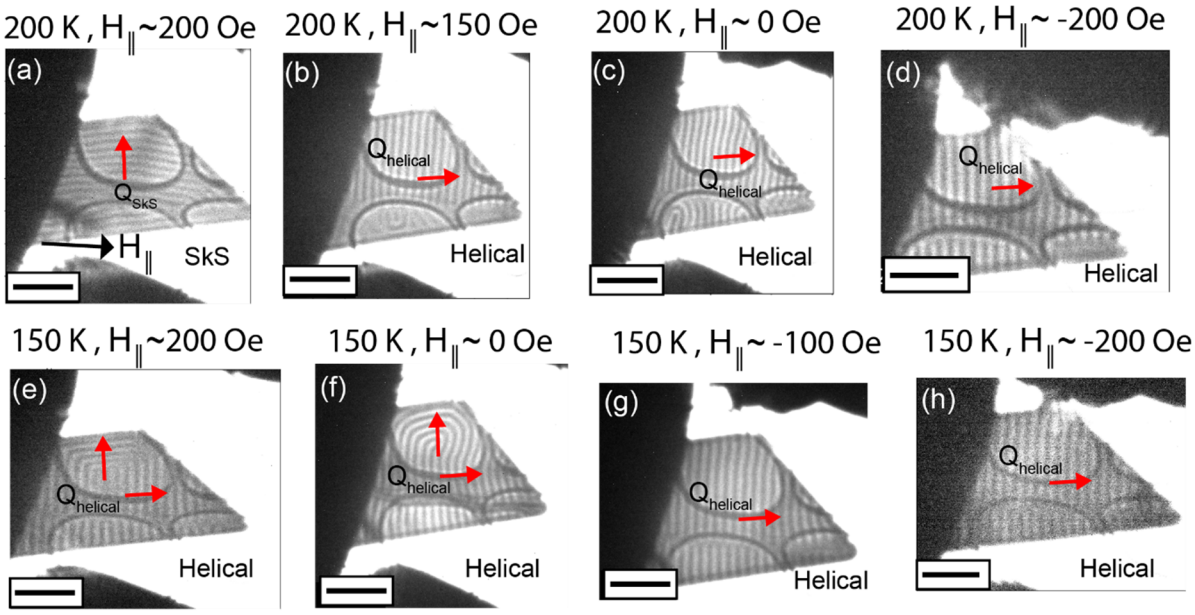

Figure A2.8 : Defocused LTEM images depict field-driven transformations of the spin-configuration in $Fe_{0.95}Co_{0.05}Ge$ NPL under pure-in-plane magnetic field. (a-d) Transformation of metastable SkS to helical phase with decreasing magnetic field at 200 K. (e-h) Transformation of multi-Q helical state (Figure 4.3l) to single-Q helical state at 150 K. SkS were generated in Figure A2.8a by field cooling to T = 200 K, a process in which the sample was rapidly cooled to temperature while holding an externally applied magnetic field constant, in this case, $H_{\|}$ = +250 Oe. The field was then decreased to zero along the positive direction and increased in the negative direction. Scale bars in all images are 500 nm.

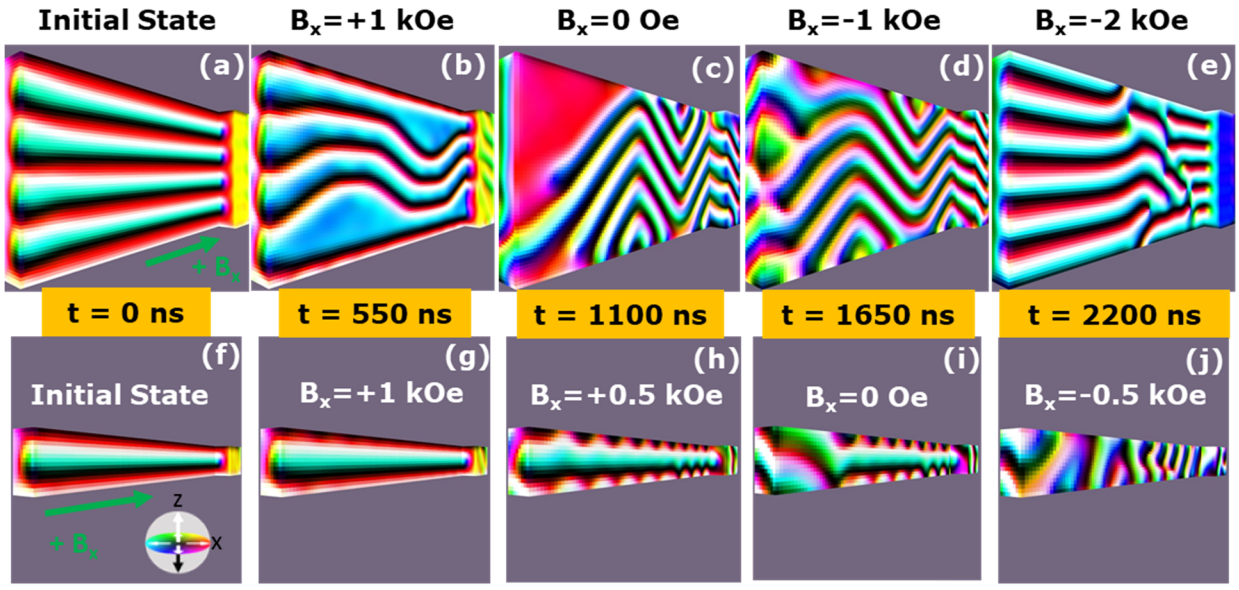

Figure A2.9 : Micromagnetic simulations of skyrmion strings stabilized in a nanoplate (NPL) and nanowire (NW) in the upper and lower row, respectively. The images are 3D representations with the top half ($0 < z < \frac{L}{2}$ for sample thickness L) cut off for all but the right-hand side end-portion of the sample for visualization purposes. The initial states are held at an applied external magnetic field of (a) B_x = +2 kOe and (g) +1.5 kOe, respectively and the states are evolved in time (shown in between the rows) by solving the Landau-Lifshitz-Gilbert equation. In (b-e) and (g-j), the applied in-plane magnetic field is decreased to -2 kOe and -0.5 kOe, respectively. The skyrmion strings present in the NPL bend until they are no longer stable at B_x = 0 Oe and transform into a helical state. The skyrmion string present in the NW is metastable even at B_x = 0 Oe. When the in-plane field is applied in the opposite direction, however, the skyrmion string annihilates.

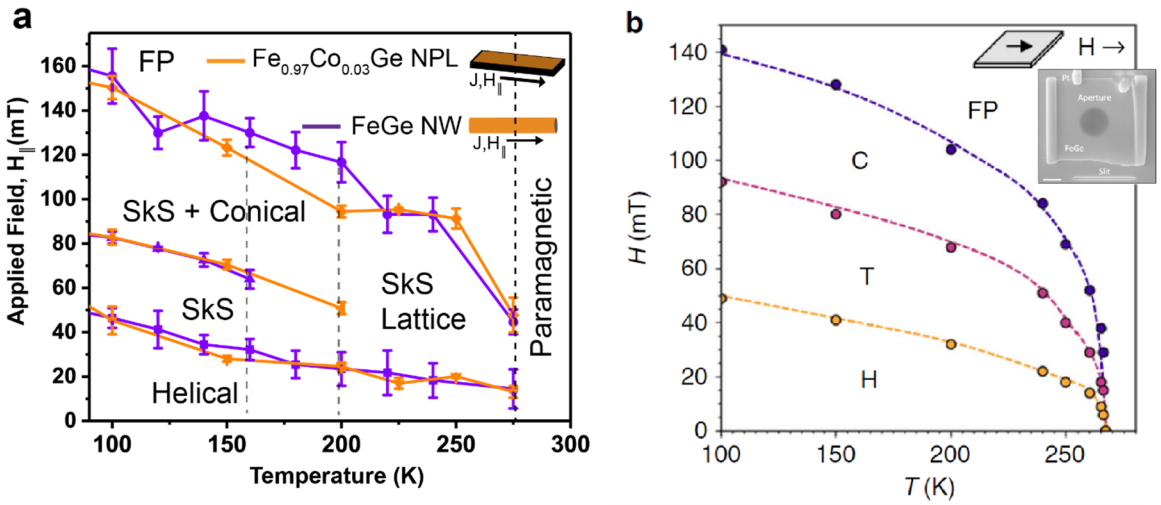

Figure A2.10 : Comparison of $H_{||}$-T plots inferred from (a) the MR measurements on FeGe nanostructures in this study and (b) magnetic X-ray diffraction experiment conduced on a FeGe lamella where the field of view is limited to the center of the lamella as shown in the inset image. Panel a is the same as the Figure 4.4 in Chapter 4 but reproduced here for the convenient comparison. Panel b is reproduced with permission from Ref [2], Copyright 2020 Springer Nature Limited.

References

[1] M. J. Stolt, S. Schneider, N. Mathur, M. J. Shearer, B. Rellinghaus, K. Nielsch, S. Jin, *Adv. Funct. Mater.* **2019**, *29*, 1805418.

[2] M. T. Birch, D. Cortés-Ortuño, L. A. Turnbull, M. N. Wilson, F. Groß, N. Träger, A. Laurenson, N. Bukin, S. H. Moody, M. Weigand, G. Schütz, H. Popescu, R. Fan, P. Steadman, J. A. T. Verezhak, G. Balakrishnan, J. C. Loudon, A. C. Twitchett-Harrison, O. Hovorka, H. Fangohr, F. Y. Ogrin, J. Gräfe, P. D. Hatton, *Nat. Commun.* **2020**, *11*, 1726.

Appendix 3: Supporting Information for Chapter 5*

Defect-Mediated Ferromagnetism in Correlated Two-Dimensional Transition Metal Phosphorus Trisulfides

Synthesis of hydroxide nanostructure precursors

Before the vapor conversion step to synthesize $Ni_{1-x}Co_xPS_3$ ($0 \leq x < 0.5$) nanosheets (NS) samples, the corresponding hydroxide nanostructure precursors were first grown on the carbon cloth. Before the growth process, the carbon cloth was cleaned using deionized (DI) water, ethanol (99.7%) and acetone (99.7%). The detailed procedures are as follows:

(1) The growth of $Ni(OH)_2$ NS. The ultrathin $Ni(OH)_2$ nanosheets (NS) were synthesized on the surface of the carbon cloth *via* a typical hydrothermal method[1, 2]. The cleaned carbon cloth (2 cm × 4 cm) was immersed in 33 mL aqueous solution containing ~1.25 mmol $Ni(NO_3)_2 \cdot 6H_2O$ (98%, Alfa Aesar) and ~2.50 mmol hexamethylenetetramine (HMT, Alfa Aesar) in a 50 mL teflon-steel autoclave. Then, the reaction was carried at 100 ºC for 10 h. After cooling the autoclave to the room temperature naturally, the products were dried at 60 ºC for the subsequent chemical vapor conversion step.

(2) The growth of $Ni_{1-x}Co_x(OH)_2$ nanosheets. In order to realize the uniform and composition tunable growth of $Ni_{1-x}Co_x(OH)_2$ ($0 < x < 0.5$) NS, we carried out an improved wet chemical growth method . First, around 1.0 g cetyltrimethyl ammonium bromide (CTAB, 99%, Aladdin) was dissolved in the mixed solution with 6 mL DI water and 30 mL ethanol (99.7 %). Then, the mixtures of $Ni(NO_3)_2 \cdot 6H_2O$ and $Co(NO_3)_2 \cdot 6H_2O$ (98-102%, Alfa Aesar) with various molar ratios were added and stirred for 15 min. Subsequently, the solution was transfer to a 50 mL teflon-steel autoclave and reacted on the carbon cloth at 140 ºC for 18 h. After cooling the autoclave to the room temperature naturally, the products were dried at 60 ºC for the subsequent chemical vapor conversion step.

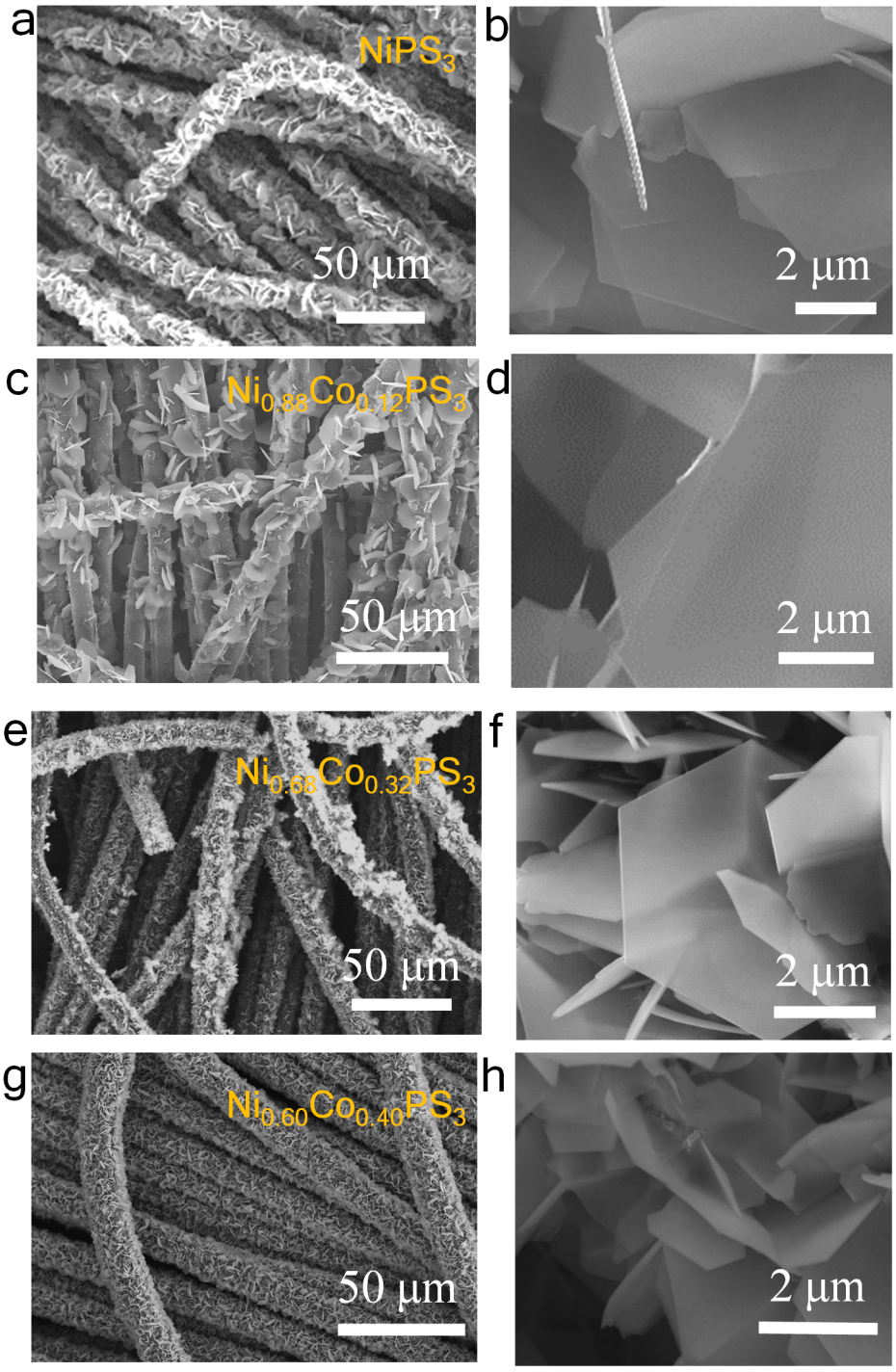

Figure A3.1: SEM images of the $Ni_{1-x}Co_xPS_3$ ($0 \leq x < 0.5$) NS grown on the surface of carbon cloth. a-b, $NiPS_3$ NS. c-d, $Ni_{0.88}Co_{0.12}PS_3$ NS. e-f, $Ni_{0.68}Co_{0.32}PS_3$ NS. g-h, $Ni_{0.60}Co_{0.40}PS_3$ NS.

a

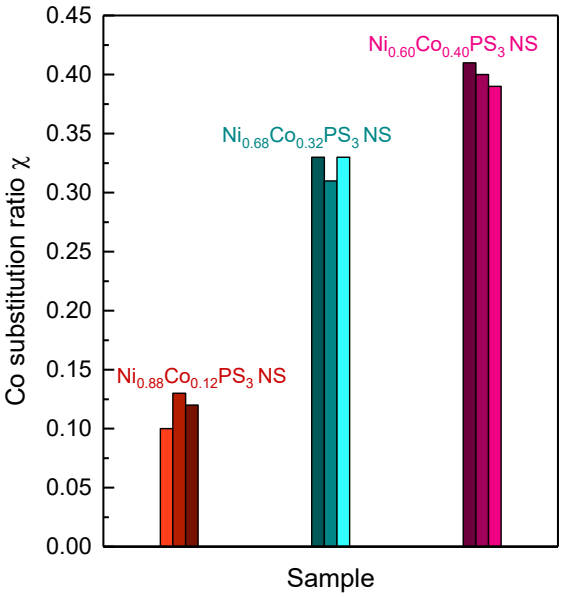

b

sample	*x*			Average	error
$Ni_{0.88}Co_{0.12}PS_3$ NS	0.13	0.12	0.11	0.12	0.010
$Ni_{0.68}Co_{0.32}PS_3$ NS	0.33	0.31	0.33	0.32	0.011
$Ni_{0.60}Co_{0.40}PS_3$ NS	0.41	0.40	0.39	0.40	0.010

Figure A3.2: The results of SEM-EDS composition analysis for a few NS from different as-grown $Ni_{1-x}Co_xPS_3$ ($0 \leq x < 0.5$) NS samples represented in the form of histograms to yield average value of *x*.

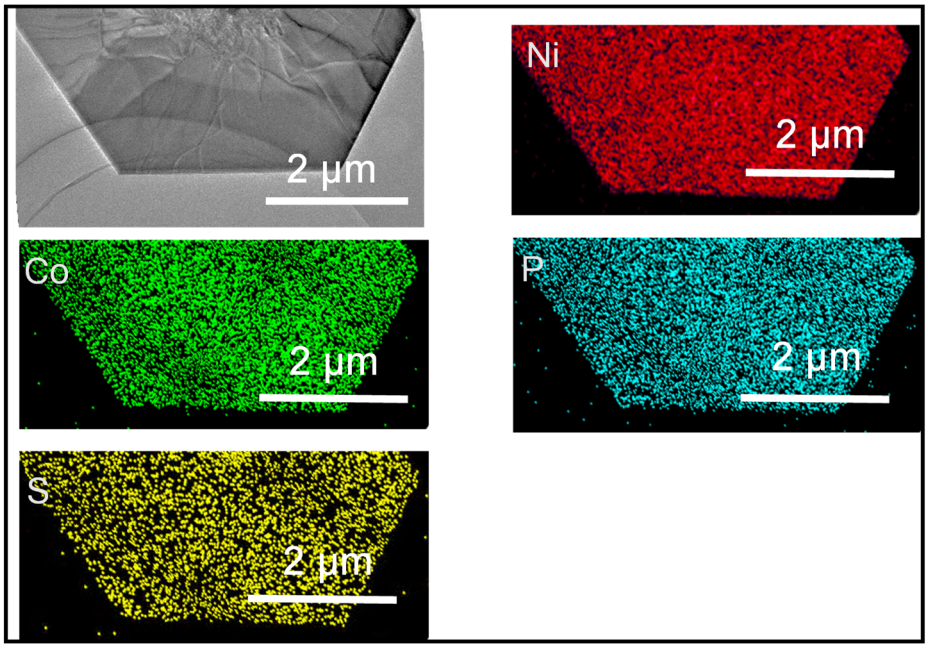

Figure A3.3: TEM image and the corresponding EDS spectral mapping of a $Ni_{0.60}Co_{0.40}PS_3$ nanosheet, demonstrating the uniform distribution of the Ni, Co, P, S elements.

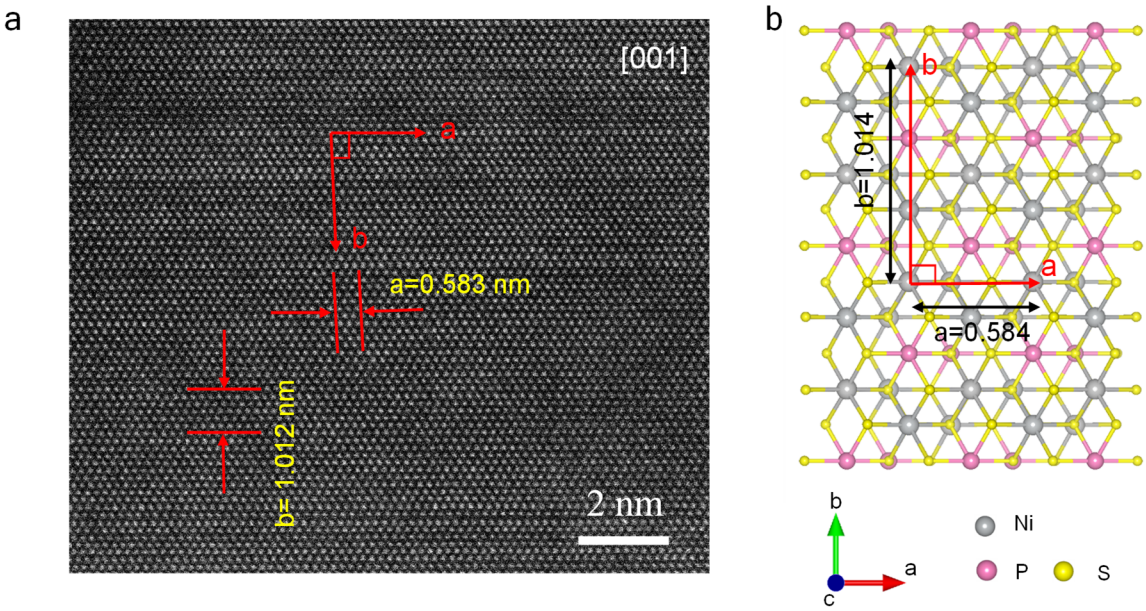

Figure A3.4 : HAADF-STEM image of a single $NiPS_3$ nanosheet marked with lattice parameters (*a* and *b*) of the unit cell and compared to the $NiPS_3$ structure model of the *ab* plane.

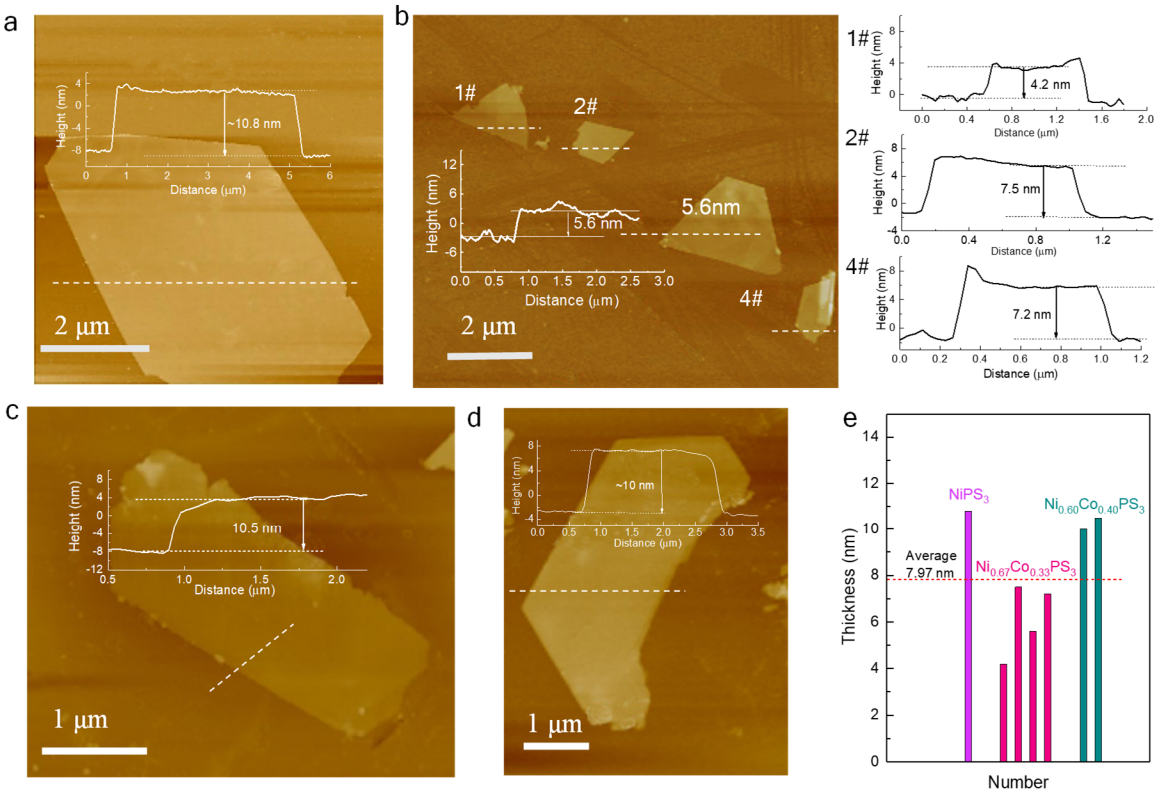

Figure A3.5: Thickness of various $Ni_{1-x}Co_xPS_3$ ($0 \leq x < 0.50$) NS. a-d, Atomic force microscopy images and the corresponding thickness line profiles of (**a**) $NiPS_3$, (**b**) $Ni_{0.68}Co_{0.32}PS_3$ and (**c-d**) $Ni_{0.60}Co_{0.40}PS_3$ NS transferred onto silicon substrates. **e**, The histogram representation of nanosheet's thickness shown in figure panels a-d yield an average thickness ~ 7.97 nm.

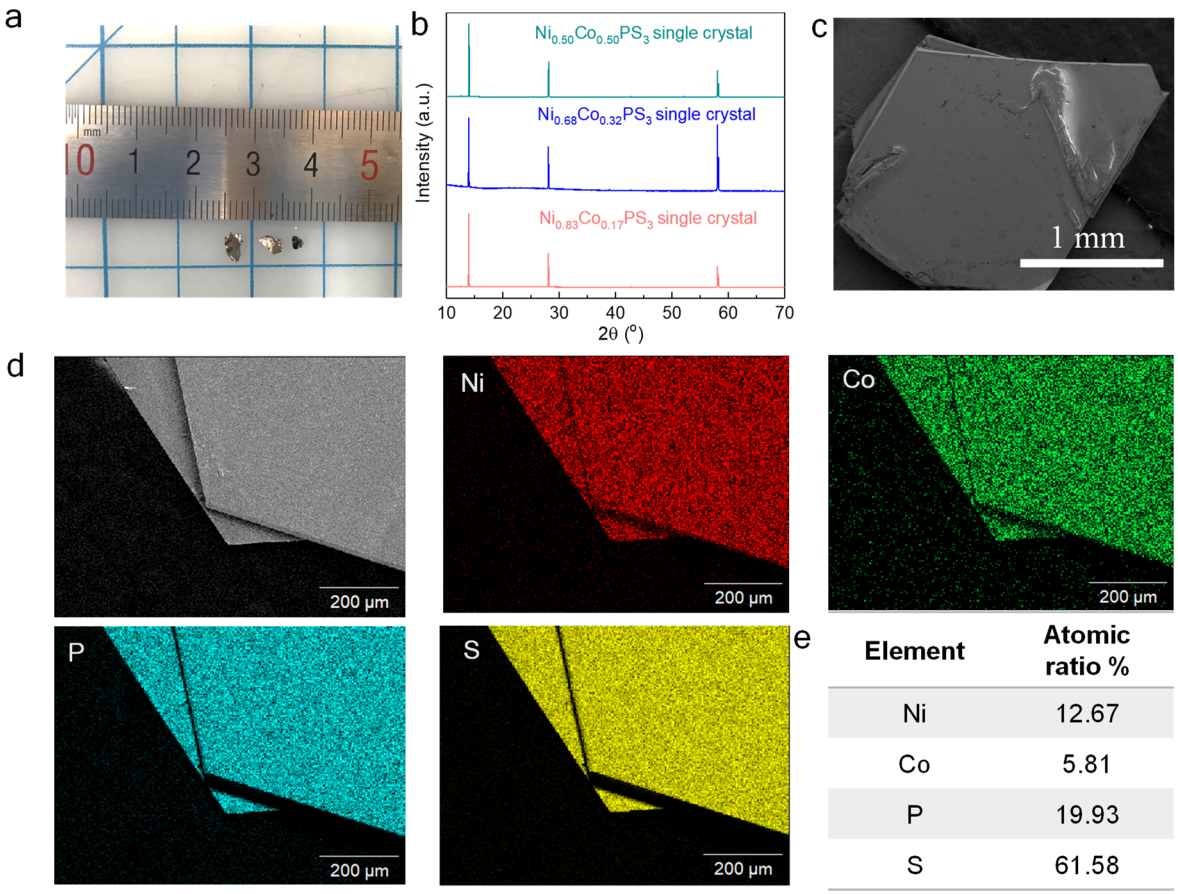

Element	Atomic ratio %
Ni	12.67
Co	5.81
P	19.93
S	61.58

Figure A3.6 : Characterization of $Ni_{1-x}Co_xPS_3$ single crystals synthesized *via* a chemical vapor transport (CVT) method. a, Photograph of various $Ni_{1-x}Co_xPS_3$ single crystals with the size of 0.2 – 0.5 cm. b, XRD patterns of the $Ni_{0.83}Co_{0.17}PS_3$, $Ni_{0.68}Co_{0.32}PS_3$ and $Ni_{0.50}Co_{0.50}PS_3$ single crystals. c, SEM image of $Ni_{0.68}Co_{0.32}PS_3$ single crystals. d-e, EDS spectral mapping of the $Ni_{0.68}Co_{0.32}PS_3$ single crystals from panel c with the elemental ratio.

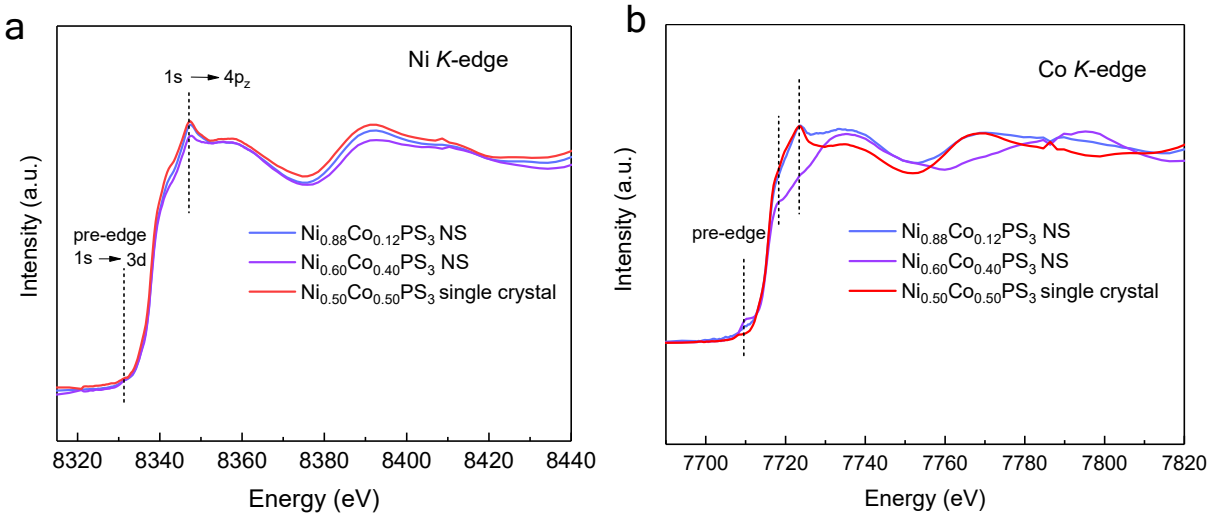

Figure A3.7: Comparison of NEXAS spectra from various $Ni_{1-x}Co_xPS_3$ samples. a, Ni *K*-edge and b, Co *K*-edge XANES spectra of $Ni_{1-x}Co_xPS_3$ (x=0.12, 0.40) NS and $Ni_{0.50}Co_{0.50}PS_3$ single crystals.

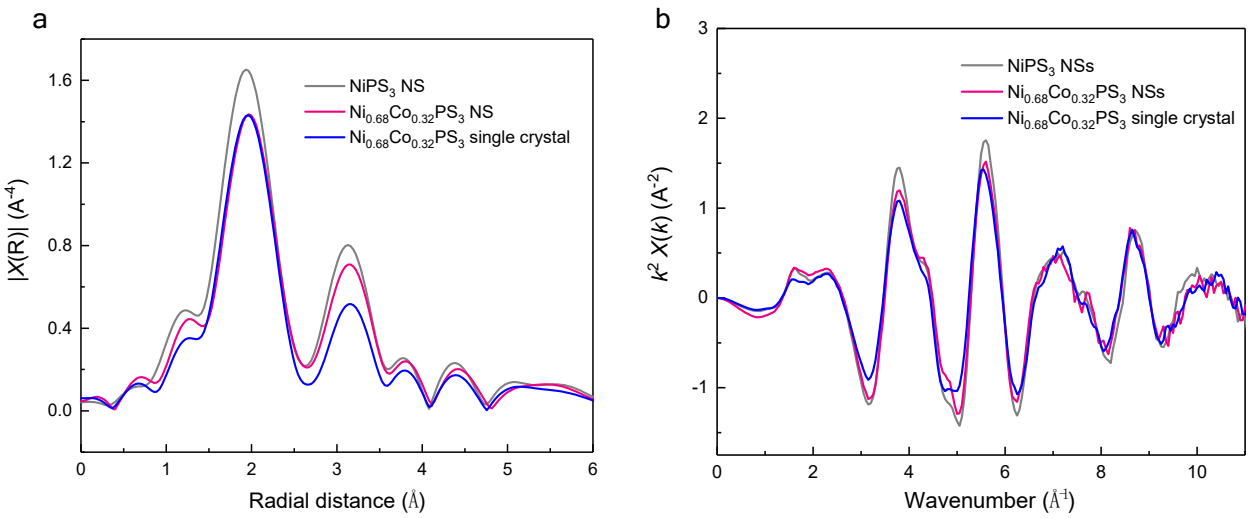

Figure A3.8 : The k^3-weighted Fourier transformation of Ni EXAFS spectra in a, *R* space and b, *k* space for $NiPS_3$ and $Ni_{0.68}Co_{0.32}PS_3$ NS and $Ni_{0.68}Co_{0.32}PS_3$ single crystals.

Table A3.1 **:** Best first shell (Ni-S) fitting of EXAFS data for different $Ni_{1-x}Co_xPS_3$ NS and single crystals[3]. The data range adopted for data fitting in *k*-space (Δk) and *R* space (ΔR) are 3-10.5 and 1-2.6 Å (S_o^2= 0.90, fitting k-weight= 3), respectively.

Sample	Shell	N[a] (standard)	CN[b] (EXAFS)	$R^{[c]}_{eff}$/Å (standard)	R[c]/Å (EXAFS)	ΔE_o [c]	σ^2 (10^{-3}, Å^2) [c]	*R*-factor[c]
$NiPS_3$ NS	Ni-S	6	5.85±1.07	2.424	2.454±0.006	2.067±0.872	8.67±0.8	0.011
$Ni_{0.68}Co_{0.32}PS_3$ NS	Ni-S	6	5.18±1.21	2.427	2.463±0.012	3.367±1.600	8.29±1.6	0.015
$Ni_{0.68}Co_{0.32}PS_3$ single crystal	Ni-S	6	5.92±1.31	2.427	2.448±0.011	2.261±1.605	8.43±1.9	0.024

[a] N (standard) is the theoretical coordination number of the absorbing Ni atom.

[b] CN is the coordination number of the absorbing Ni atom obtained through the first-shell fitting. The added uncertainty in the coordination number (CN) due to the estimation of S_o^2 has already been considered[3].

[c] R is the interatomic distance between the absorbing Ni atom and the backscattering S atom. σ^2 is the mean square relative displacement (i.e., the Debye-Waller factor). ΔE_0 is the energy shift parameter used to align the theoretical calculated spectrum to the energy grid of the measured spectrum. *R*-factor is goodness-of-fit parameter.

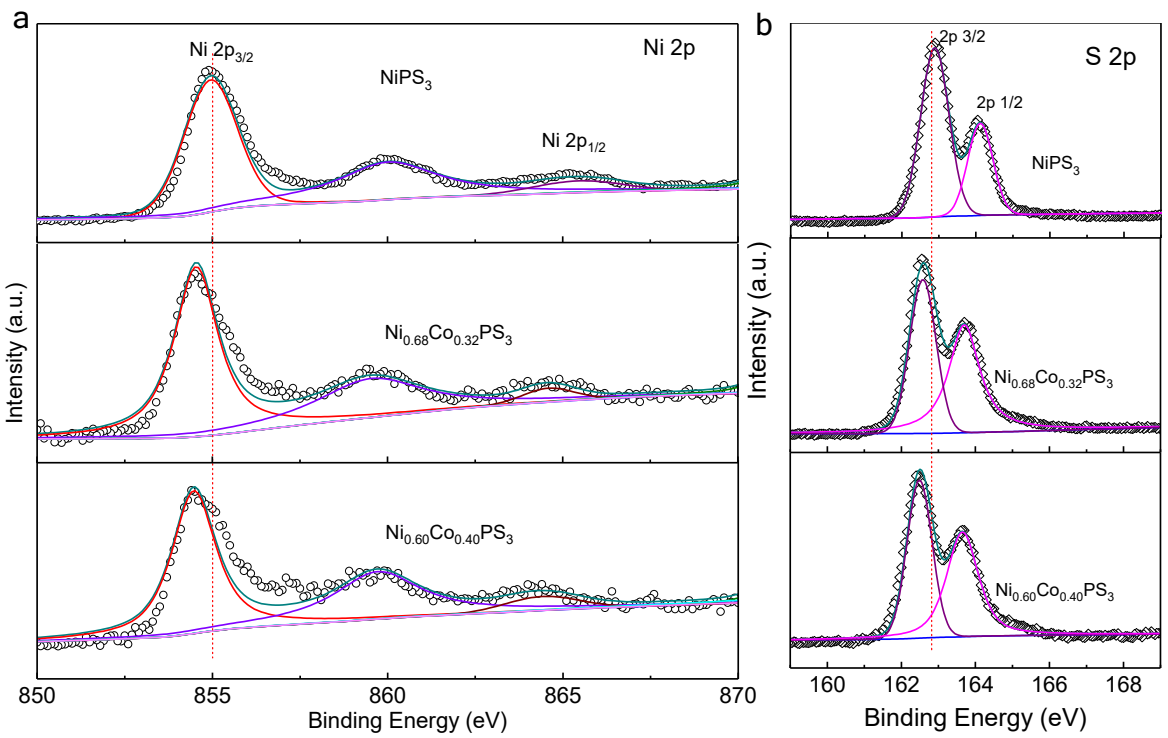

Figure A3.9 : XPS spectra of various $Ni_{1-x}Co_xPS_3$ ($0 \leq x < 0.5$) NS. The XPS high-revolution scan of a, Ni $2p_{3/2}$ and b, S 2p for $NiPS_3$, $Ni_{0.68}Co_{0.32}PS_3$ and $Ni_{0.60}Co_{0.40}PS_3$ NS.

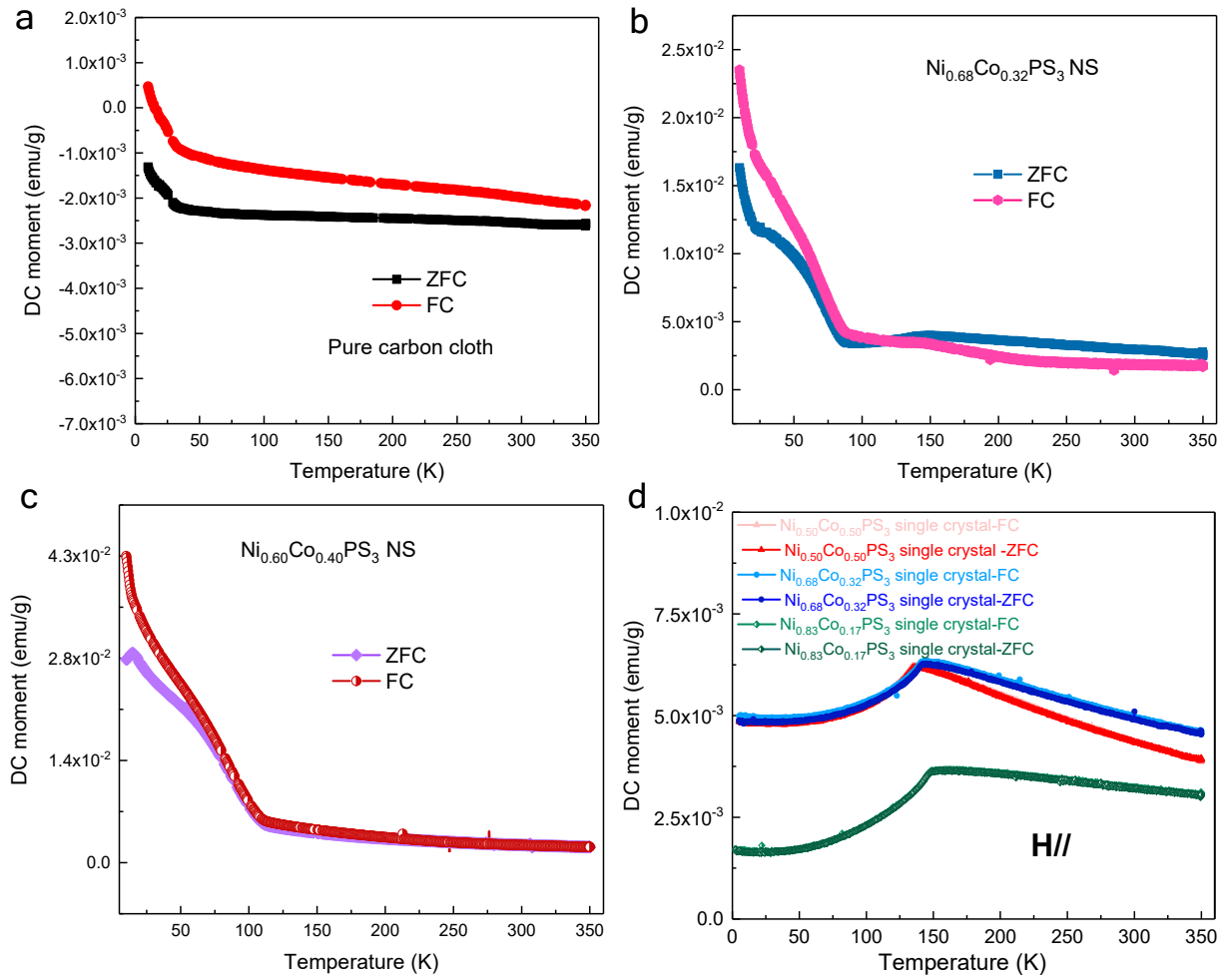

Figure A3.10 : Field cooled (FC) and zero field cooled (ZFC) *M-T* curves of a, pure carbon cloth, b, $Ni_{0.68}Co_{0.32}PS_3$ NS, c, $Ni_{0.60}Co_{0.40}PS_3$ NS, and d, $Ni_{1-x}Co_xPS_3$ (x= 0.17, 0.32, 0.50) single crystals. FC curves are obtained with applied magnetic field of 0.1 T.

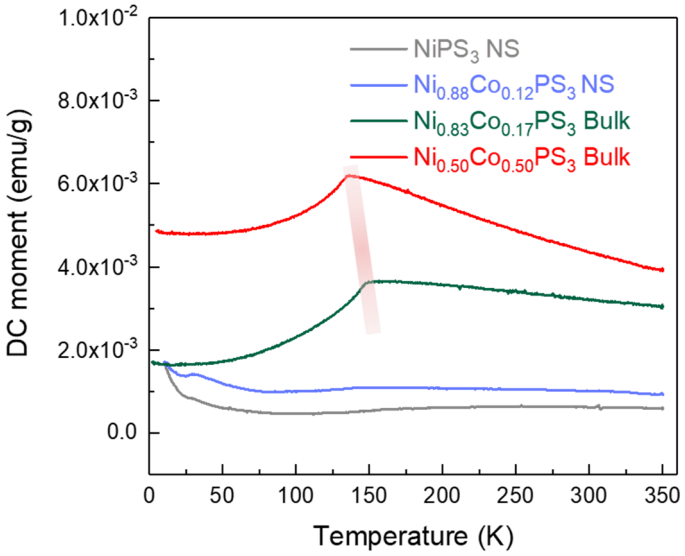

Figure A3.11: Zero field cooled (ZFC) *M-T* curves of $Ni_{1-x}Co_xPS_3$ (x = 0, 0.12) NS and $Ni_{1-x}Co_xPS_3$ (x =0.17, 0.50) single crystals.

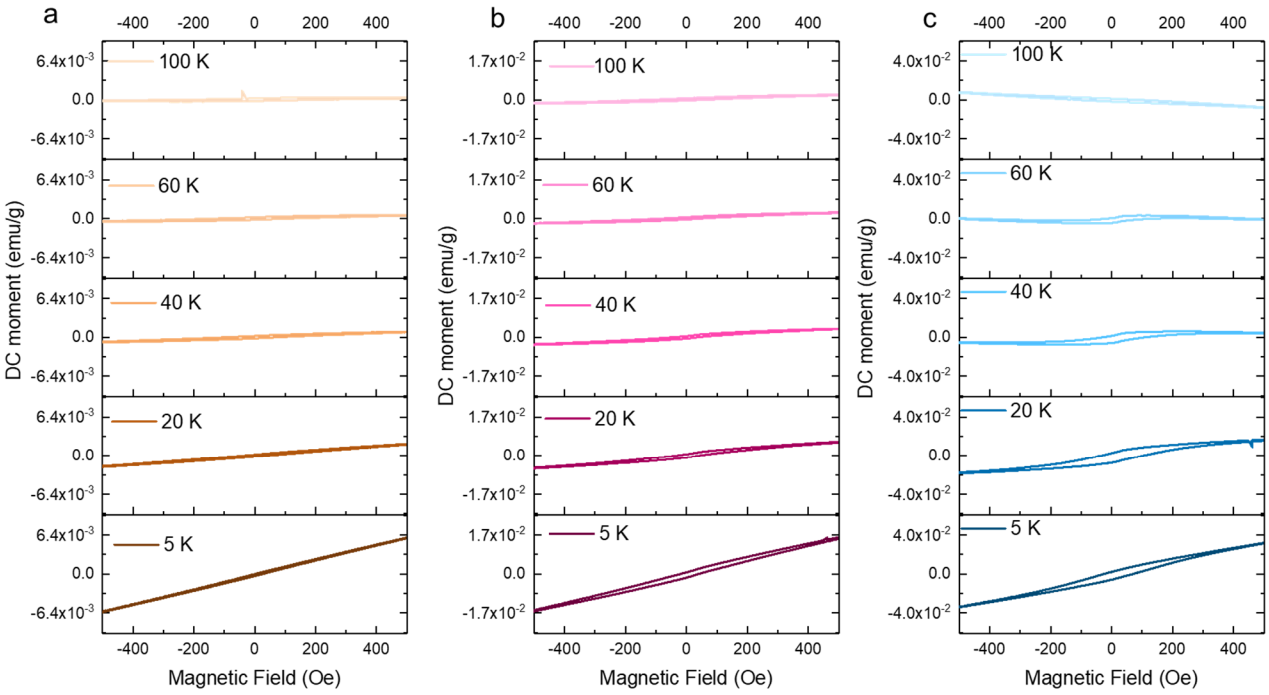

Figure A3.12**:** *M*-*H* curves of **a,** $NiPS_3$ **b,** $Ni_{0.88}Co_{0.12}PS_3$ **c,** $Ni_{0.68}Co_{0.32}PS_3$ NS at different temperatures. *H* (Oe) is the magnetic field applied to the sample and *M* is the corresponding magnetization.

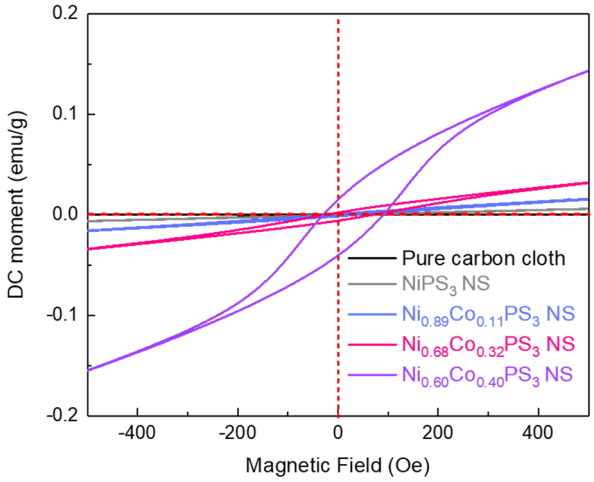

Figure A3.13 : Comparison of *M-H* curves collected from pure carbon cloth, $NiPS_3$, $Ni_{0.89}Co_{0.11}PS_3$, $Ni_{0.68}Co_{0.32}PS_3$, $Ni_{0.60}Co_{0.40}PS_3$ NS at 5 K.

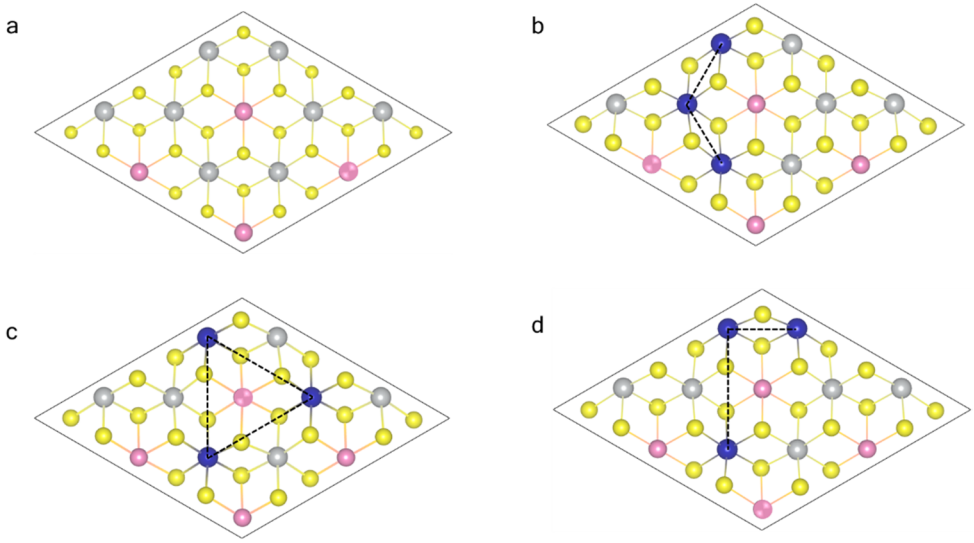

Figure A3.14 : a, A (2×2) supercell of pure $NiPS_3$ and three different Co substitution cases in $Ni_5Co_3P_8S_{24}$: b, chain substitution case (CS) c, triangle substitution case (TS) and d, right-angle substitution case (RS).

Table. A3.2: The total energy in chain substitution (CS), triangle substitution (TS) and right-angle substitution (RS) cases screened in $Ni_5Co_3P_8S_{24}$ by Co substitution, demonstrating that the CS case is the most stable one, which was used to calculate the *S* vacancy formation energy (E_v).

Substitution case	Total Energy (eV)
CS	-203.995
TS	-203.964
RS	-203.881

References

1. Wang, F.; Li, Y.; Shifa, T. A.; Liu, K.; Wang, F.; Wang, Z.; Xu, P.; Wang, Q.; He, J., Selenium-Enriched Nickel Selenide Nanosheets as a Robust Electrocatalyst for Hydrogen Generation. *Angew. Chem. Int. Ed.* **55**, 6919-6924 (2016).

2. Wang, F.; Shifa, T. A.; He, P.; Cheng, Z.; Chu, J.; Liu, Y.; Wang, Z.; Wang, F.; Wen, Y.; Liang, L.; He, J., Two-dimensional metal phosphorus trisulfide nanosheet with solar hydrogen-evolving activity. *Nano Energy* **40***,* 673-680 (2017).

3. Calvin, S., XAFS for Everyone. *Boca Raton: CRC Press*, 353-354 (2013).